Carbon-Based Materials for High-Power Accelerator Components Exposed to Extreme Radiation Conditions

Zur Erlangung des akademischen Grades Doktor-Ingenieur (Dr.-Ing.)
genehmigte Dissertation von Pascal Simon aus Groß-Gerau
Tag der Einreichung: 11. April 2023, Tag der Prüfung: 29. August 2023

1. Gutachten: Prof. Dr. Maria Eugenia Toimil-Molares
2. Gutachten: Prof. Dr. Gerhard Wilde
Darmstadt, Technische Universität Darmstadt

TECHNISCHE
UNIVERSITÄT
DARMSTADT

Fachbereich Material- und Geowissenschaften
Ionenstrahlmodifizierte Materialien

Carbon-Based Materials for High-Power Accelerator Components Exposed to
Extreme Radiation Conditions

Genehmigte Dissertation von Pascal Simon

Tag der Einreichung: 11. April 2023
Tag der Prüfung: 29. August 2023

Darmstadt, Technische Universität Darmstadt

Bitte zitieren Sie dieses Dokument als:
URN: urn:nbn:de:tuda-tuprints-246067
URL: https://tuprints.ulb.tu-darmstadt.de/24606
Jahr der Veröffentlichung auf TUprints: 2023

Dieses Dokument wird bereitgestellt von tuprints,
E-Publishing-Service der TUDarmstadt
https://tuprints.ulb.tu-darmstadt.de
tuprints@ulb.tu-darmstadt.de

Die Veröffentlichung steht unter folgender Creative Commons Lizenz:
Namensnennung – Nicht-kommerziell – Keine Bearbeitung 4.0 International
https://creativecommons.org/licenses/by-nc-nd/4.0/legalcode.de

Erklärung zur Dissertation

Hiermit versichere ich, die vorliegende Dissertation ohne Hilfe Dritter nur mit den angegebenen Quellen und Hilfsmitteln angefertigt zu haben. Alle Stellen, die aus Quellen entnommen wurden, sind als solche kenntlich gemacht. Diese Arbeit hat in gleicher oder ähnlicher Form noch keiner Prüfungsbehörde vorgelegen

Darmstadt, 13.10.2023

(Pascal Simon)

Abstract

The increasing beam power of next-generation particle accelerator facilities demands specific functional materials that can withstand extreme operation conditions, especially when interacting directly with the beam. These conditions include large thermal loads and mechanical stresses that are induced by high-intensity/high-power particle beams, which also induce radiation damage. In comparison to electron and proton accelerators, radiation damage is a particularly severe issue at heavy ion accelerators like the Facility for Antiproton and Ion Research (FAIR) under construction in Darmstadt. Carbon-based materials are commonly used in accelerator components. Graphite, for example, is employed in beam-intercepting devices like beam dumps and secondary particle production targets, while diamond is the active material in high-performance particle detectors. Both graphite and diamond are characterized by their large robustness towards radiation damage due to lower stopping power and lower activation in high-dose environments in comparison to metals. While structural radiation damage has been extensively studied in graphite and diamond, this thesis thus focuses (i) on the potential application of diamond-based composites for high-intensity heavy ion luminescence screens and (ii) on the effects of high-power single beam pulses on graphitic materials.

Diamond-based metal matrix composites, containing type Ib diamond powder, bulk monocrystalline type Ib and type IIa diamonds were irradiated with different swift heavy ions at the UNILAC accelerator of the GSI Helmholtz Centre for Heavy Ion Research, Darmstadt. On-line ionoluminescence spectroscopy was combined with in-situ UV/vis and infrared absorption spectroscopy to characterize the radiation-induced evolution of intrinsic and extrinsic defects within the diamond lattice. Radiation damage effects along the ion range were investigated with depth-resolved Raman and photoluminescence spectroscopy.

The ionoluminescence signal of diamond-based composite and type Ib diamond degraded rapidly under irradiation with swift heavy ions. UV/vis absorption spectroscopy showed no clear difference in the evolution of radiation-induced defects between type Ib and type IIa diamonds with increasing radiation fluence. While optical microscopy indicated severe loss of transmission in irradiated diamonds, significant increase of absorption occurred only at the highest ion fluences and is thus not contributing to the degradation of the ionoluminescence signal. Photoluminescence measurements along the ion trajectory reveal that color centers are produced predominantly in regions of high electronic energy loss. All color centers exhibit a non-linear trend with increasing radiation fluence that is attributed to a radiation-induced vacancy density threshold. In summary, the irradiation experiments performed on various diamond samples within this thesis indicate that diamond-based metal matrix composites have major drawbacks as a luminescence screen for high-intensity heavy ion beams.

To investigate the effects of high-power beam pulses, various graphitic materials were exposed to 440 GeV/c proton beams in a dedicated experiment at the High-Radiation to Materials (HiRadMat) facility at CERN. Such beams produce high local energy densities of a few $\mathrm{kJ\,cm^{-3}}$, which induce a dynamic response that is akin to a mechanical shock, which was monitored on-line via laser Doppler vibrometry.

Different polycrystalline graphite grades displayed a correlation between the mesostructure and damping of the beam-induced dynamic response. Smaller particle sizes and the absence of a binder phase decrease the damping of elastic pressure waves. Thermo-mechanical finite element simulations of the dynamic response of SGL R6650 polycrystalline graphite indicated a fully elastic material response up to the maximum beam intensity. Hence, these results demonstrate that this graphite grade can be safely used in the Superconducting Fragment Separator (Super-FRS) target at FAIR. A set of composite samples, that comprised tantalum cores embedded in different graphite shells, were used to create beam-induced stresses to potentially invoke failure in the graphite. The maximum surface velocity of the samples exhibited a non-linear trend with increasing beam-induced energy density within the tantalum cores, indicative of the onset of (local) failure within the graphite shells. The dynamic response of high-strength carbon-fiber reinforced graphite grades degraded more rapidly in comparison to lower strength material grades such as polycrystalline graphite or even low-density graphite foam. The broad overview of the beam-induced dynamic behavior presented within this thesis provides experimental validation of graphite grades for potential use in the FAIR accelerators and is a basis for the development of advanced material models for thermo-mechanical simulations of (anisotropic) graphite materials.

Zusammenfassung

Die stetig steigende Strahleistung moderner Teilchenbeschleuniger erfordert funktionale Materialien die unter extremsten Betriebsbedingungen standhalten, insbesonders bei der direkten Interaktion mit Partikelstrahlen. Dabei umfassen diese Bedingungen sowohl große thermische Lasten, mechanischen und thermischen Stress als auch Strahlenschäden, die allesamt durch intensive Hochleistungsstrahlen erzeugt werden. Im Vergleich zu Protonenbeschleuniger sind Strahlenschäden eine besonders große Herausforderung für Schwerionenbeschleuniger wie der Facility for Antiproton and Ion Research (FAIR) in Darmstadt. In verschiedensten Beschleunigerkomponenten finden sich dabei häufig kohlenstoffbasierte Materialien. Graphit wird z.B. in Beam Dumps oder Produktionstargets für Sekundärteilchenstrahlen verwendet, während in Teilchendetektoren Diamant als aktives Material eingesetzt wird. Graphit als auch Diamant besitzen aufgrund ihres niedrigen Bremsvermögen eine hohe Strahlenhärte gegenüber teilcheninduzierten Defekten, welche bereits umfangreich in beiden Materialien untersucht wurde. Ebenfalls von Vorteil in Hochdosisumgebungen ist der niedrige Aktivierungsquerschnitt von Graphit und Diamant im Vergleich zu Metallwerkstoffen. Diese Arbeit fokussiert sich zum einen auf die dynamischen Effekte hochintensiver Strahlpulse in Graphitwerkstoffen und zum anderen mit der möglichen Nutzung von Diamanten als Lumineszenschirm zur Strahldiagnose hochintensiver Schwerionenstrahlen.

Diamantbasierte Metal Matrix Komposite, produziert aus Typ Ib Diamantpulver, monokristalline Typ Ib und Typ IIa Diamanten wurden mit verschiedenen Schwerionen am UNILAC Beschleuniger des GSI Helmholtzzentrum für Schwerionenforschung in Darmstadt bestrahlt. Dabei wurde on-line Ionolumineszenz Spektroskopie mit in-situ UV/vis und Infrarot Absorptionsspektroskopie kombiniert, um die strahleninduzierte Änderung intrinsischer und extrinsischer Defekte im Diamantgitter zu charakterisieren. Strahleneffekte entlang der Eindringtiefe der Ionen wurden mit tiefenaufgelöster Raman und Photolumineszenz-Spektroskopie untersucht.

Das Ionolumineszenzsignal von diamantbasierten Kompositen und Typ Ib Diamanten nimmt während der Bestrahlung mit Schwerionen bereits bei niedrigen Ionenfluenzen rapide ab. Die strahlinduzierten Entwicklung von Defekten, die mit UV/vis Absorptionsspektroskopie untersucht wurden, ist nur geringfügig unterschiedlichen zwischen Typ Ib und Typ IIa Diamanten. Optische Mikroskopie von bestrahlten Diamanten zeigt deren strahlinduzierte Verfärbung, welche mit einem Transmissionsverlust einhergeht. Ein signifikanter Anstieg der Absorption wurde jedoch erst bei höchsten Fluenzen observiert, der daher nicht signifikant zur Abnahme der Ionolumineszenz beiträgt. Tiefenaufgelöste Photolumineszenzspektren zeigen, dass Farbzentren überwiegend in Bereichen von hohem elektronischen Energieverlusts erzeugt werden. Dabei besitzen alle untersuchten Farbzentren einen nichtlinearen Trend mit steigender Ionenfluenz, der durch einen Grenzwert strahlinduzierter Vakanzen erklärt wird. Die auf verschiedenen Diamantproben durchgeführten Bestrahlungsexperimente dieser Thesis weisen darauf hin, dass diamantbasierte Metal Matrix Komposite große Nachteile als Lumineszenschirme für hochintensive Schwerionenstrahlen besitzen.

Um die Effekte einzelner Hochleistungsstrahlpule zu untersuchen wurden verschiedene Graphitwerkstoffe in einem dediziertem Experiment an der High-Radiation to Material Facility (HiRadMat) am CERN mit 440 GeV/c Protonenstrahlen bestrahlt. Die dabei erzeugten Energiedichten im Bereich mehrer $\mathrm{kJ\,cm^{-3}}$ führen zu einer dynamischen Reaktion der bestrahlten Proben, die mit einem mechanischen Schock vergleichbar ist, und durch Laser Doppler Vibrometer on-line überwacht wurde.

Eine Korrelation zwischen Mesostruktur und Dämpfung der strahlinduzierten dynamischen Reaktion wurde in verschiedenen polykristallinen Graphiten observiert. Elastische Druckwellen werden von Materialien mit kleinerer Partikelgrößen weniger gedämpft, während eine zusätzliche Binderphase die Dämpfung erhöht. Thermomechanische Finite-Elemente-Simulationen von polykristallinem Graphit SGL R6650 zeigen eine elastische Materialreaktion bis hin zur maximalen Strahlintensität im Experiment. Diese Ergebnisse weisen darauf hin, dass dieser Graphitwerkstoff daher sicher im Produktionstarget des Superconducting Fragment Separator (Super-FRS) von FAIR benutzt werden kann. Kompositproben, bestehend aus verschiedenen Graphithüllen mit eingepressten Tantalkernen, wurden benutzt um strahlinduzierte Spannungen zu erzeugen, die möglicherweise zum Versagen der

Graphithülle führen. Die maximale Oberflächengeschwindigkeit dieser Proben zeigt eine nichtlineare Entwicklung mit steigender strahlinduzierter Energiedichte im Tantalkern, was auf das Einsetzen von (lokalem) Versagen der Graphithüllen zurückgeführt wird. Die dynamische Reaktion von hochfesten carbonfaserverstärktem Graphiten degradiert schneller im Vergleich zu weniger festen Materialien wie polykristallinem Graphit oder sogar niederdichtem Graphitschaum. Diese Arbeit zeigt eine breite Übersicht an Graphitwerkstoffen und deren strahlinduzierter dynamischer Reaktion und ist eine erste experimentelle Validation dieser Werkstoffe für eine mögliche Anwendung in der Beschleunigeranlage von FAIR und ist zum anderen eine Basis für die Entwicklung komplexer Materialmodelle für thermomechanische Simulationen von (anisotropen) Graphitmaterialien bei der Bestrahlung mit Hochleistungspulsen.

Contents

Abstract III

Zusammenfassung V

I Introduction 1

1 Motivation 3

2 Ion-Matter Interaction 7
- 2.1 Nuclear Energy Loss . . . 8
- 2.2 Electronic Energy Loss . . . 8
- 2.3 Absorbed Dose . . . 9
- 2.4 Ion Track Formation . . . 9
- 2.5 Nuclear Reactions . . . 11

3 Properties of Diamond and Graphite 13
- 3.1 Diamond . . . 13
- 3.2 Graphite . . . 16

II Luminescent Properties of Diamond under Swift Heavy Ion Irradiation 19

4 Diamond Accelerator Application and Interaction with Charged Particle Beams 21
- 4.1 Diamond Applications in Accelerators . . . 21
- 4.2 Ionoluminescence in Diamond . . . 22
- 4.3 Radiation Damage in Diamond . . . 23

5 Theory of Absorption and Optical Transitions 25
- 5.1 Optical Transitions . . . 25
- 5.2 Raman Scattering . . . 28

6 Experimental Details 31
- 6.1 Investigated Samples . . . 31
- 6.2 Irradiation Conditions and Experiments . . . 32
- 6.3 Depth-resolved Photoluminescence and Raman Spectroscopy . . . 36

7 Spectroscopic Investigation of Ion-Induced Effects in Diamond 39
- 7.1 Observations on Irradiated Diamonds and Diamond-based Metal Matrix Composites . . . 39
- 7.2 Ionoluminescence Spectroscopy . . . 40
- 7.3 Depth-resolved Photoluminescence Spectroscopy . . . 46
- 7.4 In-situ UV/vis Absorption Spectroscopy . . . 52
- 7.5 In-situ FT-IR Absorption Spectroscopy . . . 63

III High-Power Proton Irradiation on Graphitic Materials 67

8 High-Intensity and High-Power Accelerator Facilities 69
- 8.1 High-Power Facilities, Beam Conditions and Production Targets . . . 69
- 8.2 Material Choice for Beam Intercepting Devices . . . 70

9 Material Response to High-Power Beam Pulses 75
9.1 Phenomenological Description . . . 75
9.2 Energy Deposition, Thermal and Structural Effects . . . 76
9.3 Beam-induced Elastic Stress Waves . . . 78

10 HiRadMat FlexMat Experiment 85
10.1 HiRadMat Facility at CERN . . . 86
10.2 Experiment Layout . . . 87
10.3 Instrumentation and Data Acquisition . . . 92

11 Dynamic Response of Graphite Samples Irradiated with High-Power Proton Beams 95
11.1 Experimental Conditions . . . 95
11.2 Dynamic Response of Graphite Materials . . . 99
11.3 Dynamic Response of Tantalum-Core/Graphite Shell Samples . . . 110

IV Conclusions and Outlook 125

V Appendix 131

A Color Centers and Swift Heavy Ion Irradiation of Diamond 133
A.1 Crystallographic Defects and Color Centers in Diamond . . . 133
A.2 Photoluminescence Spectroscopy on Irradiated Diamond . . . 140

B High-Power Proton Beam Irradiation 145
B.1 Overview of Materials Irradiated with High-Power Proton Beams . . . 145
B.2 Geometry Measurement of the FlexMat Experiment . . . 151
B.3 Dynamic Response of Anisotropic Graphite Irradiated with High-Power Proton Beams . . . 151
B.4 Finite Element Analysis Workflow . . . 155
B.5 Numerical Analysis of Beam-Induced Dynamic Response . . . 157

Abbreviations IX

List of Figures XIII

List of Tables XXIII

Bibliography XXV

Part I.
Introduction

1 Motivation

Next-generation facilities like the Facility for Antiproton and Ion Research (FAIR) are continuously pushing the limit of beam energy and intensity beyond the current state of the art. FAIR, which is presently under construction at the GSI Helmholtz Centre for Heavy Ion Research, will push the intensity limit for relativistic heavy ion beams by orders of magnitude. In combination with the continuous effort to reduce the length of particle pulses, FAIR - or modern particle accelerators like the Large Hadron Collider (LHC) at CERN - reach beam powers up to the TW level.

Beam-intercepting devices, accelerators components that are directly interacting with beams, are therefore operating under very harsh conditions. Energy will be deposited by interaction with the beam in the component. Such processes can induce radiation damage, which leads to the degradation of thermal transport or mechanical material properties. This is especially compounded in heavy ion machines like FAIR, as higher particle mass leads to both increased energy deposition per unit length and increased radiation damage in comparison to lighter ions or hadrons at equal energies. Depending on the volume the energy is deposited in, which is determined by the transverse beam size and penetration depth of the particles, and timescales, which can be as small as a few tens of nanoseconds at modern pulsed facilities like FAIR, rapid increase of the temperature in the interaction volume can induce thermal stresses, that will propagate as (elastic) stress waves through the material.

In this context, graphite is one of the most commonly used material in beam-intercepting devices as well as fission and fusion applications [1–3]. The energy deposition of charged particles scales with the atomic number Z of the (target) material which is much smaller for graphite in comparison to most engineering metals [4]. High-purity graphite is also favorable in terms of radiation protection due to its low nuclear reaction cross section and the small decay time of the produced radioisotopes during interaction with high-energy particle radiation [5]. Moreover, its high thermal conductivity allows efficient heat transfer away from the volume interacting with the beam [6]. Graphite also has excellent thermal shock resistance due to its high specific heat, small coefficient of thermal expansion and small Young's modulus which make it well-suited for pulsed operation conditions [1, 7]. Albeit, graphite cannot accommodate plastic deformation as well as metals due to its brittleness [8, 9]. Another important aspect for accelerator operation is compatibility with ultra-high vacuum and service temperatures in vacuum in excess of thousands of Kelvins.

But graphite is not the only carbon allotrope that is commonly found in accelerator components. Diamond has emerged as a state of the art material for particle detectors since advances in chemical vapor deposition (CVD) processes have increased the availability of large volume, high purity samples [10]. Diamond-based particle detectors will be used in several FAIR experiments, e.g., R^3B at the Super-FRS or Compressed Baryonic Matter (CBM) experiment and is already in use at the High Acceptance Di-Electron Spectrometer (HADES) experiment at GSI [11, 12]. In comparison to silicon, diamond has a high charge collection efficiency and small signal rise time, which make it an ideal detector material for time of flight or fast beam loss measurements [13, 14].

Due to their different lattice structure, diamond and graphite have diametrically opposed material properties. Graphite consists of sp^2-hybridized carbon atoms in threefold planar coordination while diamond consists of sp^3-hybridized carbon atoms in fourfold tetrahedral coordination. Thus, graphite is opaque while diamond is transparent, graphite is an electrical conductor while diamond is an insulator, graphite is soft and diamond is hard, graphite is orthotropic while diamond is isotropic. Nonetheless, diamond and graphite share common properties. Due to the strong covalent bonds in either hybridizations, thermal conductivity is largely phonon-dominated in both materials, which makes diamond the insulator with the highest thermal conductivity, . Considering the low atomic number of carbon, the strong bonds also lead to large displacement energies which make both graphite and diamond more radiation-hard towards elastic nuclear collisions in comparison to metals lighter than copper [15].

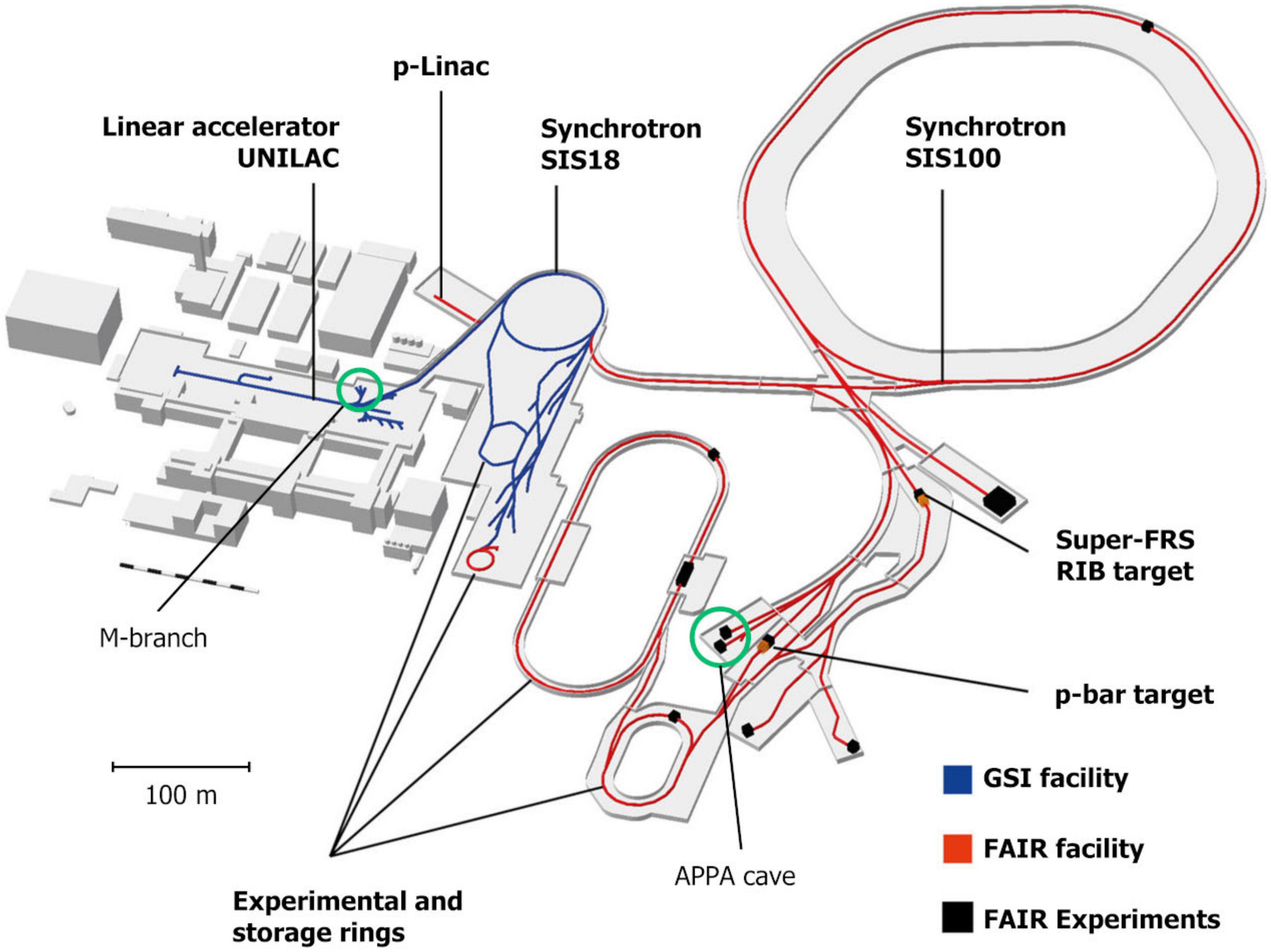

Figure 1.1.: Layout of the existing GSI (blue) and FAIR (red) accelerator facilities. High-power rare-isotope (RIB) and antiproton (p-bar) targets that will be exposed to high-power beam conditions are indicated. Swift heavy ion irradiation experiments presented in this work were performed at the M-branch. APPA cave will host new materials research beamline for relativistic heavy ion beams from the future SIS100 accelerator.

This thesis will focus on two very different applications of carbon: (i) diamond as radiation-hard luminescence screen and (ii) graphite as material for beam-intercepting devices.

(i) Few studies reported luminescence of diamond under charged particle irradiation [16–22]. Since swift heavy ion irradiation is not leading to ion track formation in diamonds [23], diamond-metal composite [24] is a potential candidate for luminescence screen beam diagnostics of high-intensity swift heavy ion beams. The current-generation of chromium-doped alumina luminescence screens are already at their limit with the beam intensities available at the existing GSI facilities [25].

(ii) Swift heavy ion-induced modification of thermal, electrical, mechanical and structural properties has been extensively characterized for graphite [6, 26–28]. Few graphite material grades were already tested in high-power beam impact experiments to study beam-induced thermal shocks [29, 30]. Beam impacts are highly non-linear events, that are characterized by strain rates of the order of a few hundred per second and (quasi-)instantaneous heating that induces peak temperatures beyond thousand Kelvin in a few microseconds. Hence, the description of such events relies heavily on finite element simulations that require precise knowledge of material properties [31]. But, the material properties of graphite – or more generally speaking graphitic materials – are heavily dependent on the specific production parameters which influence nearly all thermo-mechanical properties. Graphite grades are characterized by varying density and porosity, degree of graphitization and degree of anisotropy. For example, graphite grades relevant for this work have densities between ∼25 % to ∼100 % relative to the ideal density of graphite.

One aim of this thesis is to study the evolution of ion-induced luminescence in diamonds with increasing swift heavy ion irradiation. This is complemented by various spectroscopic measurements to identify ion-induced structural modifications. The overall goal is to quantify the light yield and especially its robustness towards ion irradiation to qualify different diamond grades as a material for beam diagnostic luminescence screens at FAIR and identify the defects involved in the luminescence.

The second aim is to study the influence of mesoscopic material properties like density, porosity and degree of graphitization and/or anisotropy towards the dynamic response during high power proton beam impacts. Studied materials include polycrystalline graphite grades that are relevant for the Super-FRS production targets and beam dumps at FAIR in addition to various other graphitic materials used in the accelerator complex at CERN.

This work is organized in three parts. The first part introduces the basic principles of ion-matter interaction and describes the general properties of graphite and diamond. Part two reports on the characterization of diamonds both during and after irradiation with swift heavy ion beams. These include on-line ionoluminescence measurements excited by 4.8 MeV/n swift heavy ion beams, in-situ UV/vis & infrared absorption and post-irradiation photoluminescence spectroscopy. Together with the theoretical basics, important crystallographic defects in the diamond lattice are described in detail that are of importance for the discussion of the obtained results. The third part describes a high-power beam impact experiment on graphite materials with 440 GeV/c proton beams. Ideal material parameters for beam-intercepting devices in the context of state-of-the-art high intensity, high power accelerator facilities are reviewed. The dynamic response of materials towards short pulse beam impacts is phenomenologically introduced and a mathematical model to describe such events is described. The design of an experimental platform with on-line measurement devices and numerical tools for data analysis are presented. Experimental data is compared to finite element simulations and used to directly extract mechanical material parameters of isotropic materials. The damping behavior is quantified and compared between different graphite grades and discussed with respect to the mesoscopic material structure.

2 Ion-Matter Interaction

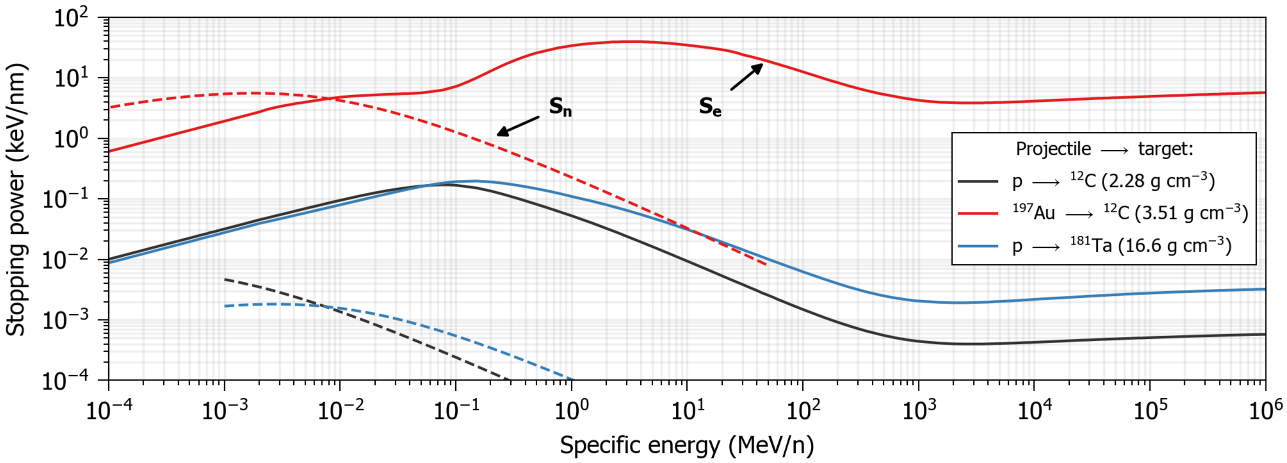

Figure 2.1.: Stopping power of ^{197}Au and protons as a function of specific energy in three different target materials. Solid lines represent the stopping power due to electronic energy loss (ionizing energy loss). Dashed lines represent the stopping power due to nuclear energy loss (non-ionizing energy loss). Calculated using SRIM-2013 [32].

When an accelerated charged particle/ion penetrates matter it loses energy along its path until it comes to rest. The energy deposition in the (target) material can be described by the average loss of kinetic energy, E, per unit path length, x, which is simply the linear energy loss $\mathrm{d}E/\mathrm{d}x$ of the projectile. Energy is lost in the target material by different processes depending on the energy of the projectile. To compare ions of different atomic mass number A, the specific energy E/A in units of MeV/n (kinetic energy per nucleon) is customarily used in place of the kinetic energy. Non-relativistic ions of different mass, but identical specific energy, have the same velocity. Nonetheless, since all following effects scale linearly with both specific and kinetic energy the following chapter will use the two terms interchangeably.

At low energies, the projectile interacts with the target nuclei by elastic collisions. This so-called nuclear energy loss results in a collision cascade and displacement of target atoms. At projectile energies larger than $\sim$0.1 MeV/n, energy is lost by inelastic interaction of the projectile with the target electrons. Electronic energy loss results in the electronic excitation and ionization of the target atoms. The evolution of nuclear and electronic energy loss for two different projectiles is shown in Figure 2.1, which clearly illustrates the different energy loss regimes as a function of specific energy. Furthermore, at relativistic ion energies, energy is lost by the production of photons by bremsstrahlung or Cherenkov radiation. At ion energies above the Coulomb barrier of the target material, the projectile has enough energy to overcome the electrostatic repulsive force of the target nuclei and can induce nuclear reactions by strong force interaction. Hence, the total energy loss of a charged particle can be described as:

$$\frac{\mathrm{d}E}{\mathrm{d}x} = \left(\frac{\mathrm{d}E}{\mathrm{d}x}\right)_{\text{nuclear}} + \left(\frac{\mathrm{d}E}{\mathrm{d}x}\right)_{\text{electronic}} + \left(\frac{\mathrm{d}E}{\mathrm{d}x}\right)_{\text{radiation}} . \tag{2.1}$$

Since the energy that is lost by the projectile is deposited in the target material, the stopping power $S(E)$ of a target material is simply[1]:

$$S(E) = -\left(\frac{\mathrm{d}E}{\mathrm{d}x}\right). \tag{2.2}$$

---

[1] This thesis will use the terms energy loss, stopping power and deposited energy interchangeably for the energy deposited in the target.

Radiative losses, which are responsible for the increase in energy loss beyond ∼1000 MeV/n that is observed in Figure 2.1, are ignored in this section, because the projectiles relevant for this thesis did not exceed energies at which radiative losses play a dominant role. The following sections introduce nuclear energy loss, electronic energy loss and qualtitatively discuss the role of nuclear reactions at relativistic energies.

2.1 Nuclear Energy Loss

Nuclear energy loss (non-ionizing energy loss) is the dominating interaction mechanism for the deceleration of the projectile in the last hundreds of nm of the projectile range. Low energy ion projectiles interact by elastic collision with the target atoms. If the energy transfer to a target atom is larger than the displacement energy, the target atom is displaced from its lattice position thereby producing a vacancy/interstitial pair. If the energy transfer is even larger, the initially displaced atom, the so-called primary knock-on atom, can interact with other target atoms and induce a collision cascade producing numerous vacancy/interstitial pairs, the so-called secondary knock-on atoms.

The extent of the collision cascade mainly depends on the energy and mass of the projectile, while the displacement energy depends on the structure and composition of the target. At energy transfers below the displacement energy, the energy is transferred into the phonon subsystem and subsequent macroscopic heating of the target material.

2.2 Electronic Energy Loss

For projectile energies in the MeV to GeV range, electronic energy loss (ionizing energy loss) is the dominating mechanism. Due to the high velocity of the projectile, the interaction time with the target atoms is small. Kinetic energy of the projectile is transferred to the target electron subsystem, consisting of electrons with considerably smaller mass and therefore smaller inertia than the target atoms. The maximum energy transfer ΔE_{max} for the impact between a heavy charged particle with mass M and kinetic energy E and an orbital electron with mass m_{e} can be approximated by the Rutherford scattering formula [33]:

$$\Delta E_{\mathrm{max}} = 4\frac{m_{\mathrm{e}}M}{(m_{\mathrm{e}}+M)^2}E \approx 4\frac{m_{\mathrm{e}}}{M}E. \tag{2.3}$$

The collision between a 4.8 MeV/n ^{197}Au projectile and an electron (at rest) will result in a maximum energy transfer of ∼10 keV to the electron. These so-called δ- or primary-electrons can induce further excitation and ionization of other target atoms. This leads to an electron cascade with additional secondary electrons.

Due to the small maximum energy transfer in a single collision, the energy loss occurs in many collisions with only a small transfer of energy over a long distance. The average energy loss per unit length by electronic stopping can be described by the relativistic Bethe-Bloch formula [34–36]:

$$-\left(\frac{\mathrm{d}E}{\mathrm{d}x}\right)_{\mathrm{electronic}} = 4\pi e^4 \frac{Z_{\mathrm{p,eff}}^2 Z_{\mathrm{t}} N_{\mathrm{t}}}{m_{\mathrm{e}} v_{\mathrm{p}}^2}\left(\ln\frac{2m_{\mathrm{e}}v_{\mathrm{p}}^2}{I_{\mathrm{t}}} - \ln(1-\beta) - \beta^2\right), \tag{2.4}$$

where e is the elementary charge, $Z_{\mathrm{p,eff}}$ is the effective charge state of the projectile, Z_{t} the atomic number of the target, N_{t} the target density, v_{p} the projectile velocity, m_{e} the electron mass, I_{t} the effective ionization potential of the target and β the ratio of the projectile velocity and the speed of light, c ($\beta = v_{\mathrm{p}}/c$).

For heavy ions with large Z_{p} the effective charge state is a function of the projectile velocity. According to Bohr's stripping theorem, all projectile electrons with orbital velocities v_{e} smaller than the projectile velocity v_{p} will be stripped off the projectile in the target resulting in a change of the charge state [37, 38]. The projectile has a statistical net charge $Z_{\mathrm{p,eff}}$ due to electrons being lost by stripping and captured by the attractive force of the nucleus, that is smaller than the atomic number Z_{p} of the projectile. The relation between projectile velocity and effective charge state of the projectile is described by Bohr's stripping theorem [39]:

$$Z_{\mathrm{p,eff}} = Z_{\mathrm{p}}\left(1-\exp\left(-\frac{v_{\mathrm{p}}}{v_0}Z_{\mathrm{p}}^{-\frac{2}{3}}\right)\right), \tag{2.5}$$

where Z_p is the atomic number of the projectile and v_0 the Bohr velocity ($v_0 = 2\pi e/h$ with h being Planck's constant).

After the projectile has entered a target, it is decelerated and, for initial projectile energies below ∼1000 MeV/n, the energy loss increases with the inverse projectile energy $1/E$ until a maximum of electronic energy loss, the so-called Bragg peak, is reached. For the heavy ion projectiles used in this thesis, the Bragg peak is at a specific energy between 3 and 5 MeV/n. For protons the Bragg peak is at about 0.1 MeV. For smaller projectile energies and further deceleration of the projectile the electronic energy loss decreases with the square root of the projectile energy $\sqrt{E}$ as described by the Lindhard-Scharff-Schiøtt (LSS) theory [40].

2.3 Absorbed Dose

To compare the absolute effect of irradiation with different charged particles, the total deposited energy has to be considered which is a product of both the number of ion projectiles impinging on the target per unit area, the fluence Φ, and energy loss of the ion projectiles. Since ions of different mass have different stopping powers at equal momentum (or equal stopping power at different momenta) a more useful metric is the absorbed dose. The absorbed dose, with its SI unit gray Gy, refers to the energy deposited by (ionizing) radiation per unit mass of the target matter $\Delta E/\Delta m$. For a charged particle, that is stopped within the target, the absorbed dose D is calculated by:

$$D = \frac{E}{L} \cdot \Phi \cdot \frac{1}{\rho}, \tag{2.6}$$

where E is the total energy of the projectile, L the range of the projectile in the target and ρ the target density. This equation just represents the average absorbed dose deposited within the radiation-affected volume. Depending on the stopping power along the projectile penetration depth, the absorbed dose can locally vary. Hence, the stopping power, $\mathrm{d}E/\mathrm{d}x$, can be used to directly calculate the dose profile as a function of depth, x:

$$D(x) = \frac{\mathrm{d}E}{\mathrm{d}x}(x) \cdot \Phi \cdot \frac{1}{\rho}. \tag{2.7}$$

2.4 Ion Track Formation

The energy deposition by electronic energy loss is exciting a cylindrical volume with a radial energy deposition that falls off with $1/r^2$ where r is the radius from the center of the ion trajectory [41]. The maximum diameter of this excitation cylinder is determined by the mean free path length of the highest energy δ-electrons produced by electronic energy loss (c.f. Equation 2.3). If the deposited energy density locally exceeds a threshold value, which depends on the target material, an ion track is produced. This ion track is a cylindrical region of amorphous (or more generalized, damaged) material. The exact mechanism of track formation is quite complex and not fully understood.

Qualitatively, in the regime of electronic energy loss the projectile ion transfers its kinetic energy to the electrons of the target atoms on timescales between 10^{-17} and 10^{-16} s. The δ-electrons induce further ionization of other target atoms resulting in an ionization cascade with a duration of 10^{-15} and 10^{-14} s [42]. Between 10^{-13} and 10^{-10} s the highly excited electronic subsystem is coupling its energy to the atomic lattice by the excitation of phonons. Depending on the energy density this results in the formation of defects, defect clusters and heating of the lattice, potentially beyond its melting point. The energy transfer process between the electrons and the atomic lattice and how the final track is generated are still disputed and a topic of research. Two models, the Coulomb explosion model [43] and the inelastic thermal-spike model [44, 45], try to quantitatively describe these processes. Except, only the inelastic thermal spike model is able to describe and predict the creation of ion tracks in many different materials [46].

The inelastic thermal-spike splits the target material in two thermal subsystems to describe ion track formation by electronic energy loss. The electronic subsystem and the lattice (or phonon) subsystem. Assuming that the temperature gradient is purely in the radial direction, the two subsystems can be mathematically described by two coupled thermal diffusion equations in cylindrical coordinates where r is the radial distance from the ion trajectory:

$$C_e(T_e)\frac{\partial T_e}{\partial t} = -\frac{1}{r}\frac{\partial}{\partial r}\left(rK_e(T_e)\frac{\partial T_e(r,t)}{\partial r}\right) - g(T_e - T_a) + A(r,t), \tag{2.8}$$

$$C_a(T_a)\frac{\partial T_a}{\partial t} = -\frac{1}{r}\frac{\partial}{\partial r}\left(rK_a(T_a)\frac{\partial T_a(r,t)}{\partial r}\right) + g(T_e - T_a). \tag{2.9}$$

$T_{e,a}$, $C_{e,a}$ and $K_{e,a}$ are the temperature, specific heat and thermal conductivity of the electron and lattice subsystem, respectively. The heat source term $A(r,t)$ describes the radial profile of the energy deposition by the projectile ion within the electron subsystem and is derived from the radial energy distribution of δ-electrons [41]. The energy dissipates as heat in the electron subsystem and is eventually transferred into the lattice subsystem. The efficiency of heat transfer between the two systems is described by the electron-phonon coupling strength g, lower coupling strength indicates less efficient heat transfer from the electron to the lattice subsystem. Ultimately, ion track formation is defined as the radial area around the ion trajectory where the lattice temperature T_a exceeds the melting temperature of the target material. Rapid quenching then freezes the molten zone into an amorphous ion track. The initial energy transfer to the lattice can be used as an input for molecular dynamics simulations to investigate the structure in and around ion tracks. A variety of experimental data of amorphous tracks in insulators is well described by the inelastic thermal spike model. The model also indicates that the electron phonon coupling strength g of insulators is approximately proportional to the square of the band gap $g \approx E_g^2$ [47].

But, there are also drawbacks to the inelastic thermal spike model. On the spatiotemporal scales involved in the model, macroscopic heat diffusion laws and equilibrium material properties are not directly applicable. An equilibrium temperature T should not be considered for a process that is far from thermodynamic equilibrium on a timescale of a few ps. Also, g is a free parameter in the model that allows to simply fit the model to experimental data [48].

2.4.1 Models of Radiation-induced Material Modifications

Ion irradiation will lead to the creation of defects along the trajectory of the ion through the target material. Depending on the nature of the defects, their production and the sensitivity of the material, radiation-induced modification can be approximated by various models.

For sake of simplicity, let's assume that the electronic energy loss of the projectile is large enough to induce amorphous ion tracks in a sample. These are approximated by a cylindrical volume with diameter r where the material inside r is fully amorphized and the material outside r is unaffected. Assuming that the radius r is constant along the ion penetration depth, every ion hitting the surface of a target is hence producing an amorphous area of cross section $\sigma_d = \pi r^2$. Overlapping ion tracks will not fully contribute to additional amorphization. The total area of the sample is $A_0 = A_v + A_a$, where A_v is the pristine area and $A_a = n\sigma_d/A_0$ is the damaged area produced by n ions. This is schematically illustrated in Figure 2.2b. At small number of ions, every ion contributes σ_d to increasing A_a. With increasing n the chances of overlapping ion hits is increasing, so only a fraction of σ_d is contributing to the surface coverage per ion. Hence, the pristine area A_v will decrease as a function of fluence (number of ions per unit area A), $\Phi = n/A$:

$$\mathrm{d}A_v = -A_0\sigma_d \mathrm{d}\Phi. \tag{2.10}$$

Under the assumption that ion hits are randomly (Poisson) distributed on the surface of the irradiated material, the solution to Equation 2.10 is:

$$f_a(\Phi) = 1 - e^{-\sigma_d \Phi}, \tag{2.11}$$

where f_a is the fraction A_a/A_0. Equation 2.11 is shown as the single impact model in Figure 2.2a. Even though this model was derived for radiation-induced amorphization it can be broadly applied to radiation-induced material degradation. Even in the abscence of an amorphous ion track, ion irradiation can create a cylindrical volume of point defects where the defect concentration roughly follows the radial energy deposition. For example, the intensity of radiation-induced color centers in LiF crystals follows the single-impact model [49]. In this context,

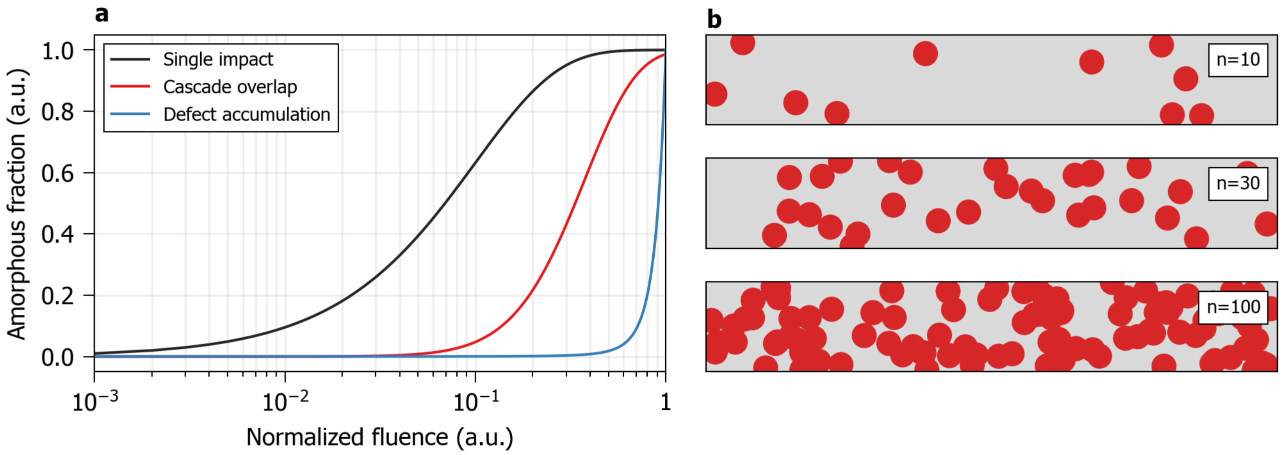

Figure 2.2.: Evolution of ion-induced amorphization in irradiated materials. Different models to describe the increase of ion-induced amorphization as a function of fluence, adapted from [50] (a). Different number n of ion hits (red area) on an arbitrary material surface (grey area) that qualitatively describes the direct (or single) impact model (b).

σ_d rather represents the effective cross section of radiation-induced defects along the ion path. Applied to the radiation-induced modification of a material property x, Equation 2.11 can be rewritten as:

$$x(\Phi) = (x_{sat} - x_0)(1 - e^{\frac{-\Phi}{\Phi_d}}) + x_0, \tag{2.12}$$

where $\Phi_d = 1/\sigma_d$ is the critical fluence by which a material property has degraded to $1/e$ of its initial value x_0 and ion tracks are starting to overlap. x_{sat} describes the material property in the saturation regime where additional radiation does not contribute to further material degradation. In the extreme case, this corresponds to the material property of the fully amorphized target material.

Other radiation damage models include the cascade-overlap model. This model describes how the overlap of several ion hits is necessary to produce a critical defect density that induces amorphization. Defect accumulation is a process in which a lattice can accomodate a large number of radiation-induced defects before breaking down rapidly beyond a critical defect density. Both models are typical for radiation damage induced in the nuclear energy loss regime. The cascade-overlap and defect accumulation model are schematically shown in Figure 2.2a. A thorough overview of the mathematical description of these models is given in [50].

2.5 Nuclear Reactions

At relativistic projectile energies that exceed the target's Coulomb barrier nuclear reactions lead to the creation of hadronic cascades and electronic showers. Hadronic cascades are dominated by inelastic nuclear reactions, namely hadron-nucleus (h-N) and nucleus-nucleus (A-A) interaction. The description of these reaction by the electromagnetic and strong force is out of the scope of this thesis. It should be noted that the interaction between projectile and target material at projectile energies above several GeV has a certain reaction cross section to produce additional hadronic particles. At projectile energies of several tens or hundreds of GeV, these particles possess a non-negligible momentum that is mainly directed in the forward direction of the projectile due to Lorentz contraction. These hadronic particles themselves lose their kinetic energy by electronic energy loss leading to a build-up of deposited energy along the projectile trajectory, even though the energy deposition by the primary projectile is effectively constant. A thorough review on the different processes involved and nuclear reactions can be found in references [51–53].

The contribution of nuclear reactions to the total energy loss is mostly relevant at relativistic projectile energies. But at projectile energies larger than the Coulomb barrier of the target, nuclear reactions induce radioactivity in the target. The Coulomb barrier scales with the product of atomic numbers of the target and projectile as $Z_t Z_p$. For example, the Coulomb barrier of carbon irradiated with protons is around 5 MeV, while a swift heavy ion like ^{197}Au has to overcome a Coulomb barrier of around 1 GeV.

3 Properties of Diamond and Graphite

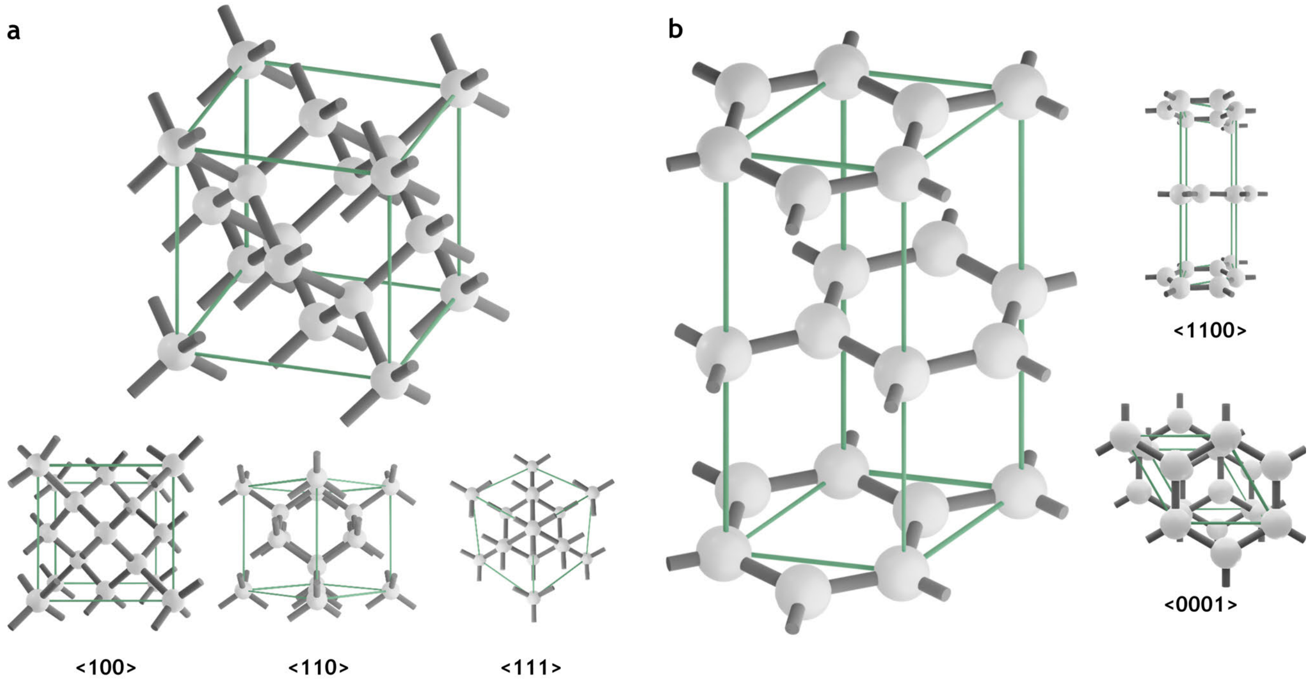

Figure 3.1.: Unit cells of the diamond and graphite lattice. Unit cell of the diamond lattice viewed off-axis and along three crystallographic directions showing four-fold (<100>), two-fold (<110> and three-fold symmetry (<111>) (a). Unit cell of the graphite lattice viewed off-axis and along the two crystallographic directions showing the large inter-planar distance (<1$\bar{1}$00>) and the six-fold symmetry along the *c* axis (<0001>) (b). Created using the Blender software [54].

Carbon can form a large number of allotropes with the most common and known being graphite and diamond [55] or more exotic allotropes like graphene [56], carbon nanotubes [57] or so-called buckyballs [58]. Furthermore, all life on earth is carbon-based since carbon readily forms bonds with itself and other elements in multiple different bond configurations. The ground state configuration of carbon is: $1s^2$, $2s^2$, $2p^2$, with the two 2p electrons in a $2p_x$ and $2p_y$ orbitals and an empty $2p_z$ orbital [59]. Only a small excitation energy, which is readily provided by the energy release during bonding, is necessary for the transition from the 2s orbital to the $2p_z$ orbitals. Once in the excited state the lowest energy configuration is realized by four equivalent bonds so the 2s orbital hybridizes with the tree 2p orbitals to form four sp^3 bonds. This leads to the tetrahedal coordination of the atoms in the diamond lattice with a valence angle of $\sim$109.5° [60]. If the 2s orbital hybridizes with the $2p_x$ and $2p_y$ orbitals three sp^2 orbitals are formed in the xy plane with a valence angle of 120° and an unhybridized $2p_z$ orbital. The sp^2 orbitals can form σ bonds by the overlap with other sp^2 orbitals while the $2p_z$ orbital can form the so-called π bond. This leads to the planar hexagonal distribution of carbon in the basal planes of the graphite structure [61]. Thermodynamically, only the sp^2 hybridized graphite structure is stable at room temperature. The sp^3 hybridized diamond lattice will, given enough energy, revert back into graphite [62].

3.1 Diamond

The diamond lattice is formed by purely sp^3 hybridized carbon atoms with a bond length of 1.54 Å, the diamond lattice is a face-centered cubic Bravais lattice with a basis consisting of two tetrahedrally bonded carbon atoms separated by $\frac{1}{4}$ of the lattice constant, 1.54 Å. It thereby corresponds to the $Fd\bar{3}m$ space group [63]. This results in an atomic density of $1.76 \times 10^{23}\,\mathrm{cm}^{-3}$, which is the highest atomic density of all materials stable at room temperature and ambient pressure, or a macroscopic density of $3.52\,\mathrm{g\,cm}^{-3}$. The diamond lattice is thermodynamically unstable and will transform into graphite and subsequently oxidize in air at about 1000 K [64] and at 2000 K in vacuum [65]. Due to the high temperatures necessary for this transformation, diamond is effectively stable on geological time scales at room temperature and below.

Diamond is an insulator with a band gap of 5.47 eV, making it transparent over a broad range of photon energies [66]. Unlike most electrical insulators, pure diamond is an excellent conductor of heat because of the strong covalent bonding within the crystal lattice that leads to efficient thermal transport by phonons. The thermal conductivity of pure diamond is the highest of any known solid. Single crystals of impurity-free diamonds can have a thermal conductivity of $2300\,\mathrm{W\,m^{-1}\,K^{-1}}$ at room temperature (in comparison, copper has a thermal conductivity of $390\,\mathrm{W\,m^{-1}\,K^{-1}}$ and silicon $150\,\mathrm{W\,m^{-1}\,K^{-1}}$) [67]. Isotopically pure diamonds, ^{12}C (99.9%), have the highest thermal conductivity, $3000\,\mathrm{W\,m^{-1}\,K^{-1}}$, of any material at room temperature, roughly 7.5 times higher than that of copper [68]. Natural diamond's conductivity is reduced by the naturally present 1.1 % of ^{13}C, which acts as an inhomogeneity in the lattice [69]. The bulk modulus of defect free diamond is 443 GPa [70] at room temperature (140 GPa for copper). The Young's modulus is ∼1150 GPa [71] (130 GPa for copper). Diamond has the highest hardness of all natural materials (together with silicon carbide) of 6000 and 15 000 HV (∼40 HV for copper). Its hardness is only exceeded by synthethic nano-grained polycrystalline diamond films [72].

The material properties of diamond are significantly influenced by the presence of impurities. The three main impurities, that are readily incorporated into the diamond lattice, are hydrogen, boron and nitrogen. Nitrogen impurities hinder the movement of dislocations in the diamond lattice and create compressive stress fields, thereby increasing hardness and toughness at the cost of reduced thermal conductivity [73]. By the incorporation of boron into the lattice, diamond can exhibit metal-like electric conduction of 0.015 Ωcm and in some cases even superconductivity [74].

The presence of nitrogen or boron, which are the most common substitutional defect in the diamond lattice, is used to classify diamonds into two different types. Type I diamonds have a detectable nitrogen infrared absorption signal. Type I diamonds are further divided in type Ia and Ib diamonds that contain aggregated nitrogen and single substitutional nitrogen, respectively. Type IaA and type IaB correspond to diamonds in which the most dominant nitrogen impurity is the A center nitrogen aggregate, two nearest-neighbor substitutional nitrogen atoms, and the B center nitrogen aggregate, four substitutional nitrogen atoms surrounding a carbon vacancy, respectively. Type II diamonds on the other hand have no nitrogen-related infrared absorption (the detection limit of nitrogen is about 0.5 ppm [75] in infrared absorption spectroscopy). Type IIa diamonds also contain no detectable boron impurities. Type IIb diamonds contain boron impurities. The type classification system of diamond is summarized in Table 3.1.

Diamond has found a multitude of different applications. The combination of its high refractive index ($n = 2.417$) and its dispersion (0.05) make it a highly brilliant gemstone [82]. Due to its exceptional hardness, diamond is being used as an abrasive in cutting and grinding of many materials. With its high thermal conductivity, it is an excellent heat spreader. Due to the large band gap and broad transparency, diamonds are excellent optical windows for high-power lasers [83] or high-power gyrotrons [84].

Furthermore, diamond is routinely used in particle detector applications in high dose environments due to its excellent charge collection efficiency and radiation hardness. An overview of accelerator-specific applications of diamond is given in section section 4.1.

Since the beginning of the 2000s, nanodiamonds (typical particle size <100 nm) produced by the detonation of high-explosives [85], milling of micron-size diamond powder [86] or pulsed laser ablation in liquids [87], have attracted large interest. It was demonstrated that fluorescent nanodiamonds can be produced by irradiation with He ions on industrial scales [88]. Due to their bio-compatibility, nanodiamonds can be used for in-vivo imaging of biological samples [89]. Furthermore, the surface of nanodiamonds can be chemically functionalized [90] and nanodiamonds can hence be used as drug delivery agents [91]. A comprehensive overview of nanodiamond synthesis and applications is found in reference [92].

Table 3.1.: Classification system of diamond, adapted from [76].

Type	Subtype		Defining feature
I			Nitrogen is detectable by IR absorption in the one-phonon region, [N] >1 ppm
	Ia		Nitrogen is in aggregated form
		IaA	Most dominant nitrogen species is the A nitrogen aggregate, two nearest-neighbour substitutional nitrogen atoms [77]
		IaB	Most dominant nitrogen species is the B nitrogen aggregate, four substitutional nitrogen atoms surrounding a vacancy [78]
		IaA/B	Combination of A and B centers
	Ib		Most nitrogen is in the form of individual substitutional nitrogen, the C center [79]
II			No nitrogen or boron can be detected by IR absorption
	IIa		Nitrogen cannot be detected by IR absorption
	IIb		Boron concentration is larger than the nitrogen concentration [80, 81]

3.1.1 Diamond Synthesis

The diamond allotrope of carbon is metastable at room temperature and ambient pressure. While it is thermodynamically unstable [62], which is shown in the pressure/temperature phase diagram of carbon in Figure 3.2, the low conversion rate to graphite makes diamond kinetically stable. For bulk diamonds, the two possible synthesis routes are (i) the thermodynamically stable high-pressure/high-temperature (HPHT) synthesis in special anvils or (ii) the metastable synthesis by chemical vapor deposition (CVD).

3.1.1.1 High Pressure/High Temperature

The natural genesis of diamonds occurs at depths of ∼200 km in the Earth at pressures of 7 and 8 GPa and temperatures between 1400 and 1600 °C [94]. These conditions correspond to the carbon phase diagram where diamond is stable (cf. Figure 3.2). High pressure/high temperature (HPHT) synthesis was the first industrialized method to produce bulk diamonds [95]. During HPHT synthesis, diamond is produced in the thermodynamically stable region of the carbon phase diagram from a carbon-rich melt in the presence of a solvent metal like iron, cobalt or nickel. The presence of the solvent metal was identified to be essential to the HPHT method [96]. The driving force of crystallization stems from the solubility gradient in the solvent caused by the temperature gradient along the reaction cell. This is achieved by placing a so-called HPHT capsule or reaction cell, that is surrounded by a graphite resistance heater, in a press. A schematic representation of a reaction cell is shown in Figure 3.3a.

The most common and simplest product of the HPHT method are micrometer-sized particles of type Ib diamonds for use in grinding and cutting applications. By tightly controlling the growth conditions in combination with long growth periods, large single-crystalline type Ib diamonds with dimensions up to ∼10 mm can be grown [97]. The addition of a nitrogen getter mixture that contains titanium, aluminum or zirconium enables the growth of type IIa diamonds with the same dimensions [97, 98]. In the presence of a getter, nitrogen is preferentially bound to the getter and precipitates at the cost of a reduced growth rate due to increased uptake of inclusions in the growing diamonds [97].

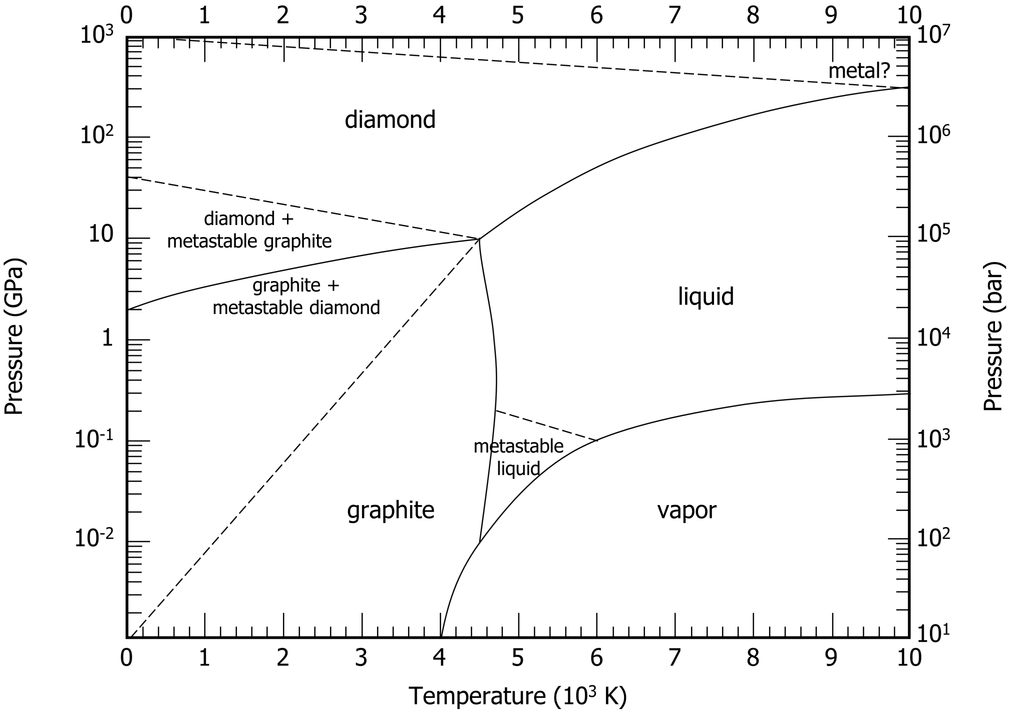

Figure 3.2.: Pressure, temperature phase diagram of carbon. Adapted from [62, 93].

3.1.1.2 Chemical Vapor Deposition

Chemical vapor deposition (CVD) synthesis of diamonds works in a regime far from thermodynamic equilibrium below ambient pressure. The CVD synthesis route was discovered almost simultaneously with the HPHT method in the 1950s, but only in the 1980s industrially relevant growth rates were achieved [99]. For the production of single-crystalline CVD (scCVD) diamond, microwave plasma-assisted chemical vapor deposition (MPCVD) is the method of choice since the first report of homoepitaxial scCVD growth was reported in 1988 [100]. Today, high quality type IIa single-crystalline diamond wafers of up to 92 mm diameter were produced by MPCVD [101].

At temperatures below 1000 °C and pressures below 10 kPa graphite is the thermodynamically stable phase (cf. figure 3.2). Atomic hydrogen, produced in a high temperature plasma medium of ~95 % H_2 and ~5 % CH_4, is preferentially etching away sp^2 bonds and thus kinetically stabilizing the addition of carbon to the diamond lattice of a diamond seed. Qualitatively, CH_x radicals adsorb on the diamond seed producing a hydrogen terminated diamond surface with the hydrogen being consecutively removed by hydrogen radicals from the plasma. For the sake of completeness it should be noted that the aforementioned 92 mm diameter scCVD diamond wafer has been grown on an iridium (001) surface by the so-called ion bombardment induced buried lateral growth mechanism [99].

scCVD diamonds are typically of type IIa but the presence of a few tens of ppm of nitrogen gas in the reaction chamber leads to an increase of growth rate by up to a factor of 5 [102]. It is believed that the incorporation of substitutional nitrogen reduces the energy barrier for hydrogen removal of the hydrogen terminated diamond surface/growth layer [103, 104]. By adjustment of the nitrogen/methane ratio in the process gas scCVD diamonds with up to 100 ppm have been produced [105]. An extensive review on the MPCVD synthesis route of diamonds and the resulting diamond properties can be found in [99, 106]

3.2 Graphite

The graphite lattice is formed by purely sp^2 hybridized carbon atoms. In contrast to the diamond lattice, bond lengths vary along the crystal directions. Carbon atoms form in-plane covalent bonds (which define the a direction of the lattice) with a bond length of 1.42 Å with three neighboring carbon atoms and a bond angle of 120°. The

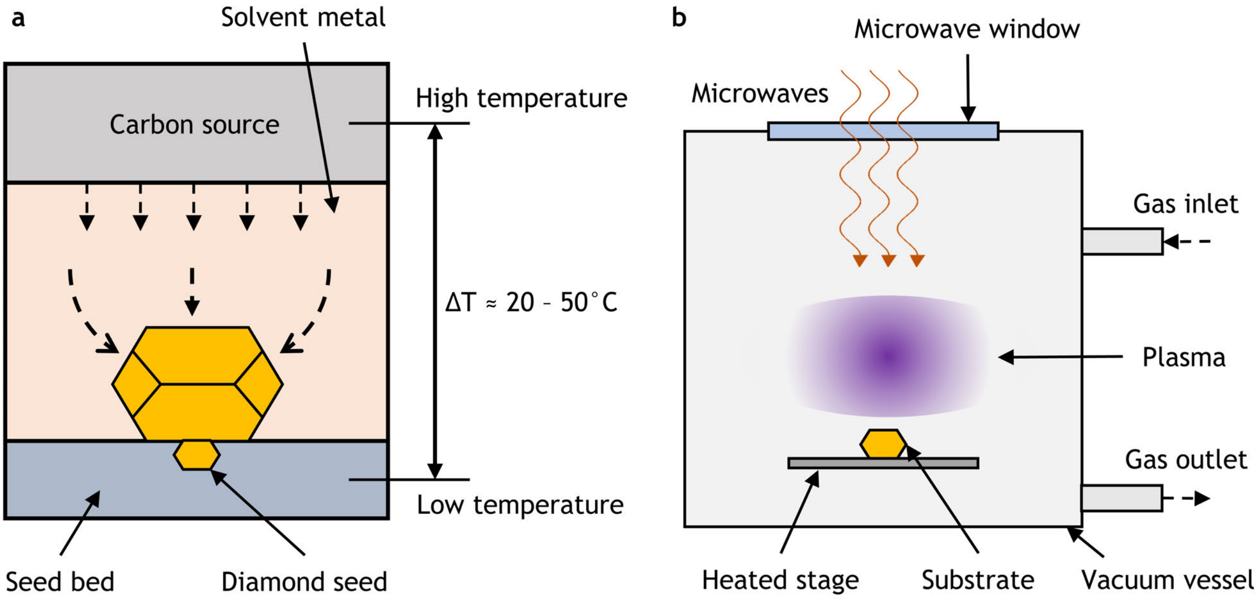

Figure 3.3.: Schematic representation of the high-pressure/high-temperature (HPHT) reaction cell and its contents. The reaction cell is surrounded by a graphite heater (not shown here) and placed in a press (a). Schematic representation of a microwave plasma chemical vapor deposition (MPCVD) reactor. Depending on the exact process the substrate can either be a seed diamond or an iridium (100) substrate (b).

resulting honeycomb structure (made of locally hexagonal carbon rings) represents a single basal plane[1]. The basal plane distance along the c direction is 3.35 Å [61]. The resulting lattice is a hexagonal Bravais lattice with a basis of two carbon atoms separated by the mentioned 1.42 Å and space group P63/mmc with lattice constants, $a = 2.46$ Å and $c = 6.71$ Å corresponding to a density of 2.265 $\mathrm{g\,cm^{-3}}$ [107].

The material properties of technologically relevant graphite materials vary largely with the used production process. For this section only the material properties of ideal graphite, which is comparable to highly-oriented pyrolytic graphite (HOPG), will be discussed. At ambient pressure graphite does not melt but sublimates at temperatures around 4000 K [108]. Graphite readily oxidizes in air at temperatures above 400 K [109], while service temperatures in vacuum are only limited by the pressure dependent sublimation temperature. Due to the large difference in bond strength between carbon atoms in-plane and between basal planes (basal planes are only linked by weak van der Walls interaction of the delocalized π-orbitals) the thermal and electrical properties exhibit a large degree of anisotropy. The in-plane thermal conductivity parallel to the basal planes is about 2000 $\mathrm{W\,m^{-1}\,K^{-1}}$ at room temperature and mainly driven by collective phonon excitation. Perpendicular to the basal planes the thermal conductivity is only 18 $\mathrm{W\,m^{-1}\,K^{-1}}$ [110] in comparison to copper with 385 $\mathrm{W\,m^{-1}\,K^{-1}}$. Similarly, the in-plane electrical resistivity of graphite is $\sim 4 \times 10^{-5}$ Ωcm along the basal planes and $\sim 5 \times 10^{-3}$ Ωcm through plane [111] (1.7×10^{-6} Ωcm for copper). Without the presence of a bandgap graphite is opaque in the visible range. The anisotropy is also prevalent in the hardness with a value of 250 HV through plane and 60 HV in-plane (40 HV for copper). Interestingly, the Young's modulus varies only between 18 GPa through plane and 15 GPa in-plane [112] (130 GPa for copper).

Graphite is found in many industrial applications due to the very broad range of graphite-based materials with varying material properties. An overview of the different graphitic materials investigated in this thesis is given in section B.1. Due to its small mosaic spread angle, highly-oriented pyrolytic graphite (HOPG) is used in monochromators for synchrotron light [113] or thermal neutrons [114]. Cheaper thermally annealed pyrolytic graphite has about the same thermal conductivity as HOPG, while having a larger mosaic spread angle, and is thus used for high performance heat sinks [115]. High-purity isotropic polycrystalline graphite (PG), so-called nuclear graphite, is traditionally used as moderator and structural material in nuclear power plants [116]. Conventional PG is used as electrodes for arc furnaces or electrical discharge machining which also represents the largest industrial application field of synthetic graphite. Low-density expanded graphite is used as gasket material in highly corrosive environments such as crude oil pipelines, chemical reactors or nuclear power plants [117]. Even lower density graphitic foams with fully open macroscopic porosity are being used as heatsinks for high power electronics [118]. High strength carbon fiber-reinforced graphite composites made of (usually) polyacrylonitrile (PAN) derived carbon fibers embedded in a graphite matrix are used as structural material in high temperature autoclaves, for rocket nozzle cladding and the nosecone & leading edges of space re-entry vehicles [119].

---

[1] Single or just a few stacked basal planes are known as graphene.

3.2.1 Graphite Synthesis

The exact production route of synthetic graphite depends on the final product. A detailed description of the specific production route for the different graphitic material investigated in this thesis is therefore provided in section B.1. But, all routes share the same basic three step process: precursor production (i), carbonization (ii) and graphitization (iii). Precursor materials can be (mixtures of) coal tar or petroleum pitch, high carbon content organic materials or polymers, natural graphite flakes or petroleum coke. Depending on the quality of the precursor only a fraction of the used weight is actually carbon. During carbonization volatile non-carbon species are removed from the precursor by pyrolization in inert atmosphere at temperatures between 700 and 1200 °C. The resulting highly porous carbonaceous material has a random sp^2/sp^3 ratio with a low degree of crystallinity. In the final graphitization step the material is heated to temperatures between 2500 and 3000 °C. At ambient pressures this leads to the conversion of sp^3 bonds into sp^2 bonds accompanied by increasing crystallinity and density. In the presence of uniaxial tensile stress, basal planes are aligning along the *c* axis resulting in a decreased mosaic spread angle [120].

Part II.

Luminescent Properties of Diamond under Swift Heavy Ion Irradiation

4 Diamond Accelerator Application and Interaction with Charged Particle Beams

4.1 Diamond Applications in Accelerators

Apart from the commonly known usage of diamonds as gem stones in jewelry (due to its optical dispersion) and industrial use as cutting and grinding tools (due to its hardness), diamond is used in several accelerator applications. The largest application in this field is diamond-based radiation and particle detectors, due to the availability of high purity diamonds synthesized by chemical vapor deposition (CVD). Other, in comparison minor, applications include diamond-based metal matrix composites used as the absorber material in the tertiary collimators of the High-Luminosity Large Hadron Collider (HL-LHC) and diamonds for crystal collimation at LHC.

4.1.1 Particle Detectors

Historically, diamond was already used as a UV detector in the 1920s and as a detector for ionizing radiation in the 1940s [121]. These detectors relied on natural diamond pieces that are, when taking the necessary purity requirements into account, limited in size and quantity. With the increasing availability of high purity diamonds synthesized by chemical vapor deposition [122], diamond has become an attractive detector material during the 1990s. Diamonds can be used as detectors for all types of ionizing radiation, UV light, X-rays, gamma rays, electrons, neutrons, protons and heavy ions [123]. This section focuses solely on the detection of particle radiation. The main advantages of diamond detectors in comparison to other semiconductor-based particle detectors are:

- **Large band-gap**: Low intrinsic charge carrier density, high resistivity; low leakage current.
- **Low dielectric constant (≈1/2 of Si and GaAs)**: Low capacitance; low noise.
- **High breakdown field**: Operation at high voltages; fast charge collection.
- **High charge carrier mobility**: Fast signal collection.
- **Large thermal conductivity**: Operation without cooling.
- **High binding energy**: Radiation hardness.

But, diamond-based detectors do suffer from drawbacks in comparison to semiconductor-based particle detectors:

- **High energy required to create an electron-hole pair**: Low signal.
- **High density of defects**: Charge trapping and recombination; unable to collect all the produced ionization signal. Polarization effect.

Although the low signal generation is partially offset by the low noise in diamond detectors. The intrinsic signal to noise ratio of diamond, in the absence of a bias voltage, is more than five orders of magnitude in comparison to silicon [124]. Two specific advantages of diamond-based detector systems should be emphasized here: due to the large displacement energy, E_d of $\sim$40 eV [15] that is necessary to displace carbon atoms in the diamond lattice, diamond-based detectors are an order of magnitude more radiation-hard than silicon detectors ($E_\mathrm{d,Si} =$ 13 eV [15]) [125]. Furthermore, small size single-crystalline CVD (scCVD) diamond detectors can achieve signal rise times down to $\sim$100 ps [126]. Even large area poly-crystalline CVD (pCVD) diamond detectors achieve signal rise times of 5 ns, two times faster than comparable silicon-based detectors [127].

Tracking systems based on the time of flight principle were pioneered at the HADES experiment of GSI and achieved a time precision of $\sim$50 ps and are used in the Proton Precision Spectrometer, the first layer of detectors of the

CMS experiment that are just a few mm away from the colliding LHC beam [13]. Future applications include the tracking of rare-isotope beams produced in the Super-FRS towards the R^3B target at the FAIR facility [128]. 3D pixel detectors based on poly-crystalline CVD diamonds are investigated for potential use in the ATLAS experiment at LHC [129].

Furthermore, diamond-based detectors are used in all physics experiments of the LHC in so-called beam condition monitors that are located close to the beam pipe. These beam condition monitors are able to quickly detect any aberrant behavior of the circulating beams in order to trigger a beam abort that leads to a dump of the beams [130, 131]. Further iterations of the system, the pCVD-based diamond beam monitor, can provide on-line bunch-to-bunch luminosity and beam spot measurements [132]. A more detailed introduction into the fabrication and characteristics of diamond-based detectors is given in references [129, 133].

4.1.2 Absorber Material in HL-LHC Tertiary Collimators

Diamond-based copper matrix (Cu-Dia) composite is one of the candidate materials for the collimator upgrade of HL-LHC. Within a series of beam impact experiments, the performance of Cu-Dia as the absorber material for the HL-LHC tertiary collimators (currently made of tungsten) was evaluated. Cu-Dia blocks managed to survive a direct beam impact of up to 1.95×10^{13} protons per pulse (ppp) and pulse length of 3.6 μs at 440 GeV/c [134]. The final collimator design was able to whitstand the same beam with an intensity of 1.73×10^{13} ppp [24]. For both cases the maximum energy density of $\sim$14 kJ cm^{-3} is about 3 times higher than the expected maximum load of $\sim$5 kJ cm^{-3} on a tertiary collimator for the design accident of an asynchronous beam dump in HL-LHC [24].

4.1.3 LHC Crystal Collimation

The channeling effect [135] of bent single-crystals can be used to bend the trajectory of relativistic particles. This effect is used in crystal-assisted collimation at the LHC to bend halo particles to larger offsets with respect to the nominal beam trajectory [136]. The deflected particles are then absorbed by the conventional collimation system of LHC. The main advantage of crystal-assisted collimation is that the conventional collimators can be retracted to increase the beam/collimator distance. This reduces the collimator-induced impedance and therefore potential impedance-induced beam instabilities. It also reduces beam losses by an increased aperture size at the collimators. Under optimal conditions, crystal-assisted collimation can reduce local beam losses by an order of magnitude [137].

Eventually, diamond was discarded for crystal collimation because producing the small bending proved to be technologically challenging. Silicon strip crystals turned out to be much better suited. Their specific mechanical properties allow to create a microscopic "secondary bending" that can be controlled by a macroscopic mechanical load of the strip crystals [138].

4.2 Ionoluminescence in Diamond

The passage of a single 2 MeV proton generates $\sim 1.5 \times 10^5$ electron-hole pairs along a penetration depth of 24 μm in a cylindrical volume of 1 to 2 μm diameter [139]. The emissive decay of electron-hole pairs by recombination can then be detected. This mechanism is used in cathodoluminescence (CL) spectroscopy where photon emission is stimulated by an external electron beam (inversely to the photoelectric effect). When using ions this technique is called ionoluminescence (IL). In addition to electron-hole pairs, electronic energy loss can excite crystallographic defects that subsequently decay radiatively.

Literature on ionoluminescence in diamonds is scarce and to the author's knowledge no studies with ions heavier than carbon were performed. Most of the studies utilized MeV protons and a single study was performed with 350 keV carbon ions. An overview of the most important studies is presented in Table 4.1 that describes the investigated diamond types and a selection of color centers that were identified in the IL spectra of the respective work. IL spectra measured on type I diamonds [20] under excitation with 1.9 MeV protons are shown in Figure 4.1a. The most common defect detected in these studies is the A-band with its broad emission from 400 nm up to $\sim$600 nm with its ZPL at $\sim$430 nm [140]. Other IL components are the H3 center, 3H center and the green band, which were

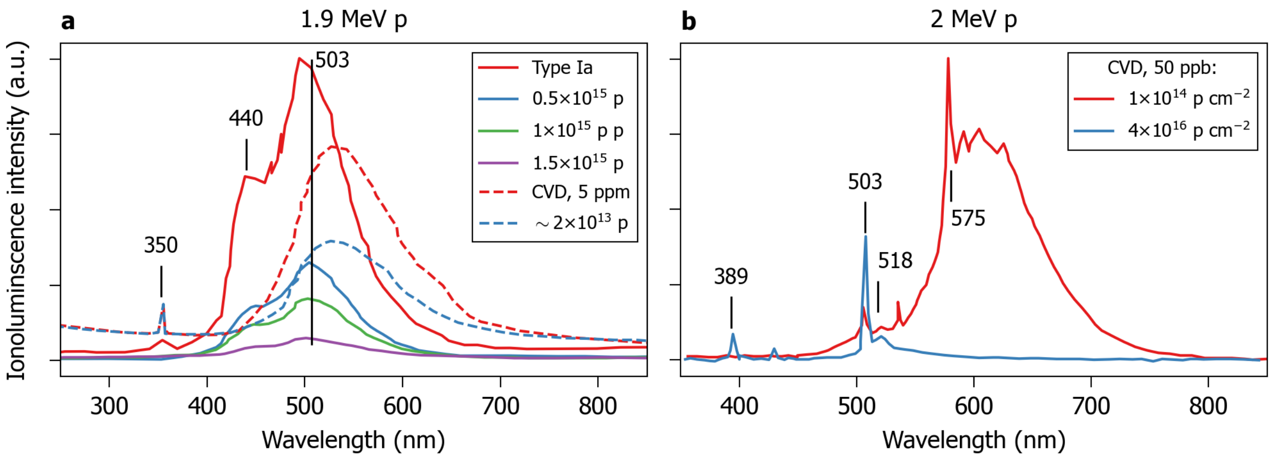

Figure 4.1.: Overview of ionoluminescence (IL) spectra under irradiation with MeV protons. IL signal at different integrated number of protons of natural type Ia diamond of unknown nitrogen impurity level and CVD diamond with 5 ppm nitrogen impurities adapted from [20] (a). IL signal of a 'detector grade' CVD diamond with ≤50 ppb at different fluences adapted from [22] (b).

identified around ~503 and ~510 nm, respectively. The IL spectrum of a type II CVD under excitation with 2 MeV protons at two different fluences [22] is shown in Figure 4.1b. These spectra are lacking the contribution from the A-band in comparison to the type I IL spectra. Due to the small sample size, it is not possible to deduce a concrete relation between dominant IL components and the diamond type or nitrogen impurity content.

4.3 Radiation Damage in Diamond

Diamond has a displacement energy between 30 and 48 eV that depends on the crystal orientation [141–143]. The displacement energy of diamond is considerably higher than the displacement energy of 17 eV in graphite simply due to the denser packing of the diamond lattice. Diamond is therefore considered a radiation-hard material (just like graphite) in spite of (defect-free) diamond being a wide band gap insulator (E_g =5.47 eV).

The electrical properties of diamond, important for particle detector applications, were extensively investigated under irradiation with MeV electrons [144], MeV–GeV protons, fast neutrons & 200 MeV pions [145] and 120 MeV/n ^{96}Zn and ^{124}Sn swift heavy ions [146]. In summary, diamond-based detector systems have a radiation hardness that is roughly an order of magnitude higher than silicon-based detectors [125].

Radiation-induced structural changes of diamond were reported for neutrons [147–149], MeV protons [150–152], alpha particles [153, 154], keV ions [155–161], <10 MeV ions [162–164], <100 MeV ions [165–167], <GeV ions [168] and ~GeV ions [169–172].

The common understanding of these studies is that radiation-induced structural damage in diamond is dominated by nuclear collisions [156]. This is in agreement with the fact that irradiation with swift heavy ions does not lead to the production of ion tracks [23]. According to MD simulations [173], swift heavy ion irradiation only creates point defects. This is attributed to a short ballistic phase of primary knock on atoms, large branching of cascades and the absence of melting by a thermal spike. All this leads to an efficient transport of the deposited energy away from the ion trajectory. Just as in graphite, these properties are related to the strong covalent bonds in both structures [173].

Based on Rutherford backscattering spectroscopy and assuming a threshold displacement energy of 45 eV, Uzan-Saguy *et al.* estimated a threshold vacancy density of 10^{22} cm^{-3} for the amorphization of diamond [158] that was consistent with prior works with different ions in the energy range between 40 and 350 keV [155]. Garcia *et al.* extended this work to swift heavy ions with electronic stopping powers <14 keV/nm and found a critical integrated nuclear energy loss threshold of 1.15×10^{15} keV nm^{-1} cm^{-2} (product of electronic energy loss and fluence) for amorphization. The threshold is independent of the electronic stopping power of the ions used [165]. Using depth-resolved Raman spectroscopy, Kazuchits *et al.* reported the same trend using 167 MeV Xe ions and observed

Table 4.1.: Overview of color centers active in ionoluminescence that were reported in literature. Ionoluminescence spectra from references [20, 22] are shown in Figure 4.1.

Beam	Diamond	Fluence (cm^{-2})	Identified color centers
30 keV ^{12}C	Nat. type IIa	9×10^{14}	A-band (430 nm) [16]
2 MeV p	CVD thin film	1×10^{18}	A-band (430 nm), H3 center (503 nm) [17]
2 MeV p	Bulk CVD	$<1 \times 10^{16}$	A-band (430 nm), green band (510 nm), ~2 eV nitrogen band [18]
2 MeV p	Meteorite inclusions	1×10^{18}	A-band (430 nm), damage peak at 512 nm [21]
2 MeV p	CVD, ≤50 ppb N_s	1×10^{14}	3H center (503 nm), NV^0center (575 nm) [22]
1.9 MeV p	Type Ia & CVD		A-band (440 nm), ~510 nm [19]
1.9 MeV p	CVD, 5 ppm N_s	$\sim 2 \times 10^{13}$	H3 center (503 nm & 350 nm), ZPLs at 530.8 & 630.3 nm [20]
1.9 MeV p	Nat. type Ia	$\sim 1.5 \times 10^{15}$	A-band (440 nm), H3 center (503 nm), N3 center (415 nm) [20]

amorphization at a vacancy density between $\sim 2 \times 10^{22}$ and $5 \times 10^{22}\,cm^{-3}$ [168]. Based on transmission electron micrographs and MD simulations of diamond irradiated with 500 keV helium ions, Fairchild *et al.* [174] have shown that the breakdown of the diamond lattice occurs sharply at a vacancy density of $2.8 \times 10^{22}\,cm^{-3}$. The diamond lattice retains the majority of its crystallinity up to a defect-induced swelling of 16 %, which corresponds to a density of $\sim 2.95\,g\,cm^{-3}$. Beyond this critical vacancy density further irradiation induces an increase of sp^2 content that stabilizes at a saturation density of $\sim 2.1\,g\,cm^{-3}$. Annealing can recover the diamond lattice at vacancy densities less than $2.3 \times 10^{22}\,cm^{-3}$ [175], while larger vacancy densities will induce further graphitization during annealing. Bunk *et al.* [167] have shown that radiation-induced amorphization is independent of the nitrogen content for type Ib and type IIa diamonds ≤200 ppm N_s.

Different diamond color centers relevant for this thesis are introduced within section A.1. It will be shown later that all of these color centers are directly created by irradiation with swift heavy ions. Along with the radiation-induced structural effects within the diamond lattice, the creation of color centers leads to dramatic changes in the color of irradiated diamonds that is easily visible to the naked eye. Depending on the type of irradiation, beam conditions, type of diamond and subsequent annealing conditions, diamonds of all colors can be produced. Diamonds containing NV centers appear pink to red [176]. High concentration of H3 or H4 centers leads to a green-yellow color [177]. The control of diamond color by radiation (in combination with heat and/or HPHT treatment) has lead to the emergence of so-called treated diamond gem stones within the diamond industry [176].

In general, only a few studies in literature present the evolution of color center luminescence or absorption intensities with increasing radiation dose [178]. One of the most studied defect in that regard is the nitrogen-vacancy center for the purpose of creating a high NV concentration for luminescence applications [179]. Even fewer studies investigated the effects of electronic energy loss by swift heavy ions toward (extrinsic) color centers. Schwartz *et al.* showed that the production of NV centers, which is believed to depend only on the availability of nitrogen [180] and vacancies in the lattice [181, 182], is more efficient in swift heavy ion irradiated diamonds [171]. Depth-resolved photoluminescence studies have indeed shown that the intensity of nitrogen-vacancies is largest in depths which experience the highest electronic energy loss [183]. The observations are attributed to either the SHI induced thermal spike or the swift heavy ion-induced δ-electrons, since it was observed that irradiation with 10 keV electrons leads to the direct production of nitrogen vacancies as well [171].

5 Theory of Absorption and Optical Transitions

This chapter introduces the necessary fundamentals to understand processes like optical absorption and photoluminescence in diamonds. The electronic or vibrational levels involved in these processes can be correlated to different defects in the diamond lattice. Even though the term optical generally refers to electromagnetic radiation with frequencies visible to the human eye (~400-700 nm), optical will be used to describe all processes involving electromagnetic radiation at wavelengths from the UV to the IR range.

5.1 Optical Transitions

The interaction by different scattering and absorption mechanisms leads to the attenuation of an electromagnetic wave propagating through a material. To explain the interaction of photons with matter let's consider an electric dipole that consists of separated positive and negative charges. In atoms, positively charged nuclei and negatively charged electrons form such dipoles that emit electromagnetic radiation when oscillating. The frequency ω of the emitted radiation is equal to the oscillation frequency of the dipole. For small displacements, the natural resonant frequency ω_0 of a nucleus/electron dipole is approximately given by:

$$\omega_0 \approx \sqrt{\frac{k}{m_e}}, \tag{5.1}$$

where k is a spring constant and m_e is the electron mass. When sufficient energy is provided to an atom to excite oscillations, electromagnetic radiation is emitted with the frequency ω_0. The reverse is true as well when electromagnetic radiation of frequency ω is interacting with an atom. The electric field can couple with the atom and excite (non-resonant) oscillations at ω. In the resonant case, where the frequency of the excitation is ω_0, energy is absorbed by the atomic dipole. The energy levels of electrons bound to a nucleus are quantized. Hence, only photons of the correct energy $\hbar\omega = E_2 - E_1$ can be absorbed that promote an electron into an excited state.

Relative motion of atoms on lattice sites can also be described by oscillation of dipoles. But due to the larger mass (or inertia) of nuclei in comparison to electrons ω_0 is lower. In this case external excitation will excite lattice phonons instead of electronic transitions.

On a macroscopic scale, absorption of light in a medium can be described by the Lambert-Beer law [184, 185]. The change in intensity $\mathrm{d}I$ of light passing through a medium of thickness t and absorption coefficient α, which is the fraction of absorbed light per unit length $\mathrm{d}z$, can be described by:

$$\mathrm{d}I = -\Gamma\, I(t)\, \mathrm{d}z. \tag{5.2}$$

By integration of Equation 5.2 for monochromatic light of frequency ω, the intensity I at position z within the medium is given by:

$$I(z,\omega) = I(0,\omega)e^{-\Gamma(\omega)z}, \tag{5.3}$$

where $I(0,\omega)$ is the light intensity when entering the medium at $z = 0$ and $\Gamma(\omega)$ is the spectral absorption coefficient. An absorption spectrometer experimentally measures the transmission $I(t,\omega)/I(0,\omega)$. The spectral absorbance $A(\omega)$ is defined as:

$$A(\omega) = -\log_{10}\left(\frac{I(t,\omega)}{I(0,\omega)}\right). \tag{5.4}$$

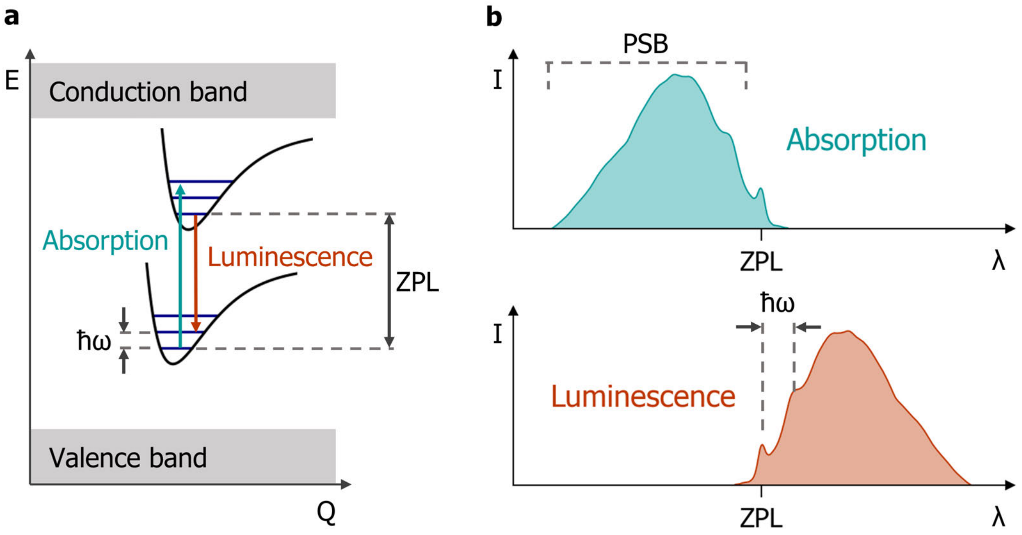

Figure 5.1.: Ground and excited state of a defect within the band gap of diamond. Each state contains several vibrational energy levels (dark blue horizontal lines) separated by $\hbar\omega$. The zero phonon line (ZPL) is the transition from and into the lowest vibrational state of the ground and excited state respectively (a). Schematic representation of the spectral shape of a defect within the band gap both in absorption and luminescence. The phonon sideband (PSB) is observed at energies larger than the ZPL in absorption while the reverse is true for luminescence (b).

Thus, spectral absorbance and absorption coefficient are connected by:

$$\Gamma(\omega) = \frac{\ln(10)}{d} A(\omega). \tag{5.5}$$

Beer [185] showed that the absorbance at a given frequency of an absorption band depends linearly on the concentration of the chemical species that is responsible for the absorption band:

$$A(\omega) = \varepsilon(\omega) c d, \tag{5.6}$$

where $\varepsilon(\omega)$ is the molar absorption coefficient defined as the absorption coefficient per unit concentration c. Hence, by measuring the spectral transmission of a sample, the absorbance will qualitatively describe the concentration of a luminescent defect that absorbs light at frequency ω.

5.1.1 Intrinsic Absorption of Diamond

In the absence of any defects diamond has an indirect band gap of 5.47 eV leading to its transparency for wavelengths >227 nm with the exception of a band from 2.6 to 6.2 µm due to multi-phonon vibrational absorption. Due to inversion symmetry of the covalent bonds between next-neighbor carbon atoms (the net dipole moment is zero), there is no one-phonon absorption in defect-free diamond.

The maximum single phonon frequency in diamond is 1332 cm^{-1} which corresponds to the zero-momentum optical phonon (in the Brillouin zone-center) and the Raman frequency. Multi-phonon absorption can occur up to integer multiples of this frequency. The largest two phonon absorption is observed at 2159 cm^{-1} with higher order absorption intensity decreasing dramatically with the reduced probability of the required phonon combination. The different characteristic ranges for (multi-)phonon absorption are shown in Figure A.3.

5.1.2 Defect-related Transitions

5.1.2.1 Electronic Transitions

Lattice distortion introduced by point defects can introduce spatially and energetically localized electronic states in the band gap of the diamond lattice. Broad spectral features are produced in transitions where the gap state is close to the continua of the valence or conduction bands. But, if the defect has (at least) two different states within the band gap, the transition between these states can be observed as a sharp spectral peak that is called zero-phonon line (ZPL).

Apart from the transition associated with the ZPL, electron-phonon coupling leads to mixed transitions that create the phonon sideband (PSB) in addition to the ZPL. An absorbed photon can provide energy for both the zero-phonon transition and a vibrational mode in the excited state. Hence, a phonon sideband will be observed at higher frequency than the ZPL in the absorption spectrum. The inverse is observed in luminescence where the energy of the emitted photon is the difference between the lowest vibration level in the excited state (according to Kasha's rule [186]) and a vibrational level in the ground state. The probability of transitions to different vibronic bands during emission and absorption is determined by the strength of the electron-phonon coupling. According to the Franck-Condon principle, the absorption and emission (luminescence) transition with the smallest change in the configuration coordinate $\mathrm{d}/Q \approx 0$ will have the highest transition probability during excitation/relaxation [186].

The energy of ZPLs in diamond can be determine with a resolution of a few meV in both absorption and photoluminescence using modern spectrometers. With this precision, ZPLs of different defects can be clearly distinguished. The measured ratio between the spectral intensity of the ZPL and its PSB depends on the temperature. At lower temperatures less vibrational modes are populated which increases the relative intensity of the ZPL in comparison to the PSB. Ultimately, the lower the temperature the easier it is to distinguish between different ZPLs of different defects.

5.1.2.2 Photoluminescence

Absorption of a photon can excite electrons bound in ground states within the band gap to higher energy levels. The excited state then decays, after some time, by relaxing either radiatively or non-radiatively. In the case of a radiative decay, a photon is emitted in the process of photoluminescence (PL). As mentioned, radiative decay of an excited state occurs from the lowest vibrational mode of the excited state to a vibrational mode in the ground state. For diamond, lifetime of excited states with radiative decay is typically on the order of a few ns.

Even though photoluminescence spectroscopy is a very sensitive technique that can detect luminescence from single isolated defects, direct determination of defect concentrations is usually not possible. Due to the various competing radiative and non-radiative relaxation pathways for the excited state, the intensity measured in photoluminescence spectra is, unlike absorption spectroscopy, not considered quantitative to directly determine defect concentrations.

5.1.2.3 Cathodo- and Ionoluminescence

Cathodoluminescence (CL) and ionoluminescence (IL) are referring to the emission of photons due to excitation by charged particles. CL refers specifically to excitation with electrons while IL includes all other charged particles.

The displacement energy of the diamond lattice is on the order of $\sim$40 eV (depending on the crystal orientation). Hence, irradiation with electrons of energy above 180 keV can result in the production of a Frenkel defect in the diamond lattice. At lower electron energies both elastic and inelastic scattering processes occur. Inelastic scattering produces secondary electrons, Auger electrons, and X-rays that all scatter themselves to ultimately produce a scattering cascade. Scattering of secondary electrons can excite electrons from the valence to the conduction band, which in turn produces a hole in the valence band. In the absence of defects with electronic states within the diamond band gap, excited electrons can recombine radiatively with holes and the energy of the emitted photon corresponds to the band gap. If defect-related (extrinsic) electronic states are available within the band gap, electrons might be directly excited from the valence band into a defect state. Alternatively, an electron from the conduction band relaxes non-radiatively into a defect state that can decay radiatively.

The exact mechanism of ionoluminescence is not as straight-forward. Ion irradiation at energies of a few MeV/n leads to a complex chain of interaction events that occur on very different time scales. In the thermal spike model the ion passage creates a highly-excited electron subsystem that further induces an ionization cascade. In the following relaxation of the electron subsystem, energy is transferred to the lattice by the excitation of phonons. Simultaneously, a fraction of the electron subsystem relaxes by exciton formation (bound electron/hole pairs) or relaxation into defect-related electronic states which in turn can decay radiatively. It should be stressed that this very simplified explanation does not consider the influence of the heated lattice, ion-induced creation & annealing of both intrinsic & extrinsic defects or existing radiation damage in the lattice.

5.1.2.4 Vibrational Modes

Lattice distortions destroy local symmetry and enable one-phonon absorption in the diamond lattice. Two cases can be considered when extrinsic substitutional atoms are introduced in the lattice. The Raman frequency corresponds to the phonon with the highest frequency and, therefore, energy that can freely propagate through the diamond lattice. A substitutional atom that is lighter than the intrinsic atoms (which is considered tightly bound) vibrates at a frequency higher than the Raman frequency. Hence, these vibrations will not propagate through the lattice and are therefore local vibrational modes (LVMs). A loosely bound extrinsic atom, which has a mass that is larger than the intrinsic atoms, vibrates at frequencies lower than the Raman frequency. These vibrational modes are referred to as resonant modes and can propagate a small distance through the lattice. They are created most notably by nitrogen impurities and, due to the abundance of nitrogen in natural diamonds, led to the type classification system of diamonds (introduced in Table 3.1).

5.2 Raman Scattering

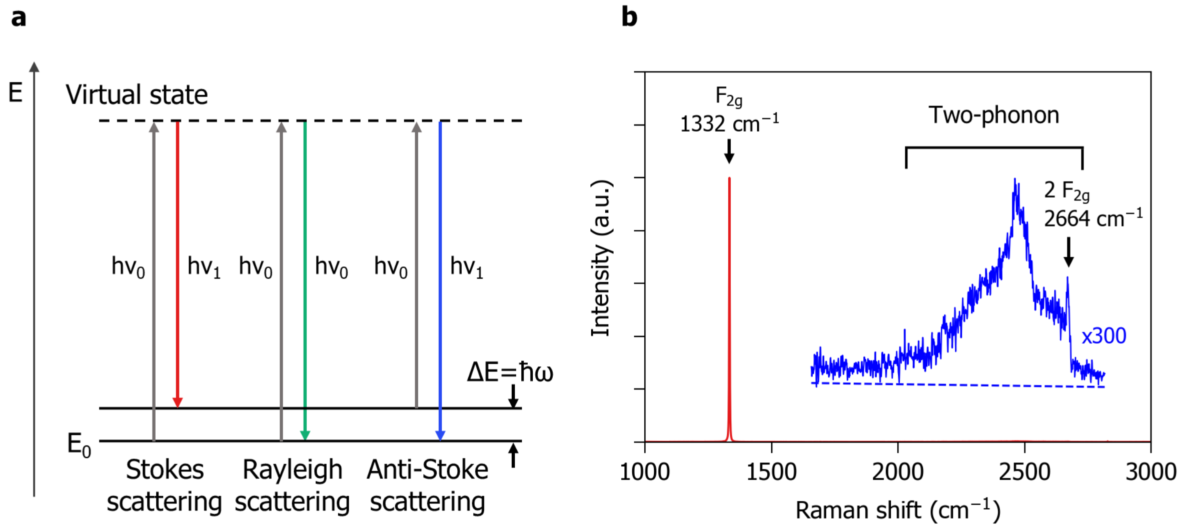

Figure 5.2.: Schematic representation of (elastic) Rayleigh scattering and (inelastic) Raman scattering. Depending on the energy difference between scattered and absorbed light, Raman scattering is split into Stokes and anti-Stokes Raman scattering (a). Raman spectrum on a low nitrogen monocrystalline CVD diamond under laser excitation with 473 nm with the Stokes Raman line at 1332 cm^{-1}. The second order Raman spectrum is zoomed in and displaced vertically for clarity. The dashed line indicates the noise level of the spectrometer (b).

Raman scattering is an inelastic scattering process of light. The absorption of an incident photon can lead to the excitation of an electron into a virtual energy level. In the case of elastic Rayleigh scattering the virtual energy level simply decays by emission of a phonon with identical energy as the incident photon. In Raman scattering the emitted photon has an energy that is different by integer multiples of the Raman frequency depending on the difference between initial and final vibrational level. In the case of Stokes Raman scattering, a phonon of energy

$\hbar\omega$ is emitted into the lattice during decay of the excited state and thus the emitted photon is lower in energy than the incident photon (redshift). In anti-Stokes Raman scattering, a phonon is absorbed during decay of the excited state and the emitted photon is higher in energy (blueshift). The sharpness and intensity of the Raman Stokes line indicates the crystallinity of the investigated lattice (at zero temperature). The ratio between anti-Stokes and Stokes Raman intensity is proportional to the temperature of the lattice. Both Rayleigh and Raman scattering are shown schematically in Figure 5.2a. The Raman shift $\Delta\omega$, in units of cm^{-1}, can be calculated by:

$$\Delta\omega[\mathrm{cm}^{-1}] = \left(\frac{1}{\lambda_0[\mathrm{nm}]} - \frac{1}{\lambda_1[\mathrm{nm}]}\right)\frac{10^7\mathrm{nm}}{\mathrm{cm}}, \tag{5.7}$$

where λ_0 is the excitation wavelength and λ_1 is the emitted light from the sample.

The Raman frequency of $1332\,\mathrm{cm}^{-1}$ in diamond corresponds to the F_{2g} vibrational mode and can be used to evaluate the crystallinity of the sp^3 hybridized diamond lattice [187]. In the context of radiation damage, sufficient radiation dose can induce the formation of two bands at $1580\,\mathrm{cm}^{-1}$ and $1360\,\mathrm{cm}^{-1}$, which correspond to the G-peak and D band of sp^2 hybridized carbon [158]. The shift and asymmetric broadening of the diamond Raman line can also be used to determine stress in the diamond lattice [188]. Raman scattering is observed simultaneously to photoluminescence during excitation with a narrow-band light source like a laser. An exemplary Raman spectrum of CVD diamond with low nitrogen is shown in Figure 5.2b. In addition to the first-order Raman peak at $1332\,\mathrm{cm}^{-1}$, the second-order two-phonon Raman band at frequencies $\leq 2664\,\mathrm{cm}^{-1}$ is shown as well. The second-order Raman band is orders of magnitude smaller in intensity, since it involves the less probable emission of two phonons into the lattice.

6 Experimental Details

This chapter introduces all the necessary experimental details with respect to the type and rationale behind the investigated diamond samples, beam parameters of all irradiation experiments and on-line, in-situ & post-irradiation measurements.

Table 6.1.: Overview of irradiation experiments and samples used. The specific energy of all ions was 4.8 MeV/n. More details about the beam parameters are provided in table 6.2.

Analysis technique	Ti-Dia	Cu-Dia	HPHT type Ib	CVD diamond
Ionoluminescence	^{197}Au	^{197}Au	^{197}Au, ^{48}Ca	^{197}Au
FT-IR absorption	–	–	^{197}Au, ^{48}Ca	–
UV/vis absorption (50 K + RT)	–	–	^{197}Au	^{197}Au
Post-irr. PL	^{132}Xe	^{197}Au, ^{238}U	^{197}Au	–

6.1 Investigated Samples

An overview of the samples and ions used in the irradiation experiments is given in table 6.1. Diamond-based metal matrix composites are investigated as a novel material for luminescence-based beam profile monitors. Beam-induced luminescence is produced in individual diamond particles with sizes from ten to hundreds of micrometer that are embedded in a metal matrix. With this approach it is possible to produce material samples with sizes of a few centimeters which is sufficient for most luminescence applications at GSI and FAIR [189]. Since the diamond phase in the composites consists of low-cost diamond powders, diamond-based metal matrix composites can be produced at a fraction of the costs of bulk diamond samples with comparable sizes. In addition to these composites, various bulk diamond samples of different extrinsic defect concentration were investigated as model systems. Overall, the different diamond(-based) materials can be summarized in four different categories. The production of synthetic diamond is introduced in section 3.1.1:

i **Diamond-based titanium matrix composites (Ti-Dia)**: Specifically engineered composite with diamond particles of smaller size. Ti-Dia consists of diamonds with 45 µm mean particle size (hot-)pressed into pure titanium (grade 2) and titanium alloy (grade 5, titanium with 6 at.% aluminum and 4 at.% vanadium, so-called Ti64). Diamonds in the composites are HPHT-synthesized, so-called "MBD8", diamonds of unknown nitrogen concentration that are mainly used in saw blades or drills via metal-bonding (producer "RHP-Technology GmbH, Austria").

ii **Diamond-based copper matrix composites (Cu-Dia)**: Cu-Dia represents standard thermal management material that is not optimized for luminescence application. Various grades with different mean diamond particle size ranging from 45 to 100 µm were tested. Diamonds in these composites were selected based on the absence of nitrogen for high thermal conductivity applications (producer "RHP-Technology GmbH, Austria").

iii **HPHT-synthesized type Ib diamonds**: Type Ib bulk diamonds served as a model system for the diamonds used in the diamond-based metal matrix composites. According to the manufacturer, they typically contain ∼200 ppm of substitutional nitrogen. Diamonds with rectangular cross section and perpendicular faces were used for spatially resolved photoluminescence mapping in the cross section of the irradiated volume. Irregularly shaped diamonds with "large" surface area (up to $2.5 \times 2.5\,\text{mm}^2$ with plan-parallel surfaces) were used for on-line ionoluminescence and in-situ absorption spectroscopy measurements (producer "Sumitomo Tools, Japan").

- iv **CVD-synthesized nitrogen-free diamonds**: These type IIa diamond samples served as a model system without extrinsic defects with a substitutional nitrogen concentration ≤5 ppb, according to the manufacturer. No nitrogen could be detected in infrared absorption in the samples. Samples of regular shape with $5 \times 5 \times 0.5\,\mathrm{mm}^3$ were used for in-situ UV/vis absorption spectroscopy at 50 K and room temperature (producer "AuDiaTec GmbH, Germany").

Due to the simple way of manufacturing, the properties of diamond-based titanium matrix composites are of main interest for this work. But the irregular shape of the embedded diamond particles makes the interpretation of photoluminescence spectra non-trivial due to scattering and reflection of the excitation laser inside the diamond particles. Absorption spectroscopy is not possible due to the fully opaque metal matrix. Commercially available bulk single-crystalline bulk diamonds with comparable defect concentration were used as the model system for absorption spectroscopy and photoluminescence studies. Since the role of nitrogen in the ion-induced luminescence is not known, effectively nitrogen-free CVD diamonds were used to cross-correlate absorption measurements.

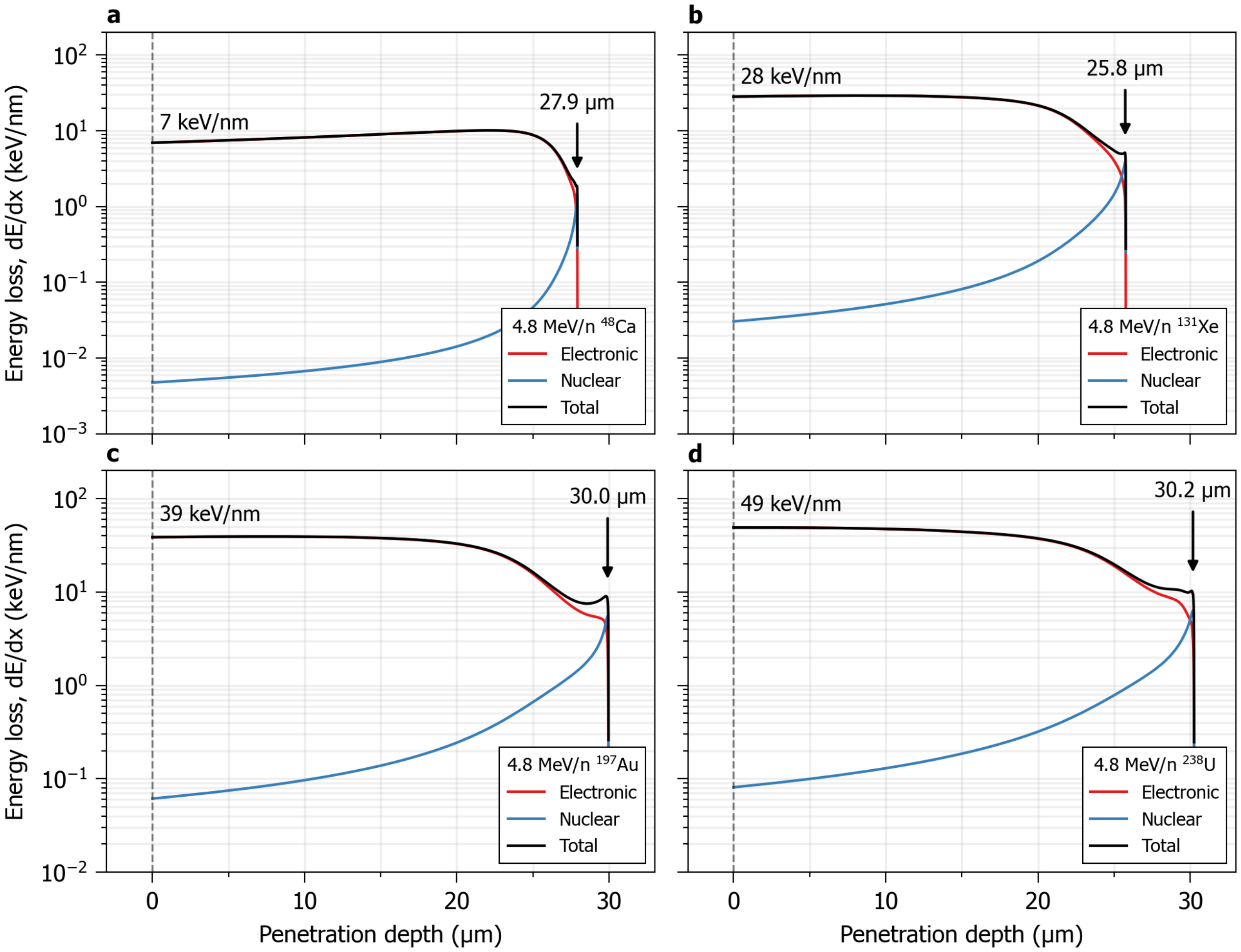

Figure 6.1.: Energy loss of 4.8 MeV/n ions as a function of penetration depth for ^{48}Ca (a), ^{132}Xe (b), ^{197}Au (c) and ^{238}U (d) in diamond with a density of $3.51\,\mathrm{g\,cm^{-3}}$. The total energy loss at the sample surface is indicated by the value in keV/nm. Calculated with SRIM-2013 [32].

6.2 Irradiation Conditions and Experiments

Samples were irradiated with four different ion species with a specific energy of 4.8 MeV/n at the M3 beamline of the M-branch at the UNILAC of GSI. The different ions comprised ^{48}Ca, ^{132}Xe, ^{197}Au and ^{238}U. During initial tests of the diamond-based metal matrix composites, ^{132}Xe and ^{238}U were used. Most of the studies were mainly performed with samples irradiated with ^{48}Ca and ^{197}Au ions. Figure 6.1 shows the energy loss, $\mathrm{d}E/\mathrm{d}x$ and range of these ions in diamond with a density of $3.51\,\mathrm{g\,cm^{-3}}$. Maximum fluences achieved during the irradiation experiments were around $\sim 5 \times 10^{13}\,\mathrm{cm^{-2}}$ with a typical ion flux of $\sim 2 \times 10^{9}\,\mathrm{cm^{-2}\,s^{-1}}$. An overview of the beam parameters is shown in Table 6.2.

Table 6.2.: Beam parameters of the ions used in this work. The specific energy of all ions was 4.8 MeV/n.

Ion	Energy MeV	Pulse length ms	Frequency Hz
^{48}Ca	230.4	1.5	5 and 50
^{132}Xe	628.8	3	50
^{197}Au	945.6	1 and 3	5 and 25
^{238}U	1142.4	0.2 and 0.5	≤2

6.2.1 UNILAC Irradiation Experiments

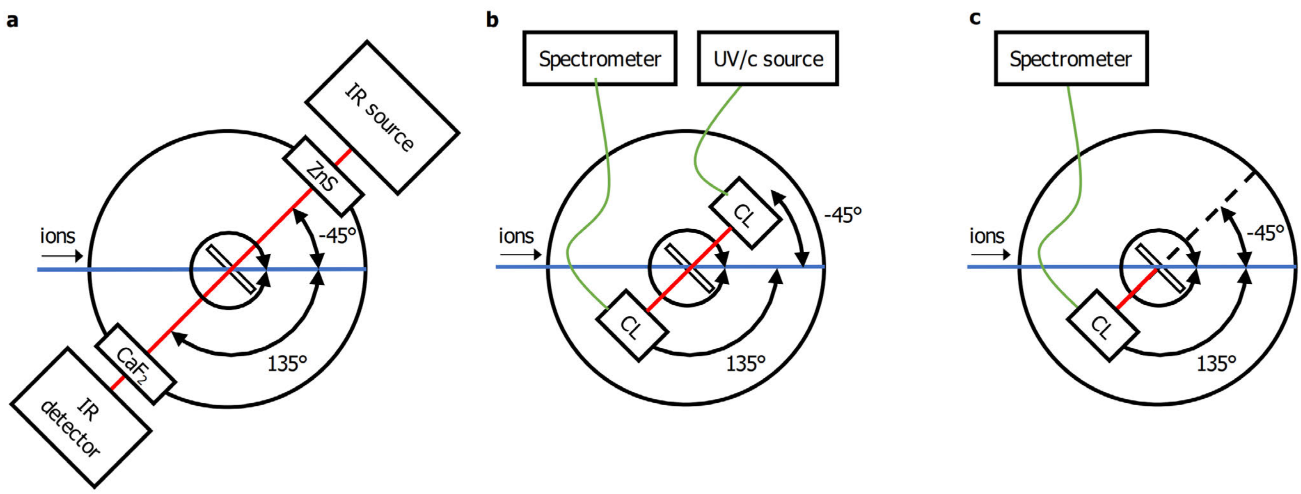

Figure 6.2.: Schematic overview of in-situ and on-line measurement set-ups at the spectroscopy chamber of the M3 beamline; in-situ FT-IR absorption spectroscopy (a), in-situ UV/vis absorption spectroscopy (b) and on-line ionoluminescence spectroscopy (c). "CL" denotes condenser lenses. During FT-IR absorption spectroscopy, infrared light is coupled in and out of the vacuum chamber using infrared transparent vacuum windows. For UV/vis and ionoluminescence the light is coupled in and out of the vacuum chamber using UV-grade optical fibers and two fiber-feedthroughs.

All irradiation experiments were performed at the M3 beamline of the M-branch at the UNILAC of GSI. The M3 beamline provides a rectangular beam spots of up to $\sim 30 \times 30\,\mathrm{mm^2}$. The desired beam spot area is created by cutting the beam using 4 slits that are situated in front of the sample. First, the beam spot is adjusted by the slits to the requested size with a luminescence target at the position of the sample. Second, a Faraday cup is inserted into the beamline behind the slits. Since the charge state of the ions and the beam spot area are known, the current measured by the Faraday cup is converted into a particle flux per area. Thirdly, since the slits used to define the beam spot area are connected to a potential the fraction of the ion beam that is impinging on the slits generates a current. If the beam spot has a homogeneous intensity distribution profile, the current measured on the slits is proportional to the current in the Faraday cup. Using this proportionality, the ion flux and therefore the accumulated fluence are monitored during irradiation.

By experience, we know that this method introduces a systematic error between ∼10 and 20 % of the accumulated fluence on the sample. All experiments were conducted in high vacuum conditions of $\sim 1 \times 10^{-7}$ mbar. The software-controlled "chopper" of the M3 control system stops the irradiation once a given fluence has accumulated on the sample.

Samples that were meant for post-irradiation measurements, so-called "off-line samples", were irradiated in the oven chamber of the M3 beamline. Three different on-line and in-situ irradiation experiments were performed in the spectroscopy chamber of the M3 beamline. A schematic overview of these experiments is shown in Figure 6.2.

6.2.1.1 In-situ FT-IR Absorption Spectroscopy

Figure 6.2a shows the schematic layout of the FT-IR absorption spectroscopy set-up at the M3 beamline. The infrared beam of a Thermo Fisher Scientific Nicolet 6700 is guided with an infrared mirror and coupled with two infrared-transparent vacuum windows (one CaF_2, the other ZnS) in and out of the irradiation chamber. The transmitted infrared radiation is then detected using a nitrogen-cooled infrared radiation (MCT-B) detector. The sample is mounted on a rotating holder. Since rotation of the sample holder takes considerable amount of time ($\sim$15 min), the sample was irradiated at an angle of 45° with the sample positioned in normal incidence to the infrared beam.

All in-situ FT-IR measurements were conducted on "Sumitomo PDXC08" HPHT-synthesized diamonds. Even though these samples exhibit an irregular shape, they have two plane-parallel (111)-surfaces obtained by cleaving. The thickness was $\sim$800 µm with a surface area smaller than $2 \times 2\,\text{mm}^2$. Absorption spectra were recorded in the wavenumber range between 4000 and 400 cm^{-1} (2.5 and 25 µm, respectively) using a spectral resolution of 4 cm^{-1}. A better spectral resolution was not achieved due to a large increase of noise at resolutions of 2 cm^{-1} and 1 cm^{-1} due to the small sample aperture of just 1.5 mm. Input spectra were recorded at least every 2 h through an empty slot in the sample holder with the same aperture of 1.5 mm.

6.2.1.2 In-situ UV/vis Absorption Spectroscopy

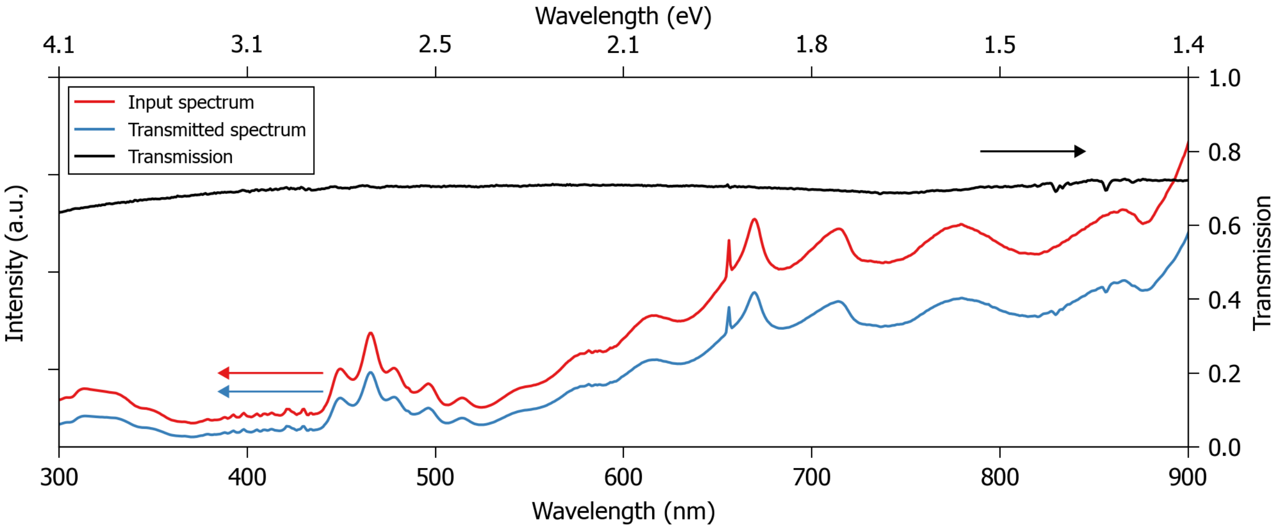

Figure 6.3.: UV/vis absorption spectroscopy. An input spectrum is generated using a combined deuterium/halogen light source. After the sample is introduced into the beam path a transmitted spectrum is measured. The transmission is determined by the ratio of the transmitted and input spectrum.

Figure 6.2b shows the schematic layout of the UV/vis absorption spectroscopy set-up. The UV/vis input spectrum is generated using an "Ocean Insight DH-2000-BAL" light source that combines a tungsten halogen lamp and a deuterium lamp with an effectively usable range of 230 and 2500 nm. The light source was coupled into a solarization resistant multimode SMA-905 fiber optic cable with a core diameter of 600 µm and 0.22 NA ("Thorlabs FG600AEA" fiber). Coupling into the high vacuum chamber was realized using two vacuum fiber feedthroughs ("VACOM T-MM600UV-FSMA") that matched the core diameter and NA of the other fiber optic cables. A solarization-resistant

600 µm UHV-compatible fiber connected the vacuum side of the feedthrough to the "input lens". The input and "output lens" were two identical planoconvex lenses, so-called condenser lenses, of unknown focal length with a diameter of 50 mm mounted in a 62 mm diameter aluminum tube each with an adjustable SMA-905 connector at the back. The distance of the output lens to the sample, 4.5 cm, was chosen so that a $2 \times 2\,\text{cm}^2$ beam spot can safely pass between the lens and the sample at an irradiation angle of $(45 \pm 1)^\circ$. The distance of the input lens to the sample was chosen so that the signal in the output lens was maximized. Using another solarization resistant optical fiber cable. the output lens was connected to a second, identical, fiber vacuum feedthrough flange. The transmitted light was then detected by an "Ocean Insights QE-Pro" dispersive spectrometer with an actively cooled CMOS detector segmented into 1044 pixels that was connected via a 1000 µm core diameter solarization resistant optical fiber cable ("Ocean Insight QP1000-2-SR"). The spectrometer has a calibrated wavelength range of 245 and 1035 nm with a spectral resolution $\Delta\lambda$ of 0.76 nm. Figure 6.3 shows the UV/vis absorption transmission spectrum together with the input spectrum of the light source in comparison to the spectrum transmitted through a pristine CVD-synthesized type IIa diamond.

Measurements were performed in the following manner: prior to irradiation a bare input spectrum was recorded through an empty slot on the sample holder (i). The sample holder was vertically moved to the measurement (and irradiation) position that contained the sample and a transmitted spectrum was recorded (ii). The light source shutter was closed using a remote-controlled 5 V TTL signal (iii). The ion irradiation was started and once a certain fluence accumulated on the sample, the irradiation was stopped, the light source shutter opened and a transmitted spectrum was recorded (iv). To check the stability of the light source, a new input spectrum was recorded about every hour. Acquisition times for the input and transmitted spectra of pristine diamonds were between 1 and 2 s (depending on the sample aperture). With increasing irradiation fluence and decreasing transmission of the irradiated diamonds, acquisition times had to be increased up to 50 s.

Investigated samples comprised "Sumitomo PDXC08" HPHT-synthesized type Ib diamonds with a thickness of ~800 µm and surface area of $\sim 2 \times 2\,\text{mm}^2$. The aperture size for these samples was 1.5 mm. Additionally, "Au-DiaTec Optical Grade" CVD-synthesized type IIa diamonds with a thickness of ~500 µm, rectangular surface area of $5 \times 5\,\text{mm}^2$ were investigated with an aperture size of 4 mm.

Two individual irradiations and measurements were performed at room temperature and at cryogenic temperatures of 50 K on each sample type. Samples were cooled down using a closed-cycle He-cryostat that is integrated into the M3 beamline. The temperature of the sample was measured with a thermocouple that was mounted on the aluminium sample holder in the vicinity of the sample.

6.2.1.3 On-line Ionoluminescence Spectroscopy

Figure 6.2c shows the schematic layout of the on-line ionoluminescence set-up. The light emitted during radiation is collected in a condenser lens, the same "output lens" used in the in-situ UV/vis absorption set-up presented in the previous section. The collection diameter D of the condenser lens was ~22 mm, determined by connecting a fiber-coupled light source to the output lens and then measuring the projected spot size on the sample holder. The collected light is spectroscopically analyzed in a fiber-coupled spectrometer.

Two different fiber-coupled spectrometers were used. An "Ocean Insight QE-Pro" (wavelength range of 245 and 1035 nm with $\Delta\lambda$ =0.76 nm) enabled triggered measurements of the full spectrum with integration times t below 10 s. Additionally, a data-acquisition system recorded the current signal of the slits that defined the beam spot, allowing to extract the flux F and fluence Φ during the ionoluminescence measurements with 100 Hz sampling rate. The two measurements were synchronized by a timing server. The spectrometer was triggered by the timing generator of the UNILAC ion source. Unfortunately, this trigger signal is jittering with respect to the actual ion beam pulses arriving at the sample. Therefore integration times of at least 2 s were necessary to average over a sufficient number of pulses. Ionoluminescence spectra could be measured up to fluences of $2 \times 10^{12}\,\text{cm}^{-2}$, after which the ionoluminescence intensity was smaller than the noise level in the spectrometer.

The spectral ionoluminescence yield Y is then calculated by normalization of the spectrometer signal I to the integration time of the spectrometer t, the collection area of the collector lens A and the ion flux F during irradiation:

$$Y(\lambda) = \frac{I(\lambda)}{I \cdot A \cdot F}. \qquad (6.1)$$

Since A is proportional to the collection diameter D, that was constant for all irradiation experiments, and the spectrometer signal having arbitrary units, the unit of the ionoluminescence yield is per ion.

In the second case, a Peltier-cooled CMOS spectrometer with a moving grating ("Horiba iHR320") was used. The main disadvantage of this spectrometer is that measurements are not synchronized by triggering and integration times are around tens of seconds per grating position (for a wavelength range of 300 and 900 nm the spectrometer measured in 4 "windows" of 150 nm width). Especially at the beginning of a fluence series, where changes are expected at fluences as low as $\sim 10^{10}\,\mathrm{cm}^{-2}$ (reached within a few seconds), the intensity over the whole spectral range is already influenced by the beam-induced changes in the sample. Hence, the integrated ionoluminescence signal has a large systematic error at the beginning of an irradiation. But, the superior signal to noise ratio of this spectrometer allowed the measurement of ionoluminescence spectra at fluences as high as $5 \times 10^{13}\,\mathrm{cm}^{-2}$ (4.8 MeV/n ^{48}Ca).

6.3 Depth-resolved Photoluminescence and Raman Spectroscopy

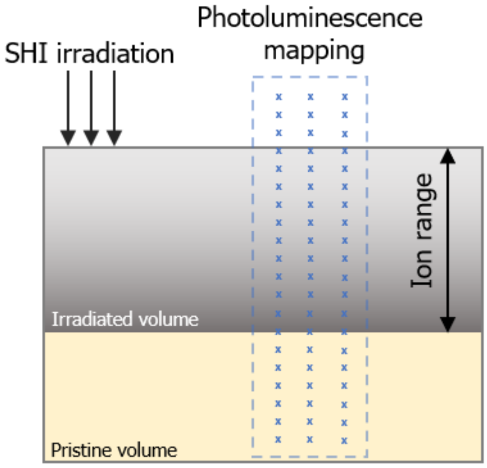

Figure 6.4.: Cross sectional view of an irradiated diamond and photoluminescence mapping. After irradiation a "mapping", usually consisting of three line mappings that start 10 µm away from the diamond surface and extended at least 50 µm deep into the diamond. Lateral distance between the line mappings is 30 µm and longitudinal distance between single measurement points is 1 or 2 µm. The ion range for 4.8 MeV/n ^{197}Au ions is 30.0 µm according to SRIM-2013 [32].

A set of diamonds with rectangular cross section ("Sumitomo SUMICRYSTAL PDX") was irradiated with 4.8 MeV/n ^{197}Au ions to different fluences between $3 \times 10^{9}\,\mathrm{cm}^{-2}$ and $2 \times 10^{13}\,\mathrm{cm}^{-2}$. After irradiation, the diamonds were measured off-line in a confocal Raman spectrometer ("HORIBA LabRAM HR Evolution") with two excitation wavelengths, 473 nm ("blue") and 632.8 nm ("red") excitation. Comparative photoluminescence measurements of irradiated type Ib diamond powders of diamond-based metal matrix composites and bulk type Ib diamonds are presented in section A.2. This section will focus solely on photoluminescence measurements of irradiated bulk diamonds since they exhibit a virtually identical trend under irradiation as the diamond powders.

To follow the radiation damage along the ion trajectory, line scans were performed on the crystal face parallel to the ion beam direction. A mapping measurement consisted of 3 line scans ranging from −10 µm to 50 µm, with 0 µm defined as the surface of the diamonds. The distance between the individual line scans was 20 µm. The distance between single measurement points along a line scan was either 1 or 2 µm. The measurement geometry is shown in Figure 6.4. To minimize the confocal depth of the system, the smallest possible confocal hole size of 20 µm was used. Due to the transparency of the diamonds, the spot size and information volume cannot be estimated accurately. The laser has a transverse spot size of ~3 µm on a fully opaque graphite sample. To ensure that each measurement point is measured with the same focus and information volume, a 3D topography map is created by a depth scan of the microscope in the spectrometer control software and then used as the "focus map".

Measurements with the blue and red laser were performed at the same position on each sample by calibrating the spectrometer for both excitation wavelengths using a silicon wafer prior to measurement. After measurement with the blue laser, the internal optics of the spectrometer were exchanged and a measurement with the red laser was performed without moving the sample.

The measurement parameters were:

- Laser wavelength: $\lambda_{\mathrm{exc}} = 473\,\mathrm{nm}$, $632.8\,\mathrm{nm}$,
- Laser power: 20 mW at the laser output, <10 mW at the sample,
- 100x Objective, 0.9 NA,
- Acquisition time: 0.1 to 2 s.
- Grating: 600 lines per mm, $\Delta\lambda = 0.5\,\mathrm{nm}$,
- Confocal hole size: 20 µm,
- Measurement range: 470 to 800 nm ($\lambda_{\mathrm{exc}} = 473\,\mathrm{nm}$), 630 to 900 nm ($\lambda_{\mathrm{exc}} = 632.8\,\mathrm{nm}$) ,
- Transverse laser spot size: ∼3 µm (determined on an opaque graphite sample),
- Focus: 3D topography map.

7 Spectroscopic Investigation of Ion-Induced Effects in Diamond

This chapter discusses the results obtained by irradiation of different diamond(-based) samples with various swift heavy ions. Radiation-induced macroscopic changes in the irradiated diamonds and ion-induced luminescence are phenomenologically described. Results from on-line ionoluminescence, in-situ UV/vis and infrared absorption and post-irradiation photoluminescence spectroscopy are quantitatively analyzed.

7.1 Observations on Irradiated Diamonds and Diamond-based Metal Matrix Composites

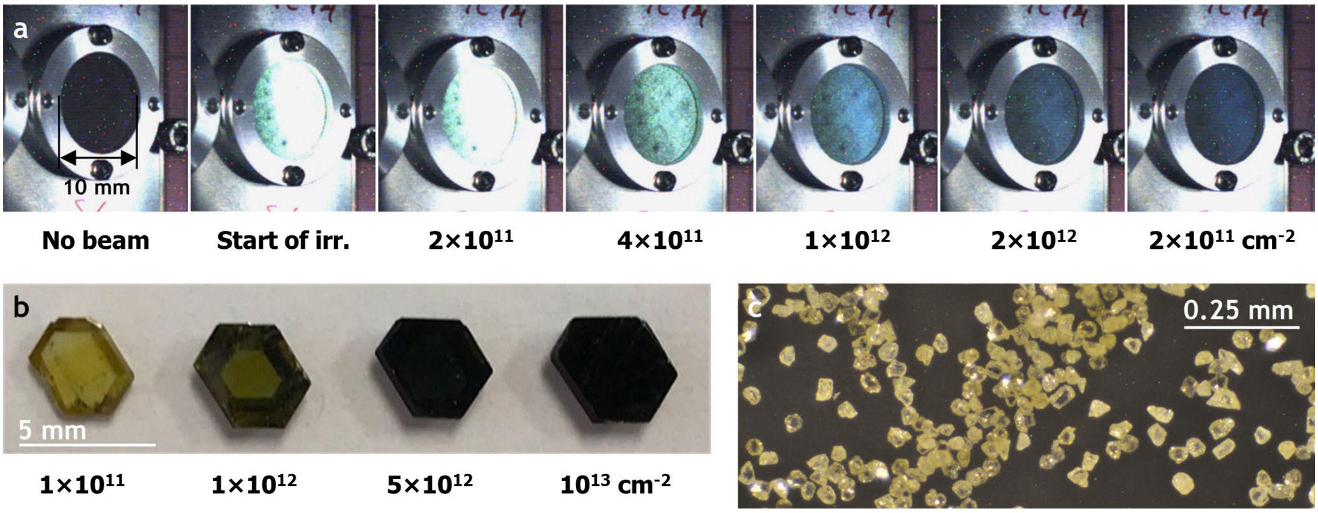

Figure 7.1.: Ionoluminescence of diamond-based copper matrix composite (Cu-Dia) with an average diamond particle size of 45 μm during irradiation with 4.8 MeV/n ^{209}Bi. Courtesy of Marilena Tomut (a). Four different type Ib HPHT diamonds after 4.8 MeV/n ^{197}Au irradiation to different fluences. The beam spot was larger than the sample size. The apparent edges are the parallel surfaces on the back of the diamonds that are still visible below 5×10^{12} cm^{-2}. (b). Micrograph of HPHT-synthesized diamond powder with 45 μm average particle size. Similar diamonds are used in the manufacturing of Cu-Dia and Ti-Dia samples (c).

Figure 7.1 presents an overview of observations on irradiated in comparison to non-irradiated diamonds. Figure 7.1a shows the ionoluminescence of a diamond-based copper matrix composite (Cu-Dia) sample at the M-branch observed with a simple CCD camera through a vacuum viewport during irradiation. With the start of irradiation, the sample starts to emit luminescence. The intensity decreases steadily with increasing ion fluence. Furthermore, the luminescence color is changing from what seems like green luminescence to a blueish hue.

Figure 7.1b shows the effect of SHI irradiation for a series of HPHT-synthesized type Ib diamond monocrystals. The light yellow color, characteristic of a type Ib diamond with a concentration of a few 100s ppm of isolated substitional nitrogen atoms (C centers) distributed within the diamond lattice, is virtually unchanged up to a fluence of 1×10^{11} cm^{-2} of 4.8 MeV/n ^{197}Au ions. At 1×10^{12} cm^{-2}, the color is already dominated by a green hue. At 5×10^{12} cm^{-2}, the diamond has an even darker shade of green and lost nearly all its transparency. At the largest fluence of 1×10^{13} cm^{-2} the diamond is completely blackened by radiation and fully non-transparent to the naked eye. In comparison, pristine HPHT-synthesized diamond powder used in the manufacturing of Cu-Dia and Ti-Dia composites is shown in Figure 7.1c. The micrograph qualitatively shows the size distribution around 45 μm and random shape distribution of the diamond powder. The light yellow color indicates indicates the presence of substitional substitional nitrogen in the lattice of these diamonds.

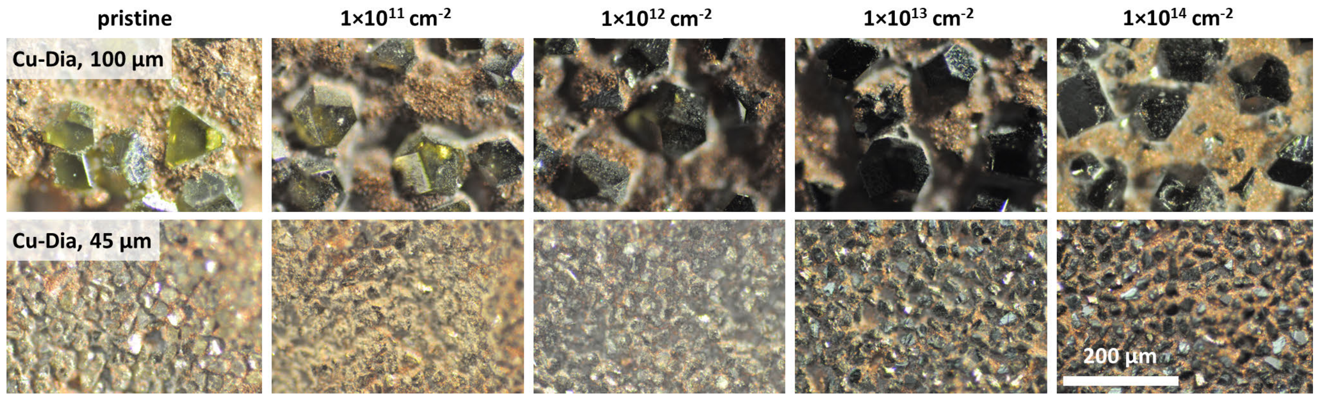

Figure 7.2.: Optical micrographs of two series of diamond-based copper matrix (Cu-Dia) composites irradiated with 4.8 MeV/n ^{238}U (top row) and ^{209}Bi ions (bottom row). Top row: Cu-Dia with an average diamond particle size of 100 µm. Bottom row: Cu-Dia with 45 µm diamond particles. The scale bar applies to all images.

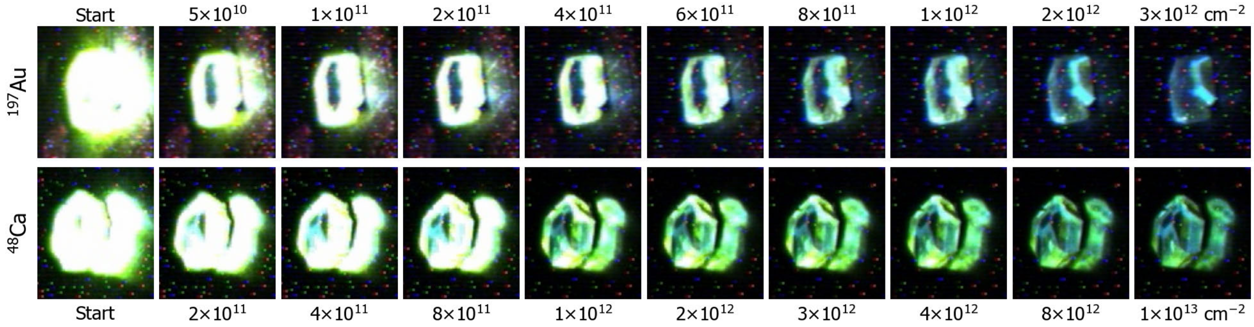

Figure 7.3.: Ionoluminescence series of two HPHT diamonds during irradiation with 4.8 MeV/n ^{197}Au (top row) and ^{48}Ca ions (bottom row) recorded with a CCD camera. The start image corresponds to the first image recorded upon beam on target. Integration time and gain setting of the camera are different between the two rows. Each column corresponds to a similar dose on the sample.

Figure 7.2 shows optical micrographs that illustrate the evolution of two different Cu-Dia composites, one with 45 µm and the other with 100 µm average diamond particle size, irradiated with ion fluences up to 1×10^{14} cm^{-2}. Just like the bulk HPHT diamond presented in Figure 7.1b, the color of the individual diamond particles in the copper matrix changes to black with increasing ion fluence. At 1×10^{11} cm^{-2}, the diamond particles already exhibit a green hue and at 1×10^{12} cm^{-2} a loss of transparency. At 1×10^{13} and 1×10^{14} cm^{-2}, the diamond particles have apparently lost all transparency.

Based on these phenomenological observations, a series of questions arises: Is the radiation-induced luminescence created by intrinsic or extrinsic defects, e.g., due to nitrogen? The ionoluminescence intensity decreases with increasing fluence, is this decrease driven by a decrease of transparency or the 'decay' of luminescent defects? Is a bulk type Ib diamond a suitable model system to investigate the radiation effects of diamond-based metal matrix composites given the difference in size and considering the unknown nitrogen content of the diamonds in the composites? Can the ionoluminescence of diamonds ultimately be used for beam diagnostic luminescence screens?

7.2 Ionoluminescence Spectroscopy

Figure 7.3 shows the ion-induced luminescence of a HPHT type Ib diamond during various stages of irradiation with 4.8 MeV/n ^{197}Au (top) and ^{48}Ca (bottom). At the start of irradiation, the diamonds emit a bright green emission that is quickly decaying within 1×10^{12} cm^{-2} for ^{197}Au and 4×10^{12} cm^{-2} for ^{48}Ca. At large fluences, the green emission intensity has virtually decayed, and the diamond only emits blueish light. This blue component starts to be

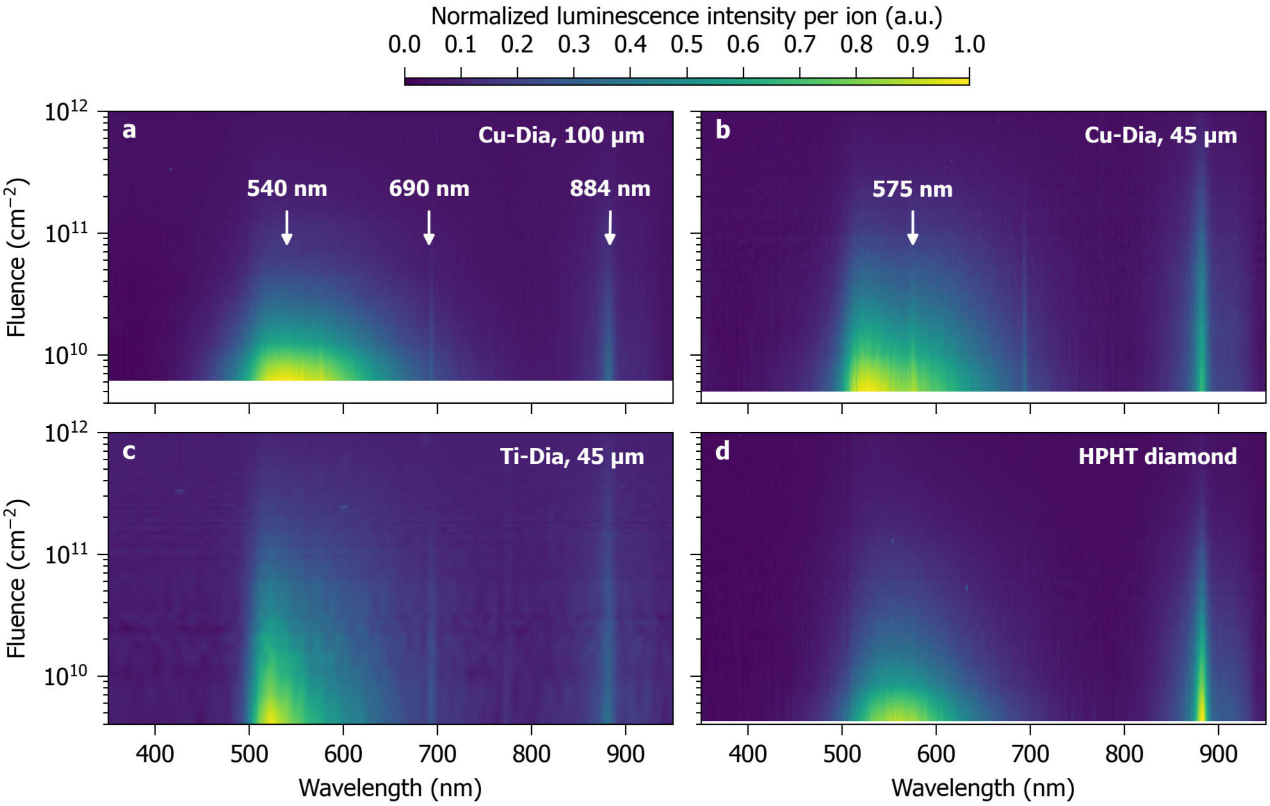

Figure 7.4.: Self-normalized spectral ionoluminescence yield heatmaps of four different samples irradiated with 4.8 MeV/n ^{197}Au up to 1×10^{12} cm^{-2}: diamond-based copper matrix composite (Cu-Dia) with 100 μm (a), Cu-Dia with 45 μm (b), diamond-based titanium matrix composite (Ti-Dia) with 45 μm (c) average diamond particle size and a HPHT synthesized type Ib diamond monocrystal (d). Spectra are normalized to the ion flux during irradiation and self-normalized to the largest ionoluminescence intensity.

visible at fluences as low as 6×10^{11} cm^{-2}. From these very basic CCD camera images, no other color components can be identified. When comparing the visual trend between the two ion species, it seems that, at equivalent dose, the green emission component 'survives' higher doses when exposed to ^{48}Ca ions. This is a potential first indication that the decay rate of the ionoluminescence signal is not simply a function of the total dose but that it also depends on the magnitude of the energy loss. While the total applied dose per ion at 4.8 MeV/n is only a factor of 4 higher for ^{197}Au, the peak electronic and nuclear stopping power are larger by at least a factor of 6 (c.f. Figure 6.1). Also, comparing the observed luminescence in Figure 7.3 with Figure 7.1a the overall trend observed on the Cu-Dia composite is well replicated.

Figure 7.3 also indicates the first drawback for the application of diamonds as a material for luminescence screens. Not only is the ionoluminescence signal quickly decaying, it is also changing its wavelength. Beam diagnostic cameras used for luminescence screens are usually equipped with narrow band-pass optical filters to increase the signal to noise ratio by excluding any parasitic light. Hence, only a fraction of the emitted ion-induced luminescence can be effectively used.

Figure 7.4 shows the ionoluminescence heatmaps of four diamond-based samples during irradiation with 4.8 MeV/n ^{197}Au ions. All samples show a virtually identical ionoluminescence response composed of two distinct emission bands. A broad emission band with a steep edge at 500 nm that extends up to ~700 nm. The second, more narrow, emission band appears between 875 and 925 nm. Emission lines ($\Delta\lambda < 5$ nm) can be identified at 690 nm in the diamond-based metal matrix composites (Figure 7.4a, b, c) and 575 nm in the two Cu-Dia samples (Figure 7.4a, b). A fluence of $\leq 1 \times 10^{12}$ cm^{-2} is sufficient to 'quench' the ionoluminescence intensity to ≤10 % of its initial intensity over the measured wavelength range of 450 and 950 nm.

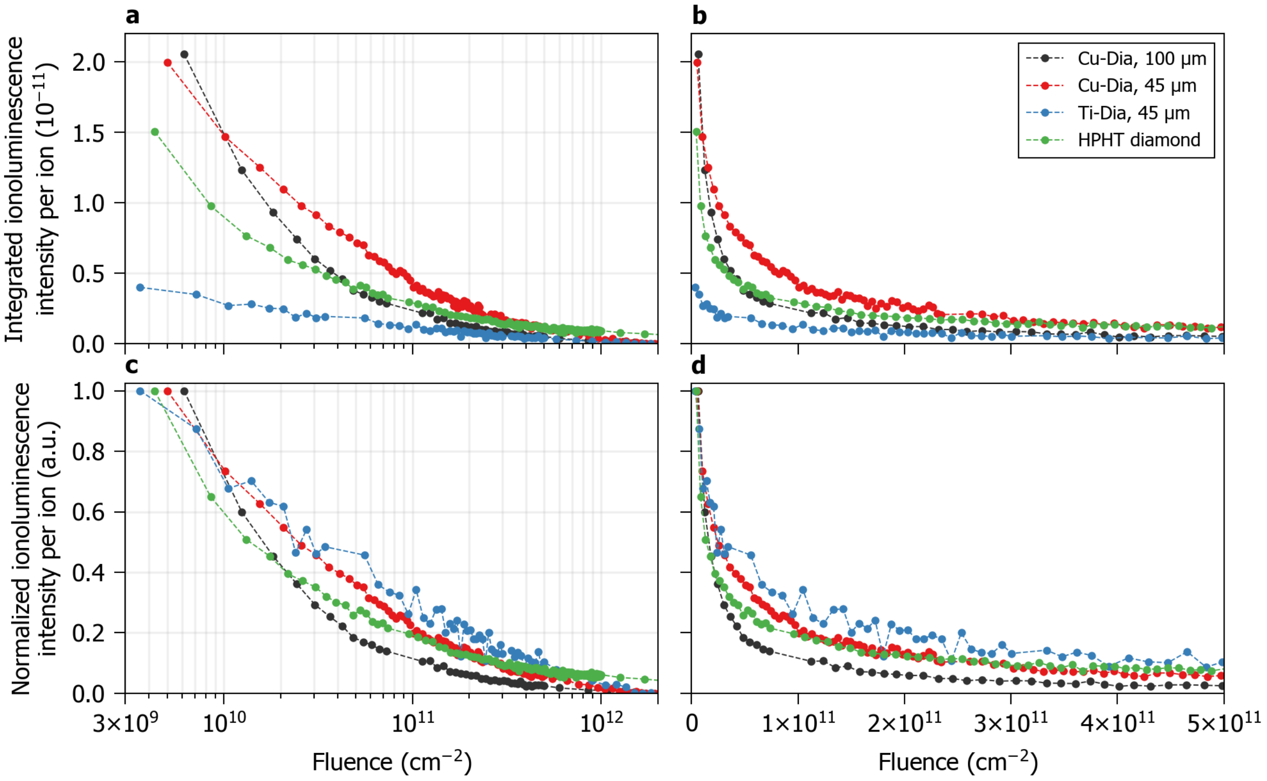

Figure 7.5.: Integrated ionoluminescence in the range between 350 and 950 nm of different diamonds and diamond-based metal matrix (Cu-Dia and Ti-Dia) composite samples irradiated with 4.8 MeV/n ^{197}Au. Integrated luminescence yield normalized by the ion flux measured during irradiation (a, b) and self-normalized (c, d). The left row has linear-log scales and the right row with linear scales.

The spectral content and related defects will be discussed in more detail later. Overall, the spectral composition of the ionoluminescence fits to the camera recording of the samples during irradiation in the same wavelength range (c.f. Figure 7.3).

The ionoluminescence yield, normalized by the ion flux during irradiation, and integrated over the whole spectrometer range from 350 to 950 nm (c.f. Equation 6.1), is shown in Figure 7.5a & b. The largest ionoluminescence yield is observed in the two Cu-Dia samples which are comparable initially. The Ti-Dia sample on the other hand has an initial yield that is $\leq 25\,\%$ compared to the Cu-Dia samples. Unfortunately, direct comparison of the composites with the HPHT diamond is not possible due to the different size (and emission area) of the monocrystalline sample in comparison with the composites.

The self-normalized integrated IL signal, shown in Figure 7.5c & d, indicates that all samples exhibit the same trend with variations on the order of $\pm 10\,\%$ at any given fluence. The IL signal of all samples decays by $\sim 80\,\%$ between 1×10^{11} and $2 \times 10^{11}\,\mathrm{cm}^{-2}$ in comparison to the initial yield and by at least 90 % at fluences larger than $1 \times 10^{12}\,\mathrm{cm}^{-2}$. While these trends look entirely exponential, fits of the single impact model (c.f.Equation 2.12) did not yield any physically meaningful fits. Figure 7.4 shows that the ionoluminescence signal has two major spectral contributions. Hence, Figure 7.6 shows the integrated and maximum IL signal in the two characteristic wavelength ranges between 450 and 675 nm (green) and 850 and 950 nm (infrared). The green emission band dominates the integrated luminescence yields by about an order of magnitude in comparison to the infrared emission band at the beginning of irradiation. The maximum luminescence intensity is also measured in the green emission band, except for the HPHT diamond in which the infrared band has a larger luminescence intensity.

To conclude the ionoluminescence studies, the spectral components are discussed in more detail. Due to the limited sensitivity of the fixed grating CCD spectrometer, used in the previous studies, it was not possible to identify the spectral component responsible for the blue emission at fluences $\geq 1 \times 10^{12}\,\mathrm{cm}^{-2}$ ^{197}Au (c.f. Figure 7.1). Another experiment was performed with a different spectrometer during irradiation with 4.8 MeV/n ^{48}Ca ions. The main

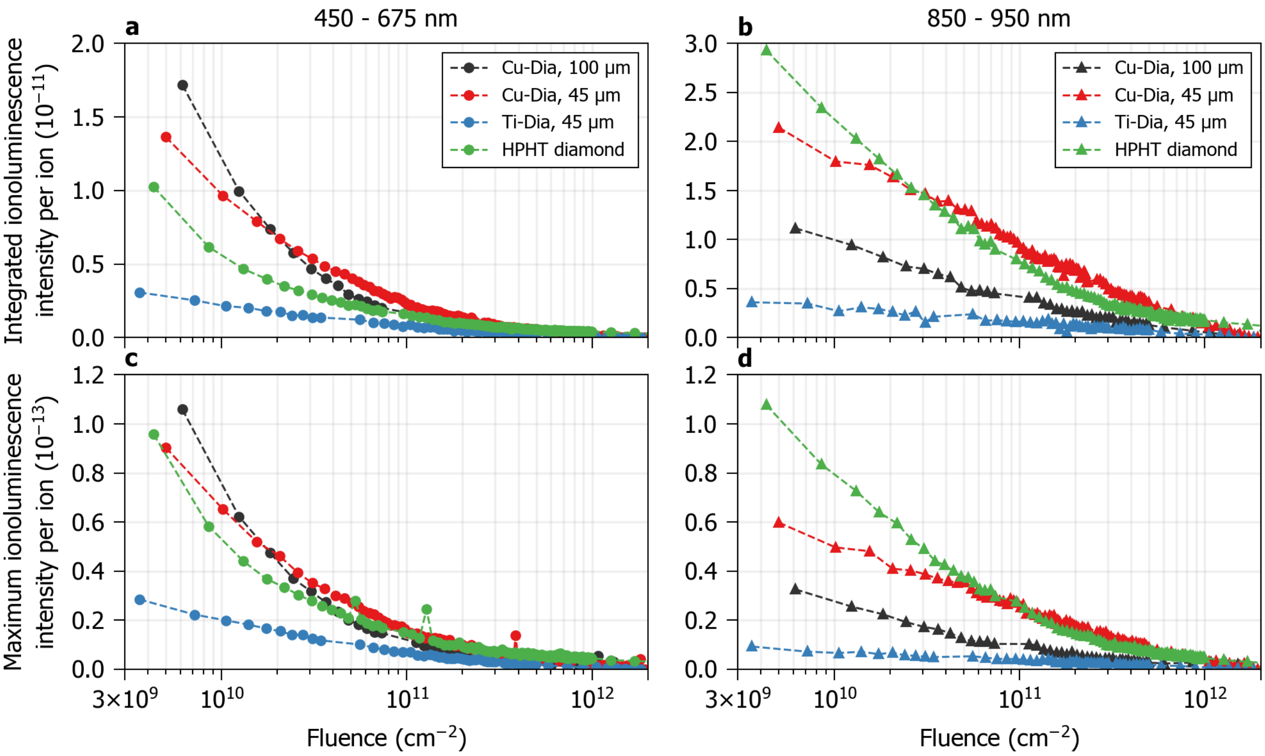

Figure 7.6.: Integrated (top row) and maximum (bottom row) ionoluminescence intensity of diamonds and diamond-based metal matrix (Cu-Dia and Ti-Dia) composite samples irradiated with 4.8 MeV/n ^{197}Au in the two wavelength ranges between 450 and 675 nm (a, c) and between 850 and 950 nm (b, d).

drawback of this measurement was the large integration time of at least 100 second for the acquisition of a single spectrum and, due to the moving grating, intensity discontinuities at the edges at ∼460 nm and ∼720 nm of the three wavelength ranges needed to cover the total spectral range between 350 and 900 nm. But, with a wavelength resolution of $\Delta\lambda = 0.5$ nm and higher sensitivity ionoluminescence spectra were recorded up to 5×10^{13} cm^{-2}.

The resulting ionoluminescence spectra are shown in Figure 7.7. Up to $\sim 4 \times 10^{12}$ cm^{-2}, the IL heatmap in Figure 7.7a coincides well with the results shown in Figure 7.4. The same spectral components around ∼530 nm and ∼880 nm are dominating the IL signal at low fluences. Additional spectral components emerge at fluences $>5 \times 10^{12}$ cm^{-2}. The featureless and broad signal around ∼530 nm evolves into two peaks at 502 nm and 532 nm that eventually split into three peaks at ∼502, ∼519 and ∼532 nm. At fluences larger than 4×10^{12} cm^{-2}, a set of 6 spectral lines between 389 nm and 440 nm evolves that is shown in Figure 7.7c. Additionally, a small peak at 492 nm on the shoulder of the peak at 502 nm can be identified as well. This set of peaks is likely responsible for the blue ionoluminescence observed at fluences $>1 \times 10^{12}$ cm^{-2} (Figure 7.3). Above 650 nm, various peaks are located at 692 nm, which was also observed in Figure 7.4, at 742 nm, at 778 nm and at 884 nm with two minor peaks at 798 nm and 820 nm.

After identifying the spectral ionoluminescence components up to 5×10^{13} cm^{-2} for 4.8 MeV/n ^{48}Ca, the different spectral lines are attributed to defects within the diamond lattice with a summary shown in Table 7.1. The spectral lines ≥389 nm are attributed to the 3.188 eV center and 2.807 eV center, which are typical radiation damage products in diamond and are attributed to the blue IL emission at high fluences. The peak at 884 nm which can be measured from the lowest observed fluence, and which is present in the ionoluminescence spectra of all investigated diamond samples, is attributed to the 1.40 eV center, NiV^-. This center is especially strong in synthetic diamonds grown with a nickel catalyst.

It is not possible to clearly attribute the main spectral component, which is responsible for the green emission, to one single crystallographic defect. Several different defects: the 3H center, an intrinsic color center related to the neutral di-split-interstitial, the H3 center, related to N-V-N aggregates and the green band have overlapping spectral features that can be associated with the observed ionoluminescence. According to literature, the green

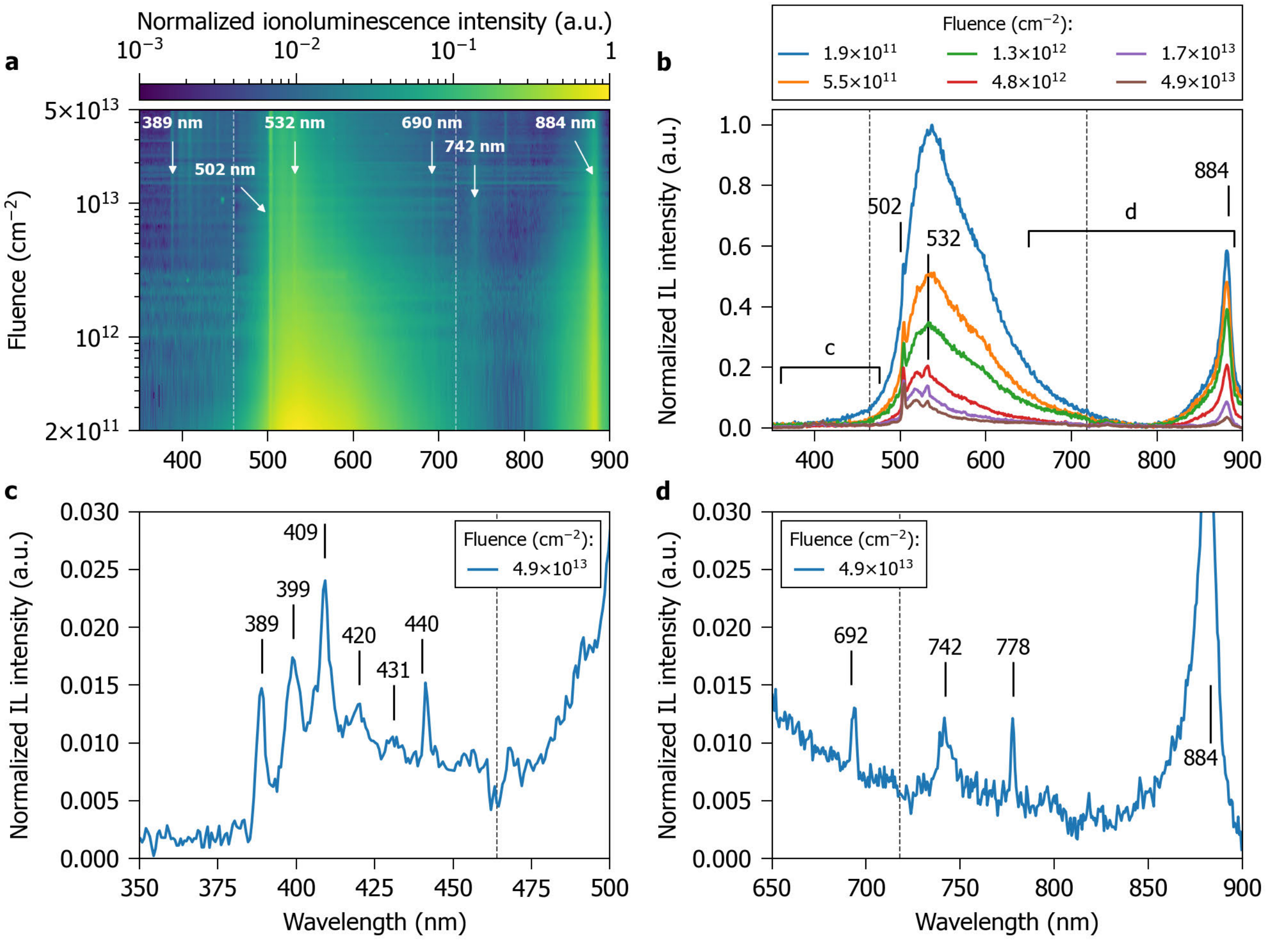

Figure 7.7.: Ionoluminiscence (IL) spectra of type Ib diamond during irradiation with 4.8 MeV/n ^{48}Ca. Ionoluminescence intensities have been normalized to the first spectrum recorded during irradiation up to 1.9×10^{11} cm^{-2}. IL heatmap with characteristic emission lines (a). Evolution of IL spectra at different ion fluences (b). IL spectra at the highest ion fluences below 500 nm (c) and above 650 nm (d). Dashed vertical lines indicate the edges of the individual spectra recorded by the moving grating spectrometer leading to intensity discontinuities. The relative error of the fluence is estimated to be at least 20 %.

band is considered to be impacted only very little by ion irradiation and it is hence the least likely out of these three candidates [140]. The spectral line at 575 nm that is observed in the IL spectrum of Cu-Dia (Figure 7.4a and b) is attributed to nitrogen-vacancy defects in the neutral charge state, the NV^{0}center.

Table 7.1.: Spectral components during ionoluminescence spectroscopy with 4.8 MeV/n ^{48}Ca shown in Figure 7.7 and attribution to crystallographic defects of diamond. All color centers are active in cathodoluminescence [140]. Measured wavelengths have a systematic error of ±2 nm, the systematic error of the energy is thus between 3 and 20 meV depending on the wavelength. Given fluences have a systematic error of ±20 % and correspond to ion fluence where a peak at the measured wavelength can be clearly identified.

Fluence (cm^{-2})	$\lambda_{\text{Measured}}$ (nm)	(eV)	$\lambda_{\text{Literature}}$ (nm)	(eV)	Description
3.188 eV center					
3×10^{12}	389	3.187	389	3.188	ZPL
3×10^{12}	400	3.100	398.5	3.111	$\hbar\omega_1$ =77 meV
3×10^{12}	409	3.031	409.6	3.027	$\hbar\omega_O$ =161 meV
3×10^{12}	420	2.952	420.3	2.950	$\hbar\omega + \hbar\omega_1$ =238 meV
3×10^{12}	431	2.877	432.6	2.866	$2\hbar\omega_1$ =322 meV
2.807 eV center					
3×10^{12}	440	2.818	441.6	2.807	ZPL
GR1 center, V^0					
1×10^{13}	742	1.671	740.9	1.673	ZPL doublet
			744.4	1.665	
1.40 eV center, NiV^-					
5×10^{12}	884	1.403	884.85	1.4008	ZPL doublet
			883.15	1.4035	
Ambiguous spectral components					
$\geq 2 \times 10^{11}$	503.5	2.462	503	2.465	3H center ZPL
			503.4	2.462	H3 center ZPL
$>2 \times 10^{13}$	520	2.384			green band or phonon replica of 3H or H3
2×10^{11}	532	2.331			green band
Unknown spectral components					
1×10^{12}	692	1.792			possibly Al_2O_3
2×10^{13}	778	1.594			
4×10^{13}	798	1.554			
4×10^{13}	820	1.512			

7.3 Depth-resolved Photoluminescence Spectroscopy

Figure 7.8 shows various photoluminescence spectra obtained at different positions and irradiation fluences of 4.8 MeV/n ^{197}Au along the ion trajectory. Different stopping regimes of the ion can be distinguished by depth-resolved measurements. By normalization to the intensity of the diamond Raman line in the pristine substrate, it is possible to correlate the measured intensity to the concentration of a given defect in a first order approximation. The overall trend observed close to the surface is in good agreement with the results obtained on the bulk PDXC diamonds (c.f. Figure A.7, in the appendix). Measurements close to the surface correspond to the region in the diamond that was subjected to the highest electronic energy loss and exhibit the largest absolute changes in photoluminescence intensity (c.f. Figure 7.8a). Regions which were subjected to the highest nuclear energy loss, close to or at the end of the ion range, show smaller changes of the luminescence intensity but a strong degradation of the intensity of the diamond Raman line (c.f. Figure 7.8d) at fluences $\geq 7 \times 10^{12}$ cm^{-2}). This is a first indicator of the general trend that will be discussed in more detail later. The production of color centers depends on the magnitude of electronic energy loss while the degradation of the diamond lattice, indicated by the intensity of the diamond Raman line, depends on the magnitude of the nuclear energy loss.

But this trend is reversing at a certain fluence. The intensity of the 3H center phonon sideband (PSB) at ~520 nm steadily increases up to a fluence of about 3×10^{12} cm^{-2}, while it decreases at larger fluences. The identical trend is also observed for the intensity of the NV$^-$ZPL at 638 nm and its phonon replicas at ~650 nm and ~685 nm. NV$^-$can be clearly identified at fluences $\geq 1 \times 10^{12}$ cm^{-2} and increases to an intensity of ~50 % of the pristine diamond Raman line intensity. In comparison, the 3H PSB already increases at a fluence as low as 3×10^{10} cm^{-2} and increases to an intensity ~3 times larger than the pristine diamond Raman line intensity indicating that ion-induced production of 3H centers is more efficient.

The fluence of maximum 3H and NV$^-$photoluminescence intensities between 3×10^{12} and 7×10^{12} cm^{-2} corresponds to the fluence range at which the vacancy-related GR1 center with its ZPL at ~740 nm can be reliably identified under 633 nm excitation. This suggests a radiation-induced vacancy density threshold that leads to the quenching of other color centers in the diamond [178]. The distribution of GR1 center exhibits an interesting peculiarity. The largest GR1 center intensity is measured at the surface of the diamonds, in the region of the highest electronic energy loss, instead of the region with the highest nuclear energy loss. But, comparison with literature of electron-irradiated diamonds confirms that the highest GR1 intensity is systematically measured in regions that experience the highest electronic energy loss [140].

Lastly, Figure 7.9 shows photoluminescence heatmaps of the irradiated diamonds. The highest luminescence intensities are systematically located at the surface of the diamonds. On the other hand, the photoluminescence signal, especially the diamond Raman line under excitation with 633 nm, rapidly degradades at the end of the ion range at fluences $\geq 1 \times 10^{12}$ cm^{-2} (c.f. Figure 7.9b). Ion-induced effects do not abruptly stop at the end of the ion-range. A change of the PL signal beyond the ion-range can be identified for both laser excitations, especially in the range of the 3H center around ~520 nm (c.f. Figure 7.9a). Reports in literature [150, 168, 174] have shown that radiation-induced stress and lattice degradation extend up to several micrometer beyond the ion range and may be responsible for the production of luminescent defects observed here. Albeit radiation-induced defects beyond the ion range are not observed systematically with increasing fluence. This is tentatively attributed to variations in the pristine samples or slightly different irradiation conditions (e.g., temperature during irradiation).

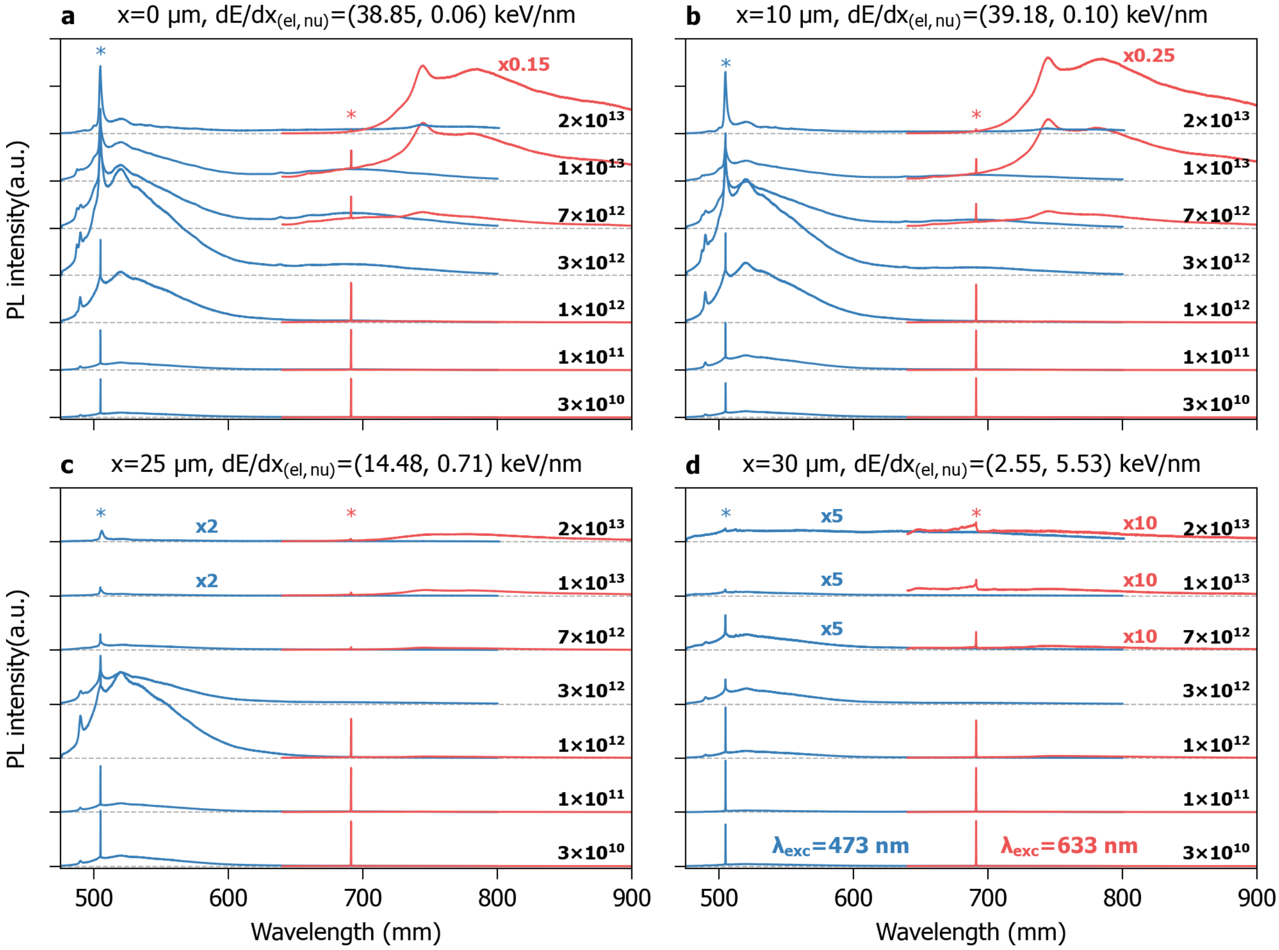

Figure 7.8.: Photoluminescence spectra of pristine and irradiated type Ib diamond samples exposed to different fluences of 4.8 MeV/n ^{197}Au in units of cm^{-2} and excited with 473 nm (blue spectra) and 633 nm (red spectra). Spectra were measured at different positions, corresponding to different electronic and nuclear energy loss $\mathrm{d}E/\mathrm{d}x$ along the ion penetration depth: 0 µm (a), 10 µm (b), 25 µm (c) and 30 µm (d). Intensities are normalized to the average intensity of the diamond Raman line between 40 and 50 µm. Spectra are displaced vertically.

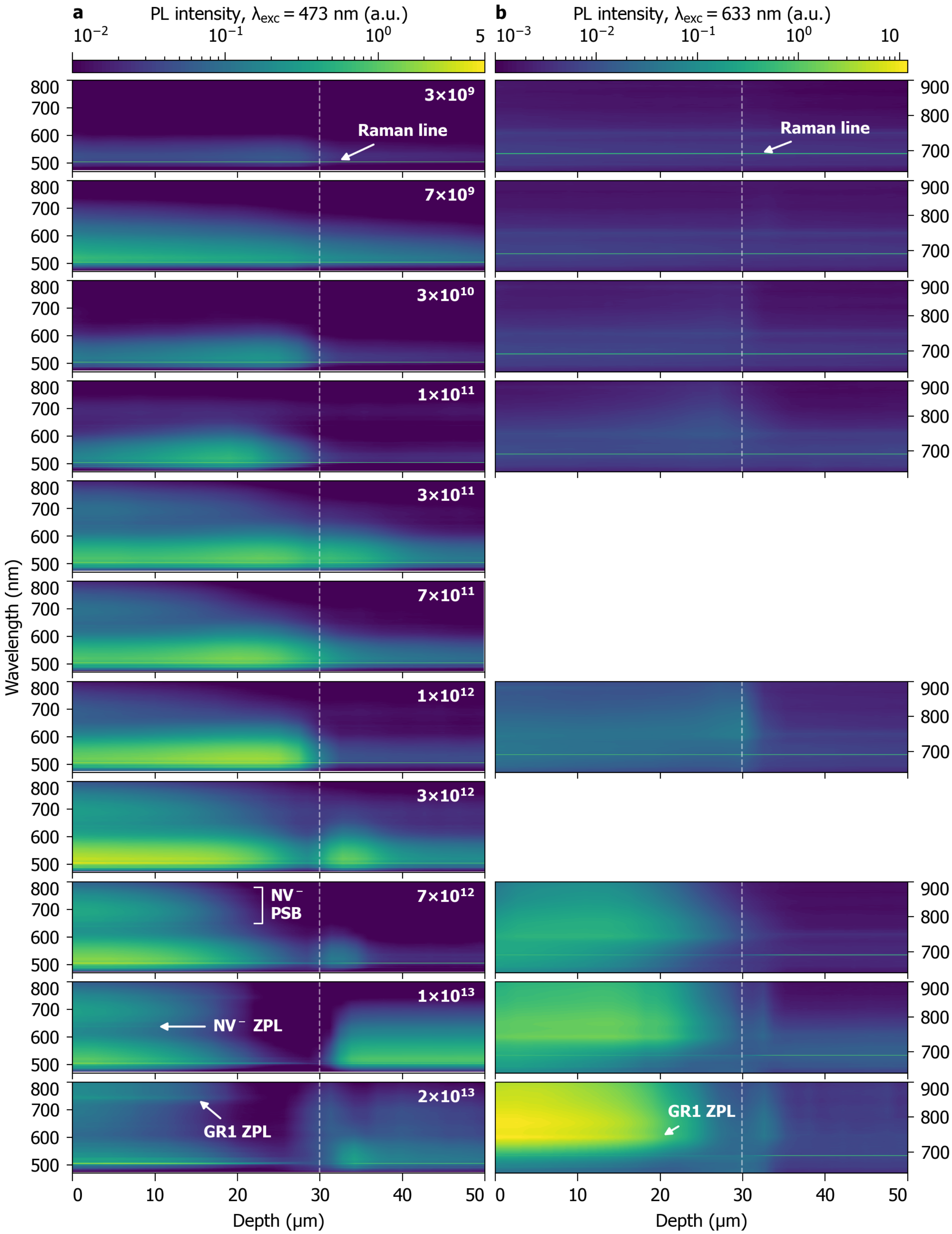

Figure 7.9.: Depth-resolved photoluminescence (PL) heatmaps of type Ib diamonds exposed to different fluences of 4.8 MeV/n ^{197}Au in units of cm^{-2}. Excitation under 473 nm (a) and 633 nm (b). The ion range is indicated by the dashed vertical line. Intensities are normalized to the average intensity of the diamond Raman line between 40 and 50 µm.

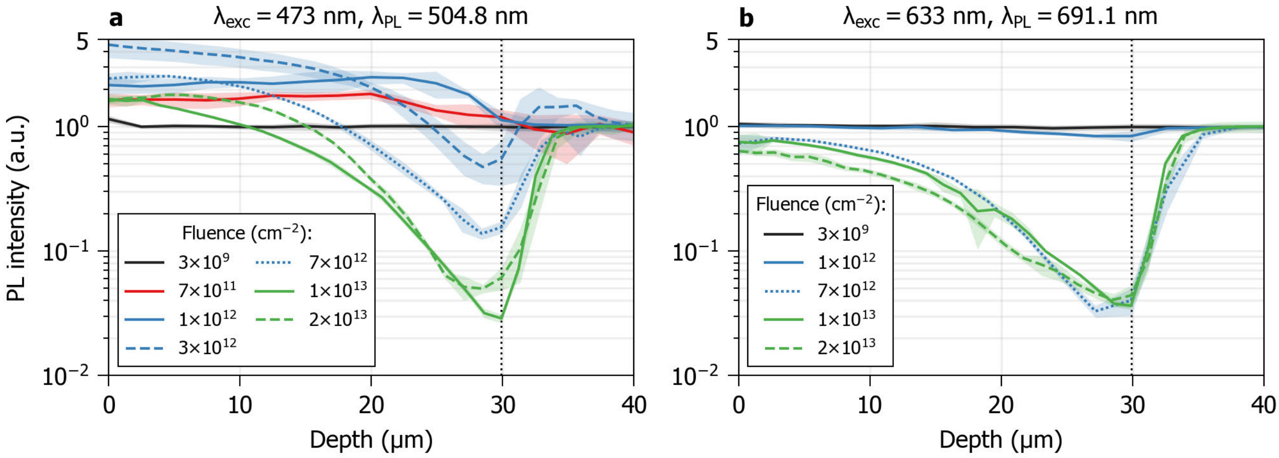

Figure 7.10.: Intensity of the diamond Raman line as a function of depth in type Ib diamonds exposed to different fluences of 4.8 MeV/n ^{197}Au under excitation with 473 nm (a) and 633 nm (b). The ion range is indicated by the dotted vertical line. Intensities are normalized to the average intensity of the diamond Raman line between 40 and 50 μm. Shaded areas indicate the standard deviation of three measurements.

A quantitative analysis of the diamond Raman line intensity under excitation with 473 nm and 633 nm is shown in Figure 7.10. Under excitation with 473 nm, the intensity of the diamond Raman line increases up to a fluence of 3×10^{12} cm^{-2} at the surface after which the intensity decreases steadily (c.f. Figure 7.10a). The intensity of the Raman line decreases to less than ~3 % of the pristine intensity at the maximum fluence of 2×10^{13} cm^{-2}. The initial increase in intensity is due to overlap of the diamond Raman line with the ZPL of the H3 center at ~504 nm (c.f. Figure 7.13).

The diamond Raman line under excitation with 633 nm shown in Figure 7.10b exhibits a considerably clearer trend without an overlap with another luminescence line. The intensity of the diamond Raman line is virtually unaffected by irradiation with fluences $\leq 1 \times 10^{12}$ cm^{-2} while larger fluences lead to a significant decrease of the intensity down to about 4 % of the pristine diamond Raman line intensity at the end of the ion range.

These figures suggest that the degradation of the diamond Raman line is saturated at fluences larger than 7×10^{12} cm^{-2}, especially with 633 nm excitation. Detailed Raman spectra close to the end of the ion range are presented in Figure 7.11. These show that the diamond Raman line is further degrading from 7×10^{12} to 2×10^{13} cm^{-2} for both excitation wavelengths. At a fluence of 2×10^{13} cm^{-2} and at the highest nuclear energy loss at the end of the ion range, no clear Raman line can be identified anymore.

No significant signal from sp^2-hybridized carbon (graphite) can be observed neither at the position of the D-peak at ~1360 cm^{-1}, indicative of defects within graphite basal planes, nor at the position of the G-peak at ~1580 cm^{-1}, indicative of graphite basal planes [6]. A band around ~1630 cm^{-1} can be identified for both excitation wavelengths. While this could be a defect-induced component of the graphite G-peak, this feature probably relates to a radiation-induced defect that is observed in diamonds irradiated with MeV ions or neutrons [140]. The signal at ~1744 cm^{-1} can only be identified under 473 nm excitation and is tentatively attributed to the 515 nm center that is observed in treated synthetic type Ib diamonds that contain nickel and exhibit luminescence from the 3H center, similar to the type Ib diamonds used in this work [140, 190]. Under both excitation wavelengths, the diamond Raman line exhibits a broadening towards lower Raman shifts which is indicative of radiation-induced tensile stresses at the end of the ion range. Reports in literature show that this trend continues with increasing radiation dose and is especially pronounced at the end of the ion range [168].

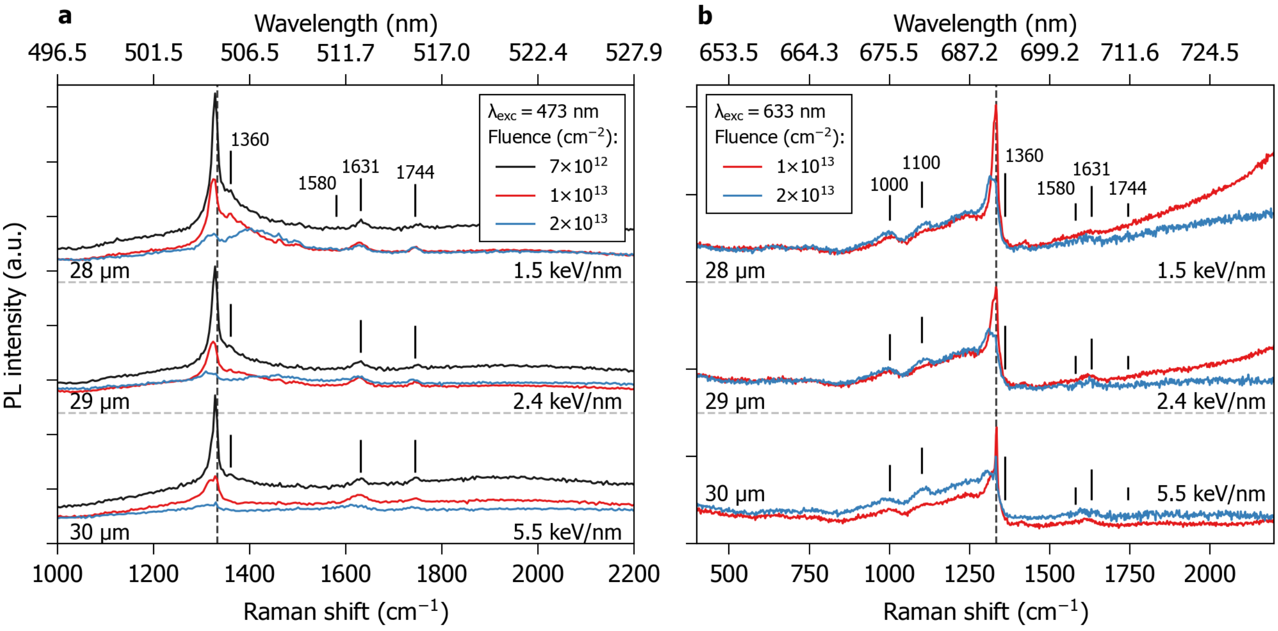

Figure 7.11.: Raman spectra around the diamond Raman line close to the end of the ion range for the three highest irradiation fluences with 4.8 MeV/n ^{197}Au ions under excitation with 473 nm (a) and 633 nm (b). Values in keV/nm correspond to the nuclear energy loss at the measured ion penetration depths. Dashed vertical lines indicate the position of the Raman line in defect-free diamond at 1332 cm^{-1}.

7.3.2 3H and Nitrogen-Vacancy Center

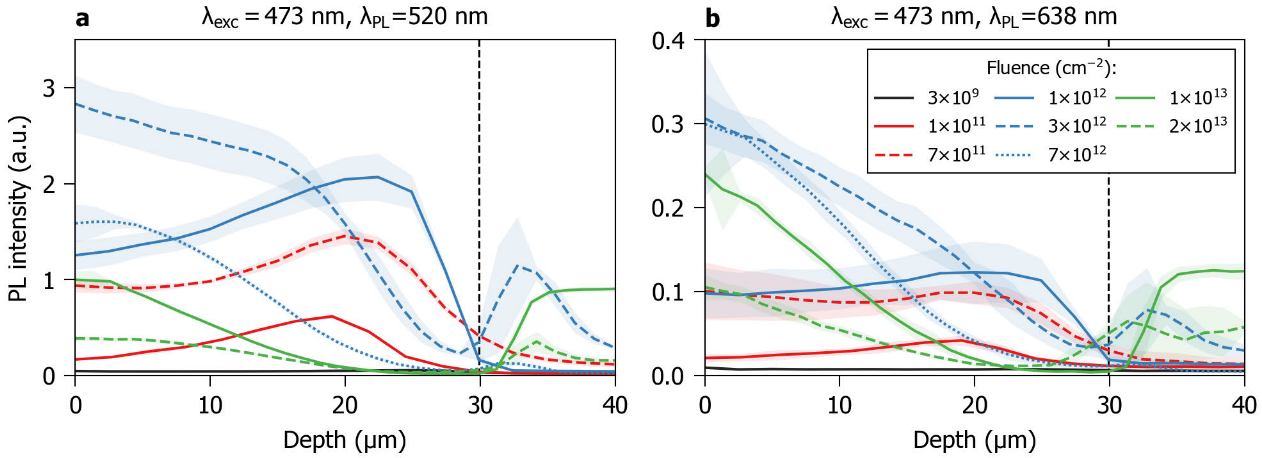

Figure 7.12.: Intensity of the 3H center phonon sideband (a) and the NV^{-}center ZPL (b) as a function of depth in diamond samples irradiated with different fluences of 4.8 MeV/n ^{197}Au in units of cm^{-2} for excitation with 473 nm. Intensities are normalized to the average intensity of the diamond Raman line between 40 and 50 µm. Shaded areas indicate the standard deviation of three measurements.

Figure 7.12 shows the photoluminescence intensity of the 3H center phonon sideband (PSB) at ~520 nm and the NV^{-}center ZPL at 638 nm. The 3H PSB was chosen as the reference intensity for the concentration of the 3H defect since the 3H ZPL overlaps with the diamond Raman line under excitation with 473 nm (c.f. Figure 7.13). Up to a fluence of 1×10^{12} cm^{-2}, both color centers have their maximum intensity at a depth of ~25 µm while the maximum intensity can be observed close to the surface at a fluence of 3×10^{12} cm^{-2}.

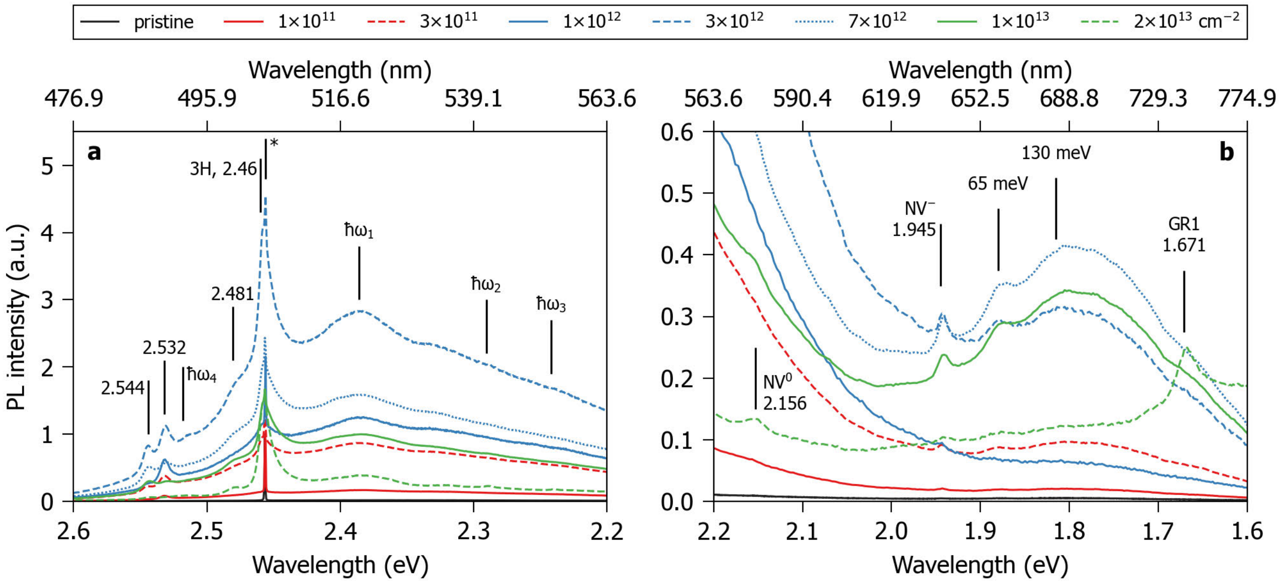

Figure 7.13.: Photoluminescence spectra of type Ib diamonds samples exposed to different fluences of 4.8 MeV/n ^{197}Au in units of cm^{-2}. Photoluminescence spectra under 473 nm excitation around the 3H (a) and the NV^0& NV$^-$centers (b) measured close to the surface (depth ~0 µm). The diamond Raman line is indicated by the *. Intensities are normalized to the average intensity of the diamond Raman line between 40 and 50 µm.

A clear correlation whether 3H or NV$^-$centers are preferentially produced in the electronic or nuclear energy loss regime is not possible. Up to 1×10^{12} cm^{-2}, the intensity profile of the two color centers might follow the profile of the electronic energy loss. While nuclear energy loss provides the necessary defects to form the color centers (keep in mind 3H and NV$^-$are ensemble defects involving multiple crystallographic lattice sites), the magnitude of the electronic energy loss determines the number of color centers that are ultimately produced. The higher the ratio between electronic and nuclear energy loss, the larger the number of produced color centers up to a threshold of lattice damage where these color centers are destroyed by additional radiation damage within the lattice [178, 191]. The results indicate that the photoluminescence intensity of 3H and NV$^-$centers are increasing up to radiation-induced vacancy densities ~5×10^{18} cm^{-3} while larger vacancy densities lead to decrease of photoluminescence intensity.

The signal at 2.46 eV (504 nm) is attributed to the 3H center (di-<100> split self-interstitial) without explanation, even though this signal could also be related to the H3 center (N-V-N) with its ZPL at 2.463 eV (503.2 nm). Overall, there is no single conclusive observation in the presented PL measurements, but multiple observations point to the 3H center instead of the H3 center.

The 3H center has a single vibrational replica in the Stokes region, $\hbar\omega_1$, that is shifted by 74 meV. H3 on the other hand has two vibrational replica shifted by 41 meV and 81 meV, which are clearly distinguishable even at room temperature [192]. Figure 7.13a shows a nearly symmetric PSB at the position of the 3H $\hbar\omega_1$ replica. Other phonon replica $\hbar\omega_2$, $\hbar\omega_3$ and $\hbar\omega_4$ occur at 169, 218, and 58 meV (anti-Stokes scattering) with respect to the 3H ZPL. Albeit these cannot be identified unambiguously. Another indicator for the 3H center is the presence of a shoulder at 2.481 eV (499.8 nm) [140]. Lastly, the intensity of 3H ZPL relative to its PSB is larger at room temperature, while the opposite is true for the H3 center [140, 193].

The NV center PL spectrum is shown in Figure 7.13b. The NV$^-$center at 1.945 eV (638 nm) can be clearly identified together with its two phonon replica shifted by 65 and 130 meV. The largest intensity of the NV$^-$ZPL can be observed at fluences of 3×10^{12} and 7×10^{12} cm^{-2}, while the largest PSB intensity occurs at 7×10^{12} cm^{-2}. NV^{0}can only be detected at the two largest irradiation fluences of 1×10^{13} and 2×10^{13} cm^{-2} after the intensity of the NV$^-$decreased. Substitutional nitrogen in the diamond lattice acts as an electron donor for NV^{0}centers, thus NV$^-$is preferentially produced by irradiation in type Ib diamonds.

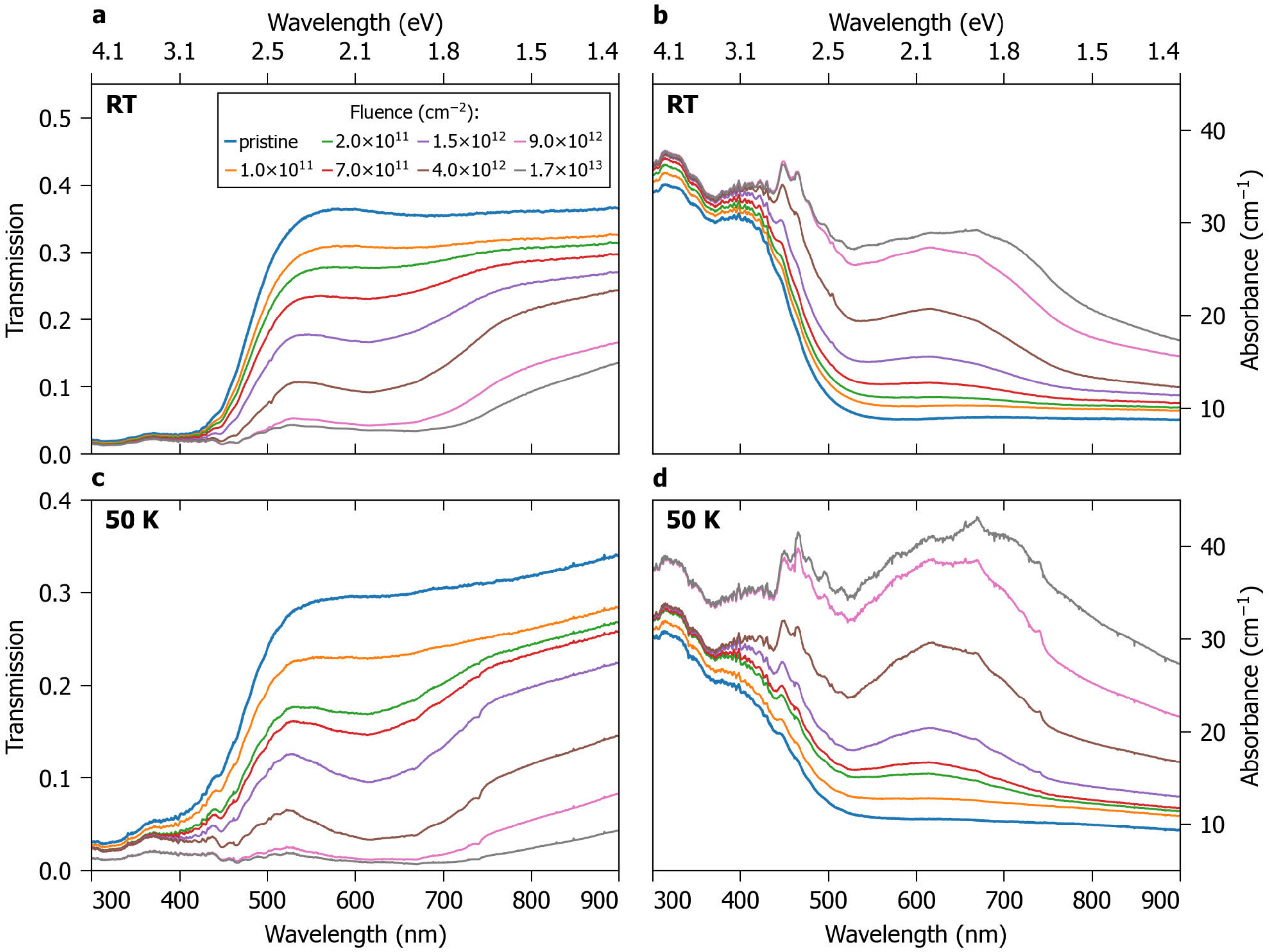

Figure 7.14.: In-situ transmission (a, c) and absorbance (b, d) of a type Ib diamond at different fluences of 4.8 MeV/n ^{197}Au ions. The upper row was measured and irradiated at room temperature, while the lower row was measured and irradiated at 50 K.

In-situ UV/vis absorption spectroscopy was conducted on type Ib and type IIa diamonds irradiated to different fluences of 4.8 MeV/n ^{197}Au ions. Both irradiation and spectroscopy measurement were conducted at room temperature and 50 K, respectively. The investigated samples comprised HPHT-synthesized type Ib diamonds with ~200 ppm N_s and CVD-synthesized type IIa diamonds with $\leq$5 ppb N_s. The used type Ib bulk samples were identified as a model system for the diamond powders used in the diamond-based metal matrix composites presented in the previous sections. Type IIa diamonds served as a quasi defect-free system to investigate the specific role of (substitutional) nitrogen on the radiation-induced evolution of defects.

7.4.1 HPHT-synthesized Type Ib Diamond

Figure 7.14 shows in-situ measurements of the spectral transmission and absorbance of HPHT-synthesized type Ib diamonds (~200 ppm N_s) at different fluences of 4.8 MeV/n ^{197}Au ions at room temperature and 50 K. Pristine transmission spectra are characterized by an absorption edge at ~450 nm. While pure diamond has an absorption edge at ~225 nm due to its bandgap of ~5.5 eV, the absorption edge of nitrogen-containing diamonds shifts to lower energies by the presence of substitutional nitrogen that acts as an electron donor [194].

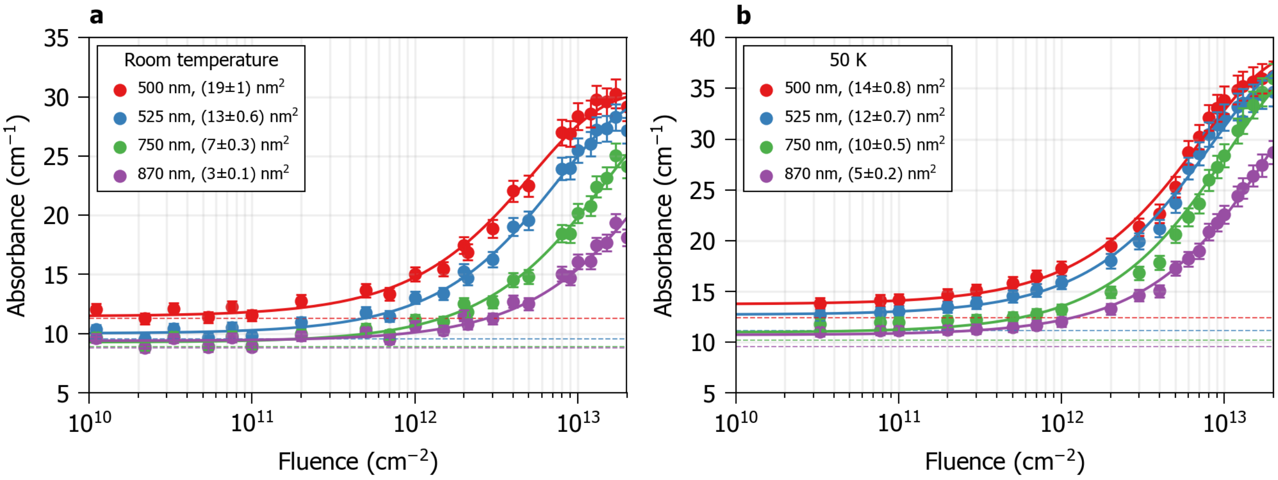

Figure 7.15.: Absorption of type Ib diamond at different wavelengths as a function fluence for irradiation with 4.8 MeV/n ^{197}Au ions at room temperature (a) and at 50 K (b). Dashed horizontal lines represent the absorption at the given wavelength of the pristine sample. Solid lines are fits of the direct impact model, Equation 2.12, to the measurement data with the damage cross section σ given in the legend.

With increasing fluence, a dominant absorption band develops between 450 and 500 nm. Comparing this to the input spectrum of the used deuterium/halogen light source shown in Figure 6.3, it is clear that this absorption[1] band is not an irradiation-induced feature but an artifact of the measurement. At high absorption levels measurements become less reliable due to the low intensity of transmitted light and are eventually dominated by the intensity variation of the input spectrum. Due to this, spectra are thus analyzed only above 480 nm (2.58 eV).

Independent of irradiation temperature, a large absorption band between ~510 nm and ~780 nm evolves with increasing fluence which is attributed to radiation-induced vacancies and interstitials. The intensity of this absorption band is larger for irradiation at 50 K. The cryogenic temperature during irradiation leads to increased defect production due to reduced beam-induced annealing. Similar absorption spectra were observed on neutron-irradiated and subsequently annealed nitrogen-free diamonds [195]. Furthermore, several zero-phonon lines (ZPLs) of known color centers can be identified at ~503 nm (~2.46 eV), ~656 nm (~1.89 eV) ~725 nm (~1.71 eV) (only at 50 K irradiation temperature) and ~741 nm (~1.67 eV) which are attributed to the di-split-interstitial defect (3H center), two irradiation features the 1.889 eV and 1.711 eV centers, and the neutral vacancy GR1 center, respectively.

The ZPL at ~503 nm (~2.46 eV) could also be related to the nitrogen-related H3 center, N-V-N, and its ZPL at 503.2 nm (2.464 eV). This possibility is discarded because neither the NV^0center at 575 nm (2.156 eV) nor the NV^-center at 638 nm (1.945 eV) can be detected in any of the absorption spectra. Photoluminescence spectroscopy measurements presented in section 7.3 also indicate that 3H centers are the most likely candidate for a defect at this ZPL position.

Figure 7.15 shows the absorption intensity at various wavelengths as a function of fluence modelled with the single impact model (c.f. Equation 2.12) at the two different irradiation temperatures. No color center absorption could be identified in direct vicinity to the wavelengths chosen for this analysis. The damage cross section σ of the single impact model is virtually equal between the two irradiation temperatures at any of the investigated wavelengths. The excellent agreement with the single impact model implies that irradiation with swift heavy ions leads to the production of a featureless and broad absorption band. This can be simply attributed to an increase of sp^2-hybridized carbon in the irradiated volume. Specifically, the origin of featureless absorption bands that are observed on so-called brown diamonds is attributed to vacancy clusters and dislocations [196].

---

[1] Absorption (intensity) and absorbance are used interchangeably to describe the negative logarithm of the transmission normalized to the sample thickness.

7.4.1.1 Room Temperature Irradiation

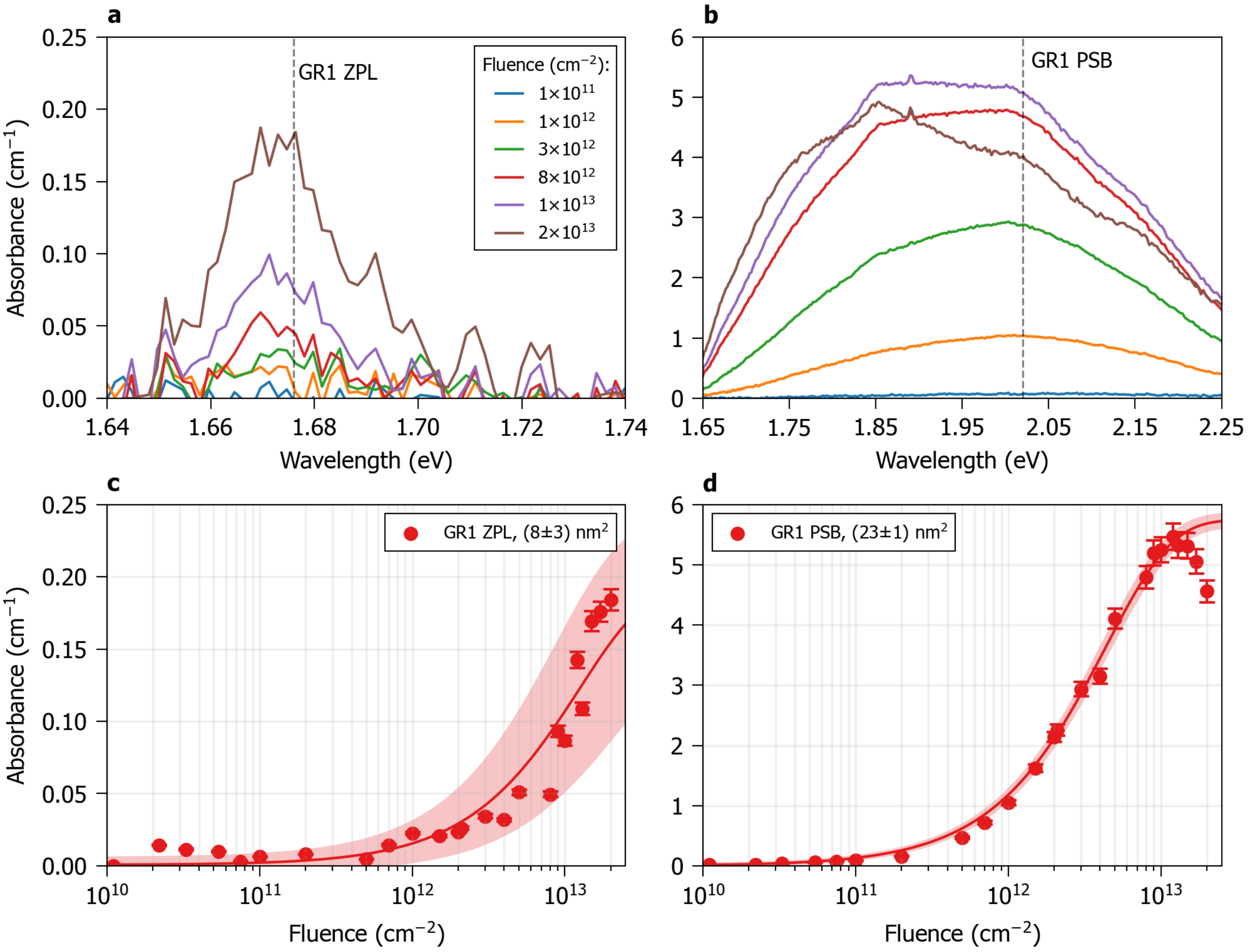

Figure 7.16.: Characteristic absorption range of the GR1 center with its ZPL (a) and phonon sideband (PSB) (b) in type Ib diamond irradiated and measured at room temperature for different fluences of 4.8 MeV/n ^{197}Au ions. All spectra are background corrected. Absorbance of the GR1 center ZPL (c) and the GR1 center PSB at 2 eV (d) as a function of fluence. Solid lines are fits of the single impact model to the measurement data with the damage cross section σ given in the legend. Shaded areas represent the standard deviation of the fit.

Figure 7.16a and b show the background-corrected absorption intensity of the neutral vacancy GR1 center with its ZPL at 1.673 eV (740.9 nm) and phonon sideband at ~2 eV (~620 nm). Background correction was performed by first subtracting the pristine absorption spectrum. For the GR1 center ZPL a linear background between 1.54 eV and ~1.74 eV was subtracted and a linear background between 1.65 eV and 2.25 eV [197] was subtracted for the sideband. The ZPL is slightly shifted to smaller energy due to expansion of the diamond lattice in comparison to cryogenic temperatures [198]. At room temperature the absorption of the ZPL, at its maximum of ~0.2 cm^{-1}, is considerably smaller than the phonon sideband of up to ~5.5 cm^{-1}. This is expected of a measurement at room temperature where the phonon population leads to an increased absorption cross section of the sideband.

The ZPL absorption intensity yields a very poor fit of the single impact model with a damage cross section of (8 ± 3) nm^2 (c.f. Figure 7.16c). The phonon sideband on the other hand yields a fit of good quality with a damage cross section of (23 ± 1) nm^2 (c.f. Figure 7.16d). The maximum absorption intensity of the phonon sideband is measured at a fluence of 1.2×10^{13} cm^{-2}, while larger fluences lead to its decrease. This effect is probably due to the quenching of existing defects or aggregation of isolated vacancies into vacancy clusters after a radiation-induced critical vacancy density is exceeded [178]. Identical trends are observed in photoluminescence spectroscopy presented in section 7.3.

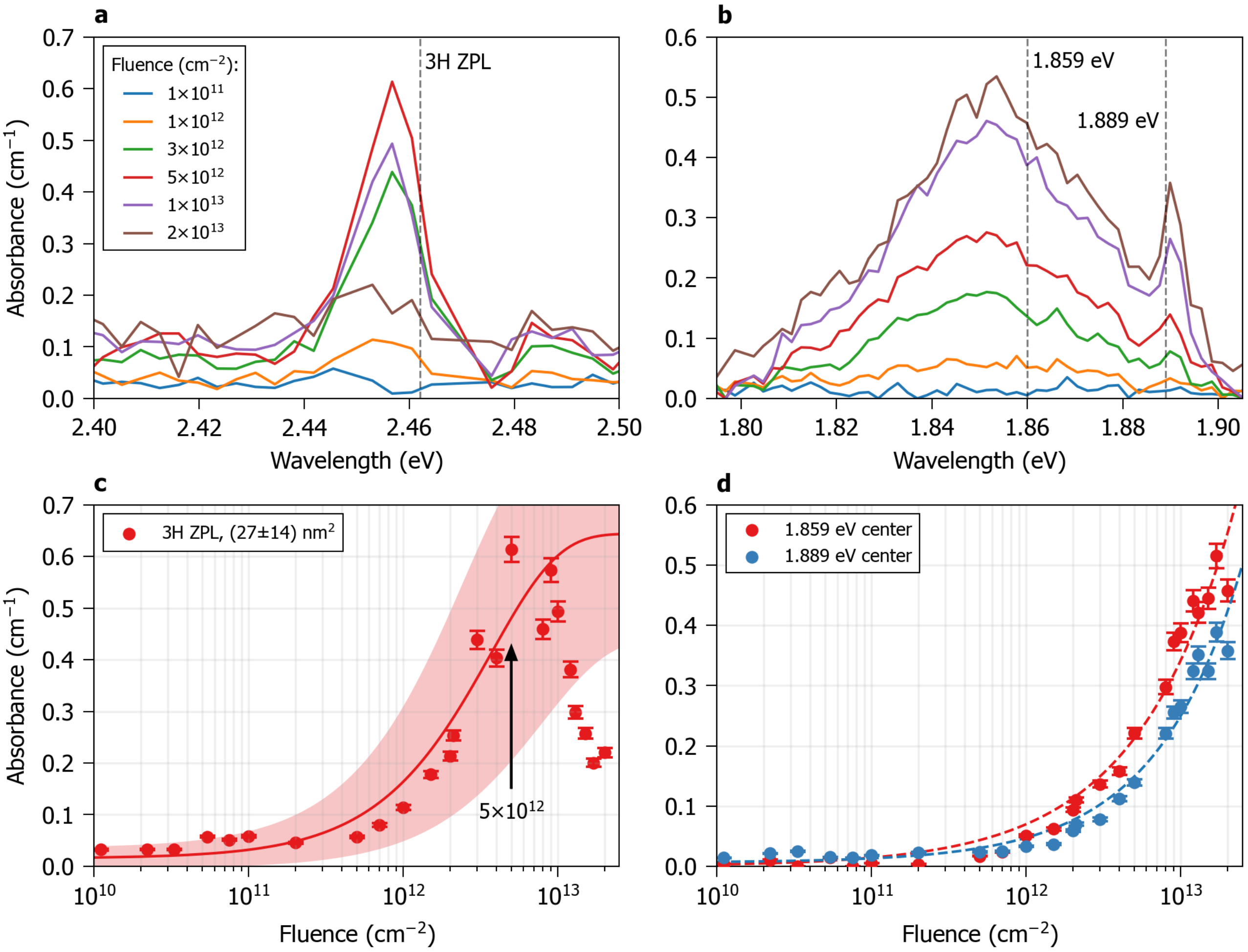

Figure 7.17.: Characteristic absorption range of the 3H center (a) and the 1.859 eV & 1.890 eV centers (b) in type Ib diamond irradiated and measured at room temperature for different fluences of 4.8 MeV/n ^{197}Au ions. All spectra are background corrected. Absorbance of the 3H ZPL (c) and the 1.859 eV & 1.890 eV centers (d) as a function of fluence. Solid lines are fits of the single impact model to the measurement data with the damage cross section σ given in the legend. Shaded area represent the standard deviation of the fit. Dashed lines are guides to the eye.

The evolution of the absorption intensity of the di-split-interstitial 3H center ZPL at 2.462 eV is presented in Figure 7.17a and c. Background correction is performed by first subtracting the pristine absorption and then subtracting a linear background between 2.4 eV and 2.47 eV. The evolution of the 3H ZPL absorption intensity exhibits the same trend as the GR1 center phonon sideband albeit with its maximum absorption intensity of 0.8 cm^{-1} at a lower fluence of 5×10^{12} cm^{-2} and a comparable damage cross section of (27 ± 14) nm^{2}.

Figure 7.17b) and d) show the evolution of the absorption of the split-interstitial 1.859 eV center, the most stable form of non-aggregated interstitials. The co-existence of split-interstitials and di-split-interstitial 3H centers is due to the energy gain of interstitial aggregation as dangling bonds are being terminated in this process. Two split-interstitials have four dangling bonds (two each) while a di-split-interstitial has two dangling bonds. Interestingly, the absorption of split-interstitial still increases at fluences $\geq 5 \times 10^{12}$ cm^{-2} where the 3H center intensity is decreasing.

The evolution of the 1.889 eV center absorption, which is an irradiation feature of unknown structure [140], is shown in Figure 7.17b and d as well. This center is only produced in highly damaged diamond lattices as it only appears at fluences well beyond 1×10^{12} cm^{-2} and its evolution does not follow the direct impact model and its trend is rather indicative of a defect accumulation process.

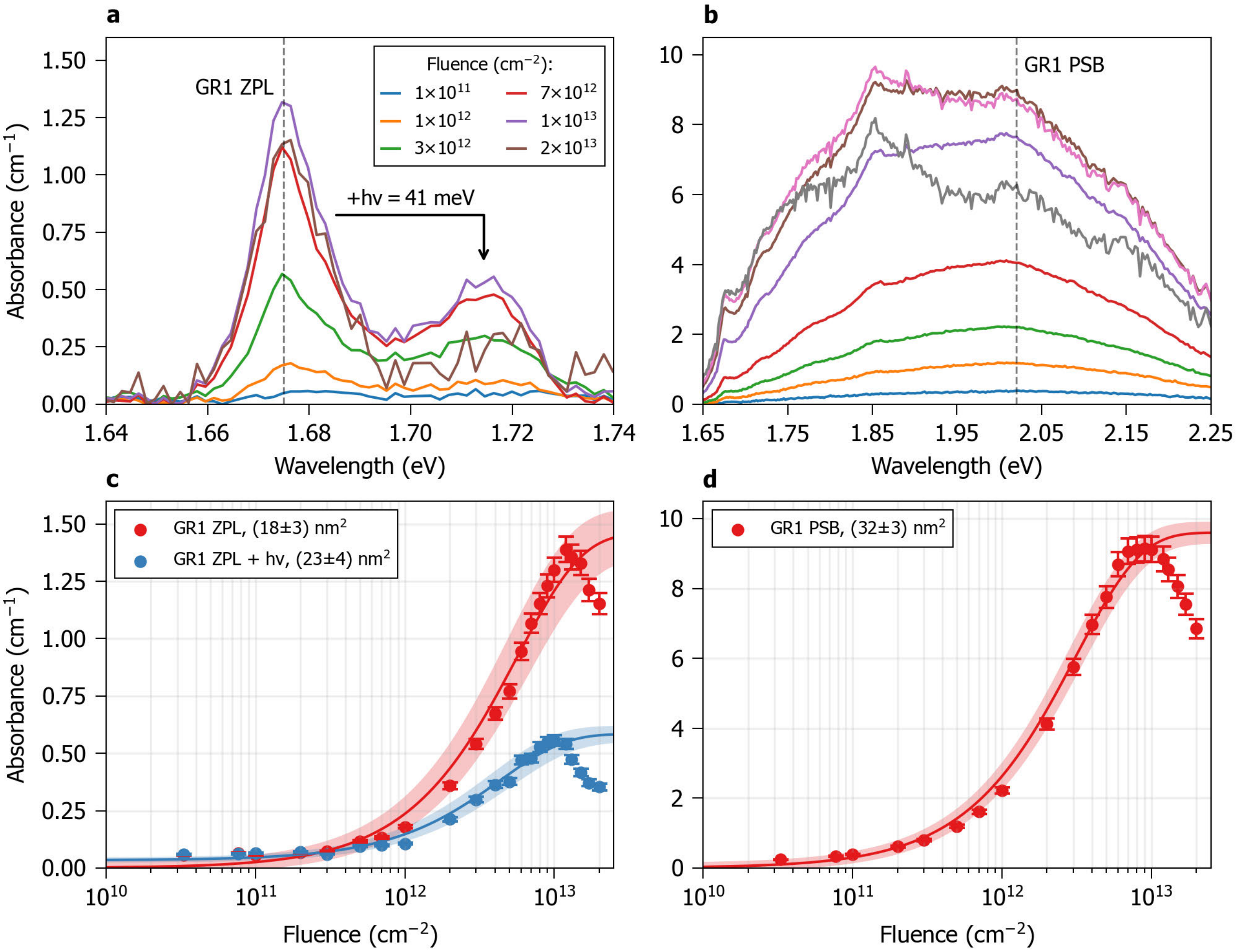

Figure 7.18.: Characteristic absorption range of the GR1 center with its ZPL (a) and phonon sideband (PSB) (b) in type Ib diamond irradiated and measured at 50 K for different fluences of 4.8 MeV/n ^{197}Au ions. All spectra are background corrected. Absorbance of the GR1 center ZPL (c) and the GR1 center side band at 2 eV (d) as a function of fluence. Solid lines are fits of the single impact model to the measurement data with the damage cross section σ given in the legend. Shaded areas represent the standard-deviation of the fit.

The background-corrected absorption intensity of the GR1 center, with its ZPL at 1.673 eV (740.9 nm) and its phonon sideband at ∼2 eV (∼620 nm) at various fluences at an irradiation and measurement temperature of 50 K is shown in Figure 7.18a and b. In comparison to the irradiation (and measurement) at room temperature the GR1 center ZPL is narrower and reaches a maximum absorption of $\sim 1.45\,\mathrm{cm}^{-1}$ at $1.2 \times 10^{13}\,\mathrm{cm}^{-2}$. The phonon sideband intensity increases up to a maximum absorption of $\sim 9\,\mathrm{cm}^{-1}$ at a fluence between 0.8×10^{13} and $1 \times 10^{13}\,\mathrm{cm}^{-2}$. Absorption intensities cannot be directly compared between the two irradiation temperatures due to the different absorption cross sections. But the fits of the single impact model, presented in Figure 7.18c and d, clearly indicate that vacancy creation is more efficient at 50 K in comparison to room temperature. The GR1 center ZPL exhibits a damage cross section of $(18 \pm 3)\,\mathrm{nm}^2$, while the sideband has a damage cross section of $(32 \pm 3)\,\mathrm{nm}^2$ (room temperature: $(8 \pm 3)\,\mathrm{nm}^2$ and $(23 \pm 1)\,\mathrm{nm}^2$, respectively). A phonon replica of the GR1 center ZPL at 1.714 eV (723.3 nm), that is created by the interaction with a quasilocal vibration with an energy 41 meV, is also well approximated by the single impact model. The damage cross section of $(23 \pm 4)\,\mathrm{nm}^2$ is in good agreement with the evolution of the ZPL absorption intensity.

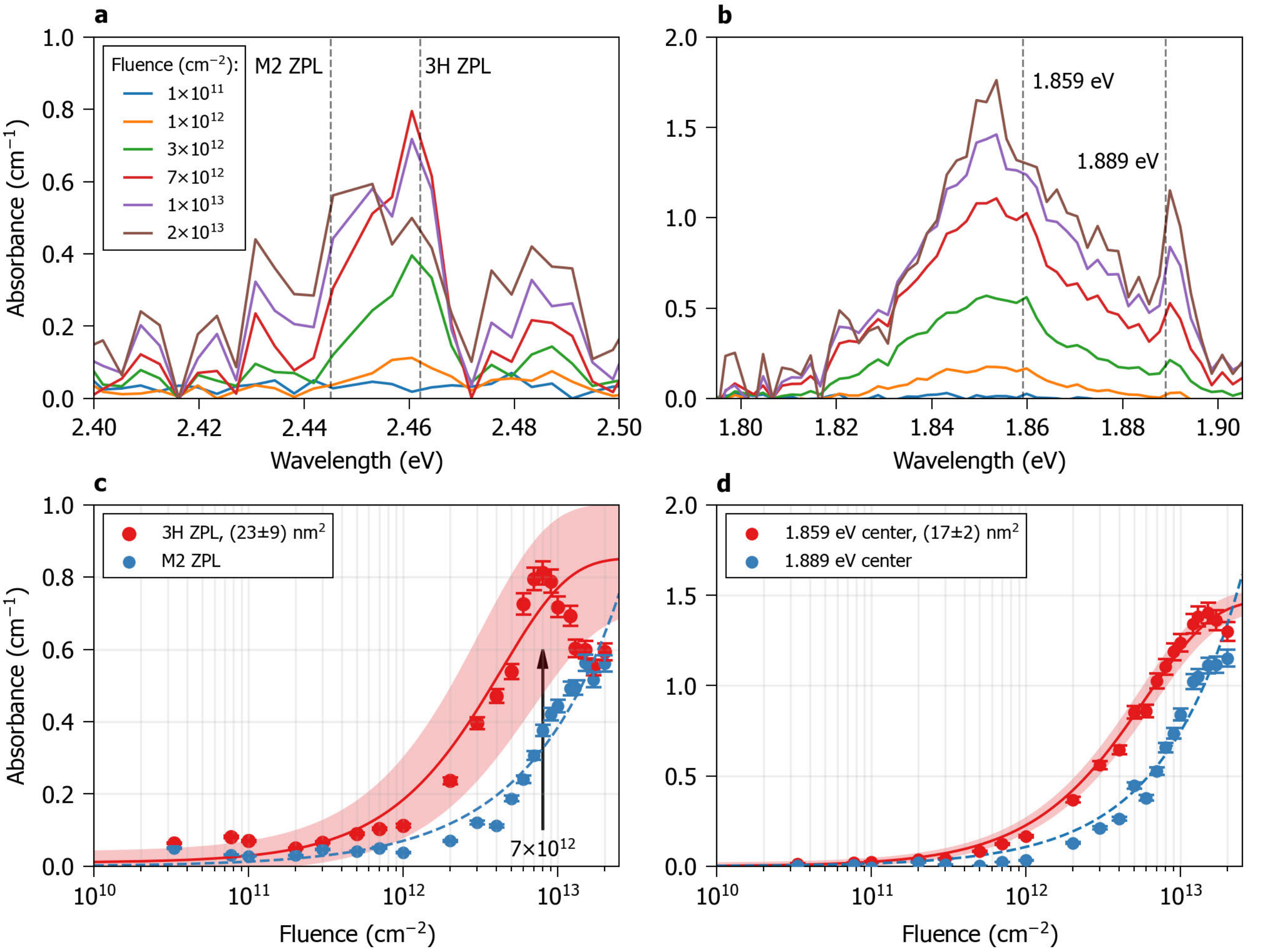

Figure 7.19.: Characteristic absorption range of the 3H center (a) and the 1.859 eV & 1.890 eV centers (b) in type Ib diamond irradiated and measured at 50 K for different fluences of 4.8 MeV/n ^{197}Au ions. All spectra are background corrected. Absorbance of the 3H ZPL (c) and the 1.859 eV & 1.890 eV centers (d) as a function of fluence. Solid lines are fits of the single impact model to the measurement data with the damage cross section σ given in the legend. Shaded area represent the standard-deviation of the fit. Dashed lines are guides to the eye.

Figure 7.19a shows the absorption spectra of M2 at 2.445 eV (507 nm) and 3H centers at 2.462 eV (503.4 nm) which are related to a radiation defect and the di-split-interstitial, respectively. The trend of the 3H ZPL absorption intensity is presented in Figure 7.19c with its maximum absorption intensity of 0.8 cm^{-1} at a fluence of 7×10^{12} cm^{-2}. The damage cross section according to the single impact model is (23 ± 9) nm^2. Taking the uncertainties of the fit and fluence measurement into account, these values are in agreement with the results obtained from the irradiation at room temperature (c.f. Figure 7.17c) which yielded a damage cross section of (27 ± 14) nm^2 and a maximum absorption intensity at 5×10^{12} cm^{-2}. The trend at 50 K clearly shows that the concentration of 3H centers is steadily decreasing beyond a certain threshold fluence. The M2 center is attributed to an intrinsic radiation-induced defect [140]. Figure 7.19c shows that the M2 absorption intensity increases monotonously with fluence and is indicative of a defect accumulation process.

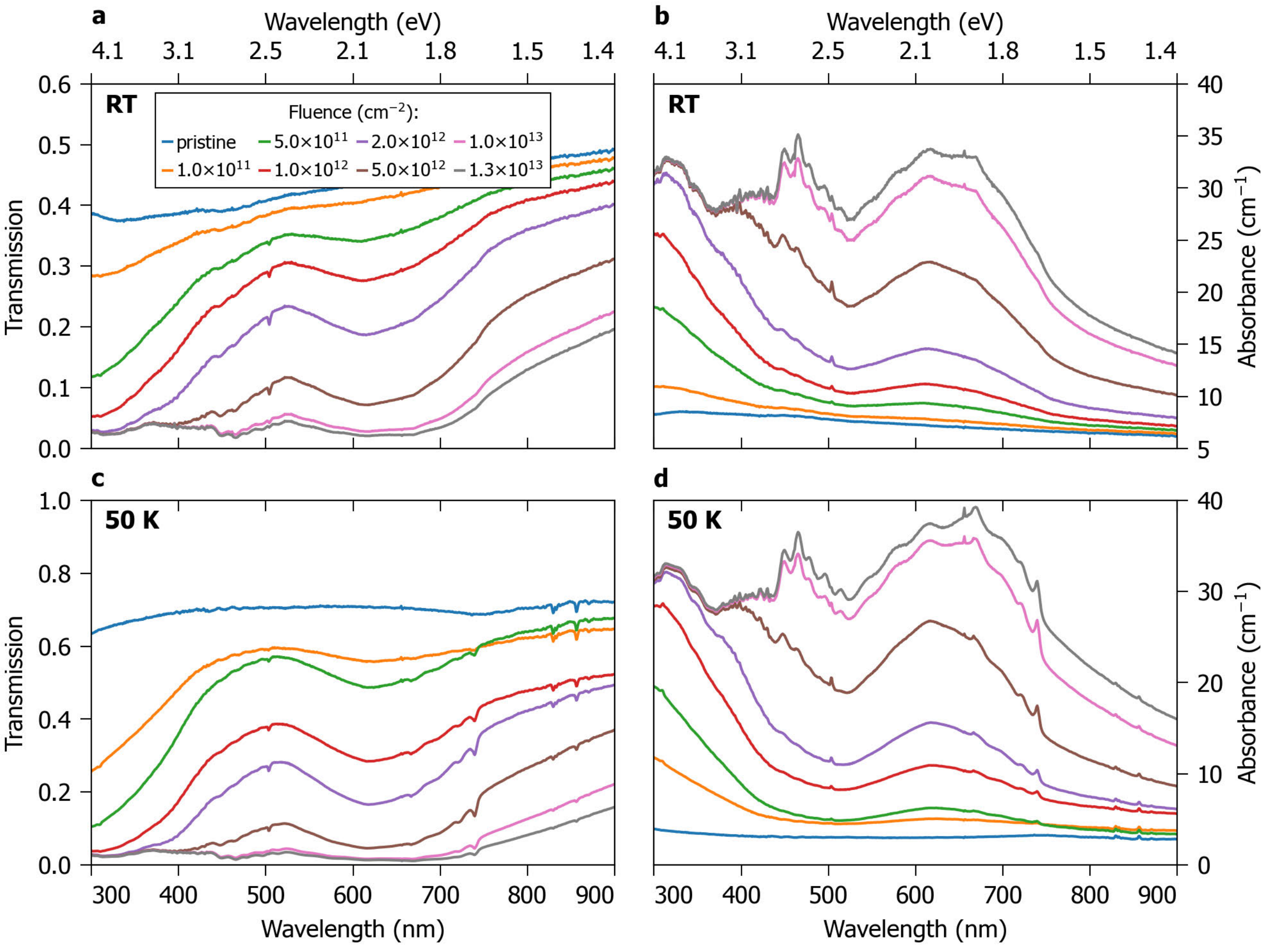

Figure 7.20.: In-situ transmission (a, c) and absorbance (b, d) measurements of a type IIa diamond at different fluences of 4.8 MeV/n ^{197}Au ions. The upper row was measured and irradiated at room temperature, while the lower row was measured and irradiated at 50 K.

Figure 7.20 shows the in-situ UV/vis transmission and absorption spectra of quasi nitrogen-free CVD-synthesized type IIa diamond ($\leq$5 ppb N_s) at different irradiation fluences of 4.8 MeV/n ^{197}Au ions. Irradiation and measurements were performed at room temperature and 50 K. Both diamonds exhibit a rather flat pristine absorption spectrum with the transmission exceeding more than 60 % at 50 K. In comparison to the type Ib diamonds (c.f. Figure 7.14), the absorption edge is below 300 nm due to the small concentration of extrinsic defects in these diamonds.

It is possible to identify multiple absorption bands in the absorption spectra shown in Figure 7.20b and d. The broad absorption band between 520 and 750 nm is connected to the presence of radiation-induced interstitials and vacancies. In this range, multiple ZPLs can be identified at about 740 nm, 656 nm corresponding to the neutral vacancy GR1 center and 1.889 eV center, respectively. At a temperature of 50 K, ZPLs can be identified at about 665 nm and 720 nm which correspond to the split-interstitial and a phonon replica of the GR1 center, respectively.

At 50 K, additional ZPLs can be identified at wavelengths of 830 nm and 855 nm, which are already detected in the pristine absorption spectrum. As the absorption intensity of these two ZPLs is virtually constant for all fluences (the non-irradiated volume acts as a quasi-infinite reservoir in comparison to the irradiated volume), the ZPLs are attributed to intrinsic absorption lines of CVD diamonds. Similar absorption bands were reported in [140].

The single impact model is fit to the absorption intensity at five different wavelengths that do not overlap with absorption bands from color centers. The results are shown in Figure 7.21a and b. At 525, 750 and 870 nm the

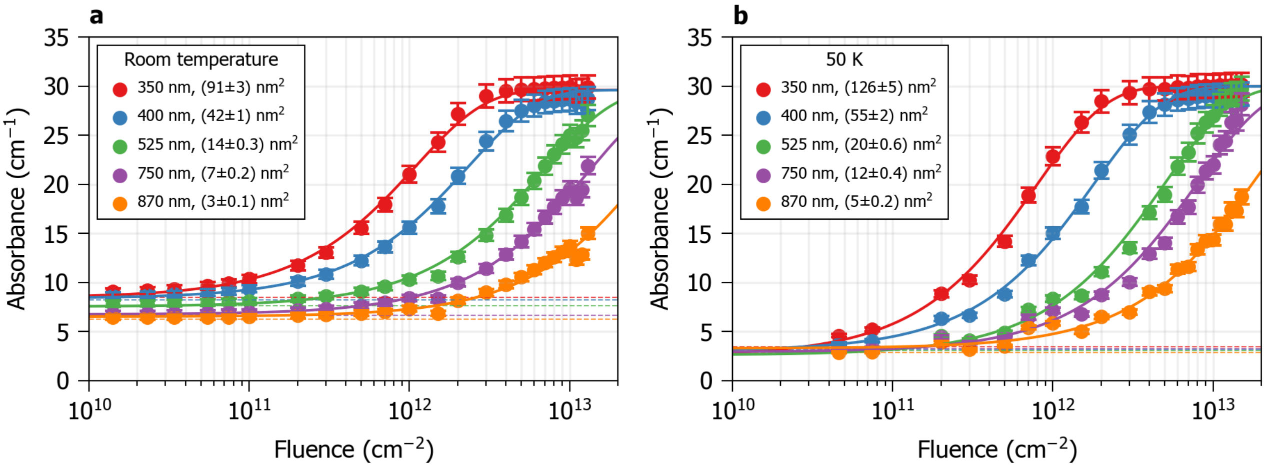

Figure 7.21.: Absorption of a type IIa diamond at different wavelenths as a function fluence for irradiation with 4.8 MeV/n ^{197}Au ions at room temperature (a) and at 50 K (b). Dashed horizontal lines represent the absorbance of the pristine sample at the given wavelength. Solid lines are fits of the single impact model, Equation 2.12, to the measurement data with the damage cross section σ given in the legend.

damage cross section is about 2 times larger at 50 K in comparison to irradiation at room temperature. Whereas the damage cross sections at 350 and 400 nm are only ∼50 % larger at 50 K.

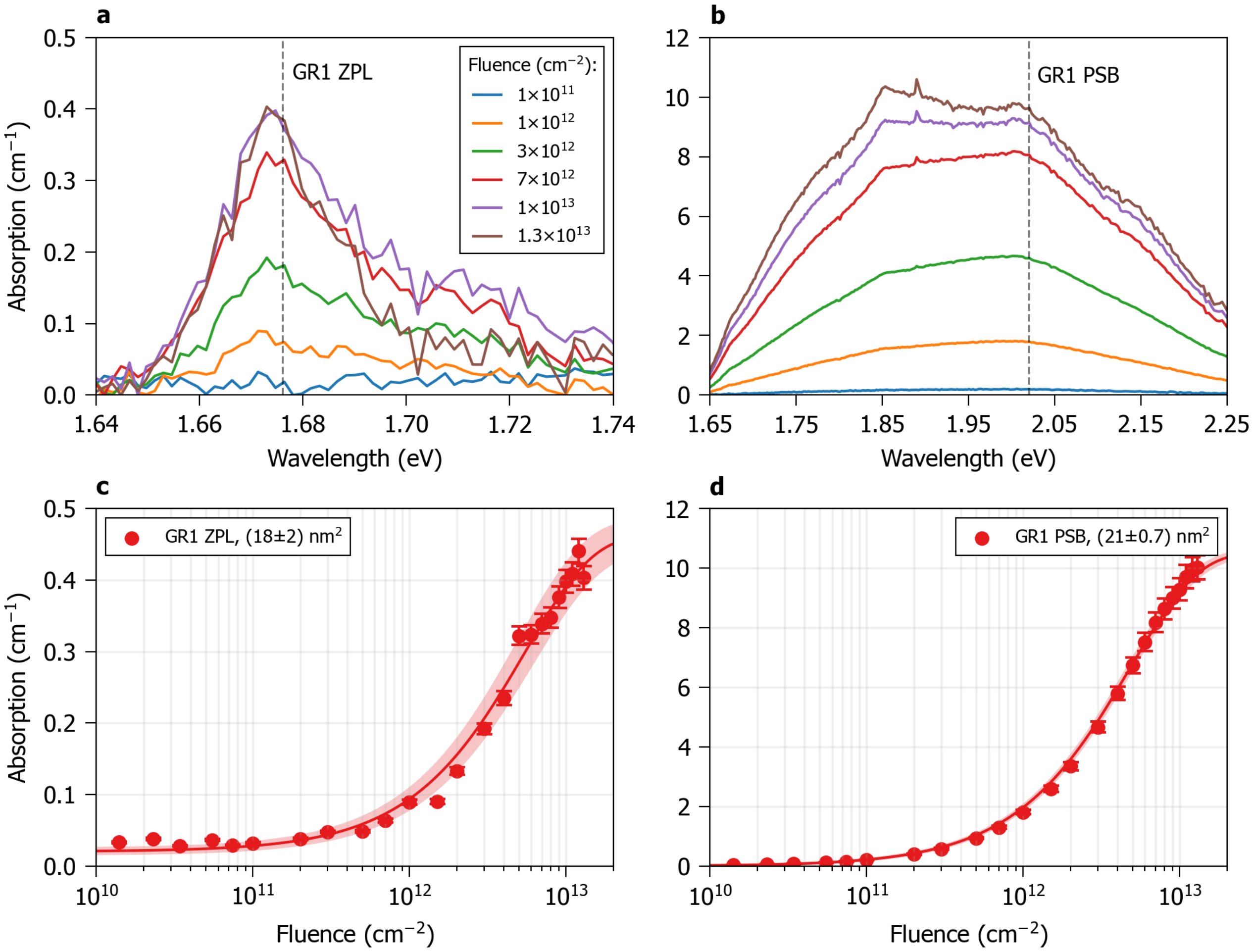

Figure 7.22.: Characteristic absorption range of the GR1 center with its ZPL (a) and side band (b) in type IIa diamond irradiated and measured at room temperature for different fluences of 4.8 MeV/n ^{197}Au ions. All spectra are background corrected. Absorbance of the GR1 center ZPL (c) and the GR1 center side band at 2 eV (d) as a function of fluence. Solid lines are fits of the direct impact model to the measurement data with the damage cross section σ given in the legend. Shaded areas represent the standard-deviation of the fit.

Figure 7.22a and b show the background-corrected absorption spectra for the GR1 center ZPL at 1.673 eV (740.9 nm) and the GR1 phonon sideband at ~2 eV (~620 nm) at room temperature. The GR1 center ZPL has an absorption intensity of about 0.4 cm^{-1} while the sideband reaches an absorption intensity of about 10 cm^{-1} at the highest fluence of 1.3×10^{13} cm^{-2}. The absorption intensity of both the ZPL and the sideband show a trend with increasing ion fluence that is well approximated by the direct impact model as shown in Figure 7.22c and d. The GR1 center ZPL has a damage cross section of (18 ± 2) nm^2 and the GR1 center phonon sideband (21.0 ± 0.7) nm^2.

The damage cross section for the increase in absorption intensity of the GR1 ZPL is considerably larger in the investigated type IIa diamond in comparison to type Ib diamond. The damage cross section for the GR1 ZPL of (8 ± 3) nm^2 (c.f. Figure 7.16) is roughly two times smaller in the type Ib diamond. On the other hand, the damage cross sections of the phonon side band are comparable with the damage cross section of (23 ± 1) nm^2 in type Ib diamond.

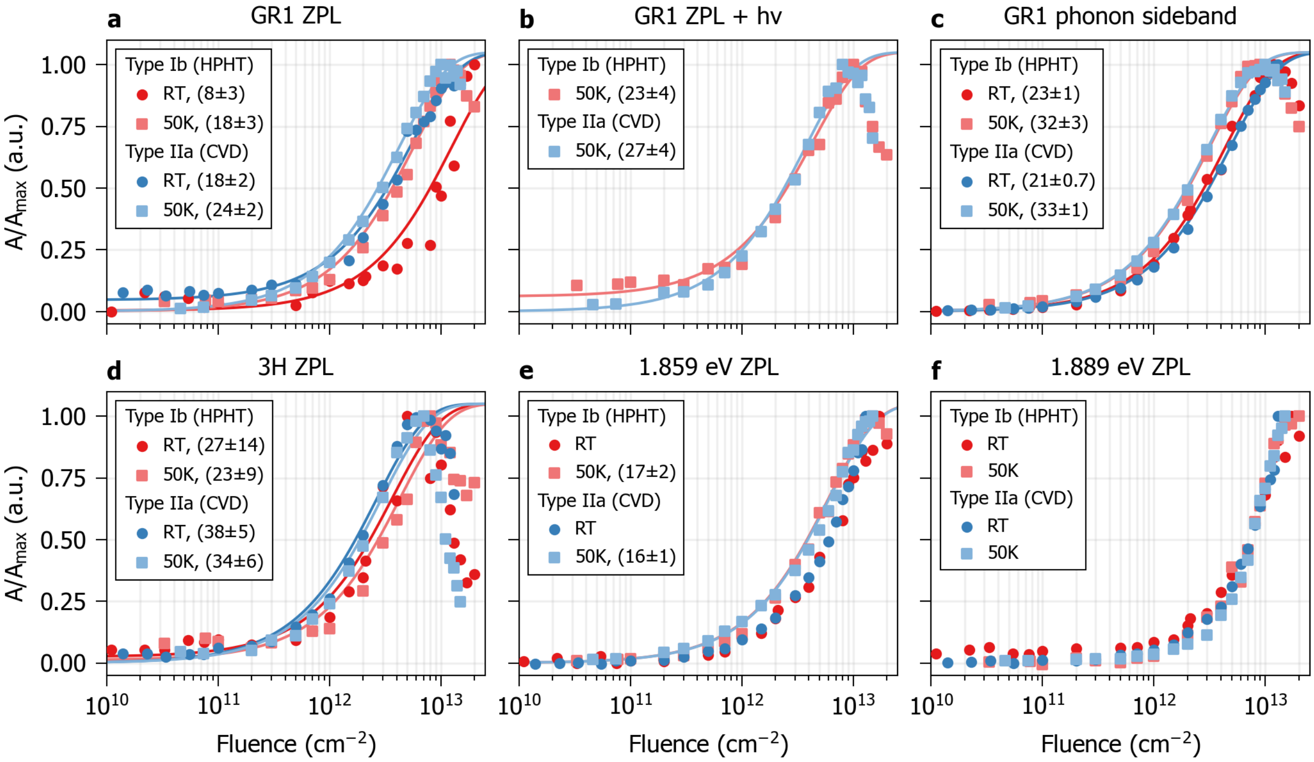

Figure 7.23.: Normalized absorbance as a function of fluence of 4.8 MeV/n ^{197}Au ions for irradiation and measurement at room temperature and 50 K in type Ib and type IIa diamond with ~200 ppm and ≤5 ppb N_s respectively. Evolution of the GR1 center ZPL (a), GR1 center ZPL phonon replica at $\hbar\omega = 41$ meV (b), GR1 center phonon sideband (c), 3H ZPL (d), 1.859 eV center (e) and 1.889 eV center (f). Errors are omitted for clarity. Solid lines are fits of the single impact model with the damage cross section σ in units of nm^2 given in the legend.

Figure 7.23 shows the normalized absorption intensity of the previously discussed color centers in both HPHT-synthesized type Ib and CVD-synthesized type IIa diamonds as a function of fluence for irradiation with 4.8 MeV/n ^{197}Au at room temperature and 50 K. Overall, the trends coincide well between the two diamond types. Damage cross sections of vacancy-related color centers are systematically larger for irradiation at 50 K (c.f. Figure 7.23a, b & c). The 1.859 eV center does not exhibit a clear saturation regime during room temperature irradiation while at 50 K its trend can be well approximated by the direct impact model (c.f. Figure 7.23e). As a color center that occurs only in irradiated diamonds, the 1.889 eV center exhibits a strong increase of absorption intensity at fluences $>1 \times 10^{12}$ cm^{-2} identifying it as a feature of a highly damaged, i.e. disordered, diamond lattice (c.f. Figure 7.23f).

There are two features that distinguish the two diamonds. The rather small damage cross section of the GR1 center ZPL in the type Ib diamond during irradiation at room temperature and the different damage cross sections of the 3H ZPL in comparison between the type Ib and CVD diamonds (c.f. Figure 7.23d).

The GR1 center ZPL exhibits a damage cross section of (8 ± 3) nm^2 in the type Ib diamond at room temperature in comparison to at least 18 nm^2 in the CVD diamond and at an irradiation temperature of 50 K. This indicates that radiation-induced production of vacancies is apparently less efficient at room temperature. Since every radiation-induced vacancy should be created simultaneously with a corresponding interstitial the same trend should be observed in the evolution of the interstitial-related 3H and 1.859 eV center and indeed, 3H center damage cross sections are well in agreement between the two irradiation temperatures in the type Ib diamond. Additionally, the damage cross section of the GR1 center phonon replica and the phonon sideband agree closely between the different diamonds and irradiation temperatures (c.f. Figure 7.23b and c. Hence, the considerable difference in the evolution of the GR1 center ZPL is attributed to radiation-induced vacancies being captured by nitrogen during room temperature irradiation.

Table 7.2.: Single impact damage cross sections σ obtained from fits of the direct impact model, Equation 2.12 to the increase of absorption for different color centers in HPHT-synthesized type Ib ($\sim$200 ppm N_s) and CVD-synthesized type IIa ($\leq$5 ppb N_s) diamonds irradiated with 4.8 MeV/n ^{197}Au ions. Spectral positions for the different color centers is taken from [140]. ** indicates fits that yielded non-physical cross sections. – indicates no change of the absorption intensity.

			Type Ib (HPHT)		Type IIa (CVD)	
			RT	50 K	RT	50 K
	Wavelength		Damage cross section σ			
	eV	nm	nm^2			
GR1 center ZPL, V^0	1.673	740.9	8 ± 3	18 ± 3	18 ± 2	24 ± 2
GR1 center ZPL + ΔE=41 meV	1.714	723.4	–	23 ± 4	–	27 ± 4
GR1 center PSB	~2	~620	23 ± 1	32 ± 3	21 ± 0.7	33 ± 1
3H center ZPL, di-<100> split interstitial	2.642	503.4	27 ± 14	23 ± 9	38 ± 5	34 ± 6
1.859 eV center ZPL, I^0	1.859	667	**	17 ± 2	**	16 ± 1

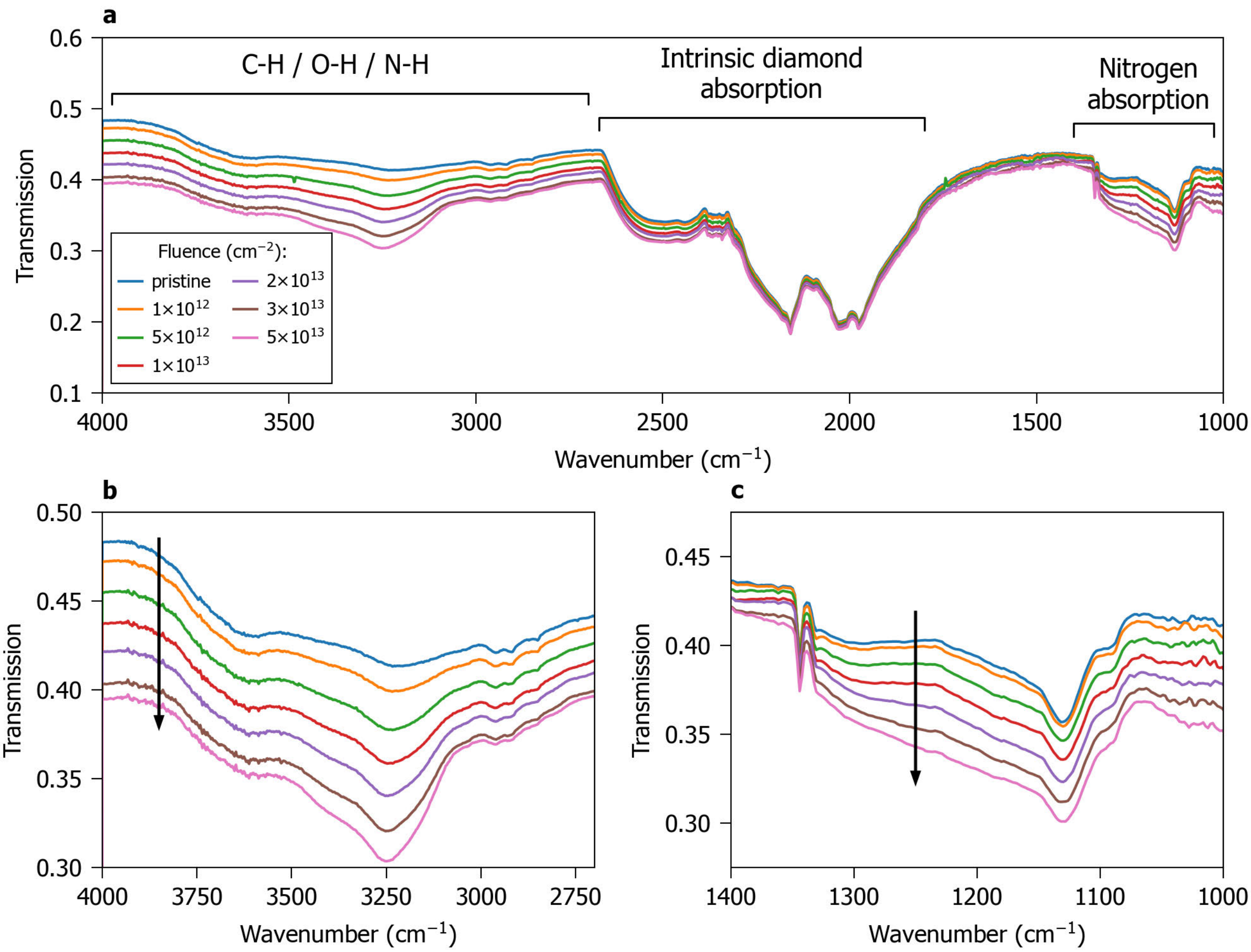

Figure 7.24.: Infrared transmission spectra of type Ib diamond irradiated to different fluences of 4.8 MeV/n ^{197}Au ions in units of cm^{-2} (a). Zoomed regions of the nitrogen absorption range (b) and the C-H / O-H / N-H bond stretching region (c). Arrows indicate increasing fluences.

In-situ infrared transmission spectra of HPHT-synthesized type Ib diamond (∼200 ppm N_s) during irradiation with 4.8 MeV/n ^{197}Au ions is presented in Figure 7.24a. The spectra are composed of three characteristic regions, the intrinsic diamond absorption region between 2800 and 1800 cm^{-1} with the main diamond absorption peak at 2160 cm^{-1}, the so-called one-phonon absorption range between 1400 and 1000 cm^{-1} which, in type I diamonds, is dominated by the absorption of nitrogen-related color centers and the hydrogen-bond absorption region between 4000 and 2700 cm^{-1}.

The intrinsic diamond absorption range is virtually unaffected by ion irradiation even at the highest fluence of 5×10^{13} cm^{-2}. No sp^2-hybridized carbon species with characteristic absorption between 1600 and 1700 cm^{-1} can be identified that would indicate significant distortion of the diamond lattice. Albeit, the transmission at 2670 cm^{-1}, which is used to normalize diamond infrared absorption spectra, decreases by about 0.05 which indicates an increasing contribution from non-sp^3-hybridized carbon species.

More significant changes are observed in the one-phonon absorption region shown in Figure 7.24c. According to the manufacturer, the investigated HPHT diamond is a type Ib diamond with a substitutional nitrogen concentration of ∼200 ppm. This is clearly the case as the absorption lines of the substitutional nitrogen C center at 1344 cm^{-1} and 1130 cm^{-1} are the most dominant features in the pristine infrared transmission spectrum. With increasing ion fluence, the absorption in the range between the two absorption lines of the C center increases. This range is

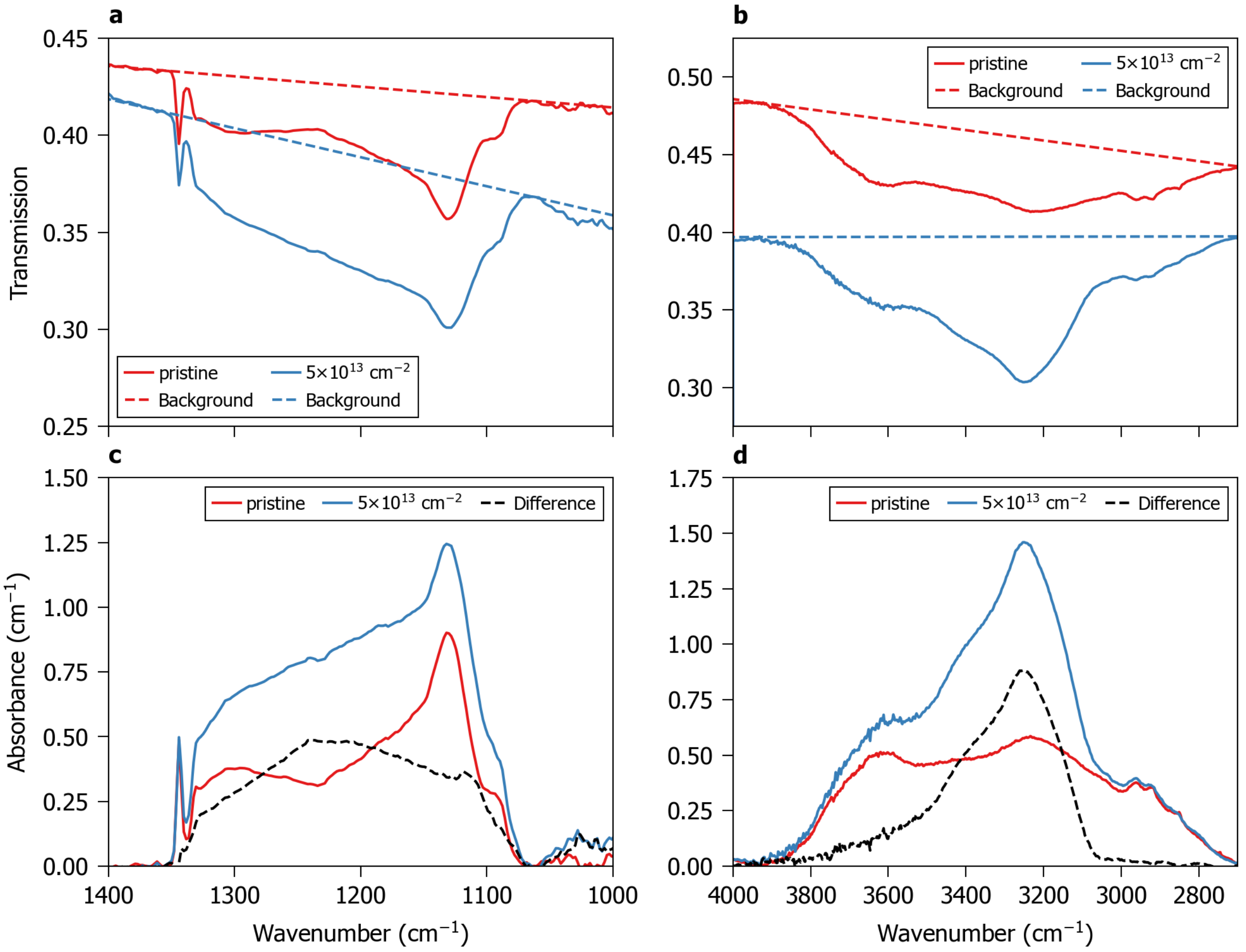

Figure 7.25.: Infrared transmission spectra of a type Ib diamond before (pristine) and after irradiation with 4.8 MeV/n ^{197}Au in the nitrogen absorption region (a) and the C-H / O-H / N-H stretching region (b). The corresponding absorption spectra after background subtraction are shown in (c) and (d), respectively.

characteristic of the A and B centers which correspond to the aggregated nitrogen defects N_2 and N_4V with their main absorption lines at 1282 cm^{-1} and 1175 cm^{-1}, respectively.

Figure 7.24b shows the evolution of the hydrogen-bond stretching region. The most distinct feature is the increased absorption at ~3250 cm^{-1}. More than 20 different hydrogen-bond vibrations that involve either carbon, nitrogen or oxygen have been identified in nanodiamonds between 2800 and 3700 cm^{-1} [199]. Hence, a clear assignment to a single bond vibration is not possible without spectral deconvolution.

The transmission at 2670 cm^{-1} is commonly used as the baseline to normalize FT-IR transmission spectra [200]. While this approach is sufficient to compare different diamonds, it is not sensitive enough to resolve the small changes within the one-phonon and the hydrogen-bond stretching region. Therefore, a careful approach to background subtraction based on simple linear backgrounds, without baseline normalization, was chosen. A linear background between 1400 cm^{-1} and the maximum transmission in the range 1060 and 1080 cm^{-1} was chosen for the one-phonon region that is presented in Figure 7.25a. The hydrogen-bond stretching region is shown in Figure 7.25d with a linear background between the maximum transmission at 4000 and 3900 cm^{-1} and the baseline transmission at 2670 cm^{-1}.

The resulting background-corrected absorption spectra of the pristine & irradiated diamond at the maximum fluence of 5×10^{13} cm^{-2} and the difference are presented in Figure 7.25c and d. The largest absorption increase of about 0.25 cm^{-1} in the one-phonon region of nitrogen-related defects is at ~1225 cm^{-1}. A centers, N_2, have their dominant absorption peak at 1282 cm^{-1} and a broad feature around 1200 cm^{-1}. B centers, N_4V exhibit a

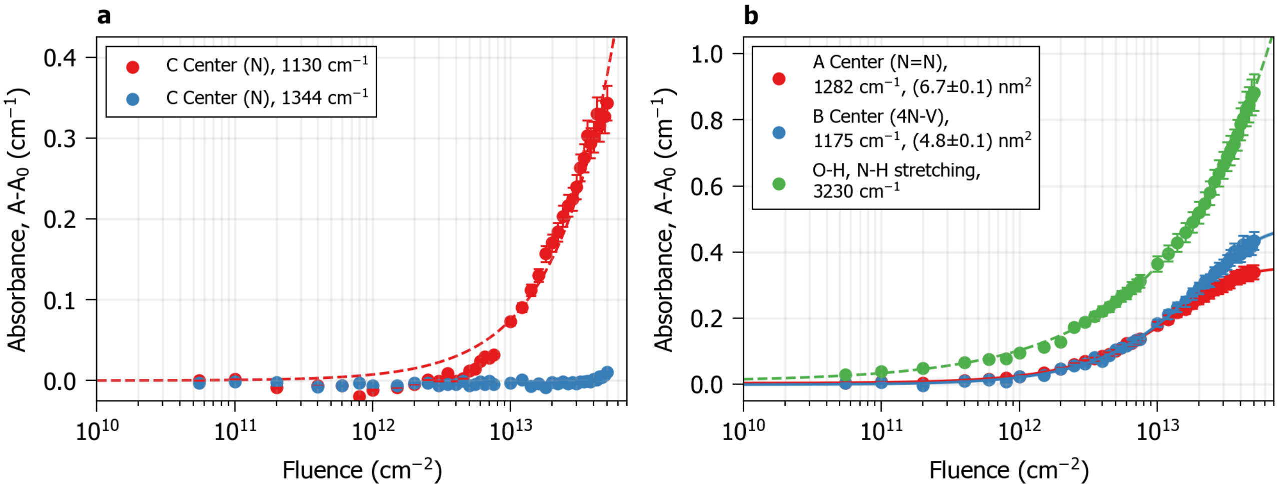

Figure 7.26.: Absorbance at different infrared wavenumbers as a function of fluence of 4.8 MeV/n ^{197}Au ions in type Ib diamond. A$_0$ is the pristine absorbance. Absorbance of the C center (N$_s$) at 1130 and 1344 cm^{-1} (a) and of the A (N=N), 1282 cm^{-1} & B center (4N-V), 1175 cm^{-1} and O-H, N-H bond stretching modes at 3230 cm^{-1} (b). Solid lines are fits of the direct impact model to the measurement data with the damage cross section σ given in the legend. Dashed lines represent guides to the eye.

set of absorption peaks at 1175 cm^{-1} and 1332 cm^{-1}, but no clear peaks can be identified at these wavenumbers. A small peak at about 1115 cm^{-1} evolves with increasing fluence that is attributed to the C+ center of positively charged substitutional nitrogen [201]. The most dominant feature of the C+ center at 1332 cm^{-1} cannot be clearly identified due to overlap with absorption features from both the B and C centers.

In the hydrogen-bond vibration region (c.f. Figure 7.25d) a clear evolution of at least a single peak can be identified with the absorption intensity increasing by more than 0.75 cm^{-1} at 3250 cm^{-1}. A distinct shoulder can be identified at ~3275 cm^{-1} with a tail towards higher wavenumbers while no significant changes occur below 3000 cm^{-1} and above 3750 cm^{-1}. Taking all of this into account, the peak is tentatively composed of three components at 3152 cm^{-1}, 3280 cm^{-1} and 3400 cm^{-1} with the first two components being assigned to asymmetric and the latter to symmetric N-H stretching vibrations. Contributions could also be coming from 3240 cm^{-1} that is attributed to O-H and N-H bond stretching vibrations [199].

Additionally, three absorption peaks at 2955 cm^{-1}, 2921 cm^{-1} and 2845 cm^{-1} are virtually unaffected by irradiation. These can be tentatively attributed to the vibration of hydrogen bonded in methane, CH$_3$, to carbon atoms of (100) and (110) lattice planes [199].

The absorption intensity of the nitrogen A, B and C centers and the hydrogen-bond vibration at their respective wavenumbers as a function of fluence is presented in Figure 7.26. The evolution of the dominant absorption features of nitrogen C centers at 1130 cm^{-1} and 1344 cm^{-1}, respectively, is shown in Figure 7.26a. In contrast to the observed trend, the absorption intensity of C centers should decrease with increasing fluence if C centers are aggregating into A and B centers. But, the absorption intensity at 1130 cm^{-1} actually increases at fluences $>3 \times 10^{12}$ cm^{-2}. Since it is overlapping with contributions from both A and B centers its trend is not directly indicative of C centers. The intensity at 1344 cm^{-1} on the other hand is virtually constant with only a small increase beyond 2×10^{13} cm^{-2}. The absence of a decrease in intensity is probably due to the small volume that is irradiated. At a sample thickness of 800 µm less than 4 %, ~30 µm (c.f. Figure 6.1), are affected by radiation-induced changes. Thus, the non-irradiated pristine volume is acting as a quasi-infinite reservoir of C centers. The increase at $>2 \times 10^{13}$ cm^{-2} on the other hand can be attributed to an overlap with the C+ center's dominant absorption peak at 1332 cm^{-1}.

Depending on the overall shape of the one phonon range (c.f. Figure A.3), the absorption intensity at 1282 cm^{-1} can be used to determine the density of either A or B centers [202, 203]. To qualitatively distinguish between the two color centers, the absorption intensity at 1282 cm^{-1} is tentatively attributed to correlate to the concentration of B centers while the intensity at 1175 cm^{-1} is attributed to B centers, respectively. The evolution of the A and

B center absorption is presented in Figure 7.26b. Both A and B centers increase with irradiation fluence by up to 0.4 cm^{-1} while strictly following the single impact model.

As expected from the annealing behavior of nitrogen in diamond, C centers are converted into A centers and ultimately B centers. Opposed to the outcome of annealing, where B centers are only observed after all C centers have already been converted into A centers, radiation-induced aggregation leads to the simultaneous existence of all nitrogen centers. Radiation-induced production of A centers does precede the creation of B centers as indicated by the larger damage cross section of A centers in comparison to B centers with $(6.7 \pm 0.1)\,\mathrm{nm}^2$ and $(4.8 \pm 0.1)\,\mathrm{nm}^2$, respectively. These damage cross sections are an order of magnitude smaller than what is systematically observed in UV/vis absorption spectroscopy (c.f. section 6.2.1.2).

The absorption intensity at 3230 cm^{-1}, which is attributed to nitrogen-hydrogen bonds, is monotonously increasing with irradiation fluence as shown in Figure 7.26b. Hydrogen is incorporated during HPHT synthesis by the residual atmosphere trapped in the reaction capsule, impurities in the carbon source or the metal catalyst (c.f. section 3.1.1). Fang *et al.* investigated the influence of co-doped hydrogen on nitrogen aggregation during annealing [204] and showed that hydrogen is potentially reducing the energy barrier for nitrogen diffusion by either hydrogen bonding interactions or as additional defect that further softens the diamond lattice. Computational studies of hydrogen in diamond [205–207] have shown the stability of various hydrogen/nitrogen-related defects like VN_xH_x or CHN in the diamond lattice. Hence, the radiation-induced increase of absorption related to hydrogen-nitrogen bond vibrations in conjunction with the increase of aggregated nitrogen species is supporting the hypothesis that hydrogen is involved in nitrogen aggregation.

Part III.

High-Power Proton Irradiation on Graphitic Materials

8 High-Intensity and High-Power Accelerator Facilities

Beam intercepting devices (BIDs) are accelerator components that have to interact with the primary beam of an accelerator by design. In general, the function of BIDs can be summarized in three different groups:

I **Safety**: These BIDs ensure safe operation of the accelerator and protect sensitive equipment from direct exposure to primary beams. At FAIR these BIDs include the internal beam dump of the SIS100 [208], the beam catchers of the Super-FRS [1] and beam windows that couple particle beams from the primary vacuum sections of accelerators to atmosphere in experimental areas.

II **Beam cleaning & control**: Collimators continuously scrape the beam from particles travelling at non-nominal beam trajectories. Due to the large interaction cross section of heavy ions with residual gas molecules, changes in charge state of the primary ions will lead to significant dynamic vacuum effects behind bending magnets of the SIS100 at FAIR that can lead to complete loss of the beam [209]. To counteract this, cryo-collimators with low beam-induced gas desorption yields will be used to absorb any non-nominal charge state ions [210]. Stripper foils change the charge state of ion beams by direct interaction with the beam [211] and are used in the UNILAC and UNILAC-to-SIS18 transfer line. Luminescence screens are used for transverse beam size diagnostics at all energies in the FAIR accelerator chain [212]. A magnetic septum is used for slow extraction operation and is exposed to the primary beam due to continuous (slow) sweeping of the beam along the septum wires [213].

III **Production targets** are used to "produce" secondary particle beams. At FAIR antiprotons (pbars) will be produced by a high-power proton beam from the p-linac impinging on a solid metallic target [214]. Rare-isotope beams will be produced by fragmentation of a heavy ion beam in the Super-FRS target [1]. Fixed-target experiments like CBM or HADES employ, e.g., gold foils of few tens of μm to probe interactions in high-energy heavy ion collisions [215].

In addition to the (instantaneous) effects of interaction with high-power primary beams, radiation damage is especially critical for heavy ions because of their large energy loss. In comparison to proton machines like the LHC at CERN, radiation damage is especially pronounced at GSI and FAIR. The lifetime of amorphous carbon stripper foils at the UNILAC of GSI is limited by the stresses associated with beam-induced graphitization that leads to compaction of the material in the beam spot [211]. The graphite of the Super-FRS beam catchers can loose up to ∼90 % of its pristine thermal conductivity in the areas exposed to the highest doses [6]. Specifically radiation-hard magnets were designed for the high-dose environments of the Super-FRS separator beamline [216] and the SIS100 slow-extraction septum [217]. The sensitivity of scintillator-based beam loss monitors of the SIS18 [218] and luminesce screens for transverse beam size measurements [219, 220] is changing significantly by radiation damage of both low-energy and relativistic heavy ion beams.

8.1 High-Power Facilities, Beam Conditions and Production Targets

Figure 8.1a shows the state of the art in terms of stored beam energy and average beam current as a function of (specific) beam momentum of various existing and next generation high-power accelerator facilities. As of today, the LHC's stored beam energy at 7 TeV/c beam momentum[1] of 340 MJ (that is per one of two counter-circulating beams) is unprecedented and will increase by a factor of 2 in the High Luminosity-LHC upgrade [223]. The next

---

[1] In comparison to the swift heavy ions with velocities of a few ten percent the speed of light that were investigated earlier, protons with a kinetic energy of a few tens of GeV already have velocities of ∼99.9 % the speed of light. For relativistic protons with increasing kinetic energy the value of the kinetic energy is asymptotically approaching the momentum. Hence, in accelerator physics it is customary to use the beam momentum as it is directly linear to the magnetic rigidity of said beam.

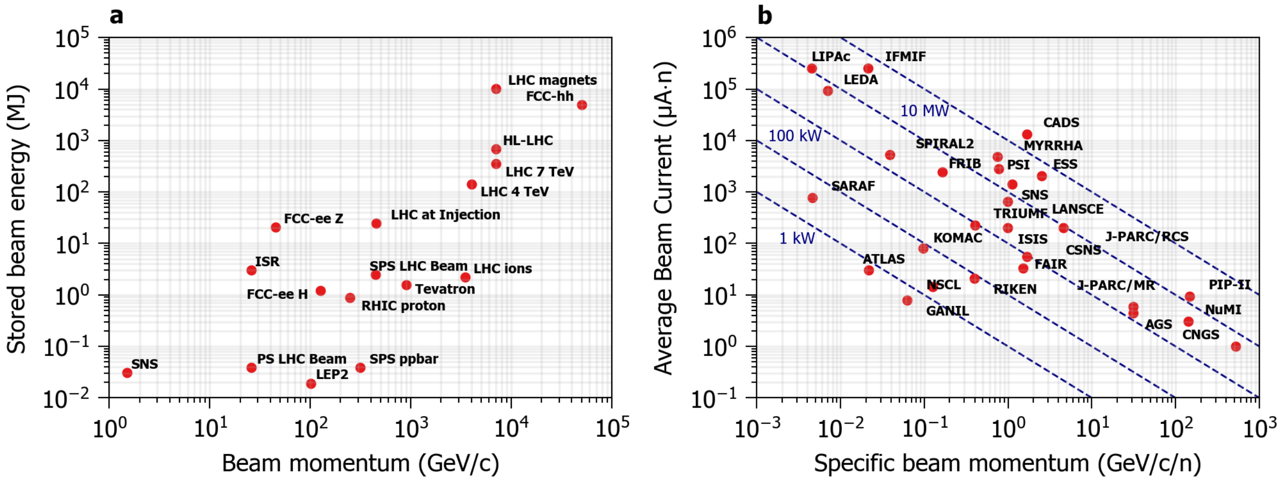

Figure 8.1.: Figures of merit for high-power accelerator facilities. Stored beam energy as a function of (specific) beam momentum of various (anti-)proton colliders (a). Average beam current (ratio of beam intensity and pulse length multiplied by mass number) as a function of specific beam momentum for various high-power production targets (b). Adapted from [221, 222].

generation Future Circular Collider (FCC), which will use the LHC as an injector, is pushing this frontier up to 8.3 GJ. Together with the maximum possible pulse lengths of 90 µs and 326 µs for LHC and FCC respectively, these energies correspond to stored beam powers of 3.8 TW and 25.5 TW [224].

Two operational scenarios for BIDs in these machines can be introduced. Steady state losses are due to continuous scraping of the circulating beam by a multi-staged collimation system that absorbs up to 500 kW during normal operation (for several hours of a physics 'fill'). Quasi-instantaneous losses are due to 'dumps' of the beams at the end of a physics fill or for machine protection by fast rise time magnets that extract the circulating beams into dedicated beam dumps (occurs only a few times per day). It should be stressed that for stored beam energies of machines like the LHC, complex magnet systems are required to create a 'dilution' pattern along the beam dump that spreads the beam over a larger transverse area. Without dilution, direct impact of the full beams would lead to the transformation of any material into plasma [224]. Hence, the local deposition of power (density) is only a fraction of the several TW stated above.

Existing state of the art secondary particle production targets are operating in conditions that result in average power conditions that reach around a MW in the neutrino target of the Neutrinos at the Main Injector (NuMI) facility at Fermilab [7]. This frontier will be pushed with future facilities like the 5 MW neutron spallation target at the European Spallation Source (ESS) [227] or the 2.4 MW neutrino production target of the Long Baseline Neutrino Facility (LBNF) at Fermilab [7]. While these power conditions are considerably lower than the peak powers achieved in colliders, the instantaneous power deposition densities are comparable. Table 8.1 presents an overview of different beam dumps and production targets and their design parameters. While the average beam power is considerably lower in comparison to the instantaneous power deposited in collider beam dumps, the peak power densities are of comparable magnitude. The peak energy deposition in the LHC beam dump of 3 kJ cm^{-3} is locally reached within 8.6 µs which corresponds to ~350 MW cm^{-3}. Neutrino production targets operate around tens of MW cm^{-3}, while the Super-FRS rare-isotope production target of the FAIR facility operates at an instantaneous power density of ~20 GW cm^{-3}.

8.2 Material Choice for Beam Intercepting Devices

Table 8.1 indicates different materials used in various BIDs. Graphite[2] is the dominant choice for relativistic beams of particles with momenta beyond a hundred GeV/c and pulse energies in the MJ range. On the other hand,

---

[2] Graphite will be used to refer to isotropic graphite (also known as 'nuclear graphite') with densities smaller than the maximum crystallographic density. Other graphitic grades will be explicitly mentioned and ideal graphite is used when referring to graphite with nominal density of ~2.2 g cm^{-3}.

Table 8.1.: Overview of different pulsed beam facilities and their (maximum) design parameters. Except CNGS all facilities are currently in operation or are expected to come on-line until 2030. The average beam power can be calculated by the ratio of pulse energy and cycle rate (in seconds).

Facility		Material	Beam type	Pulse energy	Pulse length	Peak E-density per pulse	Cycle length or rate
			Beam dumps [224, 225]				
CERN	LHC	(Expanded) Graphite	7 TeV p	340 MJ	90 µs	3 kJ cm^{-3}	$\sim 10^4$ s
CERN	SPS	Graphite	450 GeV p	5.6 MJ	8.6 µs	0.5 kJ cm^{-3}	36 s
			Neutrino targets [7, 226]				
FNAL, US	NuMI	Graphite	120 GeV p	1.2 MJ	10 µs	0.6 kJ cm^{-3}	1.2 s
FNAL, US	LBNF	Graphite	120 GeV p	2.4 MJ	10 µs	0.1 kJ cm^{-3}	1.2 s
CERN	CNGS	Graphite	400 GeV p	1.5 MJ	10 µs	1.5 kJ cm^{-3}	6 s
			Spallation neutron targets [227, 228]				
Lund, SE	ESS	Tungsten	2 GeV p	360 kJ	2860 µs	0.37 kJ cm^{-3}	14 Hz
ORNL, US	SNS	Mercury	1 GeV p	24 kJ	0.7 µs	13 J cm^{-3}	16 Hz
			Antiproton targets [229, 230]				
CERN, CH	AD	Iridium	26 GeV p	63 kJ	0.4 µs	7.5 kJ cm^{-3}	4.8 s
FAIR, DE		(Inconel)	29 GeV p	90 kJ	0.05 µs		10 s
			Rare-isotope targets [1]				
FAIR, DE	Super-FRS	Graphite	$\leq$1.5 GeV/n ^{238}U	35 kJ	0.09 µs	1.8 kJ cm^{-3}	10 s

spallation and antiproton production targets, which operate with protons at momenta of a few GeV/c are typically made of high-density, high-Z materials such as tungsten, iridium or mercury.

As introduced in the previous section, secondary particle production targets are not only chosen based on their robustness towards the primary beam but also on the fundamental nuclear processes that lead to the production of the secondary particles. Both spallation neutron and antiproton targets require high-Z target materials, either to increase the cross section of intranuclear cascades that lead to highly excited nuclear states that decay via the emission of a low energy neutron [231] or to increase the cross section of inelastic scattering of protons above 5.6 GeV with target nuclei for antiproton production [214]. To further illustrate the physics-driven choice, the iridium-based antiproton target at the AD facility of CERN is continuously exposed to beam-induced transient stresses beyond the tensile strength of iridium and requires replacement after the accumulated plastic deformation has led to a fracture-induced loss of density which ultimately reduces the pbar yield of the target after a few months of operation [229]. On the other hand, the ESS tungsten target consists of a helium-cooled wheel which rotates in the beam. Its estimated lifetime is 5 years which is ultimately limited by the accumulation of radiation damage in the stainless steel enclosure of the target [232].

Apart from the physics-driven choice of materials, why is graphite so well-suited as a target material for relativistic high-energy, high-power beams? In the most simplest assumption, a single high-power beam pulse leads to the same material response as a thermal shock (the definition of a thermal shock will be introduced in section 9.2). According to Ashby [233], the generalized robustness R of a material towards thermal shock can be defined as:

$$\mathrm{R} = \frac{\sigma_t}{E\alpha\Delta T}, \tag{8.1}$$

with σ_t the tensile strength, E the Young's modulus and α the coefficient of thermal expansion of a material. The product $E\alpha$ determines the magnitude of thermal stresses induced by an arbitrary thermal shock ΔT, which is simply assumed as 1. Hence, high thermal shock robustness refers to a large ratio between a material's tensile strength and the thermal stresses it is exposed to.

The beam-induced temperature increase ΔT is proportional to the ratio between energy density $\frac{\Delta E}{V}$ deposited by the beam and volumetric specific heat (the product of specific heat c_p and density ρ) of the target:

$$\Delta T = \frac{\Delta E}{V} \cdot \frac{1}{c_p \rho}. \tag{8.2}$$

Since $\frac{\Delta E}{V}$ is not only defined by the beam parameters but is actually a function of the target properties, ΔT in Equation 8.1 is not simply a constant in interactions with a particle beam when considering different target materials. The Bethe-Bloch formula (c.f. Equation 2.4) predicts that the energy ΔE deposited in a target by a charged particle beams is proportional to the product of atomic number and nuclei density of the target $Z_t N_t$. If both the atomic number Z and nuclei density N_t are proportional to the macroscopic density ρ of solid materials at room temperature, the term ΔE can be simplified to ρ^2. Plugging this into Equation 8.2 and then into the denominator of Equation 8.1, the thermal shock robustness can be adapted specifically for beam intercepting devices to:

$$\mathrm{R}_{\mathrm{BID}} = \frac{\sigma_t c_p}{E \alpha \rho}. \tag{8.3}$$

But, more importantly than the absolute numbers, these equations show the ideal combination of thermo-mechanical material properties for a beam intercepting device in pulsed beam conditions:

- maximize tensile strength σ_t to cope with thermal stresses,
- minimize coefficient of thermal expansion α to reduce thermal strain,
- minimize Young's modulus E to reduce thermal stresses,
- maximize specific heat c_p to decrease peak temperature increase,
- minimize density ρ (and atomic number Z) to decrease energy density deposited by the beam.

Obviously, peak temperatures during operation should be smaller than the melting point of the used material, or in the case of graphite below the service temperature in vacuum. In addition to the properties governing thermal shock robustness, the following properties should be considered as well:

- maximize thermal conductivity k to efficiently transport beam-induced energy away from the volume heated by the beam (targets and BIDs with steady state thermal loads),
- maximize electrical conductivity γ to limit RF impedance (for circular machines [234]),
- balance density ρ (and atomic number Z) with the physics needs (for production targets).

Finally, for all application, the material sensitivity to radiation damage should be as small as possible to improve component lifetime. From a radiation-protection point of view, nuclear reactions in low-Z targets generally produce radioactive isotopes with shorter lifetime than high-Z targets [235].

To put all of these aspects into perspective, a non-exhaustive overview of various accelerator-relevant materials is presented in Table 8.2. For robustness in pulsed beam conditions, graphite has the largest figure of merit according to Equation 8.1 and Equation 8.3. But taking all design parameters into account graphite cannot fulfill all requirements of accelerator applications.

Beryllium is the material of choice for beam windows located at ultra-high vacuum/atmosphere interfaces. It can be manufactured in thicknesses of a few hundred µm and diameters around 10 cm while retaining vacuum tightness (and the associated static mechanic load) in addition to dynamic beam-induced thermo-mechanical loads [236]. Oxidation in air requires temperatures in excess of 395 °C [237]. In contrast, graphite is not vacuum tight due to its inherent open porosity and will readily oxidize at temperatures <200 °C in air [238].

The beam dump of the SPS and the collimator system of LHC rely on a combination of low-Z graphite sections, that absorb most of the beam power, and high-Z 'absorbers'. These tungsten (alloy) 'absorbers' stop any secondary particles that are produced in the interaction of the primary beam with the graphite dump blocks or primary & secondary collimators within a small volume due to their high nuclear interaction cross section. At the same time the material has to be robust enough to withstand irradiation with a few LHC bunches in case of a beam steering accident [239].

Table 8.2.: Overview of materials for beam intercepting devices and their material properties. R denotes the figure of merit of materials for robustness towards thermal shock calculated with Equation 8.1. R_{BID} denotes the figure of merit for robustness of materials towards pulsed beam operation calculated with Equation 8.3. Both figures of merit are calculated using the numerical values of the different material properties for the given units and are assumed dimensionless. Glidcop is an dispersion-strengthened copper alloy with ~0.15 % alumina. Adapted from [235].

	Be	CFC	Graphite	Mo-Graphite	Copper-diamond	Glidcop copper alloy	Mo	Tungsten alloy IT180
Z	4	6	6	~6.5	~11.4	~29	~42	~70.8
ρ (g/cm^3)	1.84	1.65	1.8	2.5	5.4	8.9	10.22	18
c_p (J/g K)	1.925	0.78	0.7	0.75	0.42	0.391	0.251	0.15
α (10^{-6}/K)	18.4	4.1	4	5	7.8	20.5	5.3	6.8
k (W/m K)	216	167	70	547	490	365	138	90.5
T_m (°C)	1273	3650	3650	2589	1083	1083	2623	1400
E (GPa)	303	62.5	12	44	220	130	330	360
σ_t (MPa)	370	87	60	80	70	365	660	660
γ (MS/m)	23.3	0.14	0.07	1-18	12.6	53.8	19.2	8.6
R (a.u.)	0.07	0.34	1.25	0.36	0.04	0.14	0.38	0.27
R_{BID} (a.u.)	0.069	0.160	0.486	0.109	0.003	0.006	0.009	0.002

For the primary and secondary collimators of the LHC, graphite was also not compatible with the impedance limit of the circulating beams and its thermal deflection under steady-state losses was too large due to insufficient heat transfer. To overcome these limitation anisotropic carbon-fiber reinforced graphite (CFC) was chosen at the expense of considerably higher material cost compared to isotropic graphite [239].

Lastly, the upgrade of the collimation system for the High-Luminosity upgrade of the LHC (HL-LHC) shows the challenging choice of materials that needs to be compatible with more severe beam conditions and the existing infrastructure. The beam intensity and therefore stored beam energy of HL-LHC will increase by a factor of 2 in comparison to LHC [223]. The increase in beam energy leads to a stricter impedance limit which is incompatible with the CFC-based primary collimators [240]. The combination of reduced beam footprint and increased beam intensity made the tungsten-based tertiary collimators incompatible with the design accident scenario.

A novel composite, molybdenum-carbide graphite (Mo-Graphite), was developed for the primary and secondary collimators that is able to cope with the stricter design requirements [241]. Another solution includes thin-film coatings of copper or molybdenum on CFC that locally increases the electrical conductivity [29]. Diamond-based copper matrix (Cu-Dia) composite will be used in the tertiary collimators of HL-LHC as it fulfills the required absorption efficiency and is compatible with the design accident scenario. The addition of a diamond phase is necessary to reduce the specific energy density deposited by the beam in the design accident scenario [242, 243].

9 Material Response to High-Power Beam Pulses

For accelerators, two extremal cases can be identified: continuous (steady state) loads and (repetitive) dynamic loads on timescales below a few tens of microseconds. This chapter will give an overview of how different pulse lengths (of energy deposition) influence the dynamic response of a target material that is irradiated with a (high-power) beam using a phenomenological approach. Special focus is given to the case of fast transient (pulsed) energy deposition events and how the fast (spatially confined) temperature increase is leading to a dynamic mechanical response.

9.1 Phenomenological Description

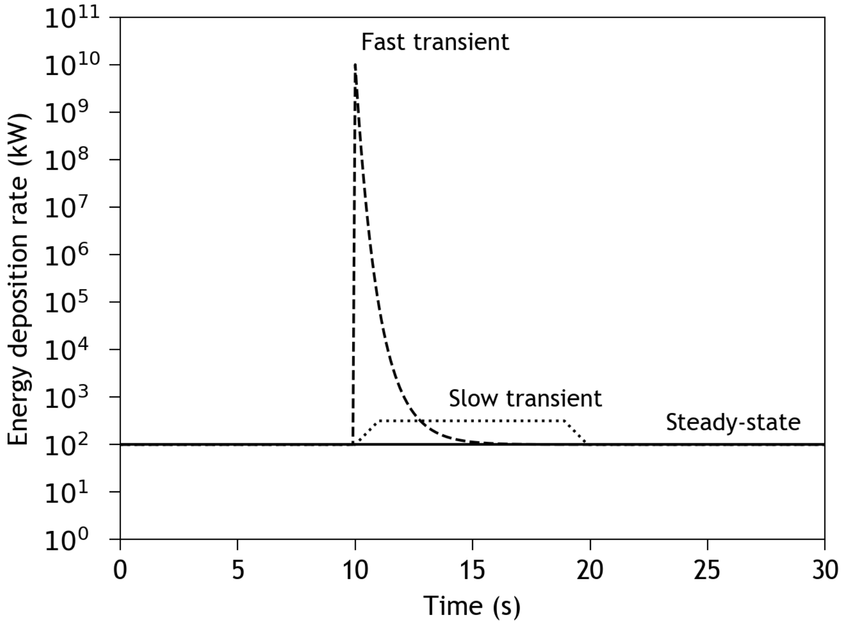

Figure 9.1.: Energy deposition rate as a function of time for (i) steady state, (ii) slow transient and (iii) fast transient energy deposition events that are experienced by beam intercepting devices. The magnitude of energy deposition rates is based on the estimated beam losses on the LHC collimation system [244].

Figure 9.1 shows the energy deposition rate as a function of time for three different energy deposition events; (i) steady state, (ii) slow transient and (iii) fast transient. These different types of energy deposition events are distinctively different with respect to the magnitude of the maximum energy deposition rate. They are representative for the operational conditions of different accelerator components like collimators, magnetic septa, production targets or beam dumps.

i **Steady state**: In steady state conditions an accelerator component is experiencing a continuous energy deposition load. This scenario is representative for collimators of circulating machines like the LHC during regular operation as the collimators are continuously scraping the halo of the beam.

ii **Slow transient**: Transient events are characterized by a rising and falling load over a certain amount of time. Slow transient events on the order of seconds are experienced by magnetic septa during slow extraction, e.g., SIS100 septa at FAIR [213].

iii **Fast transient**: Events where the energy deposition takes place on timescales far below seconds. Fast transient events occur by design due to the irradiation of a production target with a short-pulse, high-intensity beam (few ns to tens of µs), for example the Super-FRS target [1, 245] or during a beam dump in pulsed accelerators [208].

The focus of this thesis lies on the response of materials towards fast transient energy deposition events. These events lead to a thermo-mechanical dynamic response of the irradiated component, that is governed by the magnitude of the energy deposition and the material properties of the target.

9.2 Energy Deposition, Thermal and Structural Effects

Most of the energy deposited by the interaction of charged particles with a target material is converted into heat. In the case of a high-intensity charged particle beam with a pulse length of microseconds, the interaction induces an temperature increase with a similar rise time. Due to spatially confined energy deposition, thermal expansion of the interaction volume is prohibited and ultimately induces a dynamic response comparable to a mechanic impact [246]. This dynamic response is characterized by the release of the confined stress/pressure state in the material by stress/pressure waves that propagate through the target. Thermal shock conditions are achieved when the target is exposed to 'quasi-instantaneous heating' which occurs if the characteristic thermal time constant τ_{ch} is considerably longer than the thermal energy deposition length τ_{pulse} of the applied heat pulse (equivalent to the beam pulse length). The characteristic thermal time constant τ_{ch} indicates how long it takes for a physical body to thermalize:

$$\tau_{\mathrm{ch}} = \frac{L^2}{a}, \tag{9.1}$$

where L is the characteristic length of the physical body and a its thermal diffusivity. For an isotropic cylindrical target of radius R and length L, that is subjected to a finite heat pulse in its center (with constant amplitude along its length), the characteristic thermal time constant is equal to:

$$\tau_{\mathrm{ch}} = \frac{R^2}{a}. \tag{9.2}$$

For a typical isotropic graphite (e.g., SGL Carbon R6650) with a thermal diffusivity of $\sim 81\,\mathrm{mm}^2\,\mathrm{s}^{-1}$ [6] and a cylinder radius of 5 mm the characteristic thermal time constant is around 300 ms.

The magnitude of the dynamic mechanical response depends on the pulse intensity, pulse length, magnitude and rate of energy deposition, geometry of the target and strength of the irradiated material. In general, three different dynamic regimes that depend on the energy deposition rate can be identified. The three regimes are presented in Figure 9.2 for increasing strain. The strain induced by a high-power beam pulse can be assumed to linearly increase with the amount of deposited energy. The resulting dynamic regimes can be attributed to the propagation of stress waves with different amplitudes and velocities:

i **Elastic stress waves**: The amplitude of the generated stress waves is lower than the yield strength of the material. Elastic stress waves propagate with the speed of sound in the material without plastic deformation. This is the preferential regime during operation of BIDs that have to operate in pulsed conditions. Simulation of such events can be done with standard finite element (FE) codes such as ANSYS® or even analytically [246].

ii **Plastic stress waves**: If the amplitude of the generated stress wave exceeds the yield strength of the material, plastic stress waves propagate through the material at velocities smaller than the elastic speed of sound. After damping of the stress waves, permanent deformation and/or local failure by cracking can occur. By using non-linear elastic models this regime can also be well approximated using FE codes [247]. Albeit not favored, the pbar target at CERN is a BID that operates in energy deposition density regimes where plastic deformation is regularly expected [248].

iii **Shock waves**: In case the deposited energy is high enough to induce strains and stresses beyond a critical threshold, a shock wave is formed. This shock wave propagates faster than the speed of sound in the material and leads to severe plastic deformation. The interaction with high-power beam pulses creates fast shock waves that displace material radially outward from the beam axis leading to a significant decrease in density. If this happens on time scales smaller than the length of the beam pulse, following particles that have

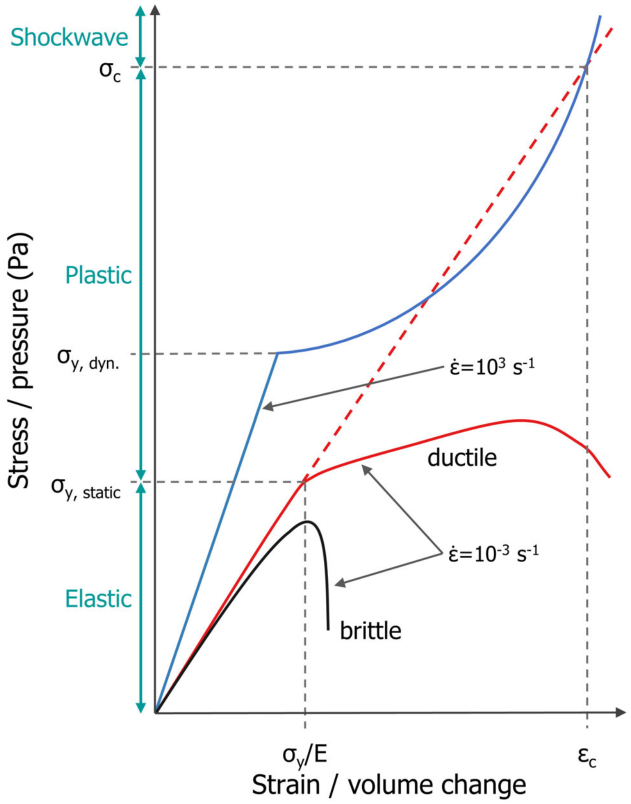
Shockwave
σ_c
Plastic
$\sigma_{\text{y, dyn.}}$
$\sigma_{\text{y, static}}$
Elastic
Stress / pressure (Pa)
$\dot{\varepsilon}=10^3\ \text{s}^{-1}$
ductile
$\dot{\varepsilon}=10^{-3}\ \text{s}^{-1}$
brittle
σ_y/E
ε_c
Strain / volume change

Figure 9.2.: Schematic stress-strain (or pressure-volume change) curve that shows the three different dynamic regimes that can be provoked by transient energy deposition events. $\sigma_{\text{y, static}}$ is the tensile strength (at a strain of $E \cdot \sigma_{y1}$) of the material under quasi-static loading conditions with a strain rate of $\dot{\varepsilon} = 10^{-3}\,\text{s}^{-1}$. $\sigma_{\text{y, dyn.}}$ denotes the tensile strength at high strain rates of $\dot{\varepsilon} = 10^{3}\,\text{s}^{-1}$. σ_c and ε_c are the critical stress and strain above which shock wave propagation occurs. Adapted from [235].

not yet interacted can penetrate deeper into the target material. This effect is known as hydro-dynamic tunneling [249]. Modelling of such events is non-trivial and generally employs explicit FE codes such as ANSYS AUTODYN® or LS-DYNA®. By employing a material's equation of state, these hydrodynamic simulations can describe non-linear events in materials at very high plastic deformations and strain rates [248, 249].

9.2.1 Damage Mechanisms

If the induced stresses and strains of the thermo-mechanical dynamic response exceed the material strength (or melting temperature), different types of damage inside the target can occur [235]:

i **Melting**: In cases where the deposited energy is leading to a local temperature increase that exceeds the material's melting temperature, the material's shear strength is locally reduced to zero and the material behaves like a liquid.

ii **Fracture**: Fracture occurs due to stress waves with amplitudes that exceed the yield strength of the material and if the overall plasticity exceeds the material's maximum ductility. Fracture can occur macroscopically as brittle failure or on the meso- and microscopical level at local defects like pores, grain boundaries or interfaces.

iii **Spallation**: Spallation is one of the main failure mechanisms during high velocity mechanical impacts and can be induced by pulsed beams as well. When compressive shock waves arrive at free surfaces they are reflected as tensile shock waves that locally exceed the yield strength of the material and fracture the material. If the amplitude of the reflected shock wave is high enough so-called "spall" fragments can be ejected from the free surface.

iv **Residual damage**: After the target has reached thermal equilibrium and all pressure waves are damped completely, residual damage includes permanent deformation (like cracks) and residual stresses.

Furthermore, the interaction of target materials with charged particle beams will lead to an accumulation of radiation damage in the target. This radiation damage is independent of the damage induced by plastic stress or shock waves (neglecting possible beam-induced thermal annealing). Radiation damage over the lifetime of a component degrades nearly all material properties [6, 26, 250, 251]. In a radiation-damaged material, beam-induced stresses can then produce plastic deformation that leads to the failure of the beam intercepting device [9, 250].

9.3 Beam-induced Elastic Stress Waves

A beam pulse leads to quasi-instantaneous heating when the beam pulse length τ_{pulse} (that is considered equal to the thermal energy deposition length) is considerably shorter than the characteristic thermal time constant τ_{ch} of the target. The resulting temperature rise ΔT in the beam-affected volume leads to thermal stresses. Due to inertia of the surrounding material, thermal stresses are invoking dynamic stresses. If the (absolute) amplitude of beam-induced stresses is below the compressive or tensile yield strength of the material, the problem can be described with basic continuum mechanics by first introducing the time-dependent beam-induced thermal field and then the resulting thermo-mechanical stresses. The model and all derivations are described in detail in references [235, 246].

To simplify the problem, the target is assumed to be an isotropic cylinder that is irradiated centrally along its axis. The beam intensity distribution is assumed to be Gaussian and eccentricity of the beam with respect to the cylinder axis is zero. Additionally, the energy deposited by the beam does not vary along the cylinder axis and is deposited with constant power during the pulse length. All thermal and mechanical material properties are considered independent of temperature. It will be shown later that this is a valid assumption for relativistic particle beams and low-Z targets like graphite with a length of ~1 cm.

All relevant variables are shown in Table 9.1. In order to reproduce the experimental data of isotropic graphite samples irradiated with high-power 440 GeV/c proton beams at the HiRadMat facility, that will be presented later, material properties are directly adapted from SGL R6650 isotropic graphite and beam parameters are an approximation of the parameters available at the HiRadMat facility [252].

Table 9.1.: Target geometry, beam and material properties used for the analytical model. Beam properties are an approximation of the beam properties at the HiRadMat facility for 440 GeV/c proton beams [252] that is relevant for the discussion of the results presented in chapter 11. Material properties reflect an isotropic graphite like SGL Carbon R6650 and are mean values over a temperature range between 300 and 1500 K.

Target geometry		
Radius	R	5 mm
Length	L	10 mm
Beam parameters		
Pulse length	τ	7.2 µs
Protons per pulse	N_p	3.45×10^{13}
Beam spot size	σ	0.3 mm
Peak deposited energy density per proton	$E_{\text{d, max, p}}$	$0.7\,\text{GeV}\,\text{cm}^{-3}\,\text{p}^{-1}$
Material properties		
Density	ρ	$1.84\,\text{g}\,\text{cm}^{-3}$
Specific heat	c_p	$1.35\,\text{J}\,\text{g}^{-1}\,\text{K}^{-1}$
Thermal diffusivity	k	$70\,\text{W}\,\text{m}^{-1}\,\text{K}^{-1}$
Coefficient of thermal expansion	α	$4.2 \times 10^{-6}\,\text{K}^{-1}$
Young's modulus	E	12.5 GPa
Poisson's ratio	ν	0.15

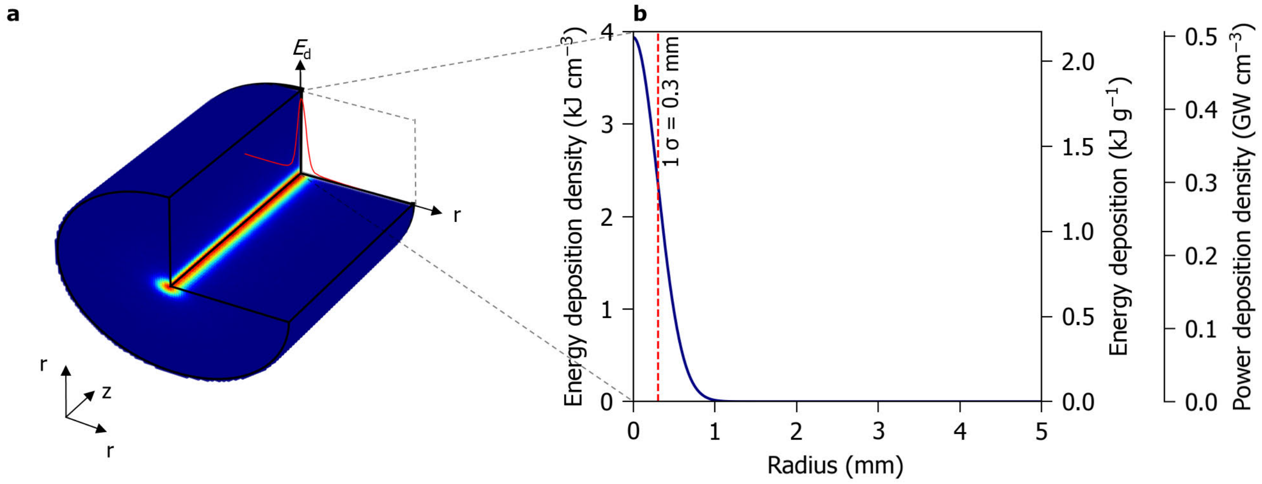

Figure 9.3.: Energy deposition distribution in a cylindrical target. Schematic representation of the target in quarter-cut geometry with the energy deposition density overlayed qualitatively (a). Radial energy deposition density of a 7.2 µs long 440 GeV/c proton beam pulse with a 1σ beam spot size of 0.3 mm in a 1.84 g cm^{-3} graphite target (b). Energy deposition can be simply calculated by dividing the deposited energy density with the volumetric mass density of the target. Power deposition density is calculated by dividing the energy deposition density by the pulse length.

9.3.1 Temperature Distribution

The radial beam intensity distribution is assumed to be a homogeneous Gaussian that is centered along the target cylinder axis z. The resulting energy deposition due to beam-matter interaction is assumed to strictly follow the identical distribution. Additionally, the energy deposition density is constant along the cylinder axis z. Figure 9.3a shows a schematic of such an energy deposition density in a cylindrical target. Thus, the beam-induced energy deposition density E_d depends only on the radial coordinate r of the cylindrical target:

$$E_\mathrm{d}(r) = N_p E_\mathrm{d,\,max,\,p} \cdot \exp\left(-\frac{r^2}{2\sigma^2}\right) = E_\mathrm{d,\,max} \cdot \exp\left(-\frac{r^2}{2\sigma^2}\right), \tag{9.3}$$

with the peak energy deposition density $E_\mathrm{d,\,max,\,p} = 3.869\,\mathrm{kJ\,cm^{-3}}$ as the product of the number of protons per pulse (beam intensity) N_p and maximum energy deposition per proton $E_\mathrm{d,\,max,\,p}$ taken from Table 9.1. The solution of Equation 9.3 is shown in Figure 9.3b. The radial temperature distribution (at the end of the beam pulse) can be directly calculated by:

$$T(r) = \frac{E_\mathrm{d}(r)}{\rho c_p} = T_\mathrm{max} \cdot \exp\left(-\frac{r^2}{2\sigma^2}\right), \tag{9.4}$$

where the maximum temperature of $T_\mathrm{max} = 1558\,\mathrm{K}$ is reached at $r = 0$ where $E_\mathrm{d} = E_\mathrm{d,\,max}$.

With the temperature distribution at the end of the proton pulse defined by Equation 9.3 and under the assumption of symmetry along the cylinder axis, the temperature distribution as a function of time can be calculated by solving the heat conduction equation in cylindrical coordinates:

$$\frac{\partial^2 T}{\partial r^2} + \frac{1}{r}\frac{\partial T}{\partial r} + \frac{1}{r^2}\frac{\partial^2 T}{\partial \theta^2} + \frac{1}{k}\frac{\partial Q}{\partial t} = \frac{1}{\alpha}\frac{\partial T}{\partial t}, \tag{9.5}$$

where θ is the polar angle, Q is the thermal energy in the system and α is the thermal diffusivity defined as:

$$\alpha = \frac{k}{\rho c_p}. \tag{9.6}$$

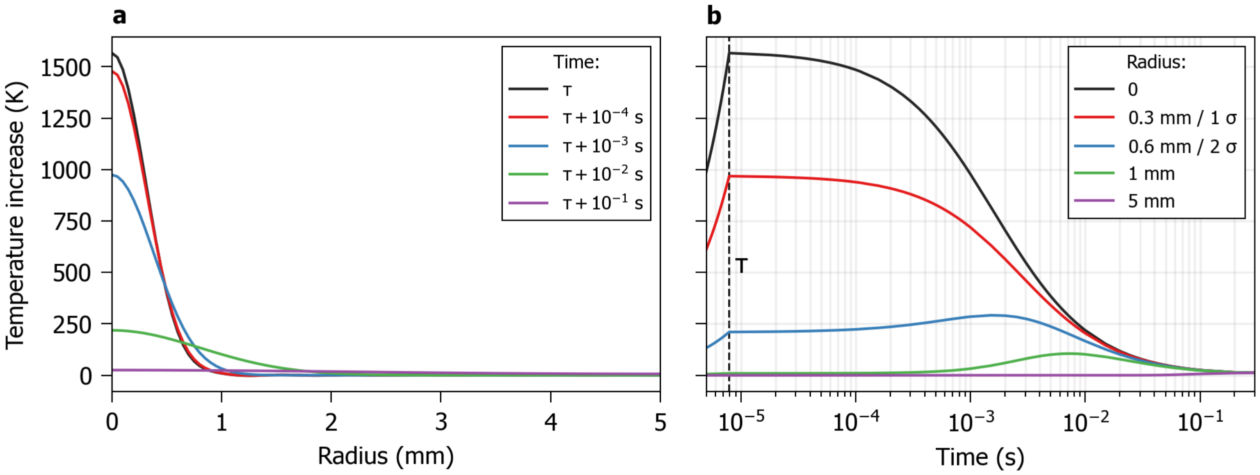

Figure 9.4.: Analytical solution of thermal field evolution with time. Radial distribution of the beam-induced temperature for different times after the beam pulse length τ (a). Time evolution of the temperature at different radial positions (b).

For the given problem, T is independent of the polar angle θ and only the temperature distribution after the beam pulse is of interest, where no heat is generated within the system ($Q = \text{const.}$). Hence, Equation 9.5 can be simplified to:

$$\frac{\partial^2 T(r,t)}{\partial r^2} + \frac{1}{r}\frac{\partial T(r,t))}{\partial r} = \frac{1}{\alpha}\frac{\partial T(r,t)}{\partial t}. \tag{9.7}$$

The initial temperature distribution $T(r, t = 0) = T_0(r)$ is defined by Equation 9.4. Together with the assumptions of radial symmetry and adiabatic heating, two more boundary conditions can be defined:

$$\frac{\partial T(0,t)}{\partial r} = 0 \text{ and } \frac{\partial T(R,t)}{\partial r} = 0. \tag{9.8}$$

With these boundary conditions the solution to Equation 9.7 is given by:

$$T(r,t) = \sum_{i=0}^{\infty} C_i J_0(\Lambda_i r)\exp(-\alpha\lambda_i^2 t), \tag{9.9}$$

where J_0 is a zero-order Bessel function of the first kind and C_i are coefficients given by:

$$C_i = \frac{\int_0^R T_0(r) r J_0(\lambda_i r)\mathrm{d}r}{\int_0^R r J_0(\Lambda_i r)^2 \mathrm{d}r}, \tag{9.10}$$

where Λ_i are the solutions for:

$$J_1(\Lambda_i R) = 0, \tag{9.11}$$

with J_1 being the first order Bessel function of the first kind. Figure 9.4 presents solutions of Equation 9.9 using the properties shown in Table 9.1. Figure 9.4a shows the radial temperature distribution for different times after end of the beam pulse τ_{pulse}. The temporal evolution of the temperature at different radial positions is shown in Figure 9.4b illustrating that the system thermalizes in less than 300 ms. In comparison, Equation 9.2 predicts a characteristic thermal diffusion time of ∼890 ms which is in reasonable agreement with the analytical solution if taken as a conservative upper limit for its magnitude.

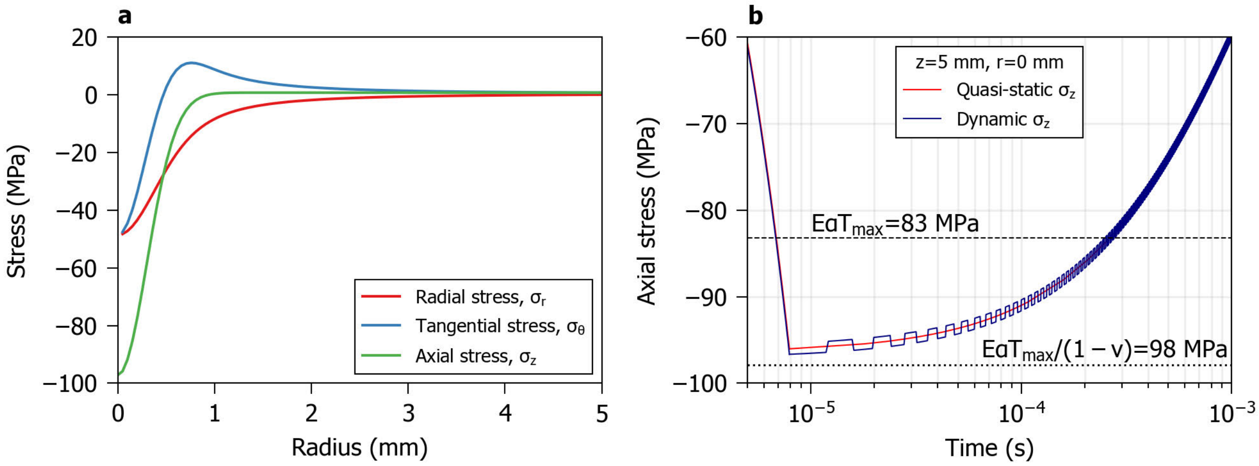

Figure 9.5.: Analytical solution of quasi-static and dynamic stresses induced by the thermal field shown in Figure 9.4. Radial distribution of the quasi-static radial σ_r, circumferential σ_θ, and axial σ_z, stress at the end of the beam pulse (a). Evolution of the quasi-static and dynamic axial stress in the center of the target (b). Horizontal dashed lines indicate two simple solutions to the thermal stress magnitude that are independent of both target geometry and spatial distribution of the thermal field.

9.3.2 Stress Amplitude

Based on the derived thermal distribution, stresses can be calculated from the differential equations of equilibrium. It should be noted that the calculated stresses are quasi-static since they are not explicitly time-dependent (as opposed to dynamic effects due to mass inertia) but only implicitly through the time evolution of the temperature within the system.

Under the assumption that the cylinder end surfaces remain planar, axial strain is constant along the cylinder axis and shear stresses and strains are zero due to axial symmetry. Hence, the following thermo-mechanical equations apply to the system:

$$\epsilon_r - \alpha T = \frac{1}{E}(\sigma_r - \nu(\sigma_\theta + \sigma_z)), \tag{9.12}$$

$$\epsilon_\theta - \alpha T = \frac{1}{E}(\sigma_\theta - \nu(\sigma_r + \sigma_z)), \tag{9.13}$$

$$\epsilon_z - \alpha T = \frac{1}{E}(\sigma_z - \nu(\sigma_r + \sigma_\theta)), \tag{9.14}$$

where r denotes stress or strain in the radial, θ in the circumferential and z in the axial direction with the equilibrium equations given by:

$$\frac{\partial \sigma_r}{\partial r} + \frac{\sigma_r - \sigma_\theta}{r} = 0 \; and \; \frac{\partial \sigma_z}{\partial z} = 0. \tag{9.15}$$

The solution to the previous equations is then given by (a full derivation for these equations is given in [235, 246]):

$$\sigma_r(r,t) = \frac{E\alpha}{1-\nu}\left(\frac{1}{R^2}\int_0^R T(r,t)r\mathrm{d}r - \frac{1}{r^2}\int_0^r T(r,t)r\mathrm{d}r\right), \tag{9.16}$$

$$\sigma_\theta(r,t) = \frac{E\alpha}{1-\nu}\left(-T(r,t) + \frac{1}{R^2}\int_0^R T(r,t)r\mathrm{d}r - \frac{1}{r^2}\int_0^r T(r,t)r\mathrm{d}r\right), \tag{9.17}$$

$$\sigma_z(r,t) = E\alpha T(r,\infty) + \frac{E\alpha}{1-\nu}\left(-T(r,t) + \frac{2\nu}{R^2}\int_0^R T(r,t)r\mathrm{d}r\right). \tag{9.18}$$

Figure 9.5a shows the radial distribution of the quasi-static stress at the end of the beam pulse calculated by Equation 9.16, 9.17 and 9.18. The stress distribution indicates that the (absolute) maximum stresses are found in the center of the cylinder at $r = 0$. Furthermore, largest stress magnitudes are also found at the end of the beam pulse ($t = \tau_{\text{pulse}}$) where the largest gradient in the radial temperature distribution occurs. For this case and knowing that $\epsilon_z = \alpha T(r,\infty) = \alpha T_\infty$, equations 9.16, 9.17 and 9.18 can be plugged into Equation 9.12, 9.13 and 9.14, respectively:

$$\sigma_r(r=0, t=\tau) = \frac{E\alpha}{2(1-\nu)}\left(T_\infty - T_0(r=0)\right), \tag{9.19}$$

$$\sigma_\theta(r=0, t=\tau) = \frac{E\alpha}{2(1-\nu)}\left(T_\infty - T_0(r=0)\right), \tag{9.20}$$

$$\sigma_z(r=0, t=\tau) = \frac{E\alpha}{1-\nu}\left(T_\infty - T_0(r=0)\right), \tag{9.21}$$

with

$$\lim_{r\to 0}\frac{1}{r^2}\int_0^r T(r,t)r\mathrm{d}r = \frac{1}{2}T_0(r=0). \tag{9.22}$$

This shows that the radial and circumferential stresses are identical and half of the axial stress in the center of the cylinder. Plugging in all necessary properties from Table 9.1, the maximum quasi-static stresses are $\sigma_z = -97\,\text{MPa}$ and $\sigma_r = \sigma_\theta = -48.5\,\text{MPa}$ which occur at the end of the beam pulse and in the center of the cylinder.

In addition to the quasi-static stresses, dynamic stresses occur due to inertia. A full derivation of the dynamic axial stress component $\sigma_z^{'}$ is outside the scope of this work. But, the two most important equations are:

$$\sigma_z^{'} = E^{'}\alpha(T_\infty - T_0), \tag{9.23}$$

where $E^{'}$ is:

$$E^{'} = \frac{E(1-\nu)}{1-\nu-2\nu^2}. \tag{9.24}$$

Equation 9.23 shows that the dynamic component of the beam-induced stress only depends on the adiabatic temperature increase T_∞ of the whole target after thermalization. In this case, axial dynamic stress will only be $\pm 0.6\,\text{MPa}$ in comparison to $-97\,\text{MPa}$ quasi-static stress. Quasi-static stresses arise from the inertia of the volume unaffected by the rapid beam-induced heating which ultimately prevents thermal expansion. But, the two ends of the cylinder are free to expand. The rapid expansion of the material at the outer ends produces two elastic tensile stress waves that are travelling at the speed of sound $c = \sqrt{E/\rho}$ towards the center of the cylinder. Upon reaching the other extremity the waves change sign with the axial oscillation frequency:

$$f_z = \frac{c}{2L} = \frac{1}{2L}\sqrt{\frac{E}{\rho}} = 130\,\text{kHz}. \tag{9.25}$$

It should also be noted that dynamic radial and circumferential stress waves occur as well. The Poisson effect leads to coupling of axial and radial waves as axial contraction or expansion will lead to the opposite deformation in the perpendicular, in this case radial, direction (with the same being true for the radial and circumferential direction). But these have even smaller stress amplitudes than axial waves. The radial oscillation frequency is defined as:

$$f_r = \frac{c^{'}}{2R} = \frac{1}{2R}\sqrt{\frac{E'}{\rho}} = \frac{1}{2R}\sqrt{\frac{E(1-\nu)}{\rho(1-\nu-2\nu^2)}} = 268\,\text{kHz}. \tag{9.26}$$

The overlay between quasi-static and dynamic axial stresses in the center of the cylinder is shown in Figure 9.5b. The magnitude of the dynamic stress is only a few percent of the quasi-static stress. Also, largest stresses are compressive. Furthermore, horizontal lines indicate two first-order approximations of the magnitude of beam-induced thermal stresses σ_t:

$$\sigma_\mathrm{t} = E\alpha(T_\mathrm{max} - T_0), \tag{9.27}$$

$$\sigma_\mathrm{t} = E\alpha(T_\mathrm{max} - T_0)/(1-\nu). \tag{9.28}$$

Where Equation 9.27 is simply Equation 9.28 with $\nu = 0$. Using the given material parameters, the solutions to these equations are 83 MPa and 98 MPa, respectively. The magnitude of these beam-induced stresses agree reasonably well with the magnitude of −97.6 MPa determined by Equation 9.18 and 9.23. Albeit these two approximations become worse with increasing T_∞ (either due to smaller target radii or larger transverse beam size σ at constant T_max), which leads to larger contribution from dynamic stresses.

9.3.3 Frequency Response and Vibration Modes

If the amplitude of beam-induced stress waves is below the tensile strength of the target material, no plastic deformation is induced in the target (c.f. Figure 9.2). Using continuum mechanics, this regime can be treated analytically for simple geometries like cylinders or bars, as introduced in the previous section. The quasi-instantaneous heating of the irradiated sample is comparable to a mechanical shock that induces vibrations of the sample. Lin [253] has derived the fundamental axial and radial vibration frequencies of thin circular plates and long cylinders.

Polar coordinates are assumed for the model where the length of the cylinder is parallel to the z axis and length and radius of the cylinder are described by L and R, respectively. In the absence of shear stresses or strains (due to axial symmetry), the following equations describe the fundamental radial vibration frequency of a cylinder:

$$f_r = \frac{c' K_r}{2\pi} = \frac{K_r}{2\pi}\sqrt{\frac{E(1-\nu)}{\rho(1+\nu)(1-2\nu)}}, \tag{9.29}$$

which can be numerically solved for values of K_r that fulfill:

$$K_r R J_0(K_r R)(1-\nu) - (1-2\nu)J_1(K_r R) = 0, \tag{9.30}$$

where J_0 and J_1 are the zero and first order Bessel functions of the first kind. For the given case introduced in section 9.3, the first solution of Equation 9.30 is $K_r = 394\,\mathrm{m}$ for the sample parameters shown in Table 9.1. Plugged into Equation 9.29 the first fundamental radial frequency is 168 kHz. Second and third solution for K_r are 1073 m and 1711 m which result in second and third order radial frequencies of 457 kHz and 730 kHz, respectively. These results are not in-line with Equation 9.26, which predicts a radial frequency of 268 kHz. It will be later shown that the model of Lin indeed reliably predicts radial frequencies for isotropic targets.

The axial frequency is given by:

$$f_z = \frac{c}{2L} = \frac{1}{2L}\sqrt{\frac{E}{\rho}} = 130\,\mathrm{kHz}, \tag{9.31}$$

which is identical to Equation 9.25.

10 HiRadMat FlexMat Experiment

This chapter will introduce the so-called ’FlexMat’ experiment conducted at the HiRadMat facility in 2018. In the experiment several material samples were irradiated with high-intensity short-pulse relativistic proton beams to induce a thermo-mechanical dynamic response that was measured on-line with strain gauges and laser Doppler vibrometry. The HiRadMat facility is outlined and special emphasis is put on the choice of investigated materials, the rationale regarding the chosen sample geometry and implementation of the on-line monitoring devices.

The experiment was designed as a proof-of-concept for a simple, flexible and re-usable experimental set-up that can fulfill the need for future testing of accelerator materials in high energy deposition density conditions that are relevant at GSI and FAIR. The choice of materials for the metallic samples was driven by candidate materials for the FAIR pbar target. Graphite materials were chosen based on relevant accelerator applications both at FAIR and other accelerator facilities like CERN and Fermilab with the overarching goal to include as many different material grades as possible to qualitatively assess differences in the material’s dynamic response with respect to different material microstructures.

It should be stressed that designing and ultimately executing such a complex experiment was a large team effort of the author’s colleagues at GSI. The final mechanical layout of the experimental chamber has been designed by Elko Schubert. FLUKA [254] simulations of the energy density deposited by the beam in the samples for finite element simulations were performed by Peter Katrik who was also responsible for the experimental samples related to the FAIR pbar target. Thermo-mechanical pre-characterization of all candidate materials was performed with the help of Fabian Jäger. Finite element simulations of the dynamic response were performed with the valuable help of Philipp Drechsel. Mounting of strain gauges on the samples was performed by Philipp Bolz. The experiment controls and all electric work was performed by Kay-Obbe Voss. The data-acquisition system and one of the laser-Doppler vibrometers were courtesy of Michael Guinchard of CERN. The organizational work of Marilena Tomut as principle investigator of the experiment is highly appreciated. Lastly, the effort of the SPS operation crew and the HiRadMat facility team at CERN are acknowledged.

10.1 HiRadMat Facility at CERN

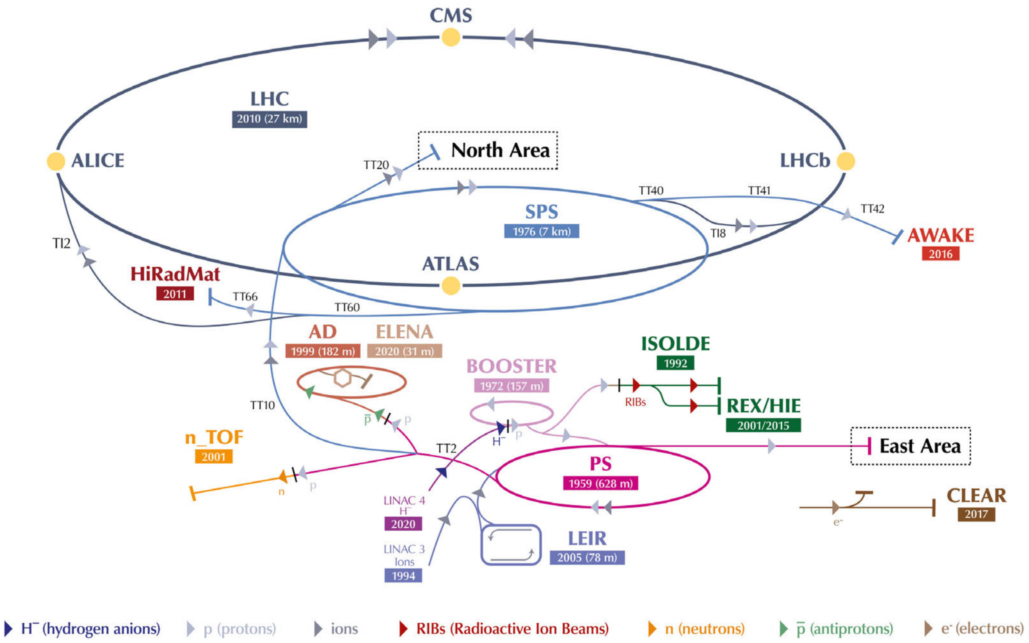
CMS
LHC
2010 (27 km)
ALICE
North Area
LHCb
TT20
TT40
TT41
TT42
SPS
1976 (7 km)
TI8
AWAKE
2016
TI2
HiRadMat
2011
ATLAS
TT66
TT60
AD
1999 (182 m)
ELENA
2020 (31 m)
ISOLDE
1992
BOOSTER
1972 (157 m)
RIBs
REX/HIE
2001/2015
TT10
p̄
p
H⁻
p
n_TOF
2001
TT2
East Area
PS
1959 (628 m)
n
p
LINAC 4
H⁻
2020
CLEAR
2017
e⁻
LINAC 3
Ions
1994
LEIR
2005 (78 m)
H⁻ (hydrogen anions)
p (protons)
ions
RIBs (Radioactive Ion Beams)
n (neutrons)
p̄ (antiprotons)
e⁻ (electrons)

Figure 10.1.: Scheme of the CERN accelerator complex with the HiRadMat facility at the TT60/TT66 extraction line of the SPS. HiRadMat delivers proton beams with a momentum of 440 GeV/c from the SPS. Reprinted with permission from [255].

The High Radiation to Materials facility (HiRadMat) at the Super Proton Synchrotron (SPS) of CERN (c.f. Figure 10.1) allows for materials and full scale accelerator components to be tested with high intensity, short-pulse relativistic proton beams [252, 256]. The facility can provide pulsed beams with variable intensity, pulse length and beam sizes. With this it is possible to deposit large energy densities up to several $\mathrm{kJ\,cm^{-3}}$ on time scales less than ∼7 µs in irradiated targets. Depending on the target material, a thermo-mechanic dynamic response can be induced that can range from elastic (non-destructive) to plastic. An optical transition radiation (OTR) based beam television (BTV) monitor measures the shape and displacement of the beam on-line for each requested beam pulse. Available beam parameters for 440 GeV/c protons are shown in table 10.1.

Table 10.1.: Proton beam parameters of the HiRadMat Facility at SPS, CERN. Values taken from [252].

Beam momentum	GeV/c	440
Max. pulse energy	MJ	2.4
Protons per bunch	ppb	5×10^{9} to 1.2×10^{11}
Number of bunches		1 to 288
Min. protons per pulse	ppp	5×10^{9}
Max. protons per pulse	ppp	3.46×10^{13}
Bunch spacing	ns	25, 50, 75 and 150
Max. pulse length	µs	7.2
1 σ beam size	mm	0.25 to 4

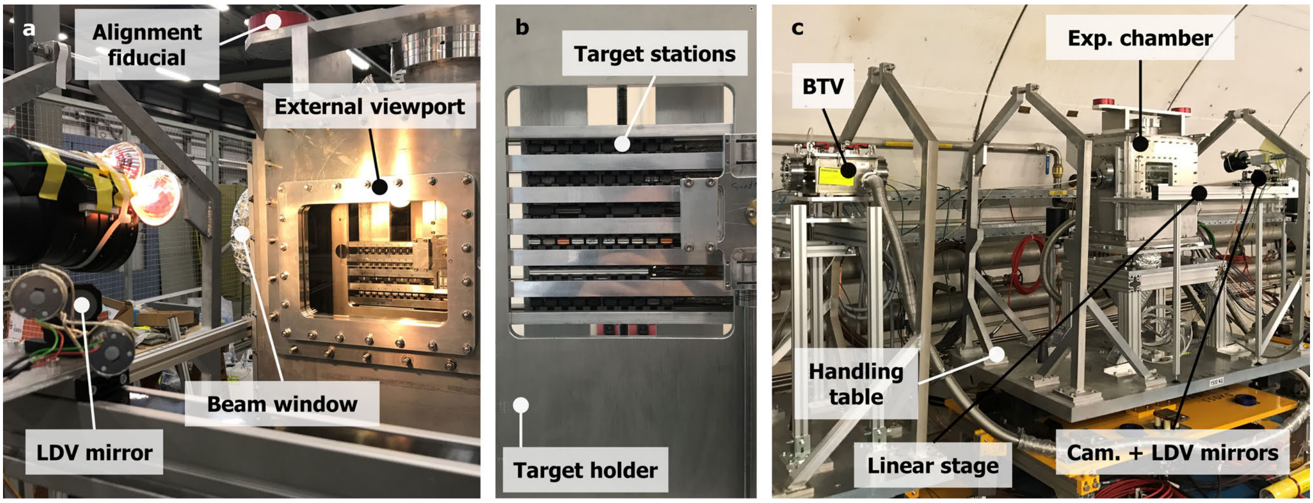

Figure 10.2.: HRMT38 FlexMat experiment. Exterior view of the experimental chamber prior to installation in the HiRadMat target area with the bending mirror for the on-line laser Doppler vibrometer (LDV) diagnostic (a). Target holder and target stations without the vacuum chamber (b). Experimental chamber inside the HiRadMat target area with the beam television (BTV) for on-line beam size and displacement monitoring and the radiation-hard camera (Cam.) (c).

10.2 Experiment Layout

The FlexMat experiment is shown in Figure 10.2a. The experiment's chamber is a stainless steel vacuum vessel that contains the target station holder (Figure 10.2b) and is mounted on an alignment support to an 'experimental table' (provided by the HiRadMat facility) that facilitates remote handling capability (Figure 10.2c). The experiment was equipped with a KF40 vacuum valve and a gas inlet that could be remote controlled. This enabled the vacuum vessel to be flushed and to operate the experiment under negative pressure of ∼0.1 bar with an inert argon atmosphere to prevent sample oxidation and attenuate any pressure spikes due to beam-induced degassing of the samples. But most importantly, in the case of a catastrophic failure of the beam windows, atmosphere would flow into the chamber thereby preventing the spread of potentially radioactive debris. Flushing was also foreseen as a means of indirect cooling by replenishing the gas atmosphere inside the experiment.

The 440 GeV/c proton beam of the HiRadMat Facility was coupled in and out of the experiment with glassy carbon beam windows consisting of 2 mm thick HTW Sigradur G plates with a CFC backplate of 2 mm SGL Carbon Premium sealed with a Viton O-ring. The sandwich design offers both robustness to the highest beam intensities (3.5×10^{13} ppp) and smallest beam spot sizes ($\sigma_{\mathrm{H,V}} = 0.25\,\mathrm{mm}$) available at HiRadMat and is compatible with primary vacuum levels of $\sim 10^{-3}$ mbar.

A massive viewport (220 mm×160 mm) made of radiation-hard glass (SCHOTT RS323G19) with a thickness of 5 mm enabled in-situ observation of the samples with a radiation-hard camera. Laser Doppler vibrometers (LDV) were used to monitor the surface velocity of two samples simultaneously. To reduce any vibration from the window being picked up by the LDVs, the viewport was inclined by 2°. A set of four radiation-hard glasses were mounted on a 'windmill-like' mechanism inside the vacuum vessel itself to protect the viewport from any high-velocity ejecta.

The internal components of the vessel consisted of 10 mm thick aluminum alloy (EN AW 5754) plates that supported the target station holder which could be vertically displaced via a spindle drive using a high torque DC servo motor. The irradiation position was defined using a mechanical switch that cut the DC current when activated by glass spheres mounted on the individual target stations. Using this simple setup a position reproducibility of $\leq 25\,\mu\mathrm{m}$ was achieved.

10.2.1 Sample Geometry

All sample in the experiment had cylindrical geometry with an outer diameter (D) of 10 mm, while the length (L) of the cylinders varied between 10, 20 and up to 100 mm. 10 mm diameter was chosen so that the beam-induced

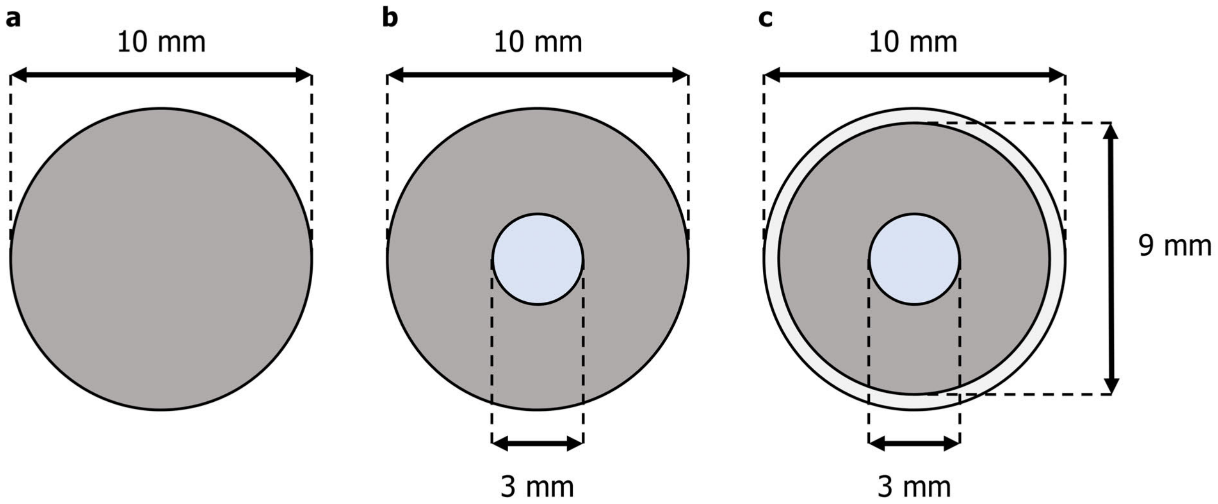

Figure 10.3.: Different sample geometries used for the FlexMat experiment in front view. Single material cylindrical samples (a). Tantalum-core graphite-shell samples (b). FAIR pbar mock-up target with inconel core, graphite shell and aluminum sleeve (c).

maximum radial surface velocity is on the order of a few 0.1 $\mathrm{m\,s^{-1}}$ on the graphite samples (radial surface velocity scales with R^{-2}), but still large enough so that pressure wave frequencies are <1000 kHz, well below the 4 MHz sampling rate of the data acquisition system. 10 mm length is sufficient to decouple axial and radial pressure wave frequencies by a factor of ∼3 in isotropic materials. 20 mm length was chosen as a means to check samples with a slower axial response.

Furthermore, cylindrical samples can be easily machined to small tolerances by lathe turning (radius and length were machined with ≤50 µm precision) and are self-centering in wedge-shaped supports. The radial size and (horizontal & vertical) position of each sample is fully determined by two simple line scans along the radius during experiment geometry measurement in comparison to rectangular cross sections which need several line scans on at least two surfaces to be fully determined.

Apart from cylindrical sample made of a single material, two types of composite sample where used: 3 mm tantalum rods embedded in different graphite shells, so-called tantalum-core samples, and a mock-up of the FAIR pbar target, that consisted of a 3 mm Inconel rod embedded in a polycrystalline graphite shell with an outer diameter (OD) of 9 mm inside an aluminum alloy sleeve (OD 10 mm) with a total length of 100 mm. A schematical overview of the sample geometries is shown in Figure 10.3.

Tantalum-core sample were chosen to overcome a fundamental limitation of the graphitic sample which is the limited energy deposited by the primary beam that inherently limits beam-induced stresses to levels below the yield strength of the investigated graphite materials. The specific energy deposition density per primary particle is up to ∼20 times larger in tantalum in comparison to graphite. Together with its small specific heat and large Young's modulus, large beam-induced stresses can be created by low(er) beam intensities (in comparison to graphite) which are eventually coupling into the graphite shell. The motivation to use tantalum is described in more detail in section B.1.7. An overview of the investigated sample materials is given in Table 10.2 with more information about the material grades and their properties presented in section B.1.

10.2.2 Target Station Design

The target holder shown in Figure 10.4c consists of six target stations with each containing up to ten individual samples. Samples are mounted on polycrystalline graphite (SGL Carbon R6650) supports. Polycrystalline graphite was chosen due to its high thermal conductivity which facilitates efficient removal of the beam-induced heat from the samples in-between consecutive pulses. Moreover, in the event of severe mis-steering of the proton beam it is expected to be robust enough towards the highest beam intensities. Its self-lubricating properties prevent the supports from getting jammed inside the negative cut-outs of the 13 mm aluminum plates that fix the different

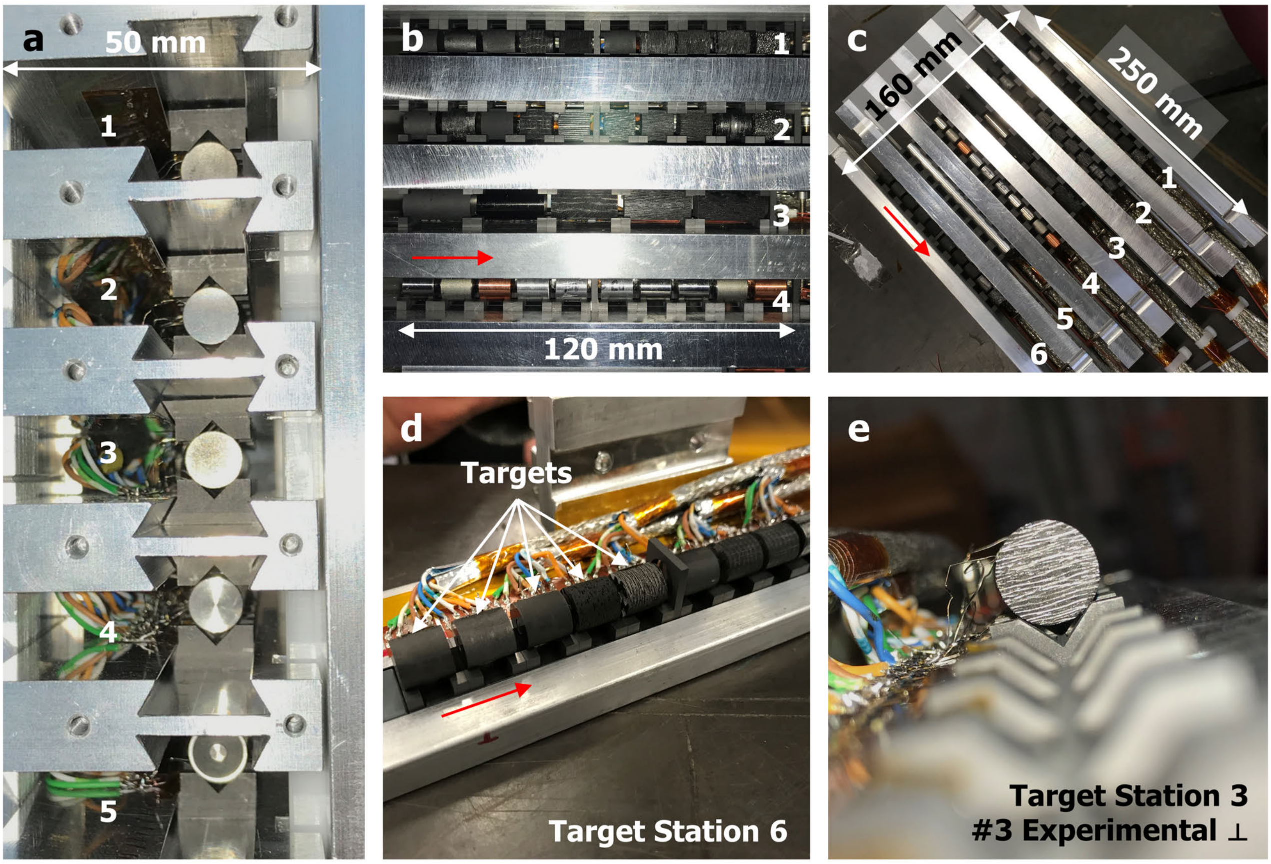
a
50 mm
1
2
3
4
5
b
1
2
3
4
120 mm
c
160 mm
250 mm
1
2
3
4
5
6
d
Targets
Target Station 6
e
Target Station 3
#3 Experimental ⊥

Figure 10.4.: Details of the target holder. Front view (in beam direction) of the target holder (a). Detail view of the target holder (b). Overview of the target holder with overall dimensions indicated (c). 10 mm long sample of target station 6 (d). Front view of a 20 mm long sample (e). Red arrows indicate the direction of the beam and numbers the respective target stations. Samples (and their materials) are summarized in Table 10.2.

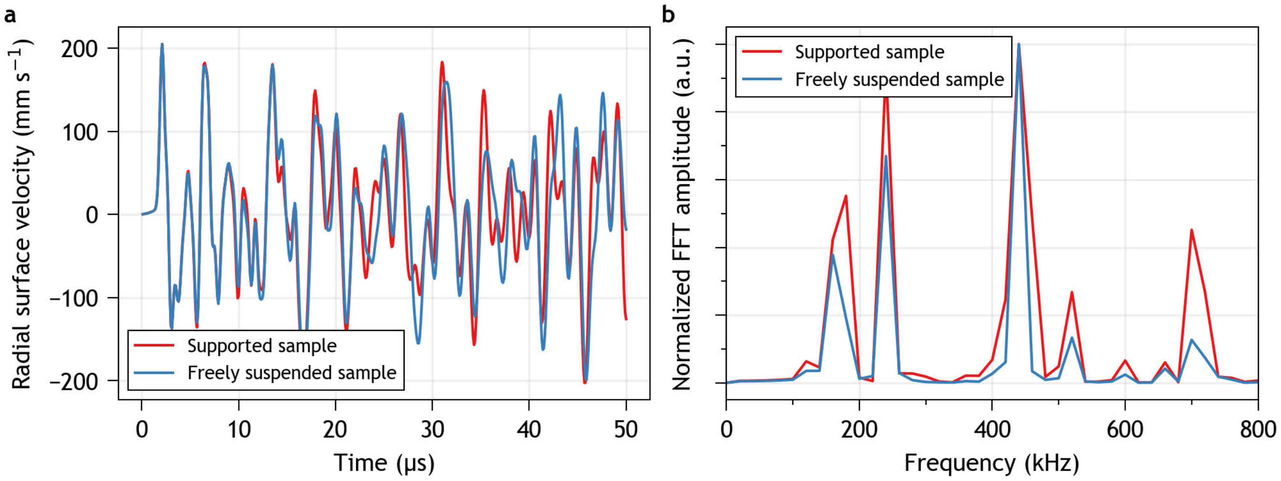

Figure 10.5.: Influence of the sample support on the dynamic response of a cylindrical polycrstalline graphite sample (diameter 10 mm, length 10 mm) irradiated with a high-intensity 440 GeV/c proton beam (7.2 µs pulse length). Simulated radial surface velocity (with energy deposition density calculated by FLUKA) at 5 mm length of the sample as a function of time after the beam pulse (a). FFT of the simulated dynamic response (b).

target stations in place. Each support has a length of 11 mm (21 mm for the samples of target station 3) with the samples self-centering on 2 mm long 90° wedges on the extremities of the supports (Figure 10.4e). Samples were fixed in place from the top with a force of ~8.3 N by compressing the springs mounted in the top support from their design length of 5.5 mm to 4 mm (spring constant 5.5 N mm^{-1}) (see the gap between the top target supports in Figure 10.4a).

The support of the individual sample was designed to achieve a beam-induced dynamic response of the samples that is as close as possible to a freely suspended sample to ultimately save computational time in finite element simulations. To check whether this statement holds true, a coupled transient thermal/structural simulation was performed in ANSYS Mechanical Release 19.2 [257] on a polycrystalline graphite sample (SGL Carbon R6650). Material parameters used in the simulation are given in Table 11.4. The three-dimensional energy deposition density of a 440 GeV/c proton beam ($\sigma_{\mathrm{H,V}}$ =0.25 mm with 3.5×10^{13} ppp and 7.2 µs pulse length) was calculated by FLUKA [254]. The simulation was performed once with a freely suspended sample and once with the full support geometry, including gravity and the spring force under the assumption of a frictionless contact between sample and support.

The radial surface velocity and frequency response of these simulations are shown in Figure 10.5. Indeed, both simulations are virtually identical between the two support variations. The largest difference can be identified in the amplitude of the high-frequency component around 700 kHz in the fast Fourier transform (FFT) of the radial surface velocity, which can be neglected since it is not the fundamental radial vibration mode of the sample (as will be shown later).

Table 10.2.: Sample distribution in the experiment target stations. Pulse intensities indicate the overall maximum pulse intensity extracted on the target station. Maximum pulse intensity per sample may be lower. Average beam sizes are calculated for all shots using the same beam optics (Target Stations 1 to 3 and Target Stations 4 & 5, respectively). Densities are taken from material datasheets provided by the manufacturer. Anisotropic samples with their main reinforcement direction parallel to the irradiated surface are indicated by ||, while anisotropic samples with main reinforcement direction perpendicular to the irradiated surface are indicated by ⊥ (c.f. Figure 10.4).

Target Station 1 - D10 mm L10 mm, 28 pulses, 3.67×10^{13} ppp, σ_H =(0.33 ± 0.01) mm, σ_V =(0.27 ± 0.02) mm

#1	#2	#3	#4	#5	#6	#7	#8	#9	#10
R6650	TPG ||	R6300	Sepcarb ||	Perf. ||	R6650 ||	Exp. ||	Premium ||	PyC ||	FOAM
1.84	2.25	1.73	1.55	1.5	1.84	1.74	1.55	1.59	0.5 $\mathrm{g\,cm^{-3}}$

Target Station 2 - D10 mm L10 mm, 29 pulses, 3.51×10^{13} ppp, σ_H =(0.33 ± 0.01) mm, σ_V =(0.27 ± 0.02) mm

#1	#2	#3	#4	#5	#6	#7	#8	#9	#10
R6650	TPG ⊥	ZEE	Sepcarb ⊥	Perf. ⊥	PyC ⊥	Exp. ⊥	Prem. ⊥	EG ||	HTC
1.84	2.25	1.77	1.55	1.5	1.59	1.74	1.55	1.0	0.9 $\mathrm{g\,cm^{-3}}$

Target Station 3 - D10 mm L20 mm, 18 pulses, 3.50×10^{13} ppp, σ_H =(0.33 ± 0.01) mm, σ_V =(0.27 ± 0.02) mm

#1	#2	#3	#4	#5
R6650	Sigradur G	Sepcarb ⊥	Experimental ⊥	Premium ⊥
1.84	1.42	1.5	1.74	1.55 $\mathrm{g\,cm^{-3}}$

Target Station 4 - D10 mm L10 mm, 94 pulses, 1.64×10^{12} ppp, σ_H =(0.56 ± 0.10) mm, σ_V =(0.51 ± 0.07) mm

#1	#2	#3	#4	#5	#6	#7	#8	#9	#10
Inconel	Invar	Copper	Inconel	Invar	Copper	Inconel	Inconel	Invar	Copper
8.47	8.05	8.02	8.47	8.05	8.02	8.47	8.47	8.05	8.02 $\mathrm{g\,cm^{-3}}$

Target Station 5 - D10 mm L100 mm, 35 pulses, 2.16×10^{12} ppp, σ_H =(0.56 ± 0.10) mm, σ_V =(0.51 ± 0.07) mm

D3 mm Inconel in OD9 mm R6650 cladding in D10 mm aluminum Sleeve

Target Station 6 - D10 mm L10 mm with D3 mm tantalum core, 79 pulses, 1.74×10^{12} ppp, σ_H =(1.46 ± 0.11) mm, σ_V =(1.02 ± 0.09) mm

#1	#2	#3	#4	#5	#6	#7	#8	#9	#10
R6650	R6300	ZEE	Premium PyC	Premium	R6650	Sepcarb	Sepcarb/EG	EG wrapped	FOAM
1.84	1.73	1.77	1.59	1.55	1.84	1.74	1.55	1.59	0.5 $\mathrm{g\,cm^{-3}}$

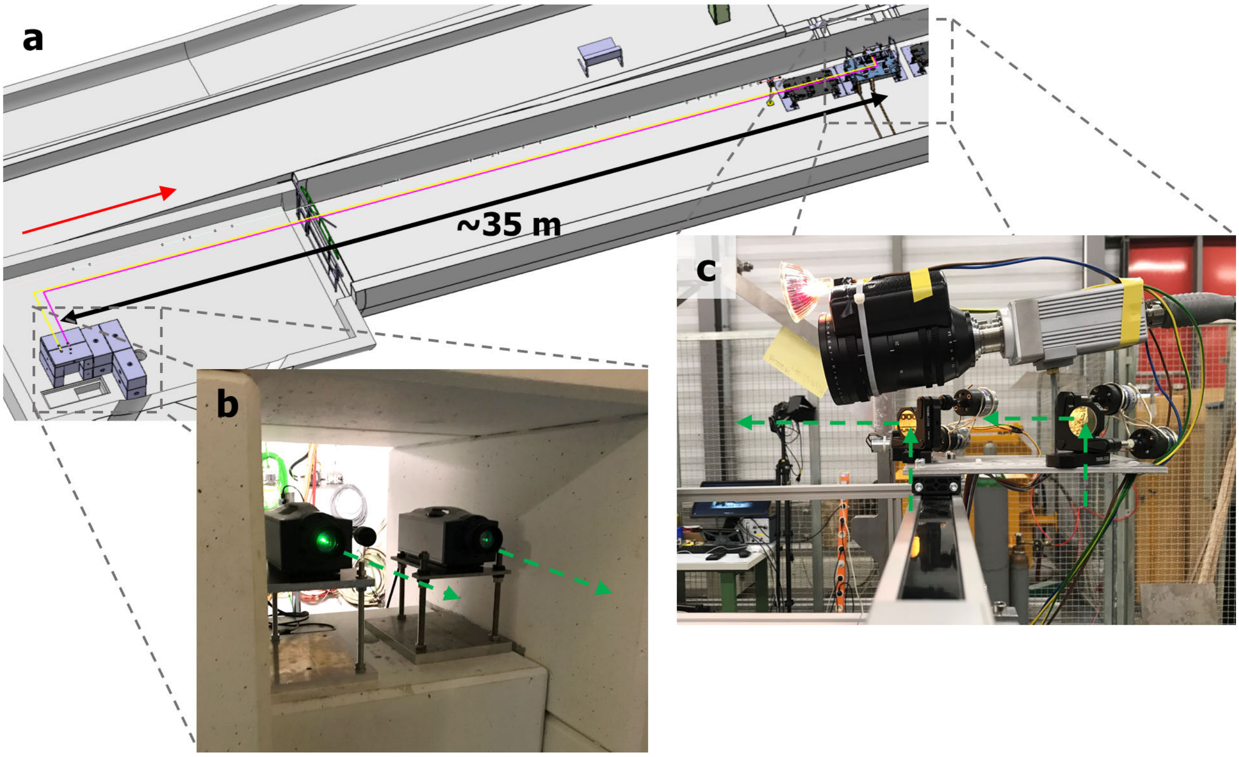

Figure 10.6.: Laser Doppler vibrometer beam paths. CAD model of the beam paths in the HiRadMat facility with yellow and pink lines indicating the beam paths of the LDVs. Courtesy of Vincent Clerc, CERN (a). Location of the two LDV measurement heads in the 'bunker' (b). Final set of mirrors installed on the linear displacement stage in front of the experimental chamber (c). Green dashed arrows indicate the LDV beam paths. The red arrow indicates the beam direction.

10.3 Instrumentation and Data Acquisition

Each sample was equipped with bi-directional strain gauges (HBM 1-XY9x-1.5/120) to record the beam-induced axial and tangential surface strain. Additionally, several PT100 thermosensors were mounted on all target stations to measure the (overall) temperature rise of the target stations due to the beam-induced heating of the samples. Any electronic measurements suffer from an electromagnetic 'blackout' of up to $\sim$15 µs that was induced by the short high-intensity beam pulses passing parallel to the strain gauge wires with a distance of <3 cm (c.f. Figure 10.4d and e). Hence, to measure the beam-induced dynamic response of the samples without any perturbations, two laser-Doppler vibrometers (LDVs) (Polytec RSV-150) were used to measure the radial surface velocity up to a maximum surface velocity of $20\,\mathrm{m\,s^{-1}}$ of two samples simultaneously . These LDVs have a depth of focus of several tens of meter and a (theoretical) measurement range of several km with GHz sampling rate.

The LDV measurement heads were located at a shielded location at a distance of about 35 m. To couple the laser beams of the LDVs into the experiment chamber two sets of two mirrors were used. One set (two Polytec LDV-rated A5 paper sheet-sized aluminum mirrors) reflected the LDV laser beams parallel to the beam line onto a second set of mirrors (two Thorlabs PF10-03-M01 2.54 cm diameter gold mirrors) directly to the samples. These mirros were mounted in kinematic holders on a linear displacement stage to select the samples to be monitored in-situ. A radiation-hard camera (Thermo Scientific MegaRad3 CID8726DX6) monitored the samples in-between beam pulses. The beam path of the LDVs inside the HiRadMat facility is shown in Figure 10.6. The radial surface velocity is proportional to the circumferential strain $\varepsilon_\theta(t)$ and given by:

$$\varepsilon_\theta(t) = \frac{1}{R}\int v(t)\mathrm{d}t, \tag{10.1}$$

where R is the radius of the samples and $v(t)$ the radial surface velocity measured by the LDV.

The multi-channel digital data acquisition system (DAQ) had a maximum sampling rate of 4 MHz that recorded the strain gage and LDV signal for a total duration of 23 ms and was triggered on the hardware signal of a beam position monitor of the HiRadMat beam line (3 ms pre-trigger). The DAQ system is described in more detail in reference [258].

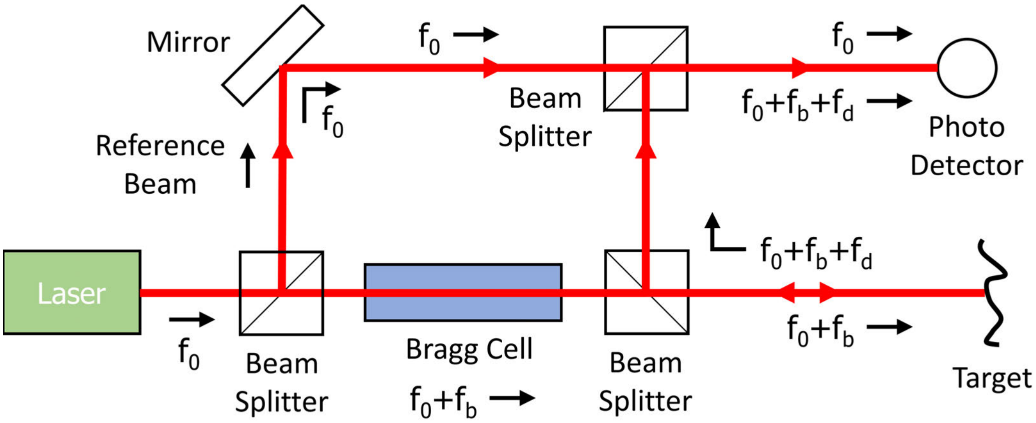

Figure 10.7.: Schematic layout of the basic components of a laser Doppler vibrometer using a laser with frequency f_0. The test beam is shifted by a known frequency f_b using an acousto-optic modulator (a Bragg cell). The reflected test beam is Doppler shifted by f_d which is proportional to the target's velocity. The interference between the test beam and the reference beam generates a frequency-modulated signal with carrier frequency f_b and modulation frequency f_d.

A laser Doppler vibrometer (LDV) uses the frequency shift induced by the Doppler effect of a moving target to measure surface velocities. In the simplest terms, a LDV is a two-beam laser interferometer that measures the frequency (or phase) difference between a reference and a test beam. When the reference beam is reflected by a moving surface, the reflected light will be shifted in frequency f_D due to the Doppler effect which is given by:

$$f_d = 2\frac{v\cos(\alpha)}{\lambda}, \tag{10.2}$$

where v is the velocity of the surface the reference beam is impinging on, α is the angle between the reference beam and the velocity vector and λ is the wavelength of the reference beam. A common Nd:YAG infrared laser of 1064 nm wavelength will be shifted by ~1.9 THz by a surface moving at $1\,\mathrm{m\,s^{-1}}$ at normal incidence ($\alpha = 0$).

The reference and test beam interfere on a photodetector. The light frequency f_0 (e.g., 1064 nm, corresponding to 282 MHz) of the reference beam is orders of magnitude larger than the frequency shift and is higher than the frequency response of most photodetectors. To overcome this limitation, the test beam is shifted by a fixed frequency f_b of few tens of MHz by an acousto-optic modulator (Bragg cell) before impinging on the target. Hence the reflected light from the surface has a frequency of $f_0 + f_b + f_d$. This set-up generates a frequency-modulated interference pattern with carrier frequency f_b and modulation frequency f_d that can be reliably measured by the photodiode. By demodulating the signal, the modulation frequency and thus the target's surface velocity can be extracted as a function of time.

11 Dynamic Response of Graphite Samples Irradiated with High-Power Proton Beams

The following chapter will present an overview of the FlexMat experimental campaign conducted at HiRadMat in 2018. Several highlights of the data measured in the experiment will be presented and the dynamic response of different graphitic samples will be discussed in detail. The numerical methods used to analyze the experimental data are described in section B.5. Parts of this work were published in reference [259].

11.1 Experimental Conditions

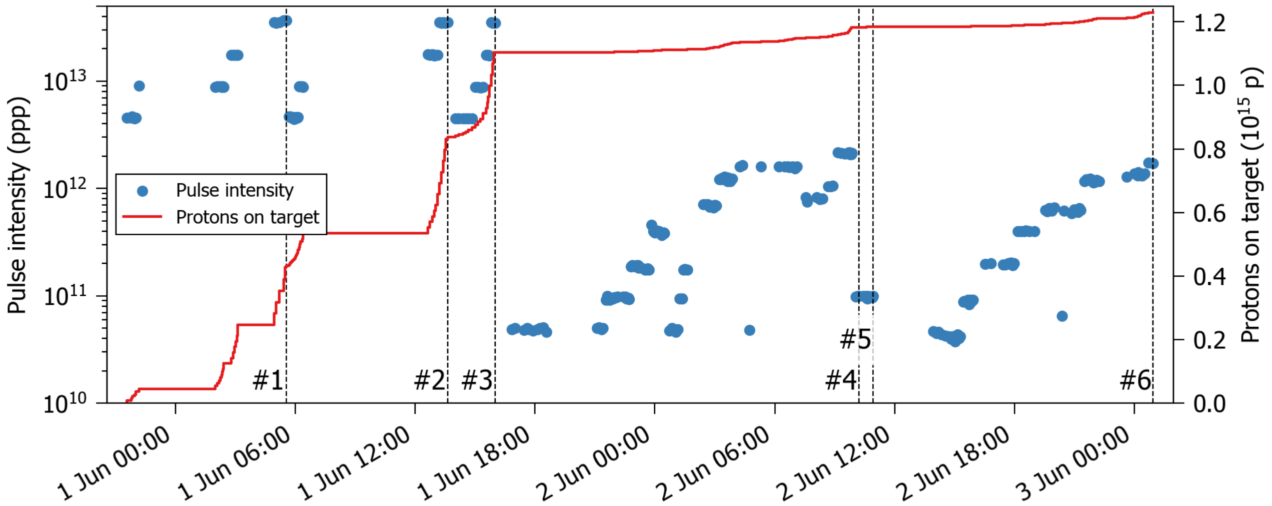

Figure 11.1.: Overview of 440 GeV/c proton beam pulses sent to the HRMT38 FlexMat experiment. Extracted beam intensity in protons per pulse (ppp) from the SPS accelerator and integrated numbers of protons on target as a function of time. Vertical dashed lines indicate the end of the irradiation for the different target stations #1 to #6.

11.1.1 Beam Parameters

Figure 11.1 shows the time evolution of 440 GeV/c proton pulses delivered to the FlexMat experiment. The maximum pulse intensity achieved was 3.67×10^{13} protons per pulse (ppp) (288 bunches with 1.27×10^{11} protons per bunch (ppb) and 7.2 µs pulse length) during irradiation on target station 1. The integrated number of protons delivered to the experiment was $\sim 1.2 \times 10^{15}$ protons delivered by a total of 262 individual beam pulses with about one extracted beam pulse per 10 minutes on average. The beam spot size and lateral beam position were measured on-line for each extracted beam pulse by the HiRadMat beam television (BTV) device using an optical transition radiation diagnostic screen. The results of these measurements are shown in Figure 11.2 for the different transverse beam spot sizes (optics), $\sigma = 0.25$, 0.5 and 1.5 mm, requested in the experiment. The horizontal and vertical position jitter of ≥90 % of all extracted beam pulses were within ±25 % of the mean measured beam spot size, independently of the requested beam spot size.

Taking the average transverse beam position into account, ≥90 % of the samples of target station 1 to 3 ($\sigma = 0.25$ mm) were irradiated within ±107 µm (2.14 % of the radius) around the beam axis. Target station 4 & 5 ($\sigma = 0.5$ mm) were irradiated within ±189 µm (3.79 %). For target station 6 ($\sigma = 1.5$ mm), the vertical beam

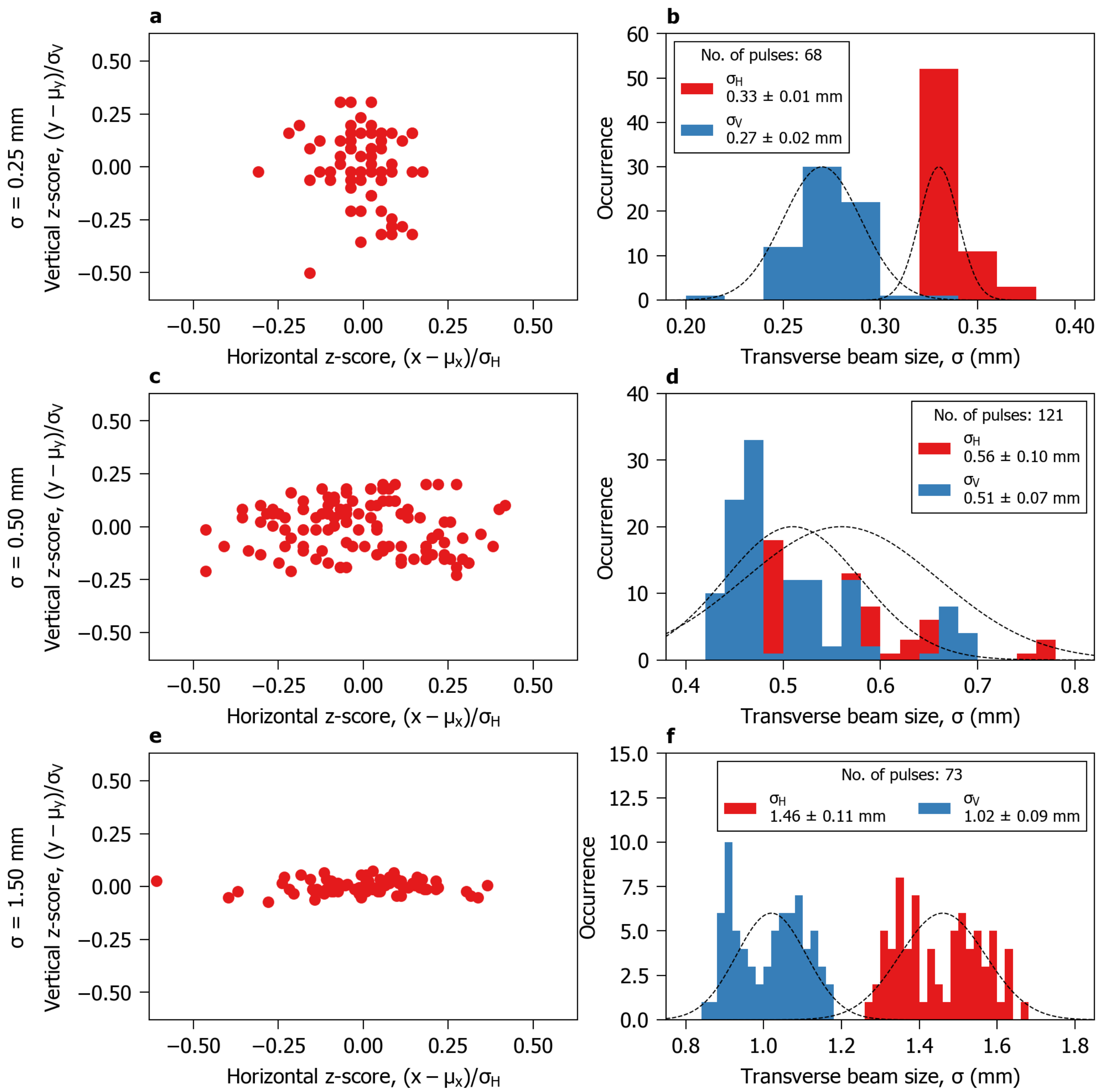

Figure 11.2.: Beam position jitter and spot size analysis recorded on the HiRadMat BTV for the different optics used in the HRMT38 FlexMat experiment. Z score of the horizontal and vertical beam displacement for a requested beam sigma of 0.25 mm (a), 0.5 mm (c) and 1.5 mm (e). Histogram of horizontal and vertical beam sigmas for the different requested beam sigmas (b, d and f).

position jitter is determined to be ≤5 %, which results in ≥90 % of the beam pulses irradiated within ±369 μm (7.37 % of the radius). The geometrical alignment precision of the experiment (data shown in section B.2) was systematically smaller than the jitter of the beam position in both horizontal and vertical position. The considerably larger scattering of the horizontal beam position for $\sigma = 1.5$ mm on target station 6 can be explained by the SPS extraction in the horizontal plane where extraction jitter propagates along the HiRadMat beamline.

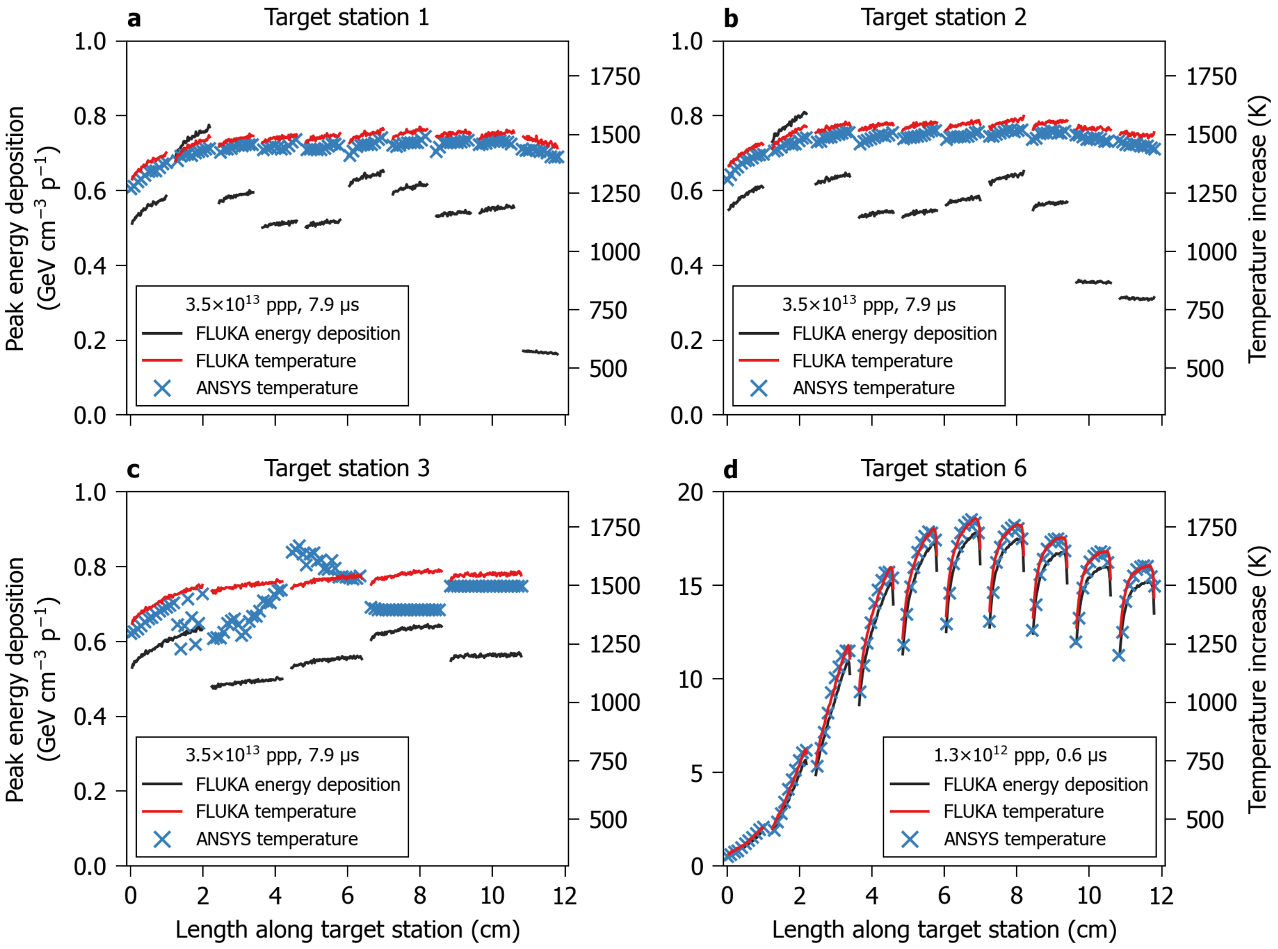

Figure 11.3.: Peak deposited energy density of per 440 GeV/c protons and peak temperature rise at the end of a beam pulse with maximum beam intensity in target stations 1 (a), 2 (b), 3 (c) and 6 (d) along the length of the target stations. FLUKA simulations were conducted taking the average beam spot size for each target station into account (c.f. Figure 11.2). The temperature rise is calculated analytically ('FLUKA temperature') and numerically ('ANSYS transient thermal' with an initial temperature of 293 K.

11.1.2 Energy Deposition and Sample Temperature

Using the average beam spot sizes during the experiment as input, FLUKA simulations [254] were performed to determine the energy density deposited by the primary beam and the beam-induced hadronic shower along the different target stations and to ultimately determine the peak (adiabatic) temperature increase in each sample. The temperature was determined with two different approaches. In the first approach the temperature increase from T_0 to T_1 (at any point of a sample) was calculated from the deposited energy density $\Delta E/\Delta V$ per proton for the respective beam intesity I_{beam} by:

$$I_{\text{beam}} \frac{1}{\rho_i} \frac{\Delta E}{\Delta V} = \int_{T_0}^{T_1} c_{p,i}(T)\, \mathrm{d}T \tag{11.1}$$

where ρ_i is the density and $c_{p,i}$ the specific heat of sample i in a target station.

In the second approach, the temperature distribution at the end of the beam pulse was simulated in a transient thermal simulation in ANSYS (c.f. section B.4). The specific heat of graphite does not vary considerably with density [260]. Hence, for all carbon-based samples of target stations 1, 2 and 3, the identical specific heat was assumed, that was based on the tabulated specific heat curve of a polycrystalline graphite standard for laser flash analysis [260]. For tantalum a polynomial function for the specific heat with parameters from [261] was used. As a general reference, the specific heat of graphite can be assumed to be 0.7 J g^{-1} K^{-1} at room temperature and 0.14 J g^{-1} K^{-1} for tantalum, respectively.

Table 11.1.: Calculated maximum axial stresses σ_t in various isotropic graphite samples induced by the highest pulse intensities. Density ρ, Young's modulus E and compressive strength σ_c were taken from the supplier datasheets. Poisson's ratio ν are estimated. Flexural strength σ_f has been determined by three-point bending and is taken from [260]. E_d corresponds to the deposited peak energy density shown in Figure 11.3 averaged over the sample length for a beam intensity of 3.5×10^{13} ppp. T_max is the resulting peak temperature calculated with Equation 11.1. The last two columns are first-order approximations of the beam-induced thermal stresses σ_t calculated with Equation 9.27 and 9.28, respectively.

Sample	ρ g/cm^3	E GPa	α 10^{-6}/K	ν	σ_c MPa	σ_f MPa	E_d kJ/cm^3	E_d/ρ kJ/g	T_max K	σ_t MPa	σ_t MPa
Target Station 1 $L = 10$ mm											
#1 R6650	1.84	12.5	4.1	0.18	150	66.9 ± 11.8	3.07	1.67	1375	55	68
#3 R6300	1.73	10	2.7	0.18	85	51.3 ± 1.3	3.24	1.87	1478	32	39
Target Station 2 $L = 10$ mm											
#1 R6550	1.83	11.5	4.2	0.18	130	67.0 ± 4.9	3.25	1.77	1424	55	67
#3 ZEE	1.77	14.5	8.1	0.18	193	146.2 ± 13.4	3.50	1.98	1531	145	177
Target Station 3 $L = 20$ mm											
#2 Sigradur G	1.42	35	2.6	0.17	480	128 ± 17	2.72	1.92	1499	136	164

The peak deposited energy densities per primary proton and the resulting peak temperatures (assuming a temperature T_0=293 K) for the highest beam intesities on the different target stations are shown in Figure 11.3. The adiabatic temperature increase that was calculated by Equation 11.1 and results of finite element simulations in ANSYS agree very well for target stations 1, 2 and 6. Some deviations between the finite element simulation and the adiabatic temperature increase can be observed for target station 3 (Figure 11.3c) with temperature differences of up to ~200 K. The difference probably arises from the rather large time step used for the simulations shown in Figure 11.3, which was necessary to simulate all samples within the target stations simultaneously.

Maximum beam-induced peak temperatures are on the order of ~1500 K in the graphitic samples of target stations 1, 2 and 3 for the maximum beam intensity of 3.5×10^{13} ppp. The first two to three samples of these target stations experience slightly smaller energy densities due to the on-going build-up of the hadronic shower, but even these samples reach >1350 K. Considering a room temperature of 293 K, a quasi-instantaneous peak temperature increase ΔT of up to ~1200 K was achieved. The deposited energy density in the tantalum cores of target station 6 varies considerably along the target station. The initial energy deposition of ~1 GeV/(cm^3 p) in the first few mm of the first sample increases up to ~18 GeV/(cm^3 p). Due to the absence of a significant hadronic shower, the gravimetric energy density is virtually flat in the graphite target stations. But, due to the large atomic number and density of tantalum, the interaction with the primary proton beam produces a significant hadron shower within the first few samples that is self-absorbed inside the subsequent samples. The hadronic shower buildup is also the reason for the 'hook'-like shape of the deposited energy density. In the small gaps between samples the secondary particles of the hadronic shower can 'escape' laterally due to their large divergence angle in the beam direction. The initial energy density will thus be lower than the maximum energy density in the preceding sample. The tantalum cores that are close to the maximum of the hadronic shower reach temperatures up to 1700 K while the first tantalum core only reaches ~400 K.

11.1.3 Expected Stresses in Isotropic Graphite Samples

The peak energy density deposited by the beam and peak temperature can be used to approximate the magnitude of beam-induced axial stresses (radial and tangential stress are simply half in the center of the sample) using Equation 9.27 and 9.28 to approximate Equation 9.18. The expected stresses are shown in Table 11.1 for a selection of isotropic samples. Based on the Young's modulus provided by the material supplier, beam-induced stresses are all lower than the compressive strength σ_c stated by the supplier. In comparison to the flexural strength σ_f, which is a more conservative approach to estimate the strength of graphite samples due to the mixed stress state during its measurement, beam-induced stresses are comparable or even larger. Hence, irradiation at the highest beam intensity could potentially induce failure in some of the samples. The 20 mm Sigradur G sample of target station 3 is indicated as the sample that is most 'at risk'. For beam intensities less or equal to 1.8×10^{13} ppp, that only induce less than half of the estimated thermal stresses, fully elastic material behavior is expected.

11.2 Dynamic Response of Graphite Materials

This section presents the results of the on-line measurements of the dynamic response during high-intensity pulsed proton beam irradiation with an emphasis on the polycrystalline graphite samples which are most relevant for applications at FAIR [1, 208, 214]. The dynamic response of carbon-fiber reinforced graphite is qualitatively discussed in section B.3. Presented experimental data will focus solely on the radial surface velocity measured on-line by the laser Doppler vibrometers. The strain gauges that were mounted on the samples were unfortunately recording no meaningful signal. It should be stressed that all results presented in the following refer to the dynamic response induced by a single beam pulse on the different samples. Samples were irradiated several times at each beam intensity, but due to the experiment layout, a maximum of two samples were monitored simultaneously per beam pulse. In the case of graphite materials, where our results indicate no plasticity of the samples, cumulative effects of multiple beam pulses are neglected.

11.2.1 Isotropic Polycrystalline Graphite

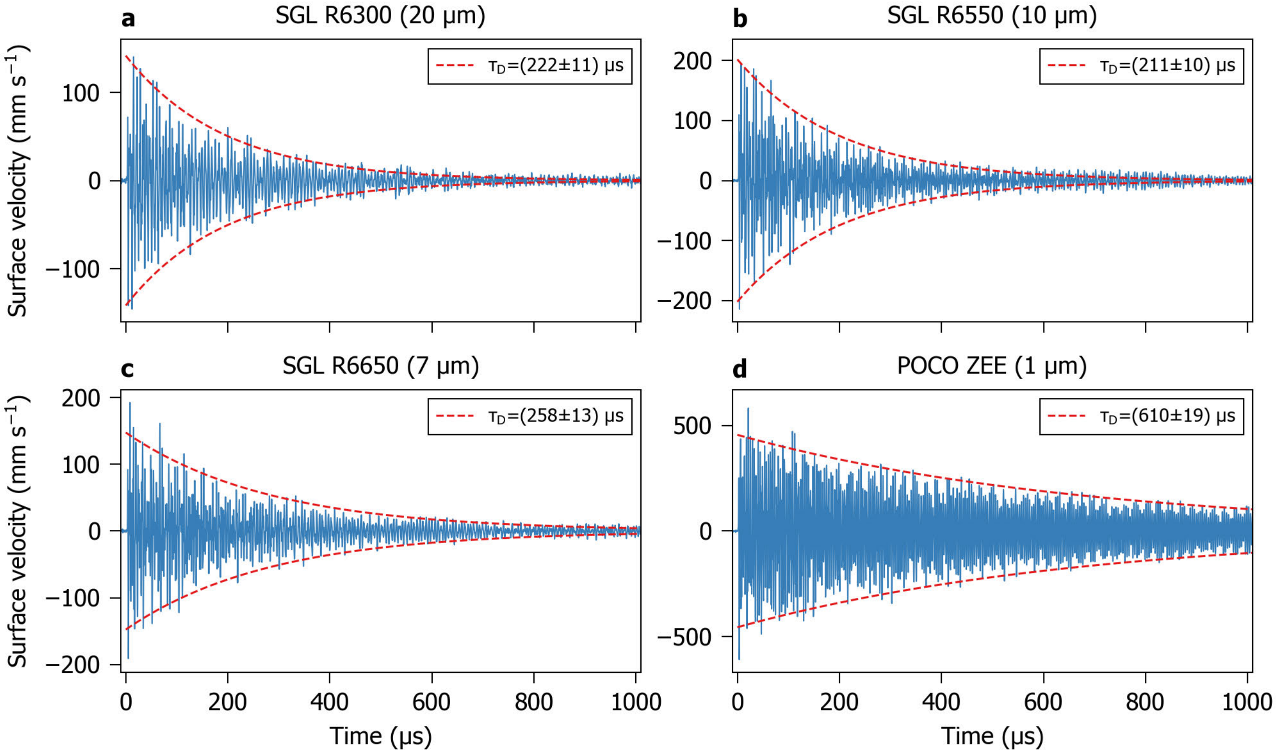

Figure 11.4.: Dynamic response of different isotropic polycrystalline graphite samples after irradiation with 4.3×10^{12} ppp 440 GeV/c proton beams (0.9 µs pulse length) with a transverse beam size of $\sigma_{x,y}{\sim}0.3$ mm. Radial surface velocity (blue line) measured by a laser Doppler vibrometer in the center of SGL R6300 (a), SGL R6550 (b), SGL R6650 (c) and POCO ZEE (d). Particle sizes according to the supplier are given in parentheses. Dashed red lines represent the damping envelope obtained by a fit of an exponential decay function to the local absolute maxima with the obtained damping time constant τ_D stated in the legend.

Four different isotropic polycrystalline graphite grades with particle sizes ranging from 1 to 20 µm (according to the supplier) were irradiated with a series of high-intensity 440 GeV/c proton beam pulses of intensities between $\sim 4.3 \times 10^{12}$ ppp (0.9 µs pulse length) and $\sim 3.5 \times 10^{13}$ ppp (7.2 µs) and transverse beam sizes of $\sigma_{x,y}{\sim}0.3$ mm. The dynamic response of these isotropic graphite grades, induced by individual pulses of the lowest beam intensity of 4.3×10^{12} ppp, is shown in Figure 11.4 for 1 ms after the beam pulse.

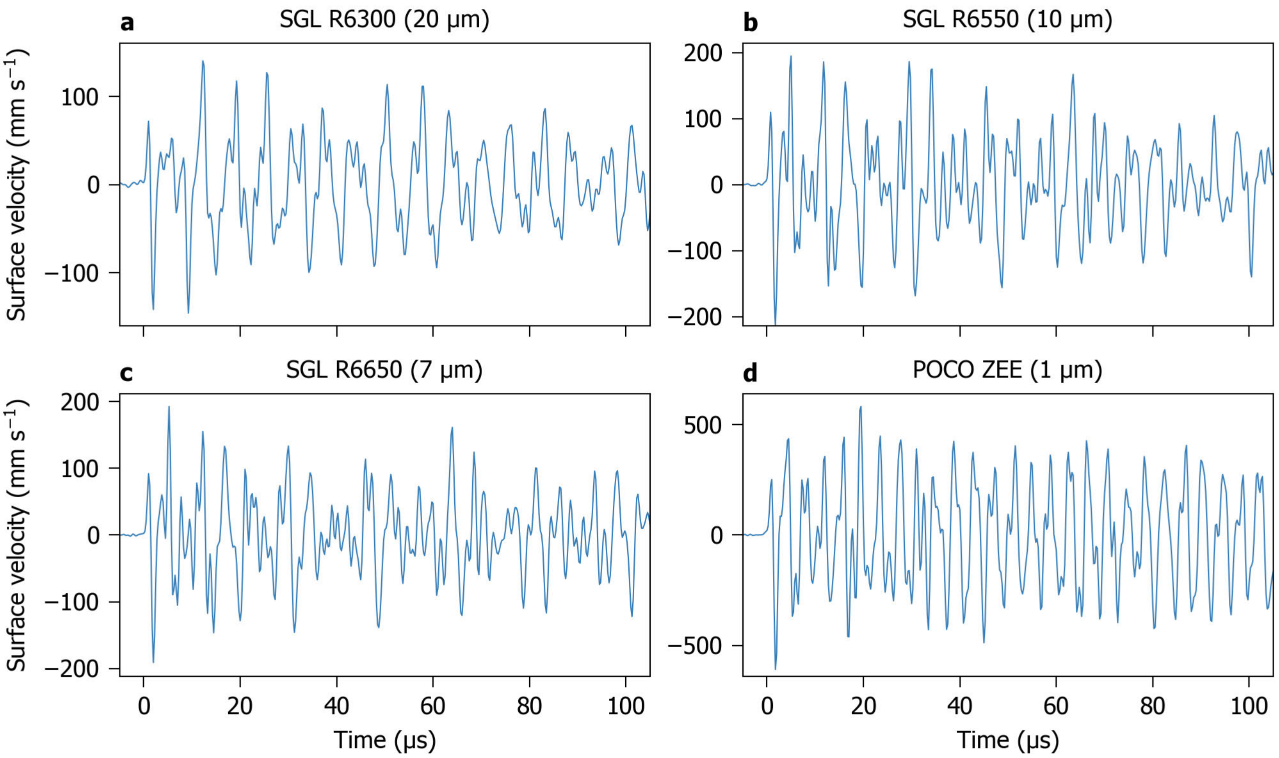

Figure 11.5.: Detailed overview of the dynamic response of different isotropic polycrystalline graphite samples after irradiation with 4.3×10^{12} ppp 440 GeV/c proton beams (0.9 µs pulse length) with a transverse beam size of $\sigma_{x,y} \sim 0.3$ mm. Radial surface velocity measured by a laser Doppler vibrometer in the center of SGL R6300 (a), SGL R6550 (b), SGL R6650 (c) and POCO ZEE (d). Particle sizes according to the supplier are given in parentheses.

All four samples were exposed to the same specific energy deposition of about $\sim 0.2\,\mathrm{kJ\,g^{-1}}$ (c.f. Figure 11.3). The magnitude of the absolute radial surface velocity is therefore scaling linearly with the coefficient of thermal expansion. Considering the coefficient of thermal expansion (CTE) at room temperature (c.f. Table 11.1) the measured surface velocities are in excellent agreement with the relative CTEs of the different sample materials. POCO ZEE with the highest CTE has the largest radial surface velocity of about $\pm 500\,\mathrm{mm\,s^{-1}}$. SGL R6550 and SGL R6650 (about half the CTE of POCO ZEE) have a radial surface velocity of about $\pm 200\,\mathrm{mm\,s^{-1}}$ and SGL R6300 (CTE is about a quarter of POCO ZEE) has about $\pm 125\,\mathrm{mm\,s^{-1}}$. This indicates that the beam-induced stresses are fully elastic at this beam intensity.

While the CTE scales inversely with the particle size in isotropic graphite [262] (CTE increases with decreasing particle size), Figure 11.4 indicates a correlation between damping of the dynamic response and the particle size as well. Under the assumption of a fully elastic dynamic response, beam-induced stress waves are only damped by internal friction. The dynamic response can hence be approximated by a damped harmonic oscillation with various frequency components and is quantified with an exponential decay that is fit to the local maxima of the absolute surface velocity. Thermalization of the samples, which leads to vanishing of the beam-induced thermal stresses (due to the thermal gradient in the samples), starts at timescales of about 100 µs but significant thermal diffusion will only occur after ∼1 ms (c.f. Figure 9.4). SGL R6300 and SGL R6550 with 20 and 10 µm particle size, respectively, have damping time constants τ_D of ∼200 µs, which is comparable to SGL R6650 (7 µm particle size) with a damping constant of (258 ± 13) µs. POCO ZEE (1 µm particle size) on the other hand exhibits less efficient damping with a larger damping constant of (610 ± 19) µs.

The dynamic response presented in Figure 11.4 is shown in Figure 11.5 for the first 100 µs after the beam pulse. The dynamic response of the samples is systematically characterized by an initial positive peak of the radial surface velocity (the surface is moving towards the LDV) and then a larger negative peak (surface is moving away from the LDV). As the samples are instantaneously heated in the interaction with the high-power beam pulse, the heated volume is in a compressive stress state because the surrounding material cannot react fast enough due to inertia.

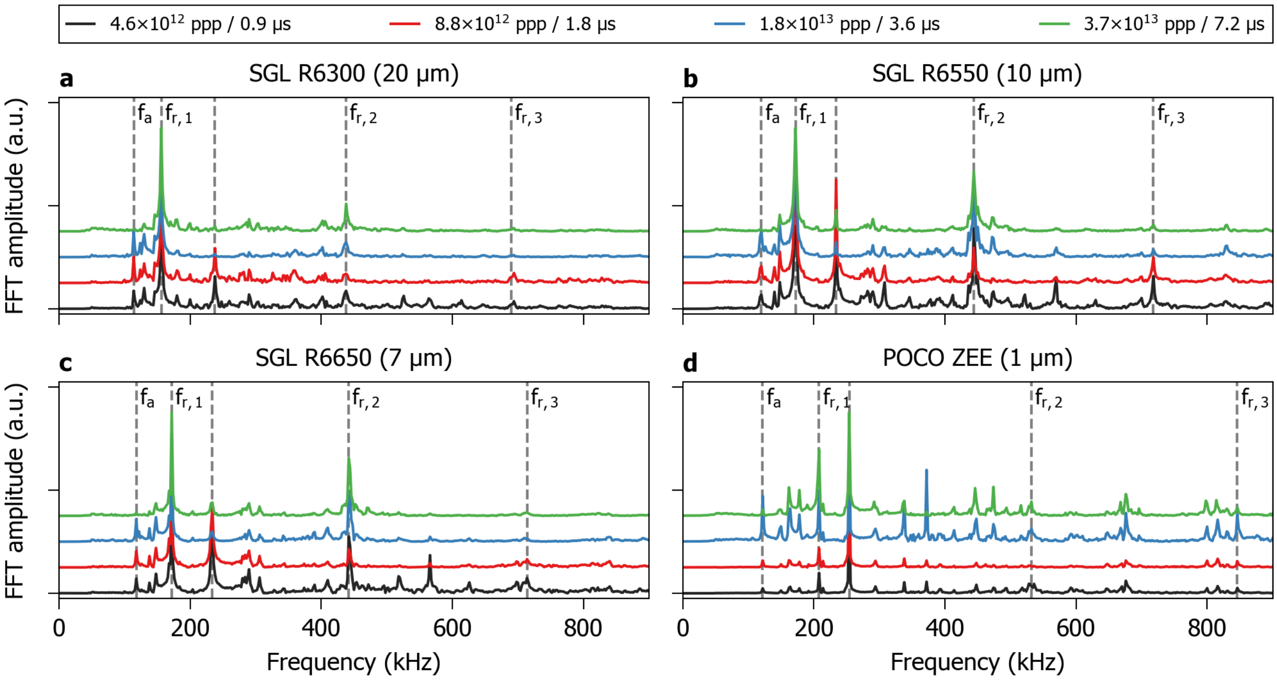

Figure 11.6.: Self-normalized fast Fourier transform amplitude of the dynamic response for different isotropic polycrystalline graphite samples after irradiation with individual 440 GeV/c proton beam pulses of increasing intensities (transverse beam size $\sigma_{x,y}$~0.3 mm). Fourier transform of the radial surface velocity measured by a laser Doppler vibrometer in the center of SGL R6300 (a), SGL R6550 (b), SGL R6650 (c) and POCO ZEE (d). Particle sizes according to the supplier are given in parentheses. Fourier transform spectra are shifted vertically for clarity. Dashed lines indicate different experimental axial f_a and i-th order radial vibration frequencies $f_{\mathrm{r},i}$.

The compressive stress state induces compressive relaxation waves that travel outwards along the radius. Once these compressive waves reach the free surface of the samples, they are reflected as tensile waves that lead to an expansion of the sample. Qualitatively, it can simply be described by an internal pressure that is acting on the surfaces of the sample which is initially negative (compression of the sample) and is then oscillating between negative and positive pressure (expansion of the sample).

Section 9.2 introduced that the beam-induced dynamic response is akin to a mechanical shock. Due to the short length of the beam pulse and thus the thermal energy deposition length, samples start to vibrate at their natural vibration frequencies. Hence, the frequency content of the dynamic response is a convolution of multiple frequencies. The simplest vibration modes are purely axial vibration (the sample is expanding and contracting along the cylinder axis) and purely radial vibration (the sample is expanding and contracting along the radius of the cylinder). But, due to the coupling of radial and axial stresses by the Poisson effect, the measured radial surface velocity does not only contain information about purely radial vibrations but also of axial vibrations.

Figure 11.6 shows the normalized Fourier transform spectra of the radial surface velocity for 200 µs after the beam pulse for the isotropic graphite samples at different beam intensities. The dynamic response of all samples contains a large number of frequencies in the range between 150 and 900 kHz while the dominating frequencies are located systematically below ~250 kHz. No considerable differences between the Fourier spectra can be identified in any of the samples at the different beam intensities. Due to the brittleness of polycrystalline graphite, (brittle) failure produces an internal interface that would dramatically change the frequency response in both amplitude and frequency [250]. Hence, the FFT spectra indicate that the beam-induced stresses in the polycrystalline graphite samples are elastic, even at the highest beam intensity of the experiment.

The frequencies f of axial f_a and radial f_r vibration modes are calculated using Equation 9.31 and 9.29, respectively. Expected frequencies were calculated based on the Young's modulus E provided by the supplier. A generic Poisson's ratio $\nu = 0.18$ was used that should be valid for isotropic graphite [250, 263]. The comparison between

Table 11.2.: Axial f_a and i-th order radial $f_{\mathrm{r},i}$ vibration frequencies in polycrystalline graphite samples ($R = 5\,\mathrm{mm}$, $L = 10\,\mathrm{mm}$). Frequencies in the rows indicated by "Supplier" were calculated using Equations 9.31 and 9.29 with the Young's modulus E provided by the supplier. Frequencies in the rows indicated by "Exp." were experimentally observed in the FFT and CWT of the dynamic response of the samples and E and Poisson's ratio ν were extracted in a parametric fit of Equations 9.31 and 9.29 to these equations. Frequencies in the rows indicated by "FEM" are observed in the FFT of the dynamic response simulated with ANSYS Mechanical using the given E and ν. In rows indicated by "Modal", frequencies correspond to modes with axisymmetric total deformation simulated by modal analysis. Experimental frequencies have a systematic error of ±2 kHz and FEM frequencies ±5 kHz.

		E (GPa)	ν	f_a (kHz)	$f_\mathrm{r}, 1$ f(kHz)	$f_\mathrm{r}, 2$ (kHz)	$f_\mathrm{r}, 3$ (kHz)
SGL R6300 20 µm, $1.73\,\mathrm{g\,cm^{-3}}$	Supplier	10	0.18	120	159	429	683
	Exp.	(10.14±0.66)	(0.194±0.047)	114	156	438	686
SGL R6550 10 µm, $1.83\,\mathrm{g\,cm^{-3}}$	Supplier	11.5	0.18	125	166	447	712
	Exp.	(10.86±0.70)	(0.231±0.038)	120	172	444	718
SGL R6650 7 µm, $1.84\,\mathrm{g\,cm^{-3}}$	Supplier	12.5	0.18	130	173	465	740
	Exp.	(10.77±0.70)	(0.233±0.038)	118	172	442	714
	FEM	11.38	0.186	120	170	435	
	Modal			117	176	450	
POCO ZEE 1 µm, $1.77\,\mathrm{g\,cm^{-3}}$	Supplier	14.5	0.18	143	190	510	813
	Exp.	(10.83±0.82)	(0.339±0.018)	122	208	532	(789-846)
	FEM	12.7	0.28	125	205	525	825
	Modal			123	188	529	

calculated and experimentally observed axial and radial vibration frequencies is shown in Table 11.2. Experimental frequencies were systematically observed within a ±2 kHz interval in all Fourier spectra, independent of beam intensity. The amplitude at these frequencies was at least 5 % relative to the maximum amplitude in the Fourier spectrum.

Frequencies of the axial vibration mode are systematically larger than the frequencies observed experimentally. The largest difference is observed for POCO ZEE, where the expected axial vibration frequency is 143 kHz, while the experimental axial vibration frequency is (122 ± 2) kHz. The experimental frequencies of SGL R6550 and SGL R6650 are virtually identical, even though the manufacturer indicates a 10 % larger E in R6650.

After identifying the axial and vibrational frequencies in the Fourier spectra, the set of experimental frequencies can be plugged into Equation 9.31 and Equation 9.29 to extract the Young's modulus and Poisson's ratio from a parametric fit. The extracted Young's modulus and Poisson's ratio are presented in Table 11.2 as well. According to the parametric fit, all polycrystalline graphite samples have a virtually identical Young's modulus. Estimated Young's moduli vary between (10.14 ± 0.66) and (10.83 ± 0.83) GPa. Poissons's ratios of the SGL Carbon polycrystalline graphite grades are virtually identical with values of (0.233 ± 0.038) and (0.194 ± 0.047), and are in reasonable agreement with the generic Poisson's ratio of 0.18 for isotropic graphite [263]. Only POCO ZEE has a considerably larger Poisson's ratio of (0.339 ± 0.018).

Based on the Fourier spectra alone, association of a peak to a certain vibration mode is ambiguous. As will be shown in section 11.2.2, Young's modulus and Poisson's ratio can be extracted from a parameter scan of finite-element simulations of the dynamic response and a modal analysis of the sample geometry. Using this approach, a Young's modulus of 11.38 GPa and Poisson's ratio of 0.186 were estimated for SGL Carbon R6650 and 12.7 GPa and 0.28 for POCO ZEE, respectively, which are overall in good agreement with the experiment.

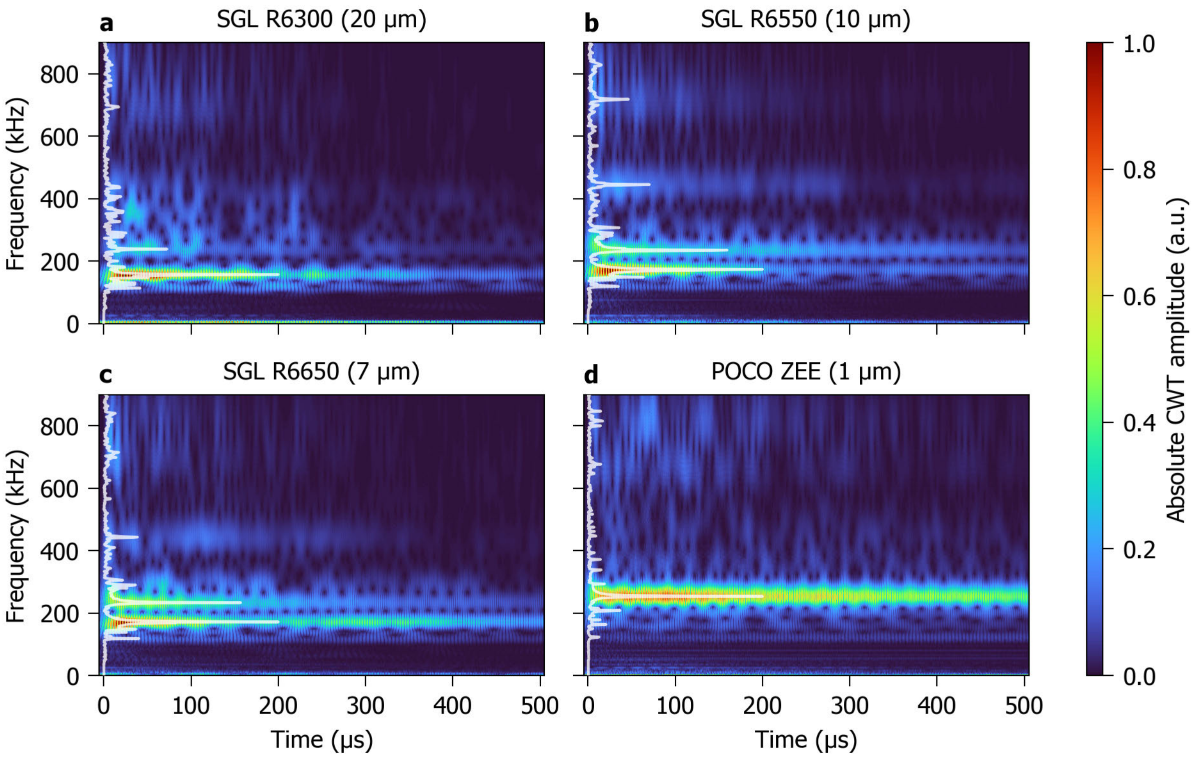

Figure 11.7.: Self-normalized absolute continuous wavelet transform. Heatmap of the CWT of the radial surface velocity for 500 µs after irradiation with ~8.6 × 10^{12} ppp 440 GeV/c proton beams (1.8 µs pulse length). Heatmap of the CWT of SGL R6300 (a), SGL R6550 (b), SGL R6650 (c) and POCO ZEE (d). Particle sizes according to the supplier are given in parentheses. Self-normalized Fourier transform spectra of the radial surface velocity are overlayed on top of the data for comparison (c.f. Figure 11.6).

Now that the dominant frequencies and associated vibration modes of the dynamic response are identified, damping of these vibration modes can be determined quantitatively. The Fourier transform of the signal contains no time information of the original signal. But, damping can be determined from the time evolution of the continuous wavelet transform (CWT) amplitude at any given frequency f_i. The self-normalized absolute CWT of the dynamic response for the isotropic graphite samples after irradiation with ~8.6 × 10^{12} ppp proton beams (1.8 µs pulse length) is shown in Figure 11.7. The FFT spectra from Figure 11.6 are overlayed for comparison.

It is expected that damping is larger at higher frequencies. The total energy of a harmonic oscillator is the sum of kinetic and potential energy which is continuously converted from one to the other with frequency f. The equivalent for an elastic wave is the conversion of kinetic energy (proportional to the strain rate) to strain energy (proportional to the displacement) of a mass element. Hence, any small losses in the conversion between kinetic and strain energy of the elastic wave will be multiplied by its frequency. Figure 11.7 shows that this is indeed true in all of the polycrystalline graphite samples. In SGL R6550 for example (c.f. Figure 11.7b) , the CWT amplitude of the third radial vibration mode at 718 kHz is damped within ~200 µs, while the second vibration mode at 444 kHz is damped within ~300 µs.

The damping time constant $\tau_{\mathrm{D},i}$ at frequency f_i is determined by fitting an exponential decay function into the absolute maxima of the CWT amplitude for time $t > 0$ after the beam pulse (c.f. Figure B.9). Overall damping is determined in the same way using the (absolute) maxima of the radial surface velocity (c.f. Figure 11.4). The resulting damping time constants of the different polycrystalline graphite samples are shown as a function of frequency for all beam intensities in Figure 11.8. In-line with expectation, the damping time constant decreases nearly linearly with increasing frequency except for a single outlier of SGL R6550 at ~230 kHz (Figure 11.8b). There might be a correlation between particle size and damping constant in the different polycrystalline graphite grades. Considering the main vibration modes with the largest amplitudes, τ_D is virtually identical between SGL R6300 and SGL R6550 with 20 and 10 µm particle size at around 340 µs. For SGL R6650 and POCO ZEE with particle sizes of 7 and 1 µm τ_D increases to (536 ± 41) µs and (843 ± 37) µs, respectively.

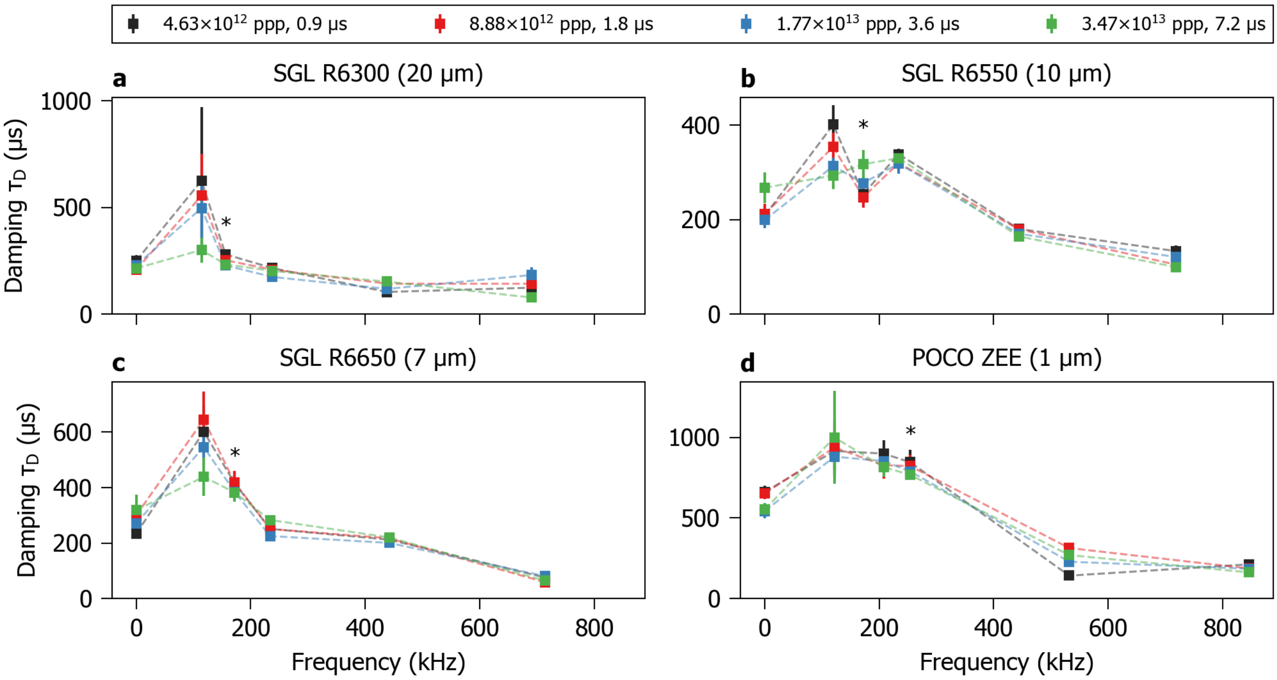

Figure 11.8.: Damping time constant τ_D as a function of frequency. τ_D has been obtained from an exponential decay fit of the local maxima of the absolute CWT at frequency f for SGL R6300 (a), SGL R6550 (b), SGL R6650 (c) and POCO ZEE (d). Damping time constant at zero frequency indicates the damping of the overall signal. Particle sizes according to the supplier are given in parentheses. * indicate the frequency with the largest amplitude in the Fourier spectrum of the dynamic response shown in Figure 11.6.

It is counter-intuitive that the graphite grades with smaller particle sizes damp stress waves less efficiently than graphite grades with larger particle sizes. It was expected that smaller particles sizes lead to more dissipation of the stress waves due to the increased number of interfaces that can act as scatterers. However, one has to consider that the particle sizes are considerably smaller than the wavelength of the elastic waves. An elastic wave of 500 kHz frequency has a wavelength of ~5 mm in graphite (speed of sound in polycrystalline graphite is ~2500 $\mathrm{m\,s^{-1}}$). The scattering and reflection at the free surfaces of the samples might hence determine the damping efficiency, which should be roughly equal for all samples in this case.

But, there is a potential explanation for the large difference in damping between POCO ZEE and the SGL Carbon polycrystalline graphites. POCO ZEE is produced without a binder phase (c.f. section B.1), whereas SGL Carbon polycrystalline graphite grades are produced with a binder phase based on phenolic resin. Micro-mechanical characterization of nuclear graphite grades indicates differences in the Young's modulus and density between the binder and filler phase [264]. The different mechanical properties between the two phases will create an acoustic impedance mismatch which will locally dissipate elastic waves by continuous reflection of a fraction of the amplitude of these waves [265].

Lastly, variance-weighted means of the damping time constants for the different axial and radial vibration modes are shown in Table 11.3 and will be used as an input for Rayleigh damping in FE simulations shown in section 11.2.2.

Table 11.3.: Damping time constant $\tau_{\mathrm{D},i}$ at different frequencies f_i in isotropic graphite determined by continuous wavelet transformation. Values are averaged over all beam intensities as variance-weighted means and errors are the standard error. f_a and $f_{r,i}$ correspond to axial and radial vibration modes, respectively. $f_{a,har}$ indicates an overtone of the axial vibration mode. * indicates the damping of the frequency with the highest amplitude in the Fourier spectra of a sample. Frequencies of these modes are given in Table 11.2. The value at zero frequency corresponds to the damping time constant of the measured LDV signal.

	$\tau_\mathrm{D}(0)$ (µs)	$\tau_\mathrm{D}(f_\mathrm{a})$ (µs)	$\tau_\mathrm{D}(f_{\mathrm{r},1})$ (µs)	$\tau_\mathrm{D}(f_{\mathrm{a,\,har.}})$ (µs)	$\tau_\mathrm{D}(f_{\mathrm{r},2})$ (µs)	$\tau_\mathrm{D}(f_{\mathrm{r},3})$ (µs)
SGL R6300 (20 μm)	(222±11)	(351±52)	(238±7)*	(203±9)	(122±4)	(114±6)
SGL R6550 (10 μm)	(211±10)	(326±13)	(268±13)*	(327±7)	(174±5)	(108±4)
SGL R6650 (7 μm)	(258±13)	(536±41)	(394±17)*	(248±5)	(210±8)	(69±3)
POCO ZEE (1 μm)	(610±19)	(913±73)	(843±37)	(783±14)*	(183±7)	(186±9)

11.2.2 Finite Element Simulation of Isotropic Samples

Analysis of the dynamic response for the isotropic polycrystalline graphite samples showed that the beam-induced stresses in these samples are most probably entirely elastic for all beam intensities in the experiment. Hence, it is possible to simulate the dynamic response in a coupled thermo-mechanical FEM simulation where stresses depend linearly on the strain with the Young's modulus as gradient and where plastic deformation can be neglected.

The deposited energy density per volume element is estimated with a Monte Carlo simulation of the interaction between the proton beam and the irradiated sample in FLUKA [254]. Both the measured transverse beam spot size in horizontal and vertical direction, assuming a bivariate distribution with two parameters σ_x and σ_y, and eccentricity Δx and Δy of the beamspot with respect to the cylinder axis of the samples are considered for a specific beam pulse (c.f. Figure 11.2).

Assuming that the deposited energy density is fully converted into heat, beam-induced heating is introduced as an internal heat source (interpolated to each mesh point) that is active from $t = 0\,\mathrm{s}$ for the duration of the beam pulse length τ_beam. For a given energy density per proton $\Delta E/\Delta V$ the power density $P/\Delta V$ for a beam pulse of intensity I_beam and pulse length τ_pulse can be directly calculated at each position (x_i, y_i) in the sample:

$$\left(\frac{P}{\Delta V}\right)(x_i, y_i) = \frac{I_\mathrm{beam}}{\tau_\mathrm{pulse}}\left(\frac{\Delta E}{\Delta V}\right)(x_i, y_i). \tag{11.2}$$

In the first step, a transient thermal simulation is solving the thermal evolution of each mesh point. In a second simulation step, the thermal field is coupled to a transient structural simulation which calculates displacements of each mesh point according to the thermal strain induced by $\alpha\Delta T$. Choosing a sufficiently small timestep, e.g., $\Delta t = 100\,\mathrm{ns}$, will reproduce a comparable dynamic response of the samples as observed in the experiment. A thorough overview on how to implement such simulations in ANSYS Mechanical is presented in section B.4.

Damping is introduced in the simulation using Rayleigh damping. Mass damping is neglected due to the high frequency of the dynamic response, hence only stiffness damping due to internal friction is considered by its coefficient β:

$$\beta = \frac{2}{\tau_\mathrm{D}(2\pi f_D)^2}, \tag{11.3}$$

where f_D is the frequency with the highest amplitude in the Fourier spectrum of the experimental dynamic response (c.f. Figure 11.15 and Table 11.2) and τ_D is the associated damping time constant (c.f. Table 11.3). The following FEM simulations in ANSYS workbench were performed in the scope of a master's thesis under supervision of the author [266]. All simulations use temperature-dependent specific heat values, while all other thermo-mechanical parameters are temperature independent.

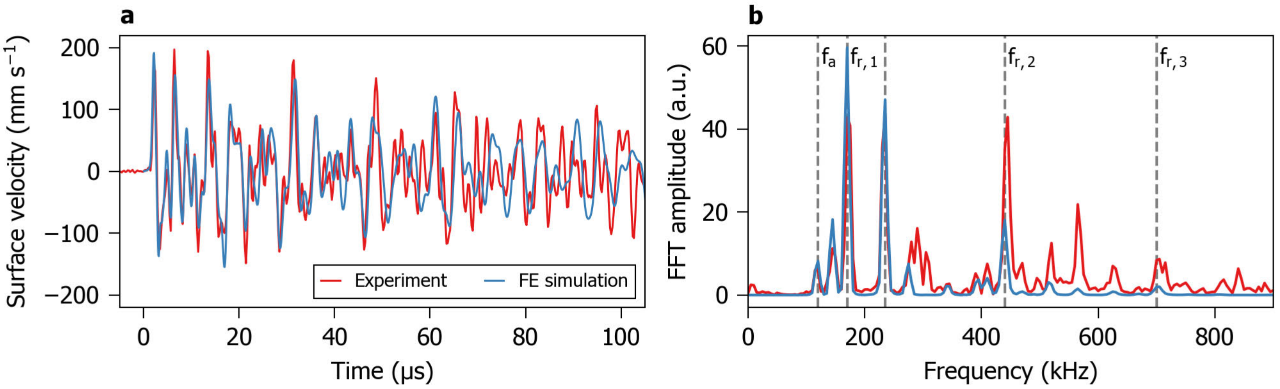

Figure 11.9.: Beam-induced dynamic response from experiment (red) and FE simulation (blue) for a SGL Carbon R6650 sample irradiated with a 4.53×10^{12} ppp 440 GeV/c proton beam (0.9 µs pulse length). Radial surface velocity as a function of time (a). Fourier transform of the radial surface velocity for 200 µs after the beam pulse (b). Dashed vertical lines indicate axial, f_a and radial vibration modes with frequencies $f_{r,i}$ that are presented in Table 11.2.

11.2.2.1 Polycrystalline Graphite, SGL Carbon R6650

Figure 11.9 shows the result of a coupled thermo-mechanical finite-element (FE) simulation of SGL Carbon R6650 irradiated with 4.53×10^{12} ppp 440 GeV/c protons (0.9 µs pulse length). Radial surface velocity of the FE simulation is evaluated at the mesh point that is in the center along the length of the cylinder axis at $z = L/2$, on the surface at $x = R$ and vertically in the center at $y = 0$. Rayleigh damping was included with a damping time constant of 394 µs at a frequency of 172 kHz. For this simulation, the coefficient of thermal expansion was introduced as a temperature-dependent magnitude measured by dilatometry [260].

The simulated and experimental radial surface velocity are in excellent agreement as shown in Figure 11.9a. The simulation is able to replicate the maximum (absolute) surface velocity within a few percent over a time scale of 100 µs. Qualitatively, the frequency content is well-matched and the overlap of the surface velocity peaks is not drifting (in time). This is also indicated by the comparison of the Fourier spectra of experiment and simulation shown in Figure 11.9b. Frequencies of the axial and radial vibration modes are well in agreement. But, the simulation overestimates the Fourier transform amplitude by about 50 % for the first radial vibration mode at $f_{r,1} = 172$ kHz and underestimates the amplitude of the second radial vibration mode at $f_{r,2} = 444$ kHz by about 50 %.

The continuous wavelet transform (CWT) shown in Figure 11.10 indicates excellent agreement of the frequency content of the dynamic response between experiment and simulation. Even the amplitude modulation of the axial vibration mode is replicated. Due to a finite energy deposition length by the beam τ_{beam}, elastic stress waves are generated during the entire pulse length and the continuous interference of these waves leads to an amplitude modulation. But, damping of the higher order radial vibration modes is considerably overestimated by the simulation. The radial vibration mode at 444 kHz can be clearly identified in the CWT of the experiment beyond 100 µs, whereas in the simulation, the signal is almost entirely damped within 150 µs (c.f. Figure 11.10a and b).

The Young's modulus E and Poisson's ratio ν, that were used for this simulation, were determined in a parameter scan of the simulation for different combinations of E in the range from 10 to 20 GPa and ν from 0.1 to 0.3. The best convergence between experiment and simulation was found for a Young's modulus of 11.38 GPa and Poisson's ratio of 0.186. This was also confirmed by a modal analysis of the sample geometry using these material parameters. Modal analysis predicted fundamental axisymmetric vibration modes at frequencies that are in reasonable agreement with the dominant frequency contributions observed in the simulation and experiment as indicated in Table 11.2. The extremal cases of the total deformation of these vibration modes are shown in Figure 11.17. The Young's modulus and Poisson's ratio determined by the parametric simulations are in reasonable agreement with the values directly extracted from the dynamic response measured in the experiment, (10.77 ± 0.70) GPa and (0.233 ± 0.038), respectively. Lastly, it should be noted that the supplier apparently overestimates the Young's modulus of this material grade.

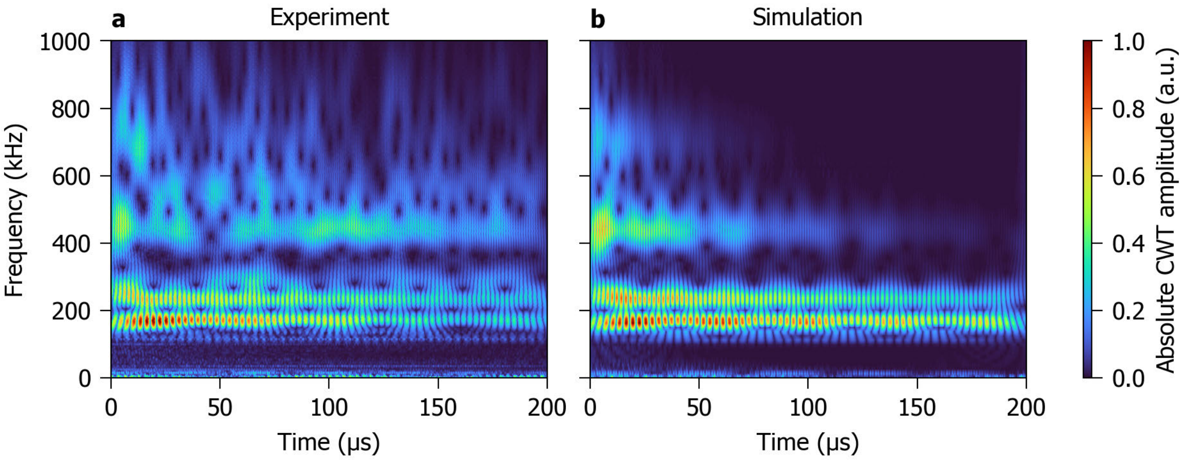

Figure 11.10.: Continuous wavelet transform (CWT) of the radial surface velocity of the SGL Carbon R6650 sample irradiated with a 4.53×10^{12} ppp 440 GeV/c proton beam (0.9 µs pulse length). Heatmap of the absolute CWT of the radial surface velocity measured experimentally (a) and of a FE simulation (b). The input signals for the continuous wavelet transformation are shown in Figure 11.9.

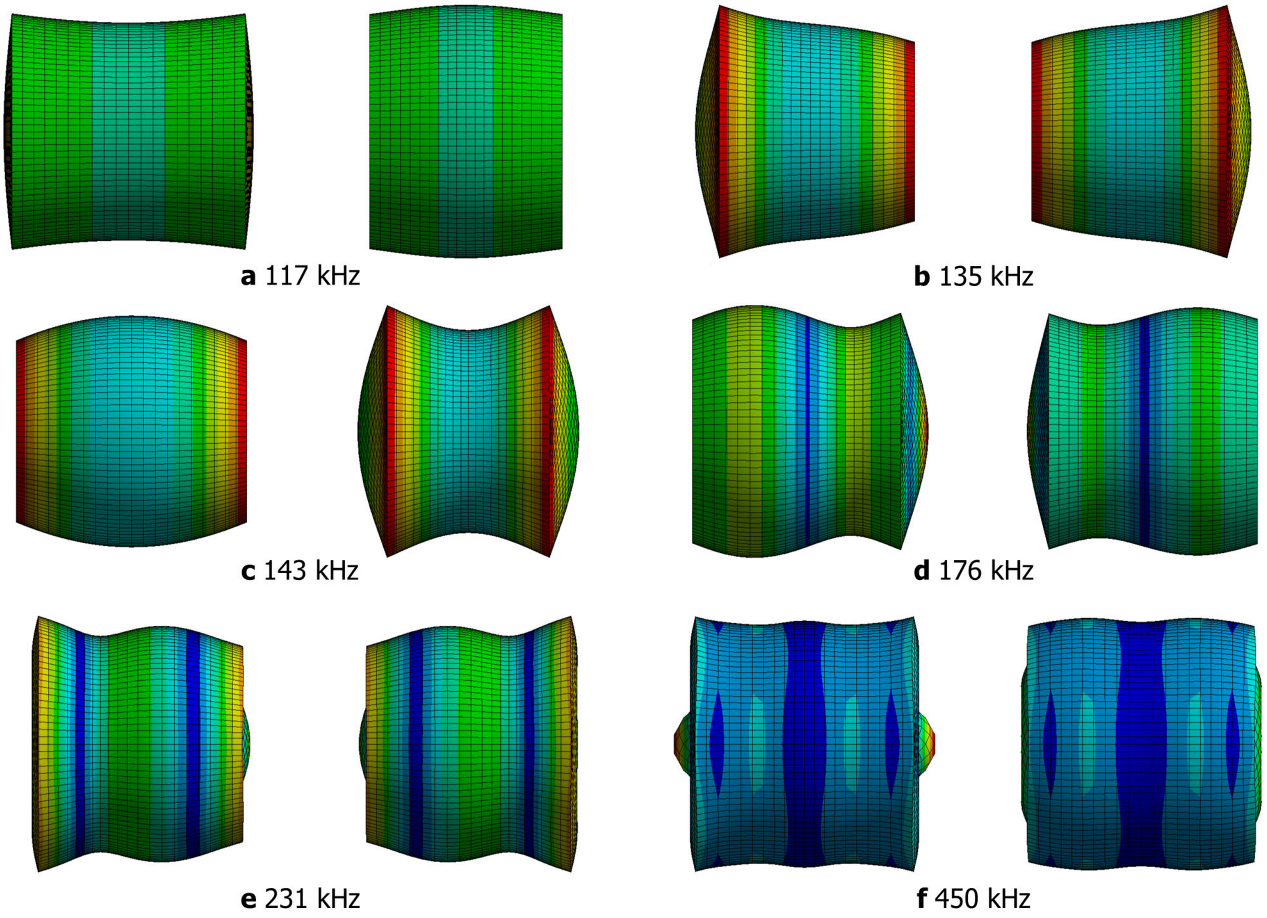

a 117 kHz **b** 135 kHz **c** 143 kHz **d** 176 kHz **e** 231 kHz **f** 450 kHz

Figure 11.11.: Modal analysis of the sample geometry with mechanical properties of SGL R6650. Extremal cases of the total deformation of different fundamental vibration modes. Blue indicates negative displacement of the mesh point from its original position, while red indicates positive displacement. (Anti-phase) Axial vibration mode with f_a (a), in-phase axial vibration mode (b), 143 kHz vibration mode (c), first radial vibration mode $f_{\mathrm{r},1}$ (d), in-phase axial vibration harmonic mode $f_{\mathrm{a,\,har.}}$ (e), second radial vibration mode $f_{\mathrm{r},2}$ (f). Length and diameter of the cylinders are 10 mm.

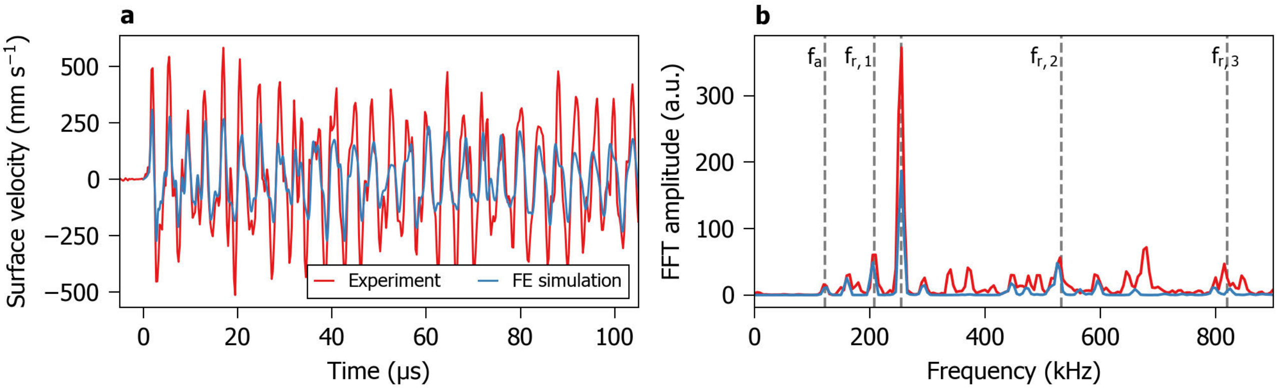

Figure 11.12.: Beam-induced dynamic response from experiment (red) and FE simulation (blue) for a POCO ZEE sample irradiated with a 4.53 × 10^{12} ppp 440 GeV/c proton beam (0.9 µs pulse length). Radial surface velocity as a function of time (a). Fourier transform of the radial surface velocity for 200 µs after the beam pulse (b). Dashed vertical lines indicate axial, f_a and radial vibration modes with frequencies $f_{r,i}$ that are presented in Table 11.2.

11.2.2.2 Polycrystalline Graphite, POCO ZEE

Another polycrystalline graphite, POCO ZEE, was simulated in a series of parametric thermo-mechanical simulations. The best estimate simulation in comparison to the experiment is shown in Figure 11.12 for irradiation with 4.63 × 10^{12} ppp 440 GeV/c proton beams (0.9 µs pulse length). Rayleigh damping was implemented in the simulation with a damping constant of 783 µs at 254 kHz. Figure 11.12a shows that the maximum surface velocities of the dynamic response are underestimated by the simulation. Since the radial surface velocity is sensitive to the coefficient of thermal expansion, a more precise simulation requires a temperature-dependent coefficient of thermal expansion. The Fourier spectrum, shown in Figure 11.12b, between simulation and experiment match up well. The relative amplitude of the different vibration modes is in excellent agreement, which indicates that the damping is well replicated in this simulation.

Figure 11.13 shows the CWT of the dynamic response of the experiment and the simulation. The time evolution of the CWT amplitudes below 400 kHz are well in agreement between experiment and simulation. The parametric simulations yield a best-estimate Young's modulus and Poisson's ratio of 12.7 GPa and 0.280, respectively. In comparison, Young's modulus and Poisson's ratio directly extracted from the experimental data are (10.83 ± 0.82) GPa and (0.339 ± 0.018), respectively. But, comparison with modal analysis has shown vibration modes at $f_{\mathrm{a}}=123$, $f_{\mathrm{r},1}=188$ and $f_{\mathrm{r},2}=529$ kHz with identical extremal deformation cases to the modal analysis shown in Figure 11.11. Hence, the estimate of the simulation for the Young's modulus and Poisson's ratio is reasonable.

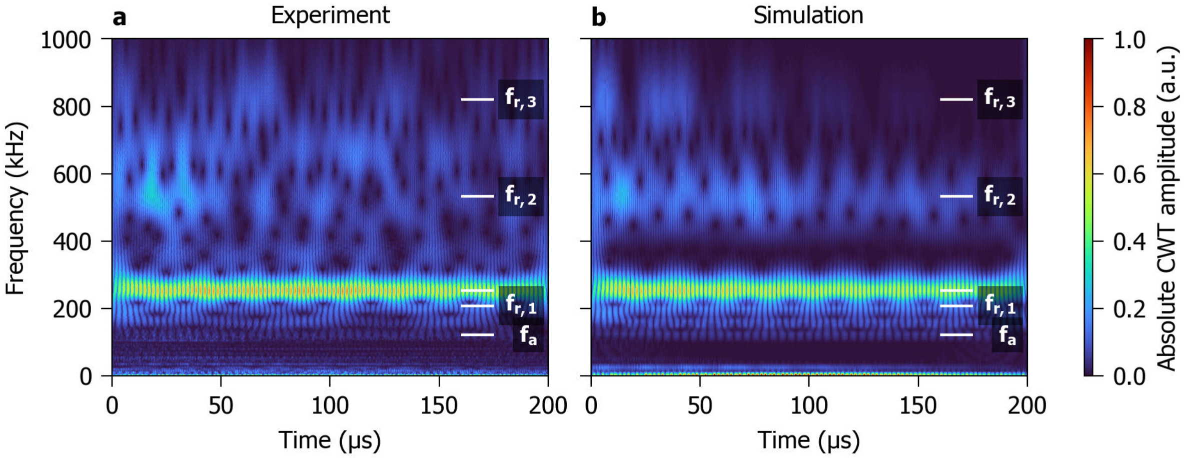

Figure 11.13.: Continuous wavelet transform (CWT) of the radial surface velocity of the POCO ZEE sample irradiated with a 4.53×10^{12} ppp 440 GeV/c proton beam (0.9 μs pulse length). Heatmap of the absolute CWT of the radial surface velocity measured experimentally (a) and of a FE simulation (b). The input signals for the continuous wavelet transformation are shown in Figure 11.12.

11.3 Dynamic Response of Tantalum-Core/Graphite Shell Samples

To check the response of graphite under larger stress loads, target station 6 contained graphite samples with a 3 mm tantalum core. The following section will present selected experimental results together with the Fourier and continuous wavelet transform with the aim of illustrating the general behavior and specific differences observed in the different materials.

Effects will be discussed in the context of different beam conditions including (i) low intensity pulses of $\sim 1 \times 10^{11}$ ppp (pulse length of 25 ns), where the response of all samples is expected to be in the elastic regime; (ii) medium intensity pulses of $\sim 6 \times 10^{11}$ ppp (300 ns) where the beam could have induced failure in several samples and (iii) high intensity pulses of at least $\sim 1.2 \times 10^{12}$ ppp (600 ns) which lead to significant changes of the dynamic response in all samples.

Materials of focus are SGL R6650 (samples #1 and #6, that are exposed to different levels of deposited energy density) and POCO ZEE (sample #3). SGL R6300 (sample #2) and SGL Premium (#5) are not shown in detail, because they show a similar behavior in comparison to SGL R6650 and SGL Premium PyC, respectively (c.f. Table 10.2). Samples comprising expanded graphite (sample #8 and #9) are also not discussed, as their complex structure leads to a complex response that is not understood.

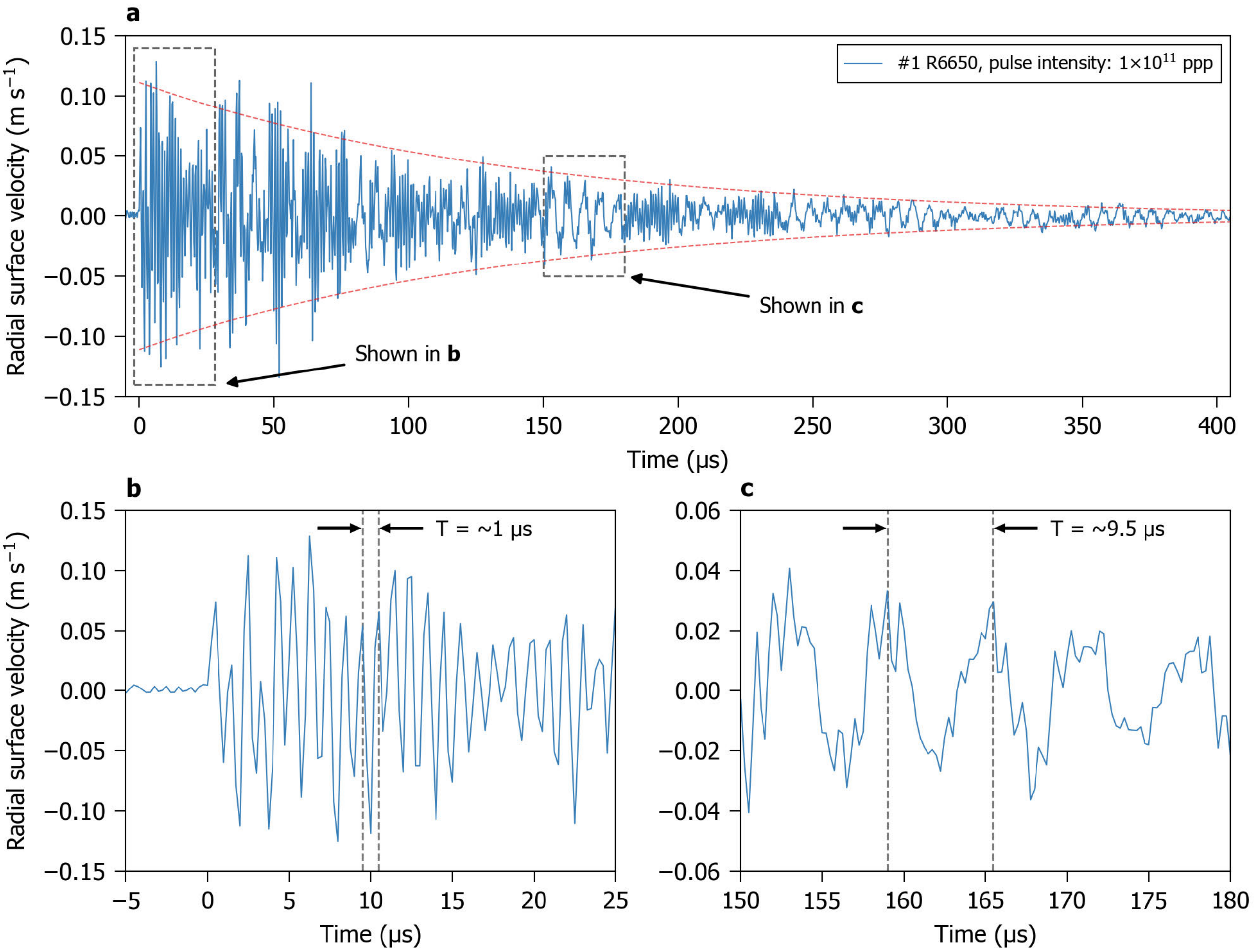

Figure 11.14.: Radial surface velocity of sample #1 R6650 after irradiation with a 1×10^{11} ppp 440 GeV/c proton beam (25 ns pulse length). Dynamic response within the first 400 µs (a). Response within the first 25 µs (b). Response between 150 and 180 µs (c). The dashed red lines represent a guide to the eye for the damping envelope.

Figure 11.14 shows the radial surface velocity measured by the LDV on sample #1 Ta/SGL R6650 at a pulse intensity of 1×10^{11} ppp (25 ns pulse length). The dynamic response is damped within ~0.4 ms to a large extend. This damping rate is orders of magnitudes faster than the damping observed in pure tantalum. Torregrosa *et al.* reported damping in pure tantalum, irradiated with a similar pulse intensity and transverse beam size, on the order of several tens of milliseconds [267]. The graphite shell surrounding the tantalum core is efficiently damping the dynamic response. The observed damping is in agreement with the damping observed on the pure graphite samples (c.f. Figure 11.4). Hence, the damping of the tantalum/graphite samples is largely dominated by the graphite.

Two distinct frequency components, a high frequency component with a period of ~1 μs (~1000 kHz) and a low frequency component of ~9.5 μs (~105 kHz), can be identified in the radial surface velocity signal (cf. Figure 11.14a and b). The high frequency component is attributed to the radial pressure wave in the tantalum core, while the low frequency component is emerging due to the axial pressure wave in the tantalum core and graphite shell. Under the assumption that equation Equation 9.31 can be applied to a two-body cylinder, the calculated axial pressure wave frequencies ($L = 10\,\mathrm{mm}$) are 167 kHz (period of ~6 μs) in the tantalum core ($E = 187\,\mathrm{GPa}$, $\rho = 16.6\,\mathrm{g\,cm^{-3}}$) and 125 kHz (~8 μs) in the graphite shell ($E = 12.5\,\mathrm{GPa}$, $\rho = 1.83\,\mathrm{g\,cm^{-3}}$, c.f. Table 11.2).

Predicting a radial wave period for the entire core-shell sample consisting of tantalum and graphite is non-trivial. But, since the energy deposition occurs mainly in the tantalum core, the frequency of the radial pressure wave within the tantalum core can be approximated with Equation 9.29. The calculated radial pressure wave frequency is 987 kHz (~1 μs) in the tantalum core ($R = 3\,\mathrm{mm}$). It should be stressed that although these frequencies were calculated for isotropic cylinders, the magnitude of frequencies agrees well with the experimental results. An earlier irradiation experiment by Torregrosa *et al.* has also shown the propagation of the radial pressure wave emerging from a tantalum core through a graphite matrix [268]. The dis- and re-appearance of the radial wave (compare the velocity trend prior to and after 150 μs in Figure 11.14c) can be attributed to the emergence of multiple radial wave frequencies. The non-uniform deposited energy density along the axis (cf. Figure 11.3d) and finite pulse length lead to an amplitude-modulated wave. Similar amplitude-modulation is observed in the bare graphite samples as well (c.f. Figure 11.22), albeit at frequencies below 300 kHz.

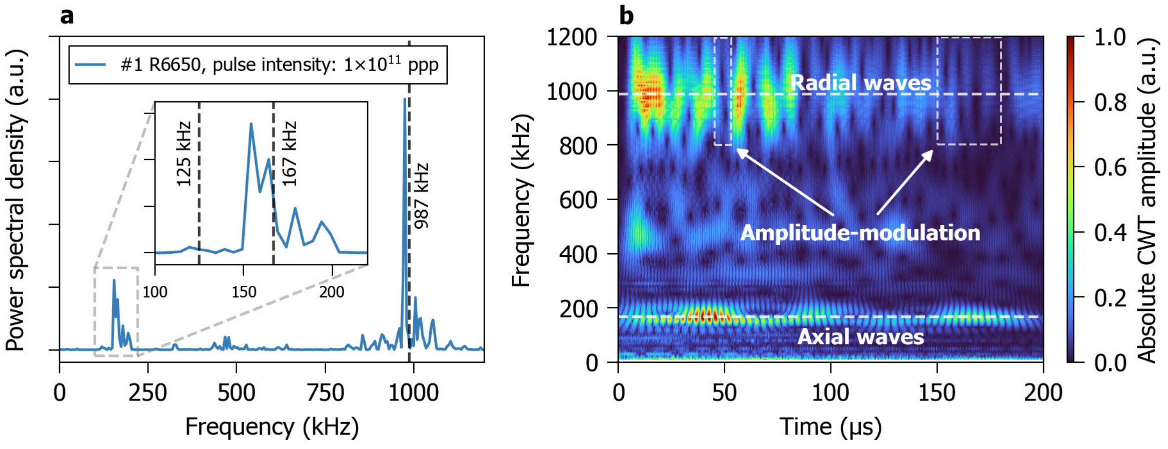

Figure 11.15.: Frequency analysis of the dynamic response of sample #1 Ta/R6650 after irradiation with 1×10^{11} ppp within the first 200 μs. Power spectral density as a function of frequency with dashed lines indicating different fundamental vibration frequencies (a). Continuous wavelet transform of the absolute radial surface velocity. Color coding represents the values of the normalized absolute radial surface velocity (b).

The mentioned periods and the amplitude-modulation can be identified in the fast Fourier transform (FFT) and continuous wavelet transform (CWT) of the dynamic response which are both shown in Figure 11.15. In the low frequency range, the axial pressure waves in tantalum, 167 kHz, and graphite, 125 kHz can be identified. In the high frequency range, the highest amplitude occurs at a frequency of (970 ± 10) kHz, relatively close to the predicted radial frequency of 987 kHz with many different high frequency contributions in the range between

Table 11.4.: Material properties of tantalum and polycrystalline graphite SGL R6650 used in the coupled transient thermal/transient structural ANSYS simulation.

Material property		Tantalum	Graphite
Density ρ	($\mathrm{g\,cm^{-3}}$)	16.6	1.83
Specific heat capacity c_p	($\mathrm{J\,g^{-1}\,K^{-1}}$)	0.151	0.7
Young's modulus E	(GPa)	187	12.5
Coefficient of thermal expansion α	($\mathrm{K^{-1}}$)	6.5×10^{-6}	4.2×10^{-6}
Poisson's ratio ν		0.35	0.18
Thermal conductivity k	($\mathrm{W\,m^{-1}\,K^{-1}}$)	54	95

850 and 1100 kHz. Other, minor contributions occur in the frequency range around ~450 and 650 kHz. The amplitude modulation of the high frequency radial waves is clearly seen in the continuous wavelet transform in Figure 11.15b.

11.3.1.1 Comparison with Simulation

To check whether the response of the sample is elastic at a beam intensity of 1×10^{11} ppp, a finite element simulation of the sample was performed in ANSYS. The same simulation approach as for the full graphite samples (presented in section 11.2.2) was used. Temperature- and strain-independent thermal and mechanical material properties were considered for tantalum and SGL R6650 graphite which are summarized in Table 11.4. No Rayleigh damping was considered in the simulation. The spatial distribution of the deposited energy was extracted from a FLUKA Monte Carlo simulation using an inhomogeneous Gaussian beam intensity profile with σ_H =1.46 mm and σ_V =1.02 mm that is impinging on the sample centrally. The interface between the tantalum core and the graphite shell was approximated using a 'rough' contact that allowed separation between the bodies in the radial direction but prohibited sliding along the cylinder axis.

Figure 11.16a shows the comparison between the radial surface velocity obtained by the finite element simulation and the corresponding experimental response for the first 20 µs after irradiation. The radial surface velocity is only slightly overestimated by the simulation and is well in agreement with the experiment for the first 10 µs after the beam pulse. It is notable that the maximum surface velocity does not occur within the first oscillation as typically observed for isotropic samples due to the acoustic impedance mismatch between tantalum and graphite. A comparison between the Fourier spectra of the experimental and simulated radial surface velocity is shown in Figure 11.16b. The simulation replicates the relative power density of the different frequency components poorly in the absence of damping. But the frequency components of the signal are replicated reasonably well. The simulation has its most dominant contribution at ~180 kHz which corresponds to the axial pressure wave in the tantalum core, while the contribution from the radial pressure wave at ~990 kHz is severely underestimated. The peak at ~460 kHz is observed clearly at a beam intensity of 6×10^{11} ppp (the dynamic response is shown in Figure 11.19), but not at 1×10^{11} ppp due to the large differences in damping between these two beam intensities. Furthermore, several peaks between 600 and 850 kHz are present in the simulation but not observed in the experiment.

To determine the physical significance of the different frequency components, a modal analysis of natural vibration modes (up to a frequency of ~1000 kHz) was conducted for the geometry of the sample in ANSYS. Seven vibration modes with frequencies that coincide with the dominant contributions observed in the experimental and simulation results were identified and are compared within Table 11.5. The opposite deformation cases of these vibration modes are shown in Figure 11.17. The two vibration modes at 153.4 and 186.4 kHz are both attributed to the axial vibration of the sample. In comparison to the modal analysis of graphite (c.f. Figure 11.17), vibration modes are more complex with a large number of zero points along the cylinder axis.

Furthermore, experimental and simulation results were analyzed by continuous wavelet transform to compare whether the different frequency components can be unambiguously identified in the experimental signal and are not simply noise in the FFT. The resulting CWT heatmaps, superimposed with the Fourier spectra, are shown in Figure 11.18. In this case a complex Morlet wavelet with bandwidth frequency 4 and center frequency 5 was used.

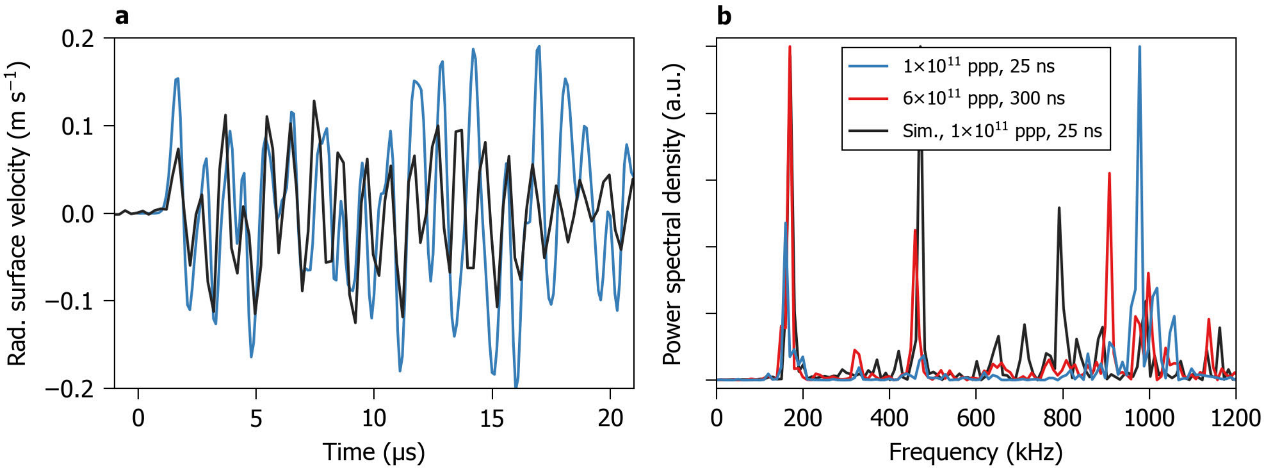

Figure 11.16.: Comparison between experimental and simulation results for sample #1 Ta/SGL R6650. Experimental (blue) and simulated (black) radial surface velocity as a function of time for 20 μs after the beam pulse of 1×10^{11} ppp (25 ns pulse length) (a). Normalized power spectral densities for the first 100 μs of the simulation and the experiment at two different beam intensities (b).

Table 11.5.: Comparison of frequency components identified in the FFT of the experimental results, the FFT of the simulations for a beam intensity of 1×10^{11} ppp and modal analysis of the sample geometry. Frequencies obtained from FFT have a systematic error of ±10 kHz.

Experiment FFT (kHz)		Simulation FFT (kHz)	Modal analysis (kHz)
1×10^{11} ppp	6×10^{11} ppp	1×10^{11} ppp	
160	170	170	153.4 / 186.4
330	330	330	319.5
460	470	480	477.3
-	810	800	804.0
910	910	880	899.7
980	990	980	978.4

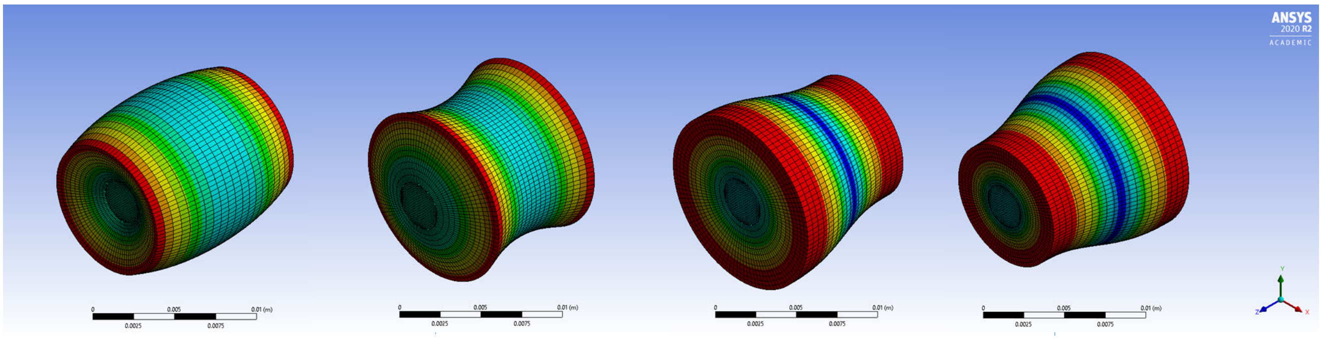
ANSYS
2020 R2
ACADEMIC
0
0.005
0.01 (m)
0.0025
0.0075

a 153.4 kHz **b** 186 kHz

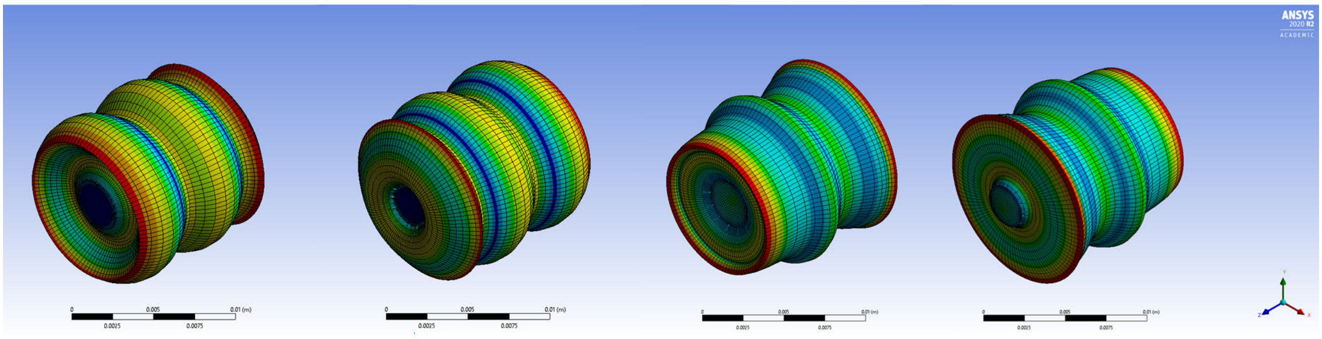
ANSYS
2020 R2
ACADEMIC
0
0.005
0.01 (m)
0.0025
0.0075

c 320 kHz **d** 477 kHz

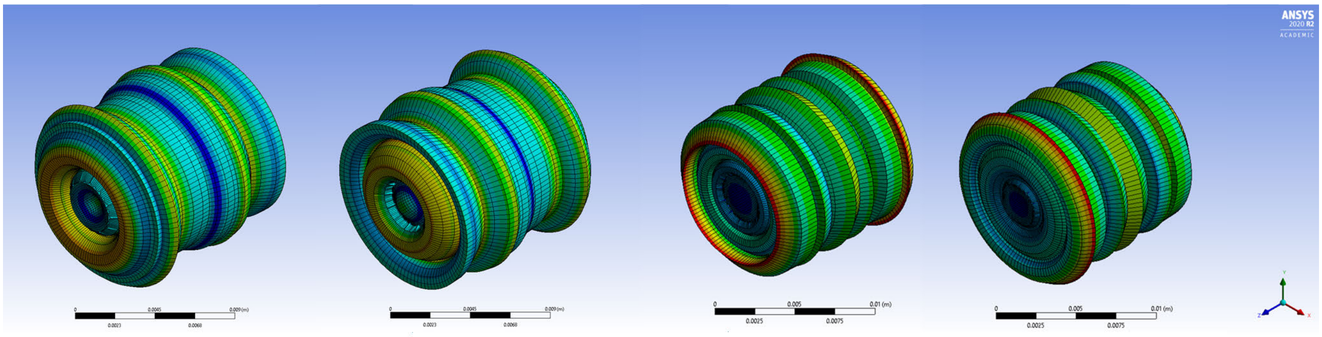
ANSYS
2020 R2
ACADEMIC
0
0.005
0.01 (m)
0.0025
0.0075

e 804 kHz **f** 900 kHz

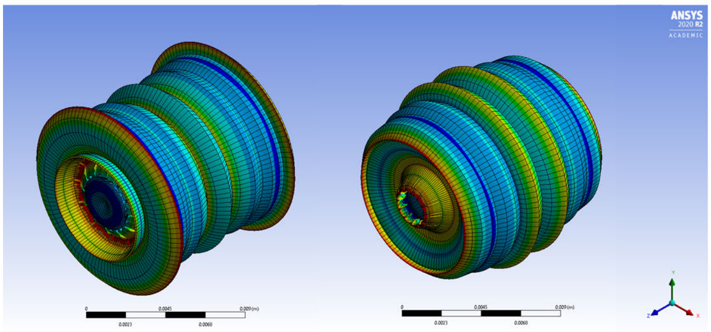
ANSYS
2020 R2
ACADEMIC

g 978 kHz

Figure 11.17.: Qualitative opposite extreme deformation (left and right) of different vibration modes obtained by modal analysis of sample #1 SGL R6650 that coincide with dominant frequency contributions measured during the experiment. The vibration modes have frequencies of 153.4 (a), 186.4 (b), 319.5 (c), 477.3 (d), 804.0 (e), 899.7 (f) and 978.4 kHz (g). Color coding qualitatively represents the normalized magnitude of deformation. Scale bars correspond to 10 mm.

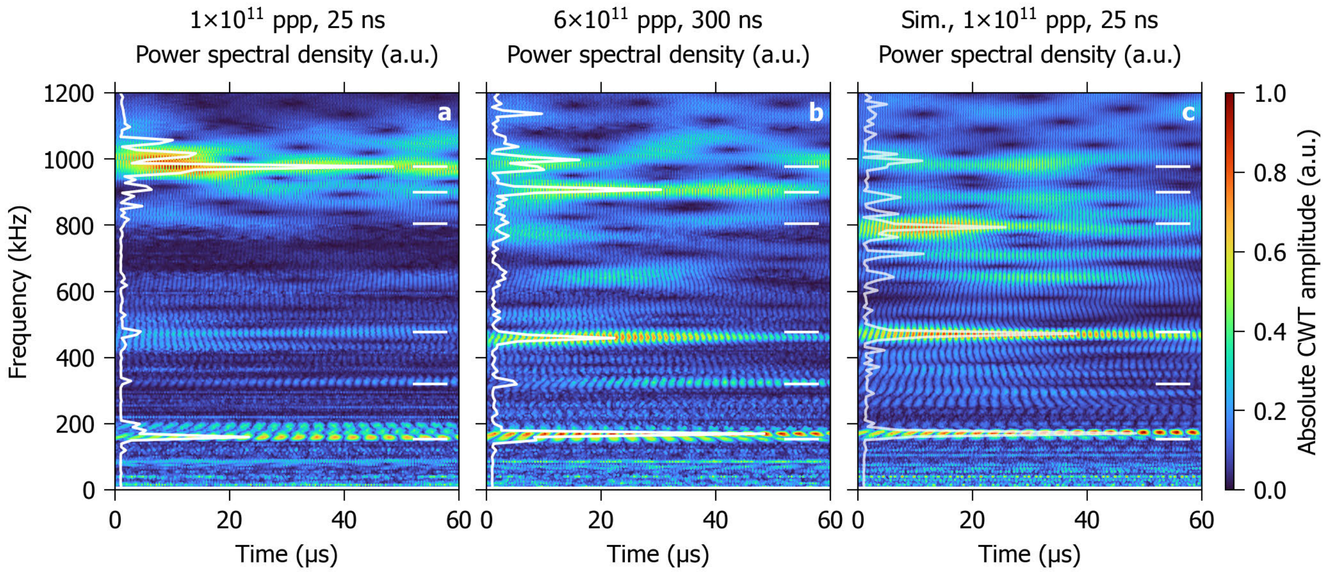

Figure 11.18.: Continuous wavelet transform of the measured and simulated radial surface velocity of sample #1 SGL R6650. The normalized power spectral density plot is overlaid in white. Solid lines indicate vibration modes of the sample geometry obtained by modal analysis. Experimental result at 1×10^{11} ppp and 25 ns pulse length (a), 6×10^{11} ppp, 300 ns (b), and simulation result at 1×10^{11} ppp, 25 ns (c).

This combination of wavelet properties leads to a frequency resolution of ~10 kHz of the CWTs, which makes them directly comparable to the resolution of the Fourier spectra. Albeit this comes at the cost of smaller temporal reproducibility. For example, the amplitude-modulation of the radial pressure wave at ~50 µs cannot be identified in comparison to Figure 11.15 for irradiation with 1×10^{11} ppp. But the CWTs clearly show that the frequency components of the simulation are well in agreement with the experiment. Hence, the dynamic response of the sample at 1×10^{11} ppp is most probably entirely elastic. Differences between the simulation and the experiment are due to the simulation not considering any damping.

11.3.2 Dynamic Response of Tantalum-Core Polycrystalline Graphites at 1×10^{11} ppp and 6×10^{11} ppp

Figure 11.19 shows the radial surface velocity measured by the LDVs for irradiation with 440 GeV/c proton beam pulses with intensities of 1 (25 ns pulse length) and 6×10^{11} ppp (300 ns) in different polycrystalline graphite samples #1 Ta/R6650, #6 Ta/R6650 and #3 Ta/POCO ZEE. At a beam intensity of 1×10^{11} ppp, the three materials exhibit similar signals that are dominated by the high-frequency radial pressure wave of the tantalum core with a period of ~1 µs. The difference in the maximum observed velocity (~0.1 $\mathrm{m\,s^{-1}}$ for #1 Ta/R6650 and ~1 $\mathrm{m\,s^{-1}}$ for #6 Ta/R6650) scales linearly with the ratio between the deposited energy density (~12) in the tantalum cores of the two samples, indicating fully elastic response of the samples at this beam intensity.

At 1×10^{11} ppp the response of #6 Ta/R6650 exhibits a degree of amplitude-modulation not observed in any other measurements. The sample was being hit eccentrically by the beam with a horizontal offset of 0.23 mm and 0.13 mm vertical offset (~5 % of the radius). Thus, beam-induced bending modes (typical frequencies are below the axial pressure wave frequency, <100 kHz) can be induced by the eccentric beam hit. But, no low-frequency signal was observed in either the FFT or CWT of the signal (shown in Figure 11.21b and Figure 11.22b).

The damping time constant, τ_D was extracted using an exponential decay function (indicated by the damping envelope shown in Figure 11.19) for the overall dynamic response. As detailed in the previous section, the dynamic response is composed of various vibration modes. To compare the trend of the overall damping of sample #1 Ta/SGL R6650 with the damping as a function of frequency, time constants were extracted from the CWT of the dynamic response for the six most dominant vibrations, that were identified by modal analysis (c.f. Figure 11.17). The damping time constants at these frequencies are shown in Figure 11.20b-g as a function of beam intensity.

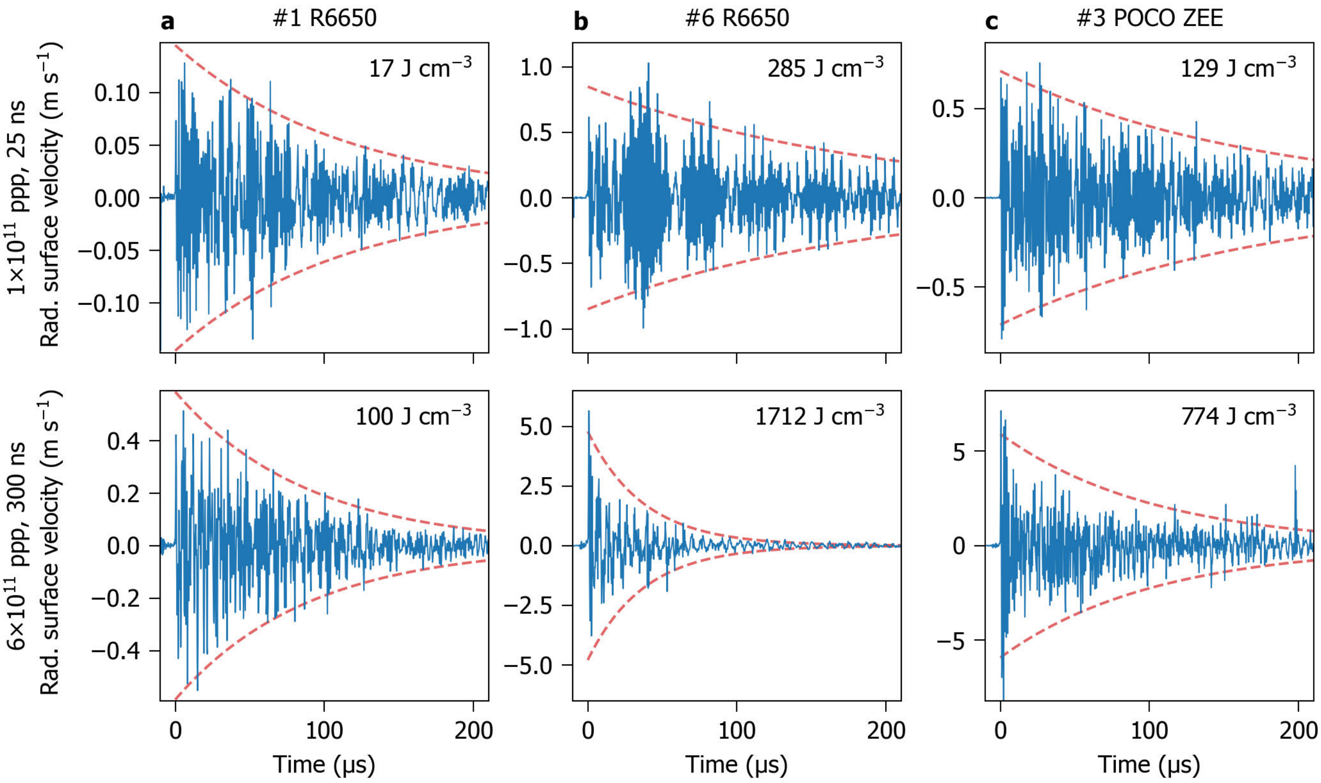

Figure 11.19.: Radial surface velocity (solid blue line) and calculated damping envelope (red dashed line) for 200 μs after irradiation of three different polycrystalline graphite samples: #1 Ta/SGL R6650 (a), #6 Ta/SGL R6650 (b), and #3 Ta/POCO ZEE (c) at beam intensities of 1 × 10^{11} ppp, 25 ns pulse length (top) and 6 × 10^{11} ppp, 300 ns (bottom) beam intensity. The energy density indicates the peak deposited energy density in the tantalum core averaged over the length of the sample calculated with FLUKA.

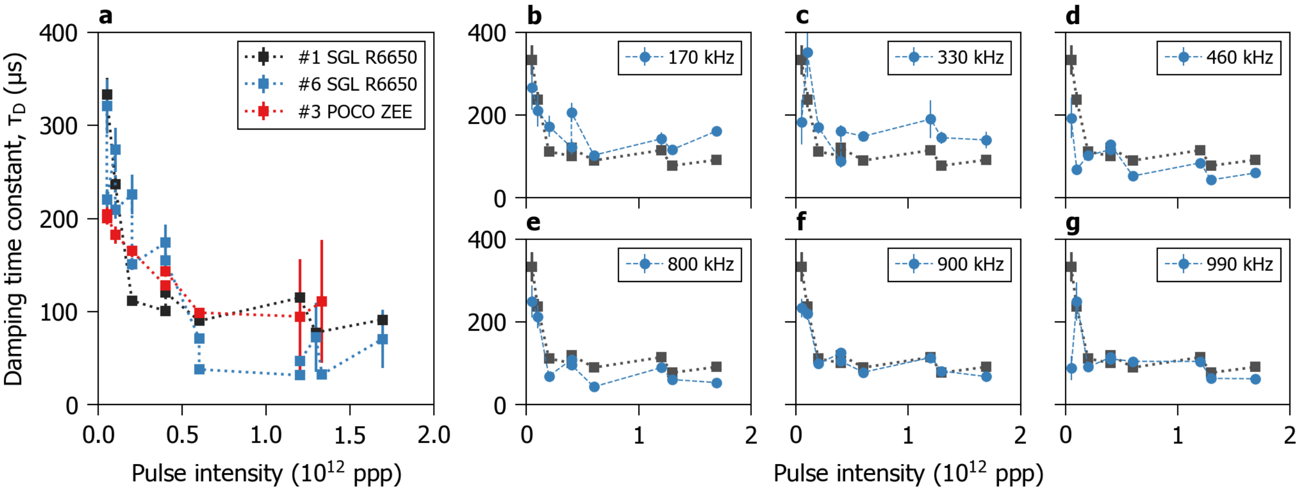

Figure 11.20.: Damping time constant τ of the overall dynamic response for samples #1 Ta/SGL R6650, #6 Ta/SGL R6650 and #3 Ta/POCO ZEE as a function of pulse intensity (a). Damping time constant as a function of beam intensity for different frequencies (blue circles) of sample #1 Ta/SGL R6650 obtained from continuous wavelet transform in comparison to the overall damping time constant (black line) of the radial surface velocity (b–g). Frequencies have a systematic error of ±10 kHz.

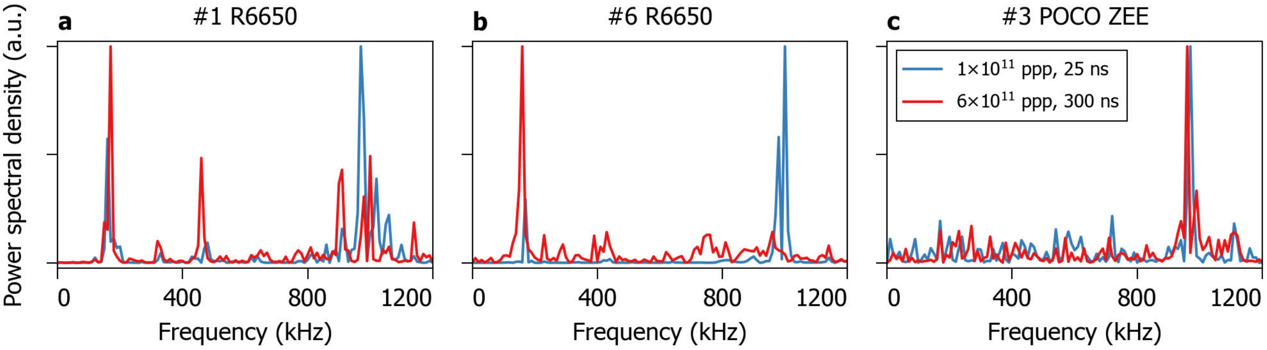

Figure 11.21.: Frequency analysis of the radial surface velocity shown in Figure 11.19. The normalized spectral power density within the first 100 µs after irradiation is shown for beam pulses with intensities of 1 and 6×10^{11} ppp of samples #1 Ta/SGL R6650 (a), #6 Ta/SGL R6650 (b) and #3 Ta/POCO ZEE (c).

There is no clear correlation between higher frequencies and decreasing damping time constant for a single pulse intensity. But all damping time constants systematically decrease with increasing beam intensity. This trend is also observed when comparing the overall damping between the different polycrystalline graphite samples, which is shown in Figure 11.20a. There is no obvious correlation between graphitic micro-structure and damping. The trend that was observed on the pure graphite samples, #3 Ta/POCO ZEE had the largest damping time constant (c.f. Table 11.3), is apparently inverse. At low beam intensities, #3 Ta/POCO ZEE has the smallest damping time constant, while the two Ta/SGL R6650 samples have larger damping time constants. The more complex sample geometry, especially the quality of the mechanical interface between the tantalum core and the graphite shell, is dominating the damping in comparison to the microstructure effect that was observed in the pure graphite samples.

The steep increase in damping, which occurs between 1×10^{11} ppp and 6×10^{11} ppp, is tentatively attributed to the beam-induced temperature increase in the tantalum cores and the onset of plastic deformation. This is also consistent with the increased damping with increasing pulse intensity observed on pure tantalum [267].

Figure 11.21 shows the self-normalized Fourier spectra of the dynamic response presented in Figure 11.19. The frequency composition does not change significantly at higher pulse intensities, with the exception of the tantalum radial pressure wave signal (at ∼1000 kHz) in sample #6 Ta/R6650. The radial pressure wave amplitude almost vanishes for the irradiation with 6×10^{11} ppp as indicated by Figure 11.21b.

To check the presence of the radial pressure wave, Figure 11.22 shows the CWT of the dynamic response for 100 µs after the beam pulse. The high frequency radial pressure wave signal is still observable in the CWT as opposed to the Fourier transform. The high frequency radial pressure wave is damped within ∼20 µs, hence its amplitude in the Fourier spectrum (which is calculated over the first 100 µs of the dynamic response) is small in comparison to the low frequency axial pressure wave. Also, the increased damping of the radial pressure wave from 1×10^{11} to 6×10^{11} ppp, that is not observed for the #1 Ta/SGL R6650 sample at lower deposited energy density, indicates that the damping might already be affected by plasctic deformation in the sample.

The large difference in the Fourier spectra and CWT of the POCO ZEE sample (shown in Figure 11.21c and Figure 11.22c) in comparison to the other two samples is not understood. In both cases, only the high frequency radial pressure wave can be identified. The axial pressure waves at ∼200 kHz can be seen in the CWT, but only barely.

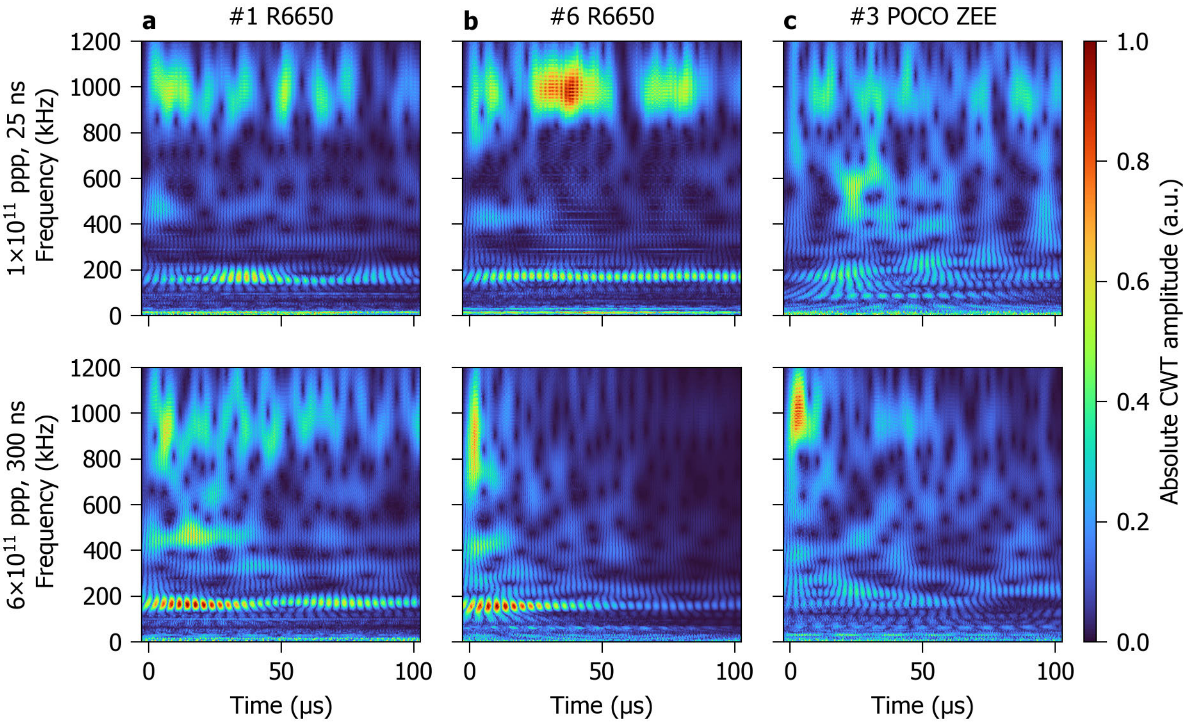

Figure 11.22.: Continuous wavelet transform of the radial surface velocity presented in Figure 11.19 for three different polycrystalline graphite samples #1 Ta/SGL R6650 (a), #6 Ta/SGL R6650 (b) and #3 Ta/POCO ZEE (c) at 1×10^{11} ppp (top) and 6×10^{11} ppp (bottom) pulse intensity.

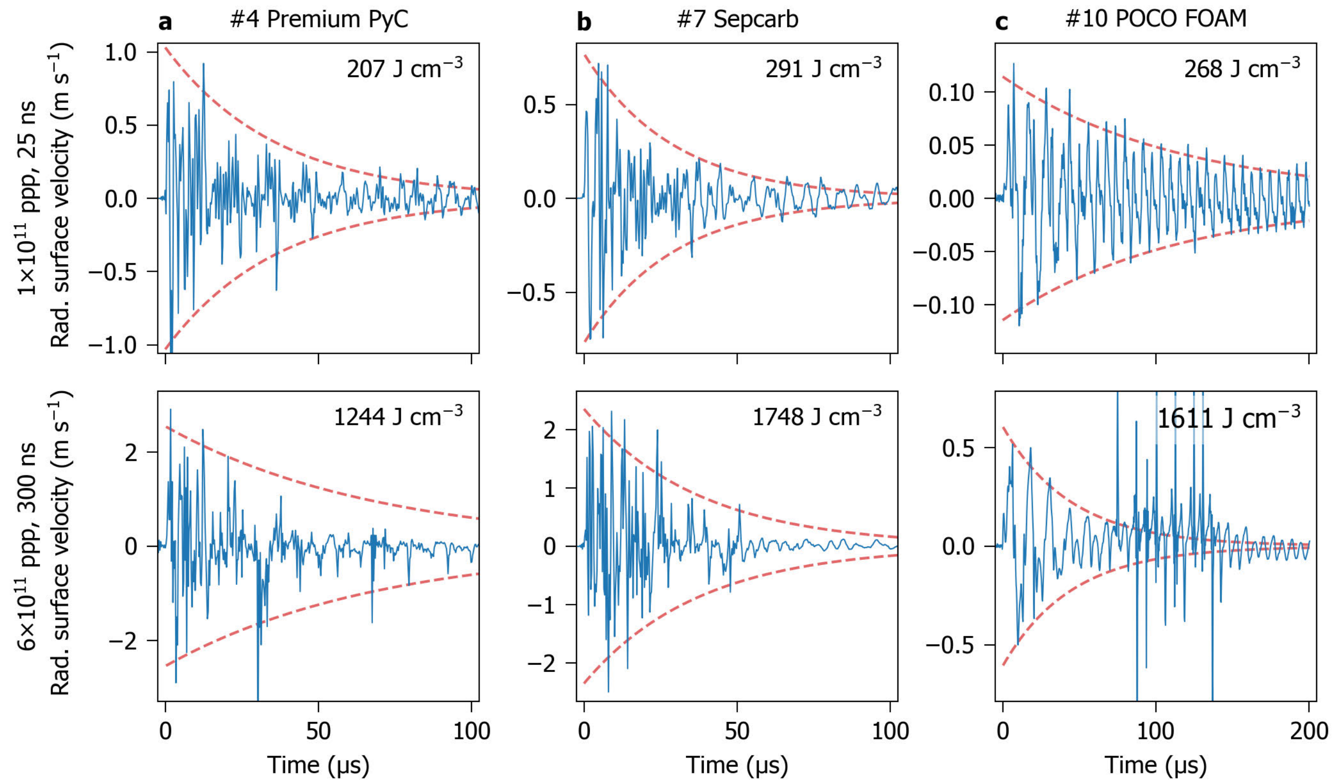

Figure 11.23.: Radial surface velocity (solid blue line) and calculated damping envelope (red dashed line) as a function of time for 100 and 200 µs after the beam pulse for two different carbon-fiber reinforced graphite composites and graphitic foam: #4 Ta/SGL Premium PyC (a), #7 Ta/ArianeGroup Sepcarb (b) and #3 Ta/POCO FOAM (c) at 1×10^{11} ppp, 25 ns pulse length (top) and 6×10^{11} ppp, 300 ns (bottom) pulse intensity. The energy density indicates the peak energy deposition in the tantalum core averaged over the length of the sample calculated with FLUKA. The perturbations in (c) are nonperiodic.

11.3.3 Dynamic Response of Tantalum-Core Carbon-fiber reinforced Graphites and Graphitic Foam at 1×10^{11} ppp and 6×10^{11} ppp

Figure 11.23 shows the radial surface velocity after irradiation with pulse intensities of 1×10^{11} and 6×10^{11} ppp in samples #4 Ta/SGL Premium PyC, #7 Ta/ArianeGroup Sepcarb and #10 Ta/POCO FOAM. The response of the fiber-reinforced graphite (CFCs) grades and the graphitic foam differs significantly from the response of the isotropic polycrystalline graphite samples discussed in the previous section (cf. Figure 11.19). Measured maximum surface velocities are considerably smaller at comparable energy densities deposited in the tantalum cores. In both CFC samples, #4 Premium PyC and #7 Sepcarb, the maximum surface velocity increased only by a factor of ∼2.5 when increasing the beam intensity from 1 to 6×10^{11} ppp. Both CFCs exhibit considerably stronger damping with time constants <100 µs in comparison to the PGs. Fiber-reinforcement planes consist of individual fibers that are bundled together in so-called rovings, which are then woven into mats that are interconnected by a discontinuous graphite matrix. The increased damping of the CFCs is ascribed to the large number of interfaces. Moreover, the average pore volume of CFCs is larger than in PGs because of the lower density of CFCs. Surprisingly, Ta/POCO FOAM has a damping time constant on the order of ∼200 µs although it has the lowest density (less than ∼30 % of the PGs), largest porosity (∼75 %) and macroscopic pore diameter of several hundreds of micron [269]. Furthermore, the response of Ta/POCO FOAM is rather 'clean' in comparison to the CFCs with a well-defined (damped) periodic response.

Figure 11.24 shows the frequency analysis of the dynamic response. Both CFCs exhibit a large number of superimposed frequencies (cf. Figure 11.24a and b), which is explained by the anisotropy of the CFCs ($E_{\perp}/E_{\parallel} \approx 5$ in Sepcarb) that leads to complex pressure wave superposition. In contrast to the PGs (cf. Figure 11.21), the high

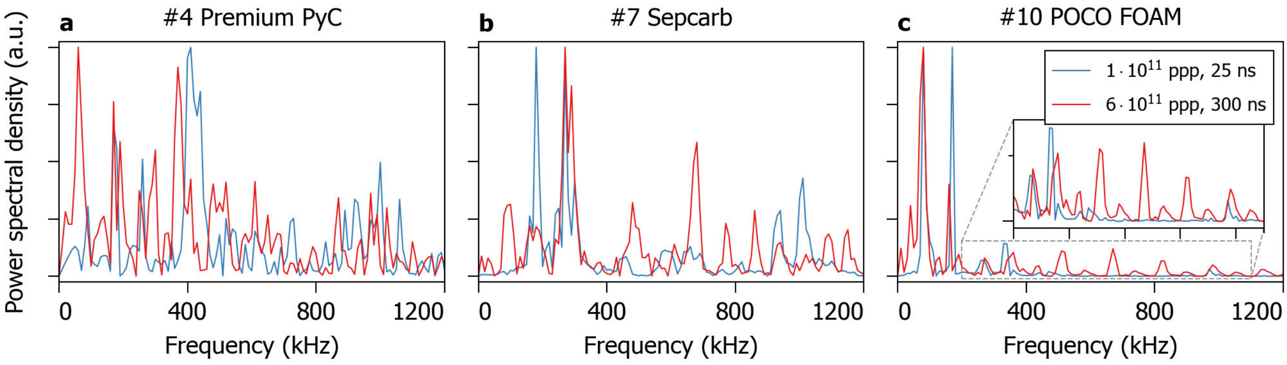

Figure 11.24.: FFY analysis of the radial surface velocity shown in Figure 11.23. The normalized spectral power density within the first 100 µs after irradiation is shown for beam pulses with intensities of 1 and 6×10^{11} ppp of samples #4 Ta/SGL Premium PyC (a), #7 Ta/ArianeGroup Sepcarb (b) and #3 Ta/POCO FOAM (c).

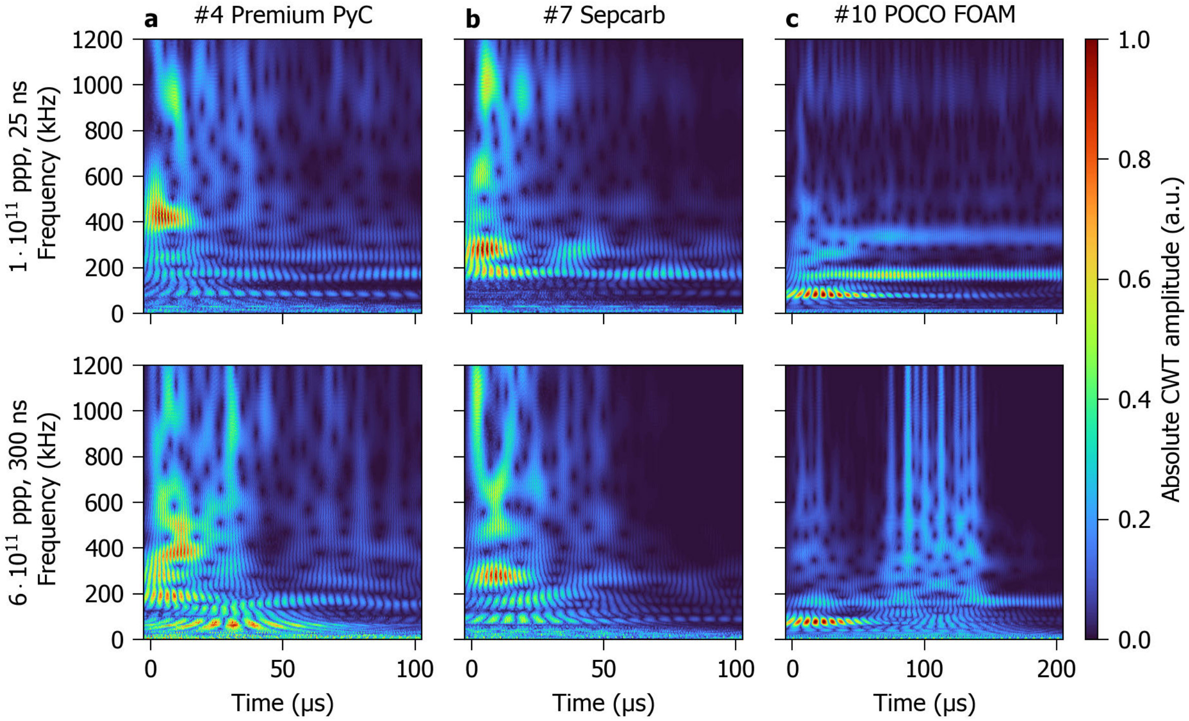

Figure 11.25.: Continuous wavelet transform of the radial surface velocity presented in Figure 11.23 for three different polycrystalline graphite samples #4 Ta/SGL Premium PyC (a), #7 Ta/ArianeGroup Sepcarb (b) and #3 Ta/POCO FOAM (c) at 1×10^{11} ppp (top) and 6×10^{11} ppp (bottom) pulse intensity.

frequency radial pressure wave of the tantalum core is rather small and broad in #4 Ta/Premium PyC and #7 Ta/Sepcarb and is suppressed in sample #10 Ta/POCO FOAM. The continuous wavelet transform of these samples is presented in Figure 11.25 and, as observed in the PGs, the radial pressure wave of the tantalum core is amplitude-modulated. Due to the strong damping, it is difficult to identify it in the velocity signal. The absence of a clear radial pressure wave in #10 Ta/POCO FOAM can be explained by the large acoustic impedance mismatch between tantalum and POCO FOAM (E =0.4 GPa [270], ρ =0.5 g cm^{-3}), which leads to a splitting of the radial signal into multiple components (cf. inset of Figure 11.24c).

11.3.4 Dynamic Response at High Intensities

Figure 11.26 shows the dynamic response of the poylcrystalline graphite samples at the highest pulse intensities of 1.2 to 1.7 × 10^{12} ppp during the experiment. The dynamic response degraded quite dramatically in comparison to irradiation with 1 × 10^{11} and 6 × 10^{11} ppp. The maximum surface velocity does not follow the beam intensity linearly, except for #1 Ta/R6650 (cf. Figure 11.19). Radial surface velocities of sample #6 Ta/R6650 should be above 10 m s^{-1} (see maximum surface velocity at 6 × 10^{11} ppp (Figure 11.19b) compared with 1.69 × 10^{12} ppp (Figure 11.26c)). Also, for #3 Ta/POCO ZEE, the surface velocity under high intensity is unexpectedly low. It can safely be assumed that failure has occurred in samples #3 Ta/POCO ZEE and #6 Ta/R6650. This is also indicated by the severe “deformation” of the first oscillation of the dynamic response in #6 Ta/R6650 and the large difference between the absolute maximum and minimum surface velocity (indicating loss of energy by plastic deformation or failure).

Determining an exact intensity, or deposited energy density, limit below which no material failure should be expected is difficult. Due to the target station layout, all samples were irradiated in-line and the observed material behavior results from the cumulative effects of several beam pulses. It is important to note that even under such high beam intensities, the axial pressure wave of the tantalum core is observed in all samples, indicating that the mechanical interface between tantalum core and graphite shell is still functional to a certain degree. This is also supported by the presence of the radial pressure wave, albeit the frequency response is heavily “smeared” compared to the response at lower beam intensities.

Figure 11.27 shows the radial surface velocity of the anisotropic samples #4 Ta/Premium PyC, #7 Ta/Sepcarb and #10 Ta/POCO FOAM induced by the highest beam intensities during the experiment. Again, in contrast to the low and medium intensity irradiation, shown in Figure 11.23, dramatic changes in the samples’ response are observed. The absolute maximum and minimum surface velocity in samples #4 Ta/Premium PyC and #10 Ta/POCO FOAM are very different. For samples #7 Ta/Sepcarb and #10 Ta/POCO FOAM the maximum surface velocity still increases nearly linear with beam intensity (cf. Figure 11.23). #7 Ta/Sepcarb shows the “cleanest” response at high beam intensities, but failure cannot be completely excluded because of the deformation of the individual oscillations.

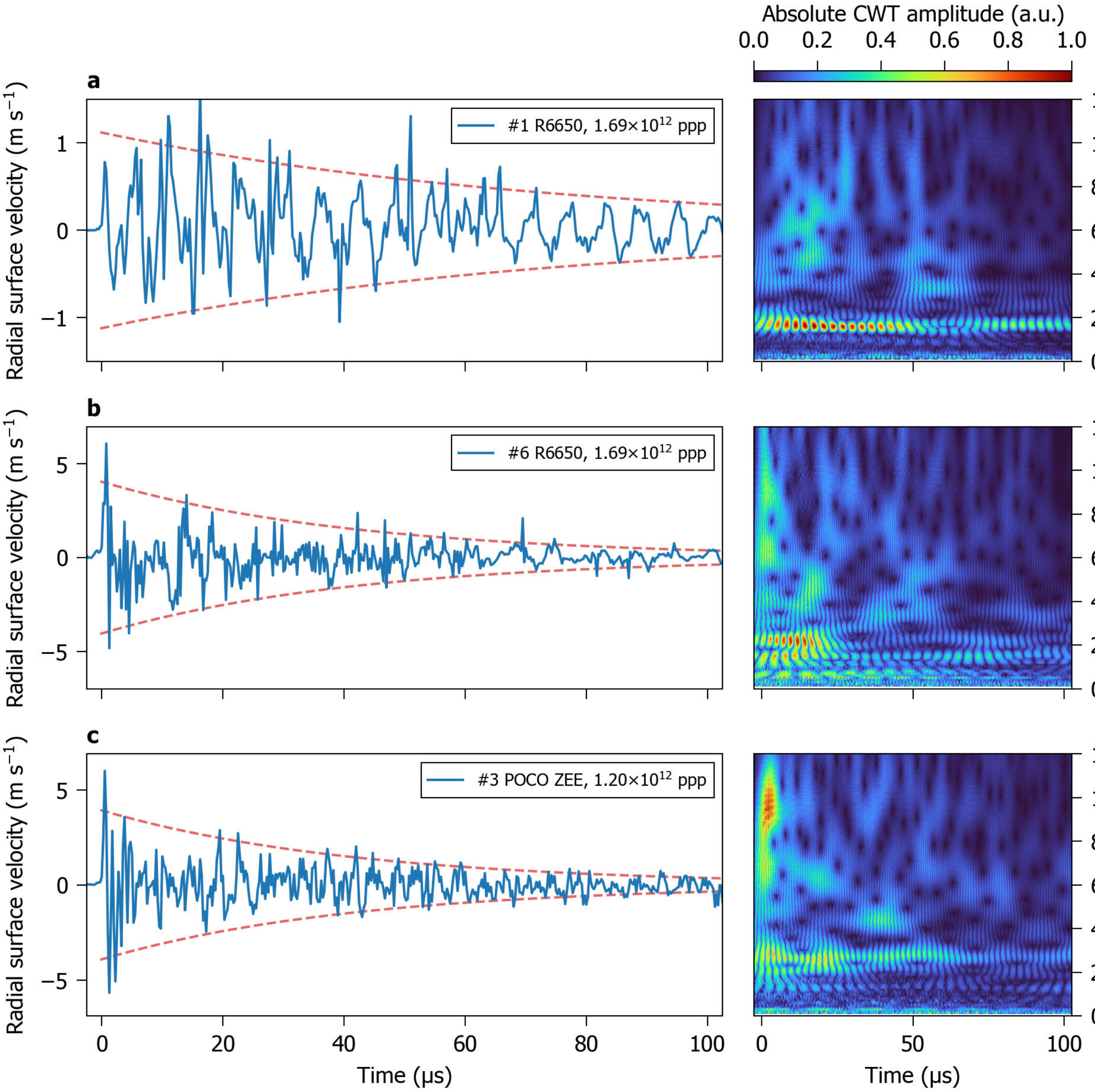

Figure 11.26.: Measured dynamic response for maximum applied pulse intensity on samples #1 Ta/SGL R6650 (a), #6 Ta/SGL R6650 (b) and #3 Ta/POCO ZEE (c). Left: radial surface velocity (solid blue line) and calculated damping envelope (red dashed line). Right: continuous wavelet transform as a function of time for 100 μs after the beam pulse.

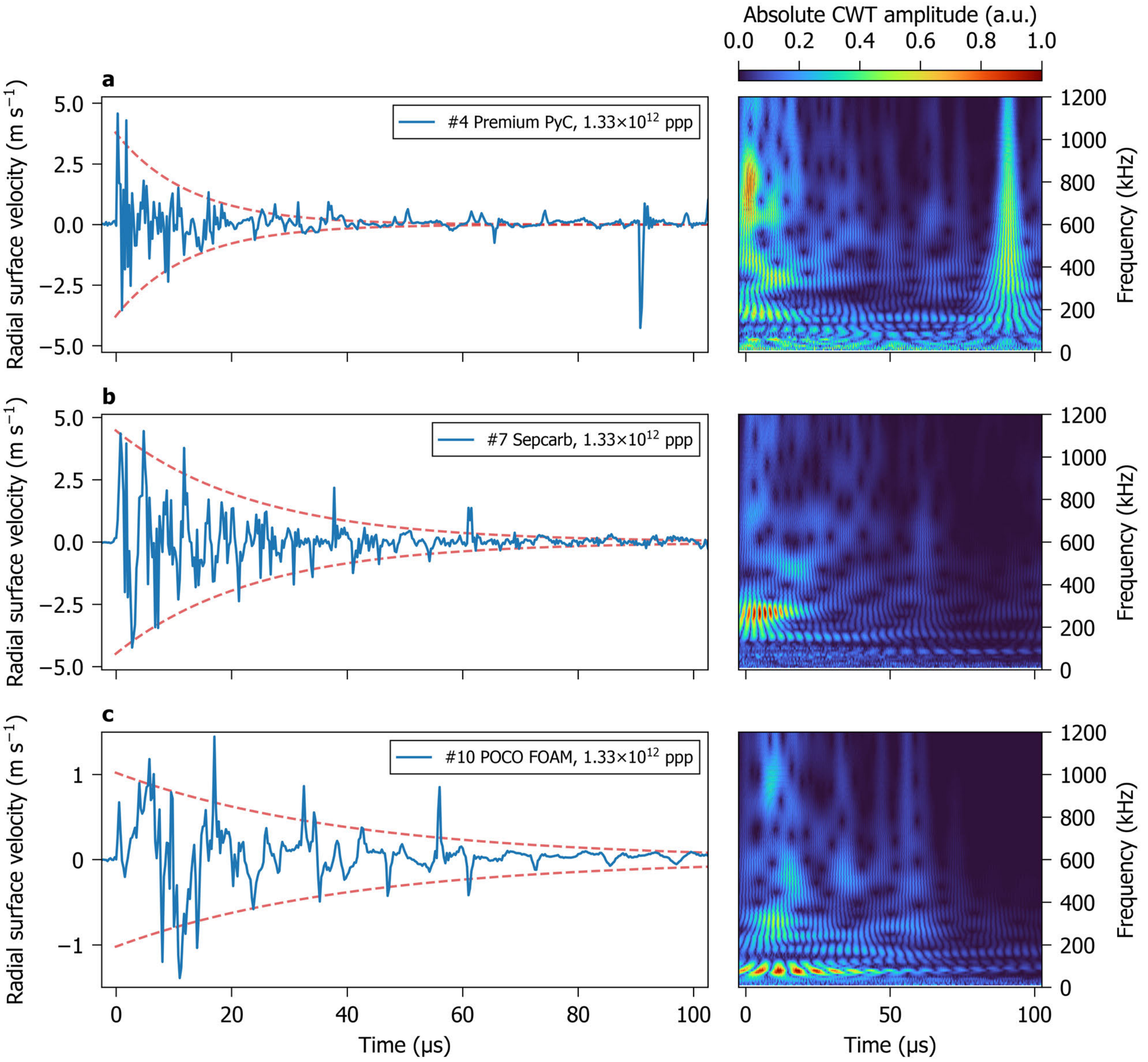

Figure 11.27.: Measured dynamic response for maximum applied pulse intensity on samples #4 Ta/SGL Premium PyC (a), #7 Ta/ArianeGroup Sepcarb (b) and #3 Ta/POCO FOAM (c). Left: radial surface velocity (solid blue line) and calculated damping envelope (red dashed line). Right: continuous wavelet transform as a function of time for 100 μs after the beam pulse.

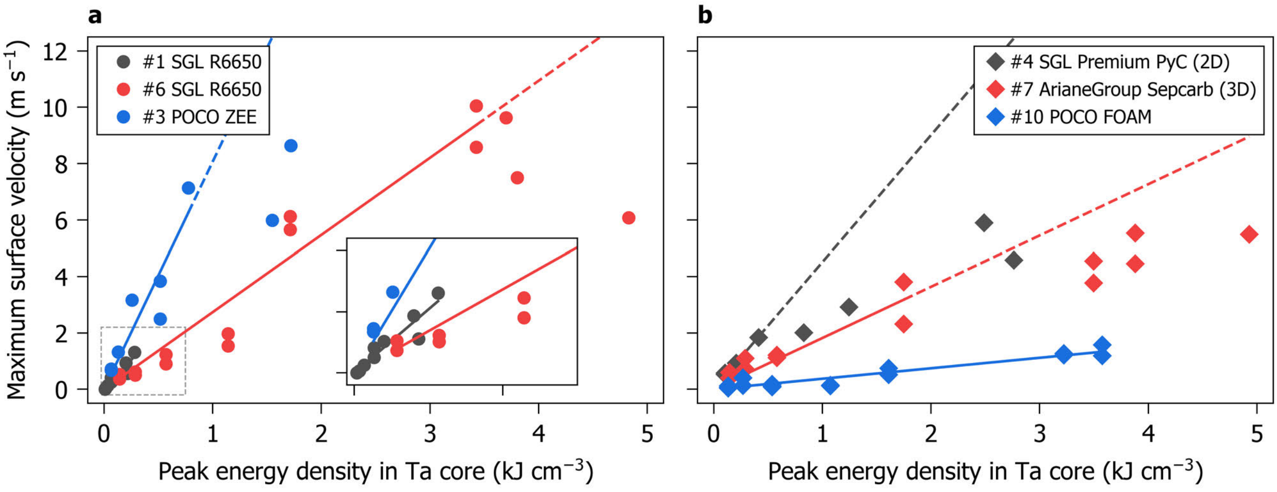

Figure 11.28.: Absolute maximum surface velocity (symbols) as a function of deposited energy in the tantalum core for samples #1, #3, and #6 (a) and samples #4, #7, and #10 (b). The inset is a blow-up of the dashed box. Lines represent a guide to the eye for the proposed range of deposited energy where the sample shows an overall elastic response. Error bars are smaller than the symbols.

11.3.5 Macroscopic Materials Response

The energy density deposited into the tantalum core of different samples depends on the position along the target station and is deduced from FLUKA simulations considering the size and intensity of the primary beam as well as the production of secondary particles (cf. Table 10.2 and Figure 11.2). Due to the complex wave superposition given by the tantalum core/graphite sample geometry, the highest radial surface velocity might occur after the first oscillation has reached the surface. Figure 11.28a and b show the absolute maximum radial surface velocity reached within 20 µs after irradiation as a function of deposited deposition density in the tantalum core.

Assuming elastic response of the tantalum core and the surrounding graphite, the radial surface velocity increases linearly with the deposited energy density (or in the frame of one sample, with the beam intensity). Sublinear surface velocities at highest beam intensities are ascribed to material failure (indicated by the dashed line in Figure 11.28a). For the given geometry, tantalum should exhibit a quasi-elastic response up to a beam intensity of at least $\sim 9 \times 10^{11}$ ppp in the most loaded sample position #6 according to literature [271], which corresponds to an energy density of $\sim 2.6\,\mathrm{kJ\,cm^{-3}}$. For the two Ta/SGL R6650 polycrystalline graphite samples (#1 and #6), the evolution of the maximum surface velocity follows the same trend. For energy densities larger than $\sim 3.5\,\mathrm{kJ\,cm^{-3}}$ the velocities are smaller than the linear trend. It is not clear why #3 Ta/POCO ZEE has a smaller range of linear response. POCO ZEE has a higher flexural strength than SGL R6650 and is hence expected to be more robust.

The dynamic response of the carbon fiber-reinforced graphite grades #4 Ta/Premium PyC and #7 Ta/Sepcarb is shown in Figure 11.28b. Both CFCs exhibit significantly smaller maximum surface velocities of up to $\sim 6\,\mathrm{m\,s^{-1}}$ in comparison to the polycrystalline graphite samples (maximum surface velocity $\sim 10\,\mathrm{m\,s^{-1}}$). At deposited energy densities below $\sim 1\,\mathrm{kJ\,cm^{-3}}$, both samples exhibit a linear trend. In #7 Ta/Sepcarb, this is followed by a sublinear behaviour at energy densities $>2\,\mathrm{kJ\,cm^{-3}}$. We do not expect that this is due to catastrophic failure but rather ascribe the effect to the low-strength matrix. Even though the investigated CFCs have the highest flexural strength of the materials studied in this work, the tensile strength of the graphite matrix in Sepcarb is only 17 MPa. Structural integrity is therefore provided by the fiber reinforcement, but local failure can readily occur in the low-strength graphite matrix and at the interface between fiber reinforcement planes and the matrix.

The macroscopic response of #10 POCO FOAM, shown in Figure 11.28b, is rather peculiar, as it fully follows a linear trend. Since POCO FOAM has a flexural strength of only 3 MPa, catastrophic failure was expected already at low pulse intensities. Even though the response degraded dramatically at high intensities (cf. Figure 11.27c), the response between 1×10^{11} ppp and 6×10^{11} ppp was virtually unchanged (cf. Figure 11.23c). This is probably the most surprising result of this work and is indicating that low-density graphitic foam might be a good candidate for high power beam dumps as the low-density leads to a significant dilution of the energy deposition density.

Part IV. Conclusions and Outlook

Accelerator componends need to fulfill the demands of ever-increasing beam intensities and the accompanying increase of stored beam power of next generation accelerator facilities. Due to the specific particle radiation-related advantages in comparison to classic engineering materials like steel, copper or titanium (alloys), graphitic materials are used in the extreme radiation environments of modern and next generation accelerators of facilities such as FAIR/GSI or CERN. Accelerator components like beam intercepting devices need to cope with beam-induced thermo-mechanical loads that are generated in the interaction with pulsed beams on timescales of a few microseconds. In addition to these quasi-instantaneous radiation effects, radiation damage limits the lifetime of components over time scales of months or years and is especially pronounced at heavy ion factilies like FAIR and GSI when compared to proton accelerators.

This thesis focused on the study of two very different aspects of radiation effects in carbon-based materials. The ionoluminescence properties of diamonds were characterized to investigate the suitability of diamond-based metal matrix composites as luminescence screens for high-intensity heavy ion beams at energies close to the Bragg peak. Various graphite grades were irradiated with high-intensity proton beams to investigate their dynamic response towards high-power pulsed beams and to identify potential correlations with their micro- or mesostructures.

Luminescence Properties of Diamond Under Swift Heavy Ion Irradiation

Various synthetic diamond(-based) samples were irradiated with 4.8 MeV/n ions ranging from ^{48}Ca to ^{238}U to investigate the suitability of diamond-based metal matrix composites for beam diagnostic luminescence screen of high-intensity swift heavy ion beams at energies close to the Bragg peak. Investigated samples comprised diamond-based metal matrix composites, bulk monocrystalline HPHT-syntesized type Ib and CVD-synthesized type IIa diamonds. Based on similar trends that were observed in both ionoluminescence and photoluminescence spectroscopy, bulk type Ib diamonds served as a model system for the diamond powders used in the diamond-based composites. Optical microscopy has shown strong ion-induced color change of type Ib diamonds from a light yellow hue over dark green towards black that indicates a near-complete loss of transparency. Ionoluminescence spectroscopy of diamond-based metal matrix composites and bulk type Ib diamonds which contain nitrogen impurities of the order of a few hundreds of ppm has shown a broad emission band in the visible green spectrum around 530 nm with a sharp edge at ∼500 nm excited by irradiation with 4.8 MeV/n ^{48}Ca and ^{197}Au ions. Possible origins of this band are the 3H center, H3 center or the green band with their ZPLs and PSB close to the emission maximum. Another band in the near-infrared at ∼885 nm can be clearly attributed to the presence of NiV$^-$ 1.40 eV centers.

The integrated ionoluminescence signal decays rapidly with increasing fluence. A moderate fluence of $\leq 2 \times 10^{11}\,\mathrm{cm^{-2}}$ of ^{197}Au ions, corresponding to ≤2.9 MGy is sufficient to reduce the integrated ionoluminescence signal to ≤20 % of its initial value. At fluences larger than $1 \times 10^{12}\,\mathrm{cm^{-2}}$ ^{197}Au ions (14.4 MGy), a blue emission is observed during irradiation. Under excitation with 4.8 MeV/n ^{48}Ca ions, a set of emission lines is identified between 380 and 450 nm at fluences $\geq 4 \times 10^{12}\,\mathrm{cm^{-2}}$ (14.5 MGy) that increase in intensity up to the ultimate fluence of $5 \times 10^{13}\,\mathrm{cm^{-2}}$ (181.3 MGy). The blue emission is attributed to the 3.188 eV and 2.807 eV centers, which are both typical radiation damage products in all types of diamonds. The maximum intensity of these centers is ≤2.5 % normalized to the maximum intensity of the first ionoluminescence spectrum measured by integrating the light between the start of irradiation up to a fluence of $2 \times 10^{11}\,\mathrm{cm^{-2}}$ (0.7 MGy). Furthermore, the broad green band decays into a structure with two peaks at 502 nm and 532 nm. Together with the broad band around 520 nm, the 502 nm peak is tentatively attributed to the ZPL of either the di-split-interstitial 3H center or N_2V H3 center. Furthermore, an ionoluminescence signal from neutral vacancy GR1 centers can be identified at fluences $\geq 1 \times 10^{13}$ cm^{-2} (36.3 MGy). Even though all investigated diamonds contained a significant amount of nitrogen (as indicated by their yellow color), only two samples had a nitrogen-related ionoluminescence signal of the NV^{0}center. Photoluminescence spectroscopy was conducted on a large number of HPHT-synthesized type Ib diamond samples with ~200 ppm substitutional nitrogen after irradiation with fluences as low as 3×10^9 (45 kGy) up to 2×10^{13} cm^{-2} (297.7 MGy) of 4.8 MeV/n ^{197}Au ions. Spatially resolved photoluminescence spectra with a resolution of 1 to 2 μm under excitation with 473 nm and 633 nm probed different energy losses along the ion trajectory, dominated by either electronic (close to the surface) or nuclear energy loss (around the maximum ion range). The intensity of the diamond Raman line under excitation with 633 nm is sensitive to the nuclear energy loss at the end of the ion range. A low fluence of 1×10^{11} cm^{-2} corresponding to a vacancy density of $(1.1 \pm 0.3) \times 10^{19}$ cm^{-3} is sufficient for the onset of degradation within the diamond lattice. At 2×10^{13} cm^{-2} the Raman line intensity is degraded by >95 % at the end of the ion range at a vacancy density of $(2.2 \pm 0.3) \times 10^{21}$ cm^{-3}.

Vacancy-related GR1 centers, on the other hand, are sensitive to electronic energy loss. Close to the surface their intensity increased by nearly 3 orders of magnitude under 633 nm excitation when exposed to 2×10^{13} cm^{-2} ^{197}Au ions. Even though the largest vacancy density is produced at the end of the ion range, this result is in line with literature [272]. It is argued that ion-induced vacancy/interstitial pairs need to separate by a sufficient distance via diffusion for the vacancies to be active as GR1 centers, while the necessary activation energy is supplied by electronic energy loss. Additionally, the increasing vacancy production (per incident ion) at the end of the ion range produces vacancy clusters rather than single vacancies. But, at the same time a non-linear dependence with the vacancy density can be identified. The maximum GR1 intensity is at a vacancy density of $(3.3 \pm 0.5) \times 10^{19}$ cm^{-3}, which is in reasonable agreement with the value of $\sim 7 \times 10^{19}$ cm^{-3} reported in literature [178].

Photoluminescence spectra under 473 nm excitation indicate that the ZPL at 502 nm can be attributed to 3H centers due to the successful identification of multiple phonon replicas of its ZPL, which supports the notion that the 3H center is a dominant component in the ionoluminescence spectra of these diamonds. Irradiation with 1×10^{11} cm^{-2} ^{197}Au ions is sufficient to create a clear ZPL and phonon sideband signal in both photo- and ionoluminescence. The intensity of the 3H phonon sideband reaches its maximum intensity at 3×10^{12} cm^{-2}, which is about three times larger than the pristine diamond Raman line.

The 3H phonon sideband intensity reaches its maximum at a vacancy density of $(4.4 \pm 0.5) \times 10^{18}$ cm^{-3} and was measured in the sample where this vacancy density was accompanied by the highest electronic energy loss. The maximum intensity occurred close to the surface after irradiation with 3×10^{12} cm^{-2} ^{197}Au ions. At this location, the nuclear energy loss is about 3 orders of magnitude lower in comparison to the electronic energy loss. In other words, the intensity of 3H centers scales with the ratio between electronic and nuclear energy loss. The intensity of 3H centers decreases steadily with increasing vacancy density beyond $(4.4 \pm 0.5) \times 10^{18}$ cm^{-3}. A similar trend is observed for the NV$^-$center with its maximum ZPL intensity between 4×10^{18} and 1×10^{19} cm^{-3}, which scales with increasing ratio between electronic and nuclear energy loss as well. Overall, the absence of the nitrogen-aggregate H3 centers and the NV^{0}centers indicates that direct production of nitrogen-related color centers by swift heavy ion irradiation is rather inefficient in comparison to intrinsic defects like the 3H or GR1 center.

In-situ UV/vis absorption spectroscopy measurements were conducted at room temperature and 50 K on a set of HPHT-synthesized type Ib diamonds with ~200 ppm substitutional nitrogen and CVD-synthesized type IIa diamonds with ≤5 ppb up to a fluence of 2×10^{13} cm^{-2} (297.7 MGy) of 4.8 MeV/n ^{197}Au ions. The hugely different nitrogen levels were chosen to investigate the influence of extrinsic nitrogen defects on radiation-induced effects. UV/vis measurements and irradiations at a temperature of 50 K were chosen to potentially detect additional absorption lines, while irradiations and measurements at room temperature were representative of the dynamics during ionoluminescence measurements. Pristine type Ib diamonds showed an absorption edge between 400 and 500 nm due to the presence of nitrogen C centers, while pristine CVD diamonds did not exhibit an absorption edge in the measurement range ≥300 nm. Loss of transmission between 350 and 870 nm was observed in both diamond types that strictly followed the single impact model for fluences $\geq 1 \times 10^{12}$ cm^{-2} independent of irradiation temperature. Single impact cross sections were systematically larger for smaller wavelengths with cross sections between (14.0 ± 1.2) and (20.0 ± 0.7) nm^2 at 525 nm in comparison to 3.0 ± 0.1 to (7.0 ± 1.5) nm^2 at 870 nm. These cross sections also indicate that loss of transmission is no major contributor to the decay of the ionoluminescence intensity below 1×10^{12} cm^{-2}.

Several color centers were successfully identified in the UV/vis absorption spectra, the vacancy related GR1 center with its ZPL, a ZPL phonon replica and its phonon sideband, the 3H center, the 1.859 eV and the 1.889 eV center, respectively. An absorption peak at the position of the 3H center ZPL was unambiguously identified in the type

IIa diamonds, which is the strongest evidence that the peak at 503 nm observed in photo- and ionoluminescence is in fact not related to any nitrogen defect. The 3H center has its maximum absorption at a fluence between 3×10^{12} and $7 \times 10^{12}\,\mathrm{cm}^{-2}$. One peculiarity is identified in the trend of the GR1 ZPL in type Ib diamond irradiated at room temperature. Its single impact cross section is $(8 \pm 3)\,\mathrm{nm}^2$ and thus considerably lower in comparison to $(18 \pm 3)\,\mathrm{nm}^2$ (at 50 K) and the CVD diamonds with (18 ± 2) to $(24 \pm 2)\,\mathrm{nm}^2$. This trend has not been observed for the GR1 phonon sideband. A possible explanation is that the GR1 phonon sideband is formed by all vacancies in the diamond, including those which are also bound in other complex defects (e.g., NV^0centers), while the ZPL absorption intensity is correlated solely with isolated vacancies. This assumption is supported by the fact that only type Ib diamond contains extrinsic defects that can potentially form complex defects with diamond vacancies. Irradiation at 50 K is severely limiting defect diffusion and hence the production of these complex defects. To investigate the ion-induced dynamics of the nitrogen A (N_4V), B (N_2) and C centers (N_s), in-situ FT-IR absorption spectroscopy was performed. The absorption of both A and B centers increases for ^{197}Au ion fluences $\geq 1 \times 10^{12}\,\mathrm{cm}^{-2}$, indicating the direct radiation-induced creation of nitrogen B centers without additional annealing. The evolution is described well by the direct impact model. The corresponding cross sections for A centers and B centers is $(6.7 \pm 0.1)\,\mathrm{nm}^2$ and $(4.8 \pm 0.1)\,\mathrm{nm}^2$, respectively. This indicates no significant nitrogen aggregation at fluences $<1.5 \times 10^{13}\,\mathrm{cm}^{-2}$. Thus, nitrogen aggregate defects do not contribute to the ionoluminescence signal of diamonds at fluences below $1 \times 10^{12}\,\mathrm{cm}^{-2}$. Together with the abscence of H3 centers (N_2V) in any PL and UV/vis measurements, and the small difference in cross section between A and B centers, indicates that N_2V is not produced in large concentrations by ion irradiation as an intermediate product in the nitrogen aggregation of A centers into B centers.

Given the presented results, diamond (-based metal matrix composite) is a poor candiate for beam diagnostic luminescence screens. Diamond and diamond-based metal matrix composites are exceptionally radiation-hard in terms of structural and thermo-mechanical stability due to the abscence of ion tracks in both the diamonds and the metal matrix. But, the luminescence properties, especially those under excitation with heavy ion beams, are changing rapidly. In comparison to chromium-doped alumina, which is presently the standard material for luminescence screens at both GSI and CERN, the use of diamond suffers from various drawbacks. The ion-induced luminescence intensity is spread over a large wavelength range with two distinct bands in the visible green (at ∼530 nm) and in the near-infrared (at ∼845 nm). While the near-infrared band decreases in intensity with increasing ion fluence, the green band also changes its shape and evolves into three different components. Diamond looses at least 80 % of its initial ionoluminescence intensity after $2 \times 10^{11}\,\mathrm{cm}^{-2}$ 4.8 MeV/n ^{197}Au ions. To induce the same loss of intensity, chromium-doped alumina requires $1 \times 10^{12}\,\mathrm{cm}^{-2}$ 5.9 MeV/n ^{197}Au (which has virtually identical peak electronic energy loss at the surface in comparison to 4.8 MeV/n) [25]. Moreover, the emission efficiency of chromium-doped alumina is at least 100 times larger than diamond under the same irradiation conditions.

Lastly, the author would like to challenge the general assumption that radiation damage in diamond is solely driven by nuclear energy loss. Depth-resolved PL measurements showed a strong sensitivity of various color centers towards electronic energy loss. These defects produce additional energy levels within the diamond band gap that influence the dielectric function. Hence, it might be possible to connect radiation-induced changes in electrical properties, that are relevant for diamond detector applications, to changes in optical properties since both depend on the dielectric function. Presently, most literature of radiation-induced degradation of electric properties in diamond is related to irradiation effects of protons or neutrons. Our results might be especially interesting for the diamond detectors in future FAIR experiments that are exposed to heavier particles and therefore higher electronic energy losses. Also, the presented results might be of interest regarding the dynamics of radio coloration in diamonds and aggregation of nitrogen on geological timescales due to natural radiation. Many of the color centers reported in this work are unambiguously connected to the presence of crystallographic defects. Future molecular dynamic simulations in combination with the thermal spike model could check if the simulations reliably predict the presence of the radiation-induced defects presented in this work.

High-Power Pulsed Radiation Effects in Graphitic Materials

The variety of commercially available graphite grades vary hugely in terms of density, anisotropy, micro- & mesostructures, thermal, electrical, and mechanical properties. While figures of merit can indicate the most suitable graphitic material for a beam intercepting device, e.g., the beam dump of SIS100 or the target of the Super-FRS at FAIR, dedicated experiments are necessary to investigate the dynamic behavior of graphite materials under these extreme conditions.

This work introduced the experimental results of high-power pulsed beam irradiation of graphitic materials. Samples were irradiated with short pulse 440 GeV/c proton beams of varying beam intensity at the HiRadMat facility of CERN. Using a set of laser Doppler vibrometers the radial surface velocity was measured on-line after pulsed beam irradiation. Investigated samples had densities between 0.5 and 2.2 $\mathrm{g\,cm^{-3}}$ and represented a cross section of materials relevant for beam intercepting devices. The level of anisotropy varied from model materials like Thermal Pyrolytic Graphite, that exhibits material properties close to ideal graphite, to fully isotropic polycrystalline graphite or glassy carbon. Between different samples of the same type of graphite, samples exhibited different microstructures, e.g., varying precursor particle size, porosity, or type of reinforcement in anisotropic carbon-fiber reinforced graphites. This work concentrated predominantly on the dynamic response of polycrystalline graphites, due to their application in beam intercepting devices at FAIR.

Various isotropic polycrystalline graphite were irradiated with a series of high-intensity 440 GeV/c proton beam pulses of intensities between 4.3×10^{12} ppp (0.9 µs pulse length) and 3.5×10^{13} ppp (7.2 µs) and transverse beam sizes of $\sigma_{x,y} \sim 0.3$ mm. At the maximum beam intensity, a peak energy density between 3 and ~3.5 $\mathrm{kJ\,cm^{-3}}$ (corresponding to a maximum specific energy of up to 2 $\mathrm{kJ\,g^{-1}}$) was deposited in the samples that induced a peak temperature increase ΔT of up to ~1200 K.

Polycrystalline graphite samples of different particle sizes showed a clear correlation between particle size and damping of beam-induced pressure waves. POCO ZEE, the material with the smallest particle size of 1 µm and no filler phase, has a damping time constant τ_D of (610 ± 19) µs in comparison to SGL Carbon polycrystalline graphites (particle sizes between 7 and 20 µm and a filler phase) with a damping time constant between (211 ± 10) and (258 ± 13) µs. Fourier and continuous wavelet transformation clearly showed components of the dynamic response at fundamental vibration frequency of these samples. Axial vibration frequencies were measured around (130 ± 10) kHz in all samples, while first order radial vibration frequencies were around (170 ± 20) kHz. Given the cylindrical sample geometry with both 10 mm outer diameter and length, these frequencies are in good agreement with analytical models of the uncoupled axial and radial vibration frequencies of long cylinders.

As Fourier spectra of the dynamic response did not degrade with increasing beam intensity, the dynamic response of all polycrystalline graphite samples is assumed to be fully elastic. Thus, Young's modulus and Poisson's ratio of polycrystalline graphite samples were estimated using the measured axial and radial vibration frequencies. The dynamic response of SGL Carbon R6650 and POCO ZEE was cross-checked with finite-element thermo-mechanical simulations using ANSYS Mechanical. Parameter scans yielded a Young's modulus and Poisson's ratio of 11.38 GPa and 0.186 for SGL Carbon R6650, and 12.7 GPa and 0.28 for POCO ZEE. In both materials the radial surface velocity was simulated with $\leq 10\,\%$ deviation with respect to the experiment. Modal analysis showed modes at natural frequencies that were consistent with the frequencies observed experimentally. Considering irradiation with the maximum beam intensity and a peak beam-induced energy density of ~3.5 $\mathrm{kJ\,cm^{-3}}$, thermo-mechanical simulations of SGL Carbon R6650 indicate a maximum compressive stress of 68 MPa, which is below the material's compressive and flexural strength. Compared to the peak energy density that will be reached in the Super-FRS production target of ~2 $\mathrm{kJ\,cm^{-3}}$, the results of this study suggest that SGL Carbon R6650 should be able to withstand the beam-induced stresses during operation at FAIR in the absence of radiation damage.

In addition to the bulk graphite samples, graphite samples that contained a tantalum core were tested in beam conditions were severe plastic deformation occurs in the tantalum cores and as indicated in this work, also in the surrounding graphite. While the non-linear behavior of tantalum can be simulated well in these beam conditions, the behavior of graphite in this highly non-linear regime is poorly understood.

Nine tantalum-core/graphite-shell samples were irradiated by high-power proton beam pulses to measure the beam-induced dynamic response. Each sample was irradiated with 440 GeV/c proton beams of increasing intensity and pulse length between 5×10^{10} (25 ns) and 1.7×10^{12} ppp (600 ns). Out of the nine materials, two isotropic polycrystalline graphite grades with different precursor particle size and microstructure, SGL Carbon R6650 with 7 µm particle size with a filler phase and POCO ZEE with 1 µm particle size and no filler phase were described in detail. Furthermore, two anisotropic carbon-fiber reinforced graphite (CFC) materials (~1.5 g cm^{-3}), pyrolyzed SGL Carbon Premium with a 2D fiber-reinforcement and 3D-reinforced ArianaGroup Sepcarb, and low-density POCO FOAM (0.5 g cm^{-3}) were presented in addition.

At the maximum beam intensity of 1.7×10^{12} ppp, the most loaded tantalum cores was exposed to a maximum of ~5 kJ cm^{-3} leading to a temperature increase of up to ~1450 K. The resulting beam-induced stresses in the tantalum core are coupling into the surrounding graphite as pressure waves. Both the radial and axial pressure wave of the tantalum core were successfully identified in the dynamic response, measured on the surface of the surrounding graphite, and agreed well with the analytical model. To cross-correlate the dynamic response, modal analysis and thermo-mechanical finite element simulations were performed on tantalum/SGL R6650 using ANSYS Mechanical. Several vibration modes with radial symmetry were identified in the modal analysis, that agree with both the dominant frequencies of the Fourier and continuous wavelet transform of the experimental data. Further comparison of the experimental data with thermo-mechanical simulations at small beam intensities $\leq 6 \times 10^{11}$ ppp ($\leq$0.1 kJ cm^{-3}) indicate fully elastic behavior of both the tantalum and surrounding graphite in these beam conditions.

In each sample, the maximum surface velocity increases linearly with increasing beam intensity (and therefore deposited energy density in the tantalum core) up to a threshold. Beyond this threshold, the surface velocity either decreases or exhibits an erratic trend by strongly deviating from linearity. This sub-linear behavior is interpreted as an indication of material failure. Unfortunately, identifying a strict failure limit for each sample is not possible. It is expected that the onset of plastic deformation in the tantalum core occurs at beam intensities between 6 and 9×10^{11} ppp (~1.7 to 2.6 kJ cm^{-3}). But due to the experiment layout, samples were irradiated multiple times with beam pulses of increasing intensities and therefore accumulated beam-induced deformation. Thus, the experimental data is not directly indicative of the pristine material response.

In SGL Carbon R6650, which surrounded the tantalum core exposed to the highest energy deposition density, the first signs of failure were observed at a pulse intensity of $\sim 6 \times 10^{11}$ ppp (~1.7 kJ cm^{-3}) where a lower amplitude of the second radial oscillation of 2.5 m s^{-1} in comparison to the first oscillation of 5 m s^{-1} was observed. But, a linear increase of the maximum surface velocity is observed up to ~3.4 kJ cm^{-3} which might indicate that the mechanical interface between the tantalum core and the surrounding graphite is still intact. Hence, it is assumed that the sublinear radial velocity trend >3.4 kJ cm^{-3} is due to failure in the surrounding graphite. On the other hand, POCO ZEE exhibits sublinear radial surface velocities at energy deposition densities >1 kJ cm^{-3}, which is attributed to (local) failure of the graphite surrounding the tantalum core.

The dynamic response of carbon-fiber reinforced graphite exhibited a dramatic change at deposited energy densities within the tantalum core <1 kJ cm^{-3}. Massive degradation of the frequency response was observed by both fast Fourier and continuous wavelet transformation. Based on the larger flexural strength of the investigated CFC grades in comparison to polycrystalline graphite, CFCs were considered more robust. The observed changes in the dynamic response are hence attributed to local failure of the low-strength graphite matrix in these materials. While fiber-reinforcement leads to high strength in the reinforcement direction, the graphite matrix in ArianeGroup Sepcarb has a tensile strength of only 17 MPa for example. The dynamic response of POCO FOAM, with the lowest strength of all investigated graphitic materials, has a strictly linear behavior with increasing pulse intensity. Up to a beam intensity of 6×10^{11} ppp (1.6 kJ cm^{-3} in the tantalum core), POCO FOAM exhibited a constant dynamic response in terms of frequency content. Degradation of the dynamic response occurred only at beam intensities larger than 1.2×10^{12} ppp (3.2 kJ cm^{-3}).

The used sample geometry, a high-Z material surrounded by a graphite shell, is indicative of a potential layout of the pbar production target at FAIR. Catastrophic failure was not observed in any of the tantalum-core/graphite-shell samples. Thus, proper operation with respect to pbar production would be ensured by all investigated graphite materials. The presented data indicates that energy densities beyond 4 kJ cm^{-3} (within the tantalum core) will lead to some kind of (local) failure in the surrounding graphite independent of the used graphite material. Ultimately, to be able to scale to the operational conditions of the FAIR pbar target, thermo-mechanical finite element simulations will be necessary. The results of this work should enable the development and benchmarking of equation of states and strength models for explicit simulations over a large range of stresses and strain rates to reproduce both the elastic behavior and gradual material failure that was observed experimentally for various graphite materials.

The results on low-density graphite foams with 0.5 and 0.9 g cm^{-3} indicate that these foams are robust enough to endure a few high-power beam pulses at least. The low density leads to lower energy loss by charged particle beams in comparison to graphite grades with higher densities. Graphite foam might be an interesting candidate material for high-power beam dumps to ’dilute’ the peak energy density deposited by high-energy particle beams. Thus, future experiments should investigate the robustness towards tens or hundreds of beam pulses to assess the performance of these materials for long term operation in beam dumps, which must function for thousands of cycles within their service life.

A post-irradiation characterization campaign of the samples was not possible within this work due to the residual radioactivity of the experiment and the samples. After sufficient radioactive cooldown, beam-induced material modification of the samples, for example internal cracks, could be identified by X-ray tomography measurements. These could be potentially correlated with the trends observed on the tantalum core samples. Raman measurements on the irradiated surfaces of the graphite samples could show microstructural modifications, that are not due to radiation damage, but due to the accumulation of high-power pulsed beam effects.

Part V.

Appendix

A Color Centers and Swift Heavy Ion Irradiation of Diamond

A.1 Crystallographic Defects and Color Centers in Diamond

The diamond lattice can host a variety of different defects that originate from (intrinsic) lattice distortions or extrinsic substitutional or interstitial impurities. These defects can be created during synthesis of the diamonds or by external stimuli like radiation (gamma rays, electrons, neutrons, protons and ions), heating or pressure. The assignment of diamonds to different types is based on the species and concentration of the major defects in the diamond lattice which in turn influence the material properties (c.f. Table 3.1). The most dramatic impact on material properties can be observed in the color of diamonds. Transparency of diamonds increases with decreasing defect concentration. Nitrogen impurities induce a yellow color, dislocation loops a brown color and boron impurities a blue color in diamonds. The electronic properties of diamond are changing together with the color as well. At high concentrations of boron, diamond can have a metal-like conductivity of $0.05\,\Omega\,\mathrm{cm}$ while retaining a thermal conductivity of $700\,\mathrm{W\,m^{-1}\,K^{-1}}$ [273].

Hundreds of different defects were identified in the diamond lattice by different spectroscopic methods [140]. Depending on the defect (structure), a defect can be "active" in one or multiple spectroscopic methods that include electron paramagnetic resonance (EPR), photoluminescence (PL), cathodo-luminescence (CL), absorption of infrared light (IR) and the absorption of UV and visible light (UV/vis). Historically, the IR absorption spectrum is used to distinguish and classify diamonds into two main group; with and without nitrogen impurities, because nitrogen is the most common impurity in natural and synthetic diamonds. Eventually, those two groups were extended to account for the state of nitrogen aggregation and the presence of boron in diamonds without any nitrogen impurities. The classification system that is widely adopted in the diamond community [76](Table 3.1) does not include all possible type of defects (and/or colors) found in natural, synthetic and/or treated diamonds [178]. Many defects traditionally have their own acronym in diamond spectroscopy which is based on the treatment of the diamond to induce/enhance the intensity of the defect, N ("Natural"), GR ("General Radiation"), R ("Radiation"), TR ("type II Radiation") or H ("Heated") followed by a number [274]. When an acronym is available for a certain defect this work will use this name when referring to said defect, otherwise the spectral position of the zero-phonon line in eV will be used.

The following sections will discuss the most important intrinsic and extrinsic defects that were identified in the diamonds investigated with photoluminescence, UV/vis absorption, IR absorption and ionoluminescence (IL) spectroscopy in this work. It shall be stressed that this overview is not exhaustive and does not necessarily include all defects which are induced by swift heavy ion irradiation, but only those which were identified in the measurements performed within this work.

A.1.1 Intrinsic Defects

Intrinsic defects are those which can occur in the diamond lattice in the absence of non-carbon atoms. These can be vacancies and interstitials in different charge states and structural configurations.

A.1.1.1 Isolated Vacancy, GR1 center

One of the most well-known and studied irradiation-induced defect in the diamond lattice is the neutral vacancy, the so-called GR1 center. GR1 is observed in nearly all irradiated diamonds [275]. It is characterized by two zero-phonon lines (a doublet), with one ZPL at 741.1 nm (1.673 eV) and the other at 750.1 nm (1.653 eV), respectively [276, 277]. Threshold displacement energies for the creation of vacancies in the diamond lattice between

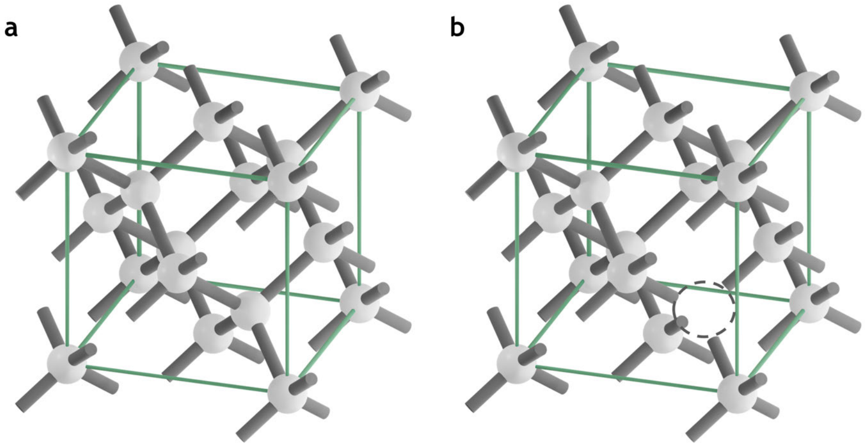

Figure A.1.: Perfect diamond lattice (a). Diamond lattice with a vacancy, indicated by the dashed circle (b).

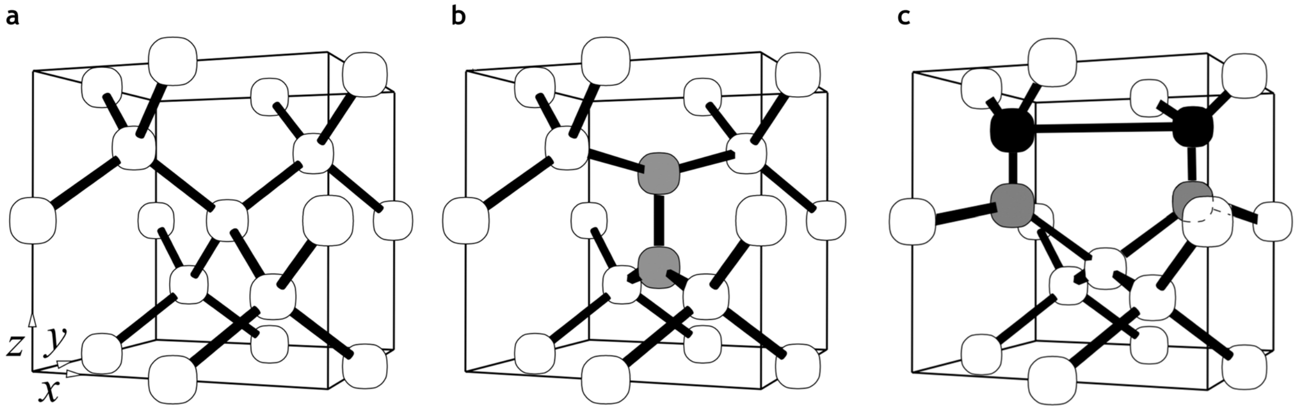

Figure A.2.: Perfect diamond lattice (a). Neutral <001>-split interstitial (b). 3H center, di-<001> split interstitial in the Humble configuration (c). Threefold coordinated interstitials are indicated in gray and fully coordinated interstitials in black. Reprinted figure with permission from Goss, J.P. *et al.* , Physical Review B, 63, 195208 2001. Copyright 2021 by the American Physical Society.

30 and 48 eV were reported [142, 143], which is considerably higher in comparison to the threshold displacement energy in graphite of 17 eV.

The migration energy of an isolated vacancy in the diamond lattice is (2.3 ± 0.3) eV determined by isothermal annealing [278, 279]. At temperatures between 600 and 700 K a substantial amount of vacancies will recombine with interstitials (simultaneously formed with vacancies) while a fraction of the vacancies can form new complexes with other defects [280, 281]. Annealing at temperatures of at least 1100 K leads to the formation of di-vacancies [282–284].

A set of absorption lines in the wavelength range between 412 and 430 nm (2.880 and 3.010 eV), the so-called GR2 to GR8 color centers, are attributed to additional excited states of the neutral vacancy [285]. Furthermore, if electron donors are present in the diamond lattice, vacancies can capture electrons to form the so-called ND1 color center with a sharp ZPL at 393.7 nm (3.149 eV) [286] that can also be used to estimate the concentration of negative vacancies [282]. The negative vacancy has a higher migration energy than the neutral vacancy [278].

Due to the ability to form a large number of different defect complexes with other (extrinsic) defects in the lattice, the production rate of vacancies by ionizing radiation is not only a function of the deposited energy and the irradiation temperature but also depends heavily on the type of diamond to be irradiated [282, 287]. The lattice structure of an isolated vacancy is shown in Figure A.1.

A.1.1.2 <001>-split Self-interstitial

Interstitials are co-produced in the formation of vacancies. The first spectroscopic signal that proved to originate from interstitials was the so-called R2 center detected by electron paramagnetic resonance in electron irradiated defect-free diamonds [288]. Only much later this defect was identified as the split interstitial by EPR measurements under uniaxial stress [287]. According to ab-initio calculations the neutral <001>-split interstitial, I^0, was found to be the most stable split interstitial configuration in the diamond lattice [289]. Two optical absorption lines at 735.8 nm (1.685 eV center) and 666.9 nm (1.859 eV center) are attributed to the <001>-split self-interstitial [290] that are consistent with calculations for the observed symmetry and structure of the defect [291].

The migration energy during thermal annealing of the <001>-split interstitial is (1.6 ± 0.2) eV [292]. Irradiation experiments showed that the annealing during electron irradiation is different to the thermal annealing of the <001>-split interstitial [281]. A highly mobile interstitial species, labelled I^*, with a migration energy as low as 0.3 eV is apparently produced by irradiation-induced electronic excitation. This highly mobile species is therefore responsible for a five-fold increase in the concentration of interstitials (and vacancies) at irradiation temperatures below 300 K. The structure of the <001>-split self-interstitial is shown in Figure A.2b.

A.1.1.3 Di-<001>-split Self-interstitial, 3H center

The 3H center is an optically active color center in luminescence and absorption with a ZPL at 503.4 nm (2.463 eV) (not to be confused with the H3 ZPL at 503.2 nm (2.464 eV)) that is produced by irradiation in all types of diamonds. However, the production rate is higher in type Ib diamonds [293]. The intensity of the 3H center is increasing with increasing irradiation dose, but it does so only erratically [290].

The production rate of 3H centers by electron irradiation at room temperature depends heavily on the presence of nitrogen aggregates in the diamond lattice. It increases linearly with increasing A center concentration and decreases linearly with increasing B center concentration [280]. Production of 3H centers was observed at irradiation temperatures as low as 80 K [274].

The intensity of 3H centers can be increased by annealing up to 400 °C, while higher annealing temperatures reduce it. This is attributed to a charge transfer effect as illumination with UV light is able to return the original intensity up to 1000 °C [197]. Furthermore, 3H centers can be optically bleached by UV or intense blue laser illumation [294]. This also points to a charge transfer effect (photochromism) that should lead to the presence of another ZPL with the same time constant for enhancement / bleaching. Furthermore, the intensity of 3H can be quenched by the presence of neutral vacancies, GR1 centers, implying that changes in the 3H center intensity do not directly correlate with changes in its concentration [294].

The structure of 3H centers was determined to be a special configuration of the di-<001>-split self-interstitial defect. The 3H center is always accompanied by the EPR active R1 center that was well replicated within ab-initio calculations by the neutral di-<001>-split self-interstitial [295]. The vibrational properties of 3H centers fit to the positively charged "Humble configuration" of the di-<001>-split self-interstitial [295]. The structure of the defect is shown in Figure A.2c.

A.1.2 Nitrogen-related defects

Nitrogen impurities are the most studied extrinsic defects in diamonds. The small mismatch in atomic radii between nitrogen and carbon leads to a significant solubility of nitrogen (together with hydrogen and boron) in the diamond lattice. Furthermore, the presence of nitrogen leads to an increased growth rate of diamonds in both HPHT and CVD synthesis (cf. subsection 3.1.1). Nitrogen concentrations as high as 5000 ppm in natural diamonds [296], 3000 ppm in HPHT synthesized diamonds [170] and 10 000 ppm in detonation nanodiamonds [297] were reported. Due to the stiffness of the diamond lattice most impurity defects are substitutional with nitrogen being one of the few extrinsic defects that also forms (complex) interstitial defects [298, 299].

The abundance of nitrogen-containing diamonds lead to the classification of diamonds based on the type of nitrogen defects. Substitutional nitrogen and more complex aggregated nitrogen defects are easily detected in infrared

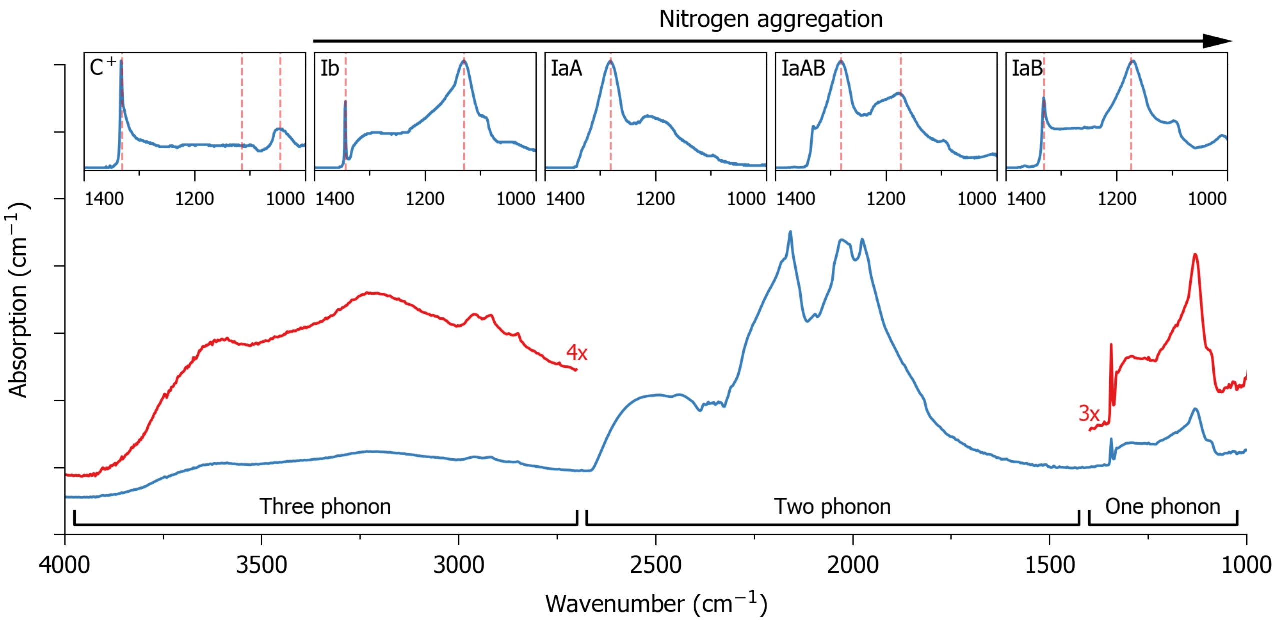

Figure A.3.: Characteristic infrared absorption of a pristine type Ib diamond. The one phonon range relates to defect-induced absorption bands and especially nitrogen. Intrinsic absorption of the diamond lattice corresponds to the two phonon region. The three phonon region is created by hydrogen-bond vibrations. Zoomed regions of the spectrum are presented in red. The insets show the features of the different nitrogen centers and the aggregation pathway by annealing. Important absorption features are indicated by the dashed lines. The standard spectra of the nitrogen centers are adapted from the "DiaMap" software [200].

absorption spectroscopy. Diamonds classified as type I diamonds contain nitrogen while type II diamonds contain only trace amounts of nitrogen (≤ 5 ppm). Type I is further divided based on the presence of aggregated, type Ia, or single substitutional nitrogen, so-called C centers, as type Ib. Type Ia is further sub-divided based on the aggregation stage of nitrogen, diamonds containing a majority of nitrogen pairs N_2, A centers, are classified as type IaA while diamonds majorly containing N_4V, B centers, are classified as type IaB [76, 290] (c.f. Table 3.1). The characteristic infrared absorption of the different type I diamonds is shown in Figure A.3.

Mixtures of different nitrogen defects occur in natural diamonds. The specific mixing and aggregation of nitrogen defects, which can be determined based on the intensity of different infrared absorption lines, can be used for geo-dating of natural diamonds and can be used to distinguish between natural and synthetic diamonds [300, 301].

Apart from infrared active defects, nitrogen forms a large number of defect complexes together with intrinsic defects that can be optically active in absorption and photoluminescence spectroscopy. A well-known example is the nitrogen-vacancy center, NV, in its neutral and negative charge state. Other defects include N_2V that depending on its charge state is either the (neutral) H3 center or the (negative) H2 center, the H4 center, N_4V_2 and N3 center, N_3V [302].

A.1.2.1 C Center

The C center is the simplest nitrogen defect in the diamond lattice. A carbon atom is substituted by a nitrogen atom in the diamond lattice as shown in Figure A.4a. Diamonds rich in substitutional nitrogen are classified as type Ib diamonds. Natural type Ib diamonds occur only rarely and are known as "canary diamonds" gemstones due to their deep yellow to brown color. Substitutional nitrogen acts as a "deep donor" that can donate an electron and form donor energy levels within the band gap. The donor electrons can be excited to the conduction band by light with a wavelengths smaller than ~564 nm (~2.2 eV) that results in the yellow color of such diamonds and can be detected as an absorption edge in UV/vis absorption spectroscopy [294].

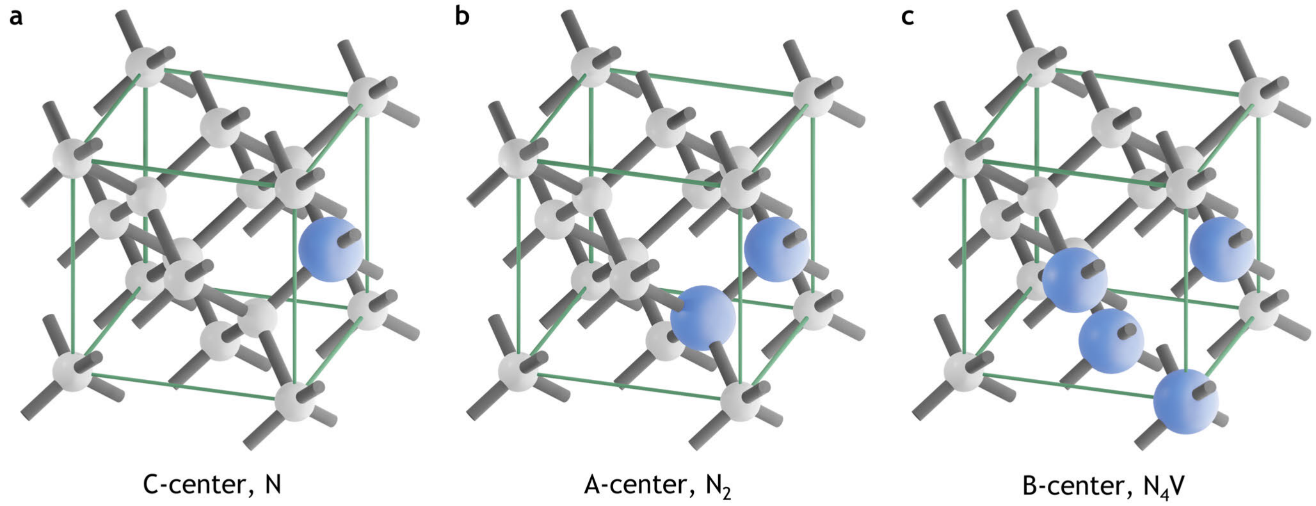

Figure A.4.: Structure of infrared active nitrogen defects in diamond. The C center, N_s (a). The A center, N_2 (b). The B center, N_4V (c). Nitrogen atoms are indicated in blue.

The infrared absorption spectrum of C centers is characterized by a sharp peak at 1344 cm^{-1} and a broad feature at 1130 cm^{-1} (c.f. Figure A.3 which are routinely used to determine the concentration of nitrogen C centers [303]. Additionally, if acceptor defects like the GR1 center, V^0, co-exist in the diamond lattice C centers can be transformed into positively charged C+ centers, N^+. The C+ center has a characteristic infrared absorption with a sharp peak at 1332 cm^{-1} and multiple broader, weaker peaks at 1115 cm^{-1}, 1046 cm^{-1} and 950 cm^{-1} [201].

A.1.2.2 A Center

The A center is the first aggregation stage of nitrogen formed by a pair of neutral substitutional nitrogen atoms on adjacent lattice sites, N_2 or N=N and is shown in Figure A.4b. It is the most common defect in natural diamonds. It does not impart color on diamonds as it produces a UV absorption edge at around ~310 nm (~4 eV) outside the visible spectrum [77]. The A center has a characteristic infrared absorption without sharp features that distinguishes it considerably from the B and C centers (c.f. Figure A.3). The strongest peak at 1282 cm^{-1} is used to estimate the concentration of nitrogen A centers. [202].

A.1.2.3 B Center

The exact atomic structure of the B center in diamonds is not exactly known since no direct spectroscopic evidence was found [304]. But, the general consensus is that the B center consists of four nitrogen atoms surrounding a vacancy, N_4V [301] shown in Figure A.4c. The B center exhibits characteristic infrared absorption with a broad feature at 1280 cm^{-1} and a shark peak at the Raman frequency of 1332 cm^{-1} (c.f. Figure A.3) with the latter being used to determine the concentration of nitrogen B centers [203].

B centers naturally do not occur together with C centers due to the nearly full conversion of C centers into A center aggregates [305]. The direct formation of B centers by irradiation has not been observed yet. But, formation of B centers (accompanied by A and C centers) after annealing of neutron irradiated type Ib diamonds was observed [147].

A.1.2.4 Nitrogen-Vacancy Centers

The nitrogen-vacancy center, NV, is the simplest defect complex that nitrogen impurities form in the diamond lattice and are optically active in their neutral, $NV^0$and negative charge state, NV^-. The negatively charged NV^-center is

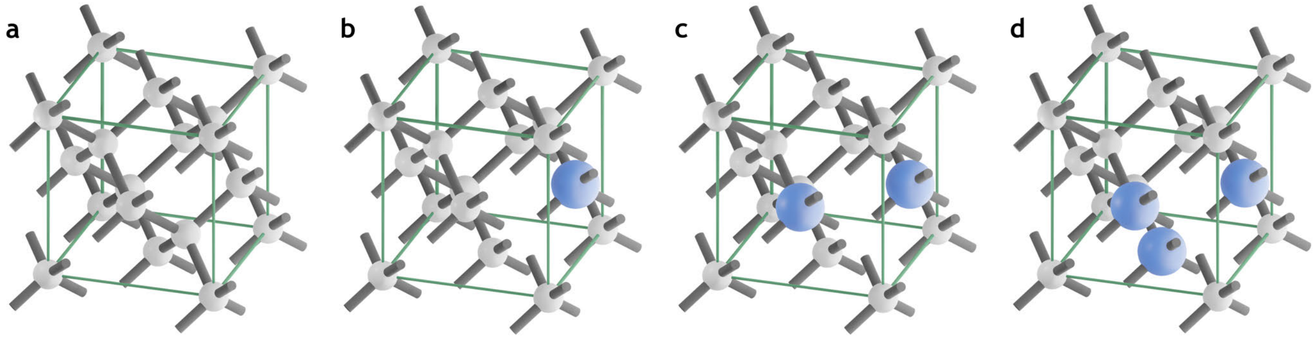

Figure A.5.: Perfect diamond lattice (a). NV center, NV (b). H3 center, N_2V (c). N3 center, N_3V (d). Nitrogen atoms are indicated in blue.

one of the most studied defects in diamond[1] due to its potential application in quantum computing and sensing. Single defects can act as single photon sources [306] and individual or ensemble defects can be used for optically detected magnetic resonance (ODMR) [307] with spin coherence times of >1 ms at room temperature [308]. For a more detailed overview of its properties the reader is referred to the review in [309]. The atomic structure of the NV^-center is shown in figure A.5b.

The characteristic features of $NV^0$and $NV^-$are their respective ZPLs at 575 nm (2.156 eV) [310] and 637 nm (1.945 eV) [311], that are active in absorption, photo- and cathodoluminescence. The structure of the NV^-center was determined by the correlation between the annealing behavior of neutral and negative vacancies, GR1 and ND1 centers [77], and confirmed by EPR spectroscopy [312].

In the absence of an EPR signal the ZPL at 575 nm was assigned to NV^0 based on the correlation between the intensities of the two ZPLs at 575 nm and 638 nm by annealing of neutron irradiated diamonds [313]. Further evidence is provided by the charge transfer between $NV^0$and $NV^-$by photoconversion [314].

The migration energy of NV centers of ∼4.5 eV [182, 315, 316] is considerably lower than the migration energy of substitutional nitrogen, 6.3 eV. This difference is experimentally observed in the increased aggregation rate of irradiated diamonds during annealing [305]. Nitrogen vacancies can be created by electron or neutron irradiation of type Ib diamonds and subsequent annealing at temperatures of >600 °C [317, 318], directly by irradiation with swift heavy ions [171] or ion-implantation of nitrogen into type IIa diamonds and subsequent annealing. The latter approach even allows to control the spatial distribution of nitrogen vacancies [317].

In addition to the previously introduced A and B center nitrogen aggregates, there are several multi-nitrogen-vacancy defects, N_nV. Photoluminescent active ZPLs at 986 nm (1.257 eV) and 503.2 nm (2.463 eV) belong to the negative and neutral charge states of the di-nitrogen vacancy, N_2V, the so-called H2 and H3 center, respectively. The structure of N_2V^- was directly identified by its EPR signal [319] while the connection between H2 and H3 centers was established based on the observed photochromism between the two centers [320, 321]. The formation energy of N_2V (in the neutral charge state) is 5.41 eV according to ab-initio density functional theory (DFT) calculations [182]. The structure of the H3 center is shown in Figure A.5c.

A.1.2.5 Nitrogen Aggregation

Annealing at high temperatures (up to >2000 °C) and possibly high pressures (several GPa) leads to the aggregation of single substitutional nitrogen into complexes such as N_2 [202] and at longer annealing times and/or higher temperatures N_4V [203]. In its simplest form this process can be described as:

$$4\,\mathrm{N} \rightleftharpoons 2\,\mathrm{N}_2 \rightleftharpoons \mathrm{N}_4\mathrm{V} + \mathrm{I}\cdot \qquad \{1\}$$

Where each step is the result of different (multi-staged) aggregation pathways that can occur in reverse as well. The extent of aggregation and the specific mixing of different aggregate species can be used to estimate the time and temperature experienced by natural diamonds in the Earth mantle and to distinguish between natural and synthetic diamonds [300, 301].

---

[1] http://apps.webofknowledge.com/CitationReport.do?product=WOS&search_mode=CitationReport&SID=E48HIB3gMNTr3GORzCE&page=1&cr_pqid=1&viewType=summary&colName=WOS

The aggregation of C centers into A centers ($2\,\mathrm{N} \longrightarrow \mathrm{N}_2$) is significantly enhanced by the presence of radiation damage at annealing temperatures of 1500 °C [305]. It was observed that the concentration of aggregated nitrogen exceeded the vacancy concentration by a factor of 100, implying that substitutional nitrogen is a much more efficient trap for vacancies than N_2. At high temperatures NV defects diffuse through the lattice and eventually capture another N to form N_2V. Afterwards the vacancy can be emitted to repeat the process. The vacancy mediated process can be described as:

$$\begin{aligned} \mathrm{N} + \mathrm{V} &\rightleftharpoons \mathrm{NV} && \text{(step 1)} \\ \mathrm{NV} + \mathrm{N} &\rightleftharpoons \mathrm{N_2V} && \text{(step 2)} \end{aligned} \tag{2}$$

which shows how a small number of vacancies can significantly increase the nitrogen aggregation rate. To produce NV centers by annealing of irradiated type Ib diamonds, the annealing temperature and pressure need to be chosen so that the undesired second step in the reaction above occurs as slow as possible. DFT calculations have shown another possible pathway involving nitrogen interstitials for nitrogen aggregation at lower temperature that is mediated by carbon interstitials, which are co-produced with vacancies [316]. The process can be described as:

$$\begin{aligned} \mathrm{N} + \mathrm{I} &\rightleftharpoons \mathrm{C} + \mathrm{N}_i && \text{(step 1)} \\ \mathrm{C} + \mathrm{N}_i + \mathrm{N} &\rightleftharpoons \mathrm{N_2} + \mathrm{I} && \text{(step 2)} \end{aligned} \tag{3}$$

where the final carbon interstitial is able to repeat the process. Interstitial mediated aggregation is most probably observed in synthetic HPHT diamonds grown with a Ni or Co-containing catalyst as it is believed that substitutional Ni or Co, incorporated during growth, release interstitials that mediate aggregation [322].

The exact formation mechanism of N_4V is disputed but in the easiest form N_4V aggregation can be described by:

$$\begin{aligned} \mathrm{N_2} + \mathrm{V} &\rightleftharpoons \mathrm{N_2V} && \text{(step 1)} \\ \mathrm{N_2V} + \mathrm{N} &\rightleftharpoons \mathrm{N_3V} && \text{(step 2)} \\ \mathrm{N_3V} + \mathrm{N} &\rightleftharpoons \mathrm{N_4V} && \text{(step 3)} \end{aligned} \tag{4}$$

which is supported by the fact that N3 centers, N_3V (shown in Figure A.5d) are nearly always observed together with B centers,N_4V [301].

A.1.2.6 Nickel-related Defects

Since nickel is a catalysts for the growth of synthetic diamonds during HPHT synthesis, quite a number of diamond color centers are associated with nickel. Generally, due to the large size difference between nickel and carbon, nickel is preferentially incorporated as an interstitial into the diamond lattice [323] even though substitutional nickel defects can also form [324]. The most studied nickel-related defect is the NiV defect that can have charge states of 0, 1- and 2- [325]. The NiV^- 1.40 eV center has a ZPL doublet at 884.85 and 883.15 nm and is active in PL and CL [326, 327]. It is observed in synthethic CVD and HPHT diamond. Another nickel-related defect is the 2.157 eV center with its ZPL at 574.8 nm which is a center that is only observed in high-nitrogen synthetic diamonds grown in the presence of nickel and annealed at temperatures beyond 1700 °C.

A.1.2.7 Radiation-induced Defects

Radiation-induced defects are usually well studied in the context of electron irradiation due to the inherent connection to cathodoluminescence spectroscopy [191]. Radiation-induced defects naturally occur as competing and therefore undesired by-products during implantation of nitrogen for the (controlled) creation of nitrogen-vacancy centers [178]. Since irradiation with ions (and electrons for that matter) is both a source of newly created lattice defects and radiation-induced annealing, radiation-induced defects cannot be strictly separated from defects created by annealing. For example, most of the nitrogen-related defects introduced previously can be created by a combination of irradiation and annealing, while the 3H center is directly created by irradiation [178]. As already mentioned, data on the evolution of color center intensity with increasing fluence is scarce and, if available, the information is usually reported for low energy ion irradiation in the range of a few keV.

The most intuitive radiation-induced defect is the GR1 center (neutral vacancies). Most striking in the context of radiation damage is the observation that GR1 production is most efficient in the high electronic energy loss regime [191]. Furthermore, the creation efficiency is higher for lighter ions, whereas irradiation with heavy ions produces vacancy clusters rather than isolated vacancies [178]. Also, the luminescence intensity of GR1 and 3H center has a non-linear fluence dependence. Both are enhanced by irradiation until reaching a maximum before decreasing with fluence due to aggregation of vacancies. The maximum GR1 intensity was observed at a vacancy density of $\sim 7 \times 10^{19}\,\mathrm{cm}^{-3}$ [178].

A.2 Photoluminescence Spectroscopy on Irradiated Diamond

To complement ionoluminescence spectroscopy measurements a large number of pristine and irradiated diamonds, both bulk and embedded in metal matrix composites, were characterized with photoluminescence spectroscopy. The first section qualitatively discusses the irradiation-induced changes in different diamond-based metal matrix composites and the measurement-related issues with these types of samples.

A.2.1 Diamond-Based Metal Matrix Composites and Bulk HPHT Diamond

Different diamond-based metal matrix composites were irradiated with increasing fluences of 4.8 MeV/n ^{132}Xe, ^{197}Au and ^{238}U ions. High-statistics photoluminescence (PL) measurements under 473 nm excitation, based on at least 100 individual measurements, are presented in Figure A.6. The peculiar representation of the measurement data is necessary because a representation of a simple average and a standard deviation would indicate non-physical (negative) intensities for wavelengths with the largest intensity scattering. A fully quantitative analysis of comparable data on model system diamonds is presented in section 7.3.

The photoluminescence spectra of the pristine samples can be divided in two characteristic regions; below and above ∼600 nm. The region below 600 nm is dominated by the Raman line at 504.8 nm ($1332\,\mathrm{cm}^{-1}$) and PL signals from the 3H or H3 center and their phonon replicas, both in the stokes and anti-stokes region with respect to their ZPLs at 504.6 nm and 504.4 nm, respectively. Above 575 nm, spectra are dominated by the ZPLs and the phonon sideband (PSB) of the neutral nitrogen-vacancy $\mathrm{NV}^-$and negative NV^-centers at 575 nm and 638 nm, respectively.

Pristine diamond-based titanium matrix (Ti-Dia) composite exhibits the overall smallest scattering between different measurement positions while the diamond-based copper matrix composites with 45 µm (Cu-Dia45) exhibits strong scattering in the range above 600 nm and diamond-based copper matrix composite with 100 µm average diamond size (Cu-Dia100) exhibits strong scattering over the whole wavelength range.

With increasing fluence all samples show the same qualitative trend. At a fluence of $1 \times 10^{12}\,\mathrm{cm}^{-2}$ the intensity of NV centers is increasing in all samples while the 3H/H3 range is rather stable. For larger fluences the intensity of NV centers decreases while a change within the 3H/H3 range below 600 nm can be observed. The intensity is decreasing inhomogeneously between the different samples and ions while the peak at the position of the Raman line is broadening. At the highest fluences of $5 \times 10^{13}\,\mathrm{cm}^{-2}$ and $1 \times 10^{14}\,\mathrm{cm}^{-2}$ spectra of both Cu-Dia45 and Cu-Dia100 have a peak around ∼740 nm that can be attributed to the GR1 center which is related to isolated vacancies within the diamond lattice.

The scattering between different measurement locations becomes smaller with increasing irradiation fluence. This 'spatial homogenization' is explained by the homogeneous coverage of the diamond with multiple ions at high fluences. Furthermore, the observed radiation-induced discoloration can be explained by a loss of transmission. This loss of transmission, or increase of absorption, within the irradiated volume leads to the excitation laser being attenuated more in comparison to the pristine sample thus leading to a smaller probing volume which is thus assumed to be more homogeneous.

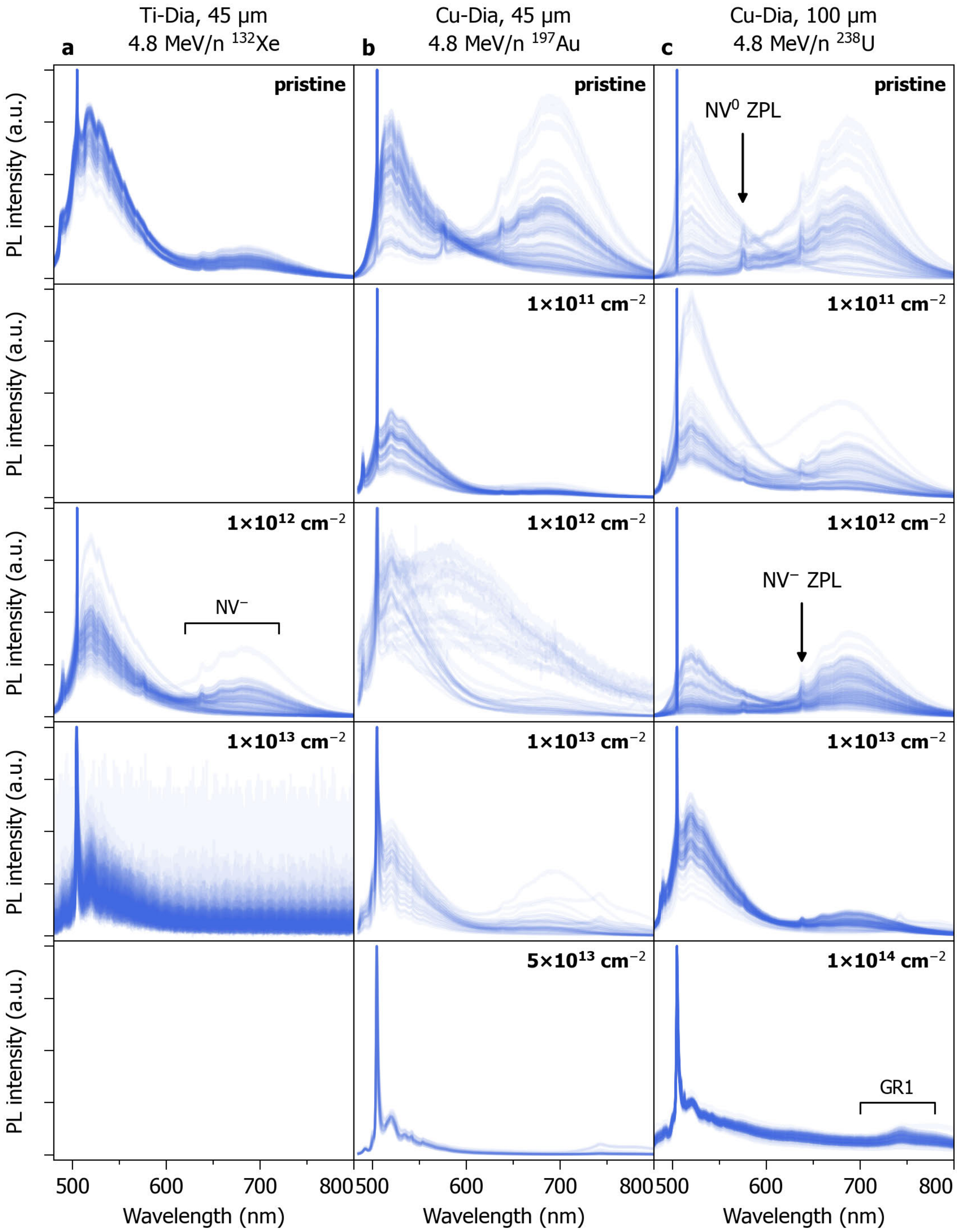

Figure A.6.: Photoluminescence spectra of different diamond-based metal matrix composites under 473 nm excitation irradiated with different 4.8 MeV/n ions. Spectral intensities are normalized to the intensity of the diamond Raman line at 504.8 nm. Diamond-based titanium matrix (Ti-Dia) composite under irradiation with ^{132}Xe (a), diamond-based copper matrix (Cu-Dia) composite with 45 µm average diamond size and irradiation with 4.8 MeV/n ^{197}Au (b) and Cu-Dia with 100 µm average diamond size and irradiation with ^{238}U. Color coding represents the normalized probability to measure a given photoluminescence intensity as a function of wavelength for at least 100 individual measurement locations. Higher opacity indicates higher probabilities.

These observations indicate the major obstacles in the photoluminescence characterization and comparison between different diamond-based metal matrix composites. In pristine samples, spectra depend heavily on the measurement position and large statistics are necessary for representative measurements. This is tentatively attributed to the large mean free path length of the excitation laser within the diamond particles in combination with the random shape of the diamond particles which leads to multiple internal reflections of the excitation laser within the diamond.

In combination with the different diamond grids and processing parameters used in the production different PL spectra are measured in the pristine composites. Another aspect is the significance of the measured intensity. Even though the intensities of individual measurements are normalized to the intensity of the diamond Raman line, the presence of either the 3H and/or H3 center (identified by the presence of their phonon sidebands) with ZPLs as close as a nanometer to the diamond Raman line, is obscuring the 'true' intensity of the diamond Raman line. Hence, it is impossible to properly deconvolve the intensity of the diamond Raman line. Or simply put, the used normalization approach has little significance in the absence of a true standard.

Some of the measurements exhibit a periodic modulation of the spectral intensity, e.g. Ti-Dia at $1 \times 10^{13}\,\mathrm{cm}^{-2}$ and Cu-Dia100 in the pristine state and at $1 \times 10^{11}\,\mathrm{cm}^{-2}$. Similar intensity modulations can be observed in nanodiamonds [328] and infrared transmission measurements of samples with plane-parallel surfaces [329]. Even though measurements were performed through a 'flat' surface of a diamond (cf. Figure 7.1) and the photoluminescence spectrometer is equipped with confocal optics the random orientation and shape of the diamonds leads to multiple scattering and reflection within the diamonds. The measured intensity at any wavelength is therefore not indicative of the diamond volume within the confocal plane but is convoluted with contributions from multiple scattering and/or reflections.

A.2.2 HPHT Diamond

The suitability of Sumitomo PDXC HPHT diamonds as the appropriate model system for the characterization of ionoluminescence properties with respect to the diamond-based metal matrix composites was already discussed in section 7.2. Figure A.7 shows PL measurements on these diamonds before and after irradiation with 4.8 MeV/n ^{197}Au ions under excitation with 473 nm and 633 nm. Measurements on these diamonds exhibit a scattering that is small enough to use a simple representation of a single spectrum, without statistical normalization. Intensity scattering from point to point is less than 5 %.

Even though these diamonds exhibit a similar ionoluminescence spectrum in comparison to the composite samples, the PL spectra show significant differences. The pristine samples have a smaller signal below 600 nm and virtually no intensity in the NV center related wavelength range above 600 nm. Since it will be shown later that the signal below 600 nm can be clearly attributed to the interstitial-related 3H center, it can be assumed that the bulk HPHT diamonds simply have a considerably lower defect density in their pristine state.

The absence of a significant NV^0or NV^-center signal in the pristine HPHT diamonds in comparison to the composites is attributed to the annealing of the composites during production. During hot isostatic pressing in the production of the composites; 30 min between 700 and 900 °C for Ti-Dia and Cu-Dia45 and up to 240 min at 900 °C for Cu-Dia100 can already lead to significant nitrogen-vacancy creation [330]. And indeed, the sample which was exhibited to the longest thermal treatment exhibits the largest nitrogen-vacancy signal as shown in Figure A.6c.

With increasing fluences a similar trend can be observed in both the bulk HPHT diamonds and composite samples. Below $1 \times 10^{12}\,\mathrm{cm}^{-2}$ the peak close to the diamond Raman line at 503 nm is very sharp and the phonon sideband at ∼520 nm increased to its maximum intensity. Simultaneously, the vacancy-related GR1 center with its ZPL at ∼745 nm is now clearly detectable. For increasing fluences the 3H/H3 peak at the diamond Raman line under blue excitation is broadening significantly while the GR1 center color center intensity is larger than the Raman line under 633 nm excitation.

In conclusion, PL measurements on irradiated HPHT diamonds replicate the trend observed on the irradiated composites well enough, from the difference in the NV center related signals, which is attributed to the thermal annealing of the diamonds in the composites during production. The large volume and high lattice quality (indicated by the absence of interstitial-related 3H PL signal in the pristine sample) leads to a much reduced scattering of the measured PL intensity. Albeit, there are two drawbacks to be mentioned: the diamond geometry still doesn't allow

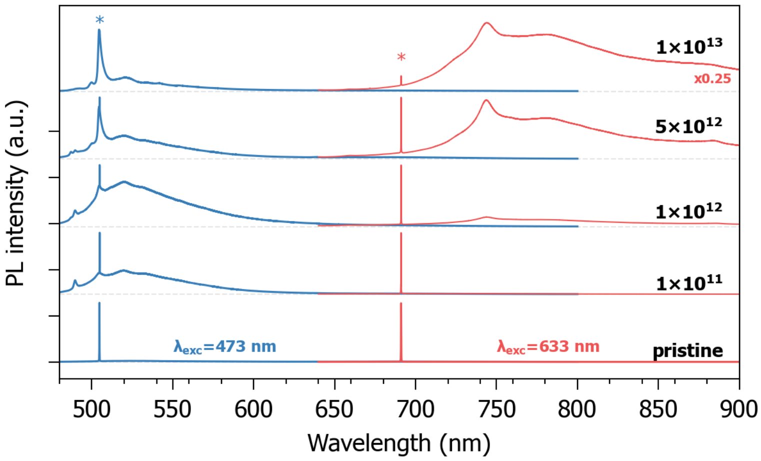

Figure A.7.: Photoluminescence spectra of Sumitomo PDXC HPHT diamonds on pristine and irradiated samples with different fluences of 4.8 MeV/n ^{197}Au in units of cm^{-2} excited with 473 nm (blue spectra) and 633 nm (red spectra). Spectra are normalized to the intensity of the diamond Raman line indicated by the star sign and are displaced vertically for easier visibility.

scanning along the ion trajectory and the (normalized) intensity still has little (physical) significance since PL measurements were conducted through the irradiated surface. Even though a confocal spectrometer was used depth scans with confocal optics are considered ambiguous [331]. Hence, a different diamond with a more appropriate geometry was ultimately chosen for PL characterization.

B High-Power Proton Beam Irradiation

B.1 Overview of Materials Irradiated with High-Power Proton Beams

A broad range of carbon-based materials are applied in high-dose environments like accelerators and fusion or fission reactors. The current section will give a thorough overview of the production processes and thermo-mechanical properties of the different materials investigated in this thesis. In general, the materials in this thesis can be grouped into six different material classes:

i **Isotropic polycrystalline graphite** is a high density ($\sim 1.8\,\mathrm{g\,cm^{-3}}$) graphite material that exhibits isotropic material properties. Used as structural and moderator material in nuclear power plants. Regularly used as absorber material in accelerator collimators and beam dumps.

ii **Carbon-fiber-reinforced graphite** is a medium density ($\sim 1.5\,\mathrm{g\,cm^{-3}}$) composite material of greatly enhanced strength due to reinforcement with carbon-fibers. Strong anisotropy depending on the number of fiber reinforcements. Used in potentially highly loaded beam intercepting devices like the LHC primary collimators.

iii **Expanded graphite** is a low density ($\sim 1\,\mathrm{g\,cm^{-3}}$) graphite-based material with very high in-plane thermal conductivity. Limited thickness (<1 cm) due to production process and machinability. Used for high temperature gasket seals in nuclear power plants. Energy diluter in the LHC beam dump and matrix material for the p-bar target at CERN.

iv **Graphitic foam** is a highly graphitic low density ($\sim 0.5\,\mathrm{g\,cm^{-3}}$) material with macroscopic pores. Low strength, but high thermal conductivity with little anisotropy. Developed for high power heat sink applications that has emerged as a potential energy diluter material for the Future Circular Collider beam dump.

v **Glassy carbon** is a non graphitizing fully sp^2 bonded carbon with medium density ($\sim 1.5\,\mathrm{g\,cm^{-3}}$). Very low thermal and electrical conductivity with high hardness and strength. Chemically inert material for electrochemistry and high temperature crucibles. Disordered model material for highly irradiated graphite. Accelerator applications include beam windows and diagnostic screens for relativistic particle beams.

vi **Pyrolitic carbon** is a high density ($\sim 2.2\,\mathrm{g\,cm^{-3}}$) graphite material with high microstructural order of individual graphite basal planes. Highly anisotropic with material properties close to that of ideal graphite. High performance heat sink material. Model system of ideal graphite to investigate radiation effects of graphite-based materials.

B.1.1 Isotropic Polycrystalline Graphite

Isotropic polycrystalline graphite (PG) is produced from the mixing of a filler and a binder phase. The filler is usually petroleum coke, while the binder is petroleum or coal tar pitch. The particle size of the final material is determined by the particle size of the filler that can be controlled by pre-milling of the filler. After mixing the filler/binder mixture is pressed into a green body by cold isostatic pressing (CIP) at ~200 MPa. The green body is then carbonized between 700 and 1200 °C that results in a carbonaceous but porous material due to the removal of volatile gases. Additional impregnation with binder and subsequent carbonization is used to decrease the average pore size and increase the density. In the final step the material is exposed to temperatures between 2500 and 3000 °C that leads to graphitization of the material and removal of volatile impurities.

For nuclear applications, which require very low level of impurities, especially those of high neutron capture cross section like boron, the filler and binder are chemically pre-treated with chlorine or fluoride compounds that bind boron in gaseous species upon heating to 1000 and 2000 °C. Due to the random orientation of the coke particles in combination with isostatic pressing the final material exhibits fully isotropic material properties. Particle sizes can vary from several hundreds of micrometer all the way down to 1 µm. In general, the grades of available polycrystalline graphite are closely related to their particle size. Smaller particle sizes lead to a higher density and higher strength at the cost of higher thermal expansion [262].

For fine-grain polycrystalline graphite grades with particle sizes between 1 and 20 µm, densities of 1.7 and 1.9 $\mathrm{g\,cm^{-3}}$ at a porosity of 10 and 20 % can be expected with pore sizes that are of a similar size. Thermal conductivity varies between 70 and 140 $\mathrm{W\,m^{-1}\,K^{-1}}$ with a coefficient of thermal expansion (CTE) between 4×10^{-6} and $8 \times 10^{-6}\,\mathrm{K^{-1}}$, that is roughly inversely proportional to the particle size. Mechanical strength is on the order of 40 and 100 MPa. The combination of high thermal conductivity and low CTE in comparison to metals make polycrystalline graphite highly resistant to thermal shock.

As mentioned isotropic polycrystalline graphite is used as a structural material or moderator in nuclear power plants, commonly called "nuclear graphite" [116]. Isotropic graphite is a candidate material for the heat shield and island divertor in the Wendelstein X-7 stellarator fusion device [332]. Due to its excellent performance in high dose environments, polycrystalline graphite is the material in the Super-FRS production target and beam catchers at FAIR [333]. Polycrystalline graphite is the absorber material in the injection and extraction beam dumps of SIS100 at FAIR [334]. At CERN isotropic graphite is employed in the internal beamdump of the SPS [225], as the collimator material for the pre-HiLumi SPS-to-LHC transfer lines [335] and the LHC beam dump [336]. Polycrystalline graphite is used in the 1 MW neutrino production target NOvA [337] and is the baseline material for the 2.4 MW production target of the future Long Baseline Neutrino Facility (LBNF) at Fermilab [338].

B.1.2 Carbon Fiber-Reinforced Graphite

Carbon fiber-reinforced graphite (CFC)[1] is a composite material that contains carbon fibers embedded in a graphite matrix. Carbon fibers are usually produced using polyacrylonitrile (PAN), repeating unit $(\mathrm{C3H3N})_n$, yarns. After oxidization in air at ∼300 °C, oxidized PAN yarns are then carbonized at temperatures between 1000 and 2000 °C and ultimately graphitized in an inert atmosphere at 2000 and 3000 °C. Figure B.1 schematically shows the orientation of graphite basal planes in such a PAN derived carbon fiber [339]. Another production route is the synthesis via melt spinning of mesophase pitch. Fiber diameters are generally on the order of about 5 and 15 µm. High quality PAN fibers usually exhibit a higher tensile strength of up to ∼10 GPa and a Young's modulus of ∼300 GPa while pitch derived fibers have a lower tensile strength of ∼4 GPa, they can have a considerably higher Young's modulus of up to ∼1000 GPa [340]. This is mainly attributed to the larger size of carbon crystallites in pitch derived fibers and higher ultimate carbon content [341]. This difference is also apparent in the thermal conductivity of the two different fibers: PAN fibers have a thermal conductivity between 20 and 130 $\mathrm{W\,m^{-1}\,K^{-1}}$, while pitch derived fibers have thermal conductivities that can be up to 800 $\mathrm{W\,m^{-1}\,K^{-1}}$ at room temperature [342].

Fiber-reinforced composites are produced by multiple different ways, usually determined by the degree of reinforcement. For this work 2D- and 3D-reinforcement are of importance. In 2D-reinforced CFCs carbon fiber yarns are bundled together in rovings which are then woven into fabric mats. These mats are then laminated with resin or just simply stacked [343]. In the case of 3D-reinforcement, carbon fiber plies (sheets with a uni-directional orientation of fibers) are stacked in two directions. The third reinforcement direction is achieved by a so-called needling process [344, 345].

The carbon fiber laminate is then carbonized at 800 and 1000 °C. As the resulting matrix has a large porosity, additional densification is performed by liquid impregnation or chemical vapor deposition. During impregnation, liquid resin or pitch is introduced and pre-graphitized. This is repeated several times until the desired density is achieved. During chemical vapor deposition, hydrocarbon gases are used to infiltrate the matrix at elevated temperatures of 700 and 2000 °C. Densification through CVD has the advantage that fiber laminates can be densified without the need of resin, enabling a higher degree of graphitization, hardness and density of the final material. The process is inherently slow and more expensive in comparison to liquid impregnation.

Due to the large anisotropy of the carbon fibers, CFCs also exhibit anisotropic properties. With an increasing number of reinforcement directions (up to 6 [346]) this can be counteracted at the main drawback of increased manufacturing costs. Material properties of CFCs vary hugely, depending on type of used fiber, roving size, laminate structure, matrix composition, densification route and final graphitization parameters.

---

[1] There are several names for composites of carbon fibers embedded in a highly graphitized carbon matrix; carbon fiber-reinforced carbon (CFRC), carbon-carbon (C/C) or reinforced carbon-carbon (RCC). Carbon fiber-reinforced graphite (CFC) will be used throughout this thesis.

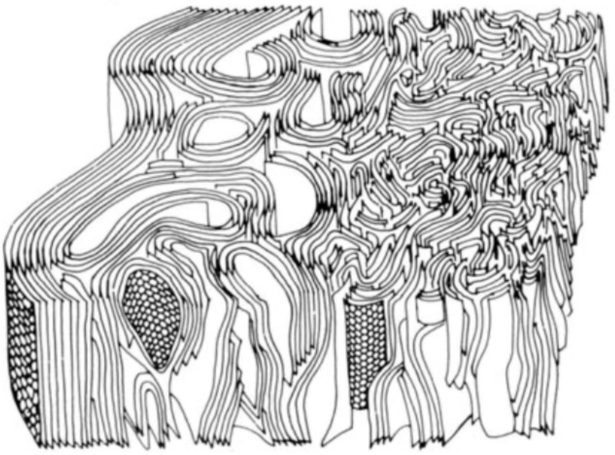

Figure B.1.: Schematic representation of the graphite basal plane orientation in PAN-derived carbon fibers. Reprinted with permission from [339]

Since CFCs combine high strength at high temperatures they are routinely used in furnace charge carriers, aircraft brakes, rocket nozzles, nose tips and leading edges of re-entry vehicles [119, 343]. All of these applications demand service temperatures in excess of 2000 °C. 2D-CFCs are used in the current generation of the LHC primary collimators, but will be exchanged with molybdenum-carbide/graphite composite material [241] in the HiLumi upgrade due to impedance restrictions [240]. CFC is regularly used as backplate which supports the vacuum sealing components in beam windows for relativistic particle beams and was employed in the beam windows of the FlexMat experiment (c.f. section 10.2). Furthermore, the extraction absorber of the SPS and the collimators of the SPS-to-LHC transfer lines at CERN are made of 3D-CFC [30].

B.1.3 Graphitic Foam

The production of graphitic foam can be divided in three sub steps: foaming, carbonization and graphitization. Foaming creates the general structure of the foam while carbonization and graphitization remove residual volatile material and adjust the final thermomechanical properties of the foam [347].

Liquid mesopitch precursor is heated in inert atmosphere slightly above its softening point during foaming. The pitch decomposes and releases volatile gas bubbles in the subsequent melting step. As these gas bubbles rise to the surface, mesophase crystals are oriented "upright" inside the melting pitch. With increasing temperature, the viscosity of the liquid mesophase is increasing and gas bubbles are eventually captured in the liquid pitch. Once the temperature is high enough only a solid skeleton of non-melting pitch is left. Subsequent carbonization between 600 and 1000 °C breaks down the remaining organic compounds into a pure carbon structure, while the mesophase crystals are growing. In the final grahitization process the carbon structure is transformed into graphite at temperatures above 2800 °C. The final structure exhibits fully open porosity of 60 and 80 % with a normal pore size distribution of average pore diameter of up to several hundreds of micrometer.

Due to the alignment of the mesophase crystals during foaming, graphitic foam produced in this way exhibits anisotropic material properties with thermal conductivities of 135 and 245 $\mathrm{W\,m^{-1}\,K^{-1}}$ along the bubbling direction, or out of plane direction[2], and 35 and 70 $\mathrm{W\,m^{-1}\,K^{-1}}$ in the in-plane direction. The density varies between 0.5 and 1 $\mathrm{g\,cm^{-3}}$. Compared to the other materials presented in this section graphitic foam has the lowest mechanical strength with a flexural strength below $\leq$10 MPa.

The combination of low density and high thermal conductivity makes graphitic foam a commonly used material for heat sinks of high-power electronics. This has also translated to heat sink applications in particle detectors. Graphitic foams will be used in the upgrade of the inner tracking detector (ITk) of the ATLAS detector for HL-LHC [348] and the micro vertex detector system of the PANDA experiment at FAIR [270, 349]. Furthermore, due to its even lower density than expanded graphite, graphitic foam is a candidate material for the energy diluter of the FCC beamdump [350] if its mechanical strength is sufficient to withstand the beam-induced stresses during a beam dump.

---

[2] During production this is called the Z-direction, while manufacturers regularly call this the "out of plane" direction.

B.1.4 Glassy Carbon

Glass-like carbon, or glassy carbon[3], is produced by slow pyrolysis of thermosetting polymers or cellulose at temperature between 600 and 3000 °C. By keeping the heating rate sufficiently low the development of pores due to the outgassing of the precursor is suppressed.

The resulting microstructure is related to fullerene-like, randomly-interconnected tortuous graphitic sheets with 100 % sp^2 bonded carbon [351–354]. Even though glassy carbon only has sp^2 bonds, graphitic sheets are heavily bend due to the presence of heptagonal or octagonal carbon rings in comparison to ideal hexagonal rings. At low pyrolization temperatures many small domains form that agglomerate to larger, less curved flakes at higher temperatures. As a result, thermomechanical material properties depend strongly on the pyrolization temperature during production [355]. Furthermore, glassy carbon has a large amount of nano-sized pores while exhibiting fully closed porosity that leads to low densities between ∼1.4 and 1.5 $\mathrm{g\,cm^{-3}}$ and very low gas and liquid permeability.

Due to the random interconnection of individual sheets, glassy carbon exhibits fully isotropic material properties. It has low thermal conductivity, usually below $\sim 10\,\mathrm{W\,m^{-1}\,K^{-1}}$, high temperature resistance (depending on the grade, service temperature in vacuum can be up to 3000 °C), high hardness and high strength with flexural strength ≥100 MPa. Glassy carbon is routinely used as an electrode material in electrochemistry, high temperature crucibles and prosthetics [356]. Accelerator-based applications include the use of glassy carbon as diagnostic screens for relativistic beams and, in combination with CFC, as beam windows (c.f. section 10.2). It is also assumed that glassy carbon is the structure of graphite material after high fluence irradiation with swift heavy ions [6].

B.1.5 Thermally Annealed Pyrolitic Graphite

Thermally annealed pyrolytic graphite (TPG) is a form of highly anisotropic graphite that is comparable to highly-oriented pyrolytic graphite (HOPG). The pyrolytic graphite precursor is grown in a chemical vapor deposition (CVD) process in which hydrocarbon gases are broken down to form basal planes on a substrate. After deposition, pyrolytic graphite is annealed at temperatures in excess of >2500 °C to induce further graphitization. In comparison, HOPG is produced by the annealing of pyrolytic graphite in the presence of an additional compressive force that leads to an even better alignment of the basal planes with mosaic spread angles ≤1°.

Due to a nearly perfect ABAB stacking of the basal planes in thermal pyrolytic graphite it exhibits material properties very close to ideal graphite. TPG has a density of 2.26 $\mathrm{g\,cm^{-3}}$ and all thermomechanical properties exhibit strong anisotropy. The thermal conductivity parallel to the basal planes, in plane, is $\sim 1500\,\mathrm{W\,m^{-1}\,K^{-1}}$ while the out of plane thermal conductivity is only $\sim 20\,\mathrm{W\,m^{-1}\,K^{-1}}$. The CTE is close to zero in plane, while out of plane it is $\sim 25\,\mathrm{K^{-1}}$ at room temperature. The flexural strength of TPG is ∼40 MPa when the graphite planes are parallel to the bending force, while in the other case it is ∼100 MPa. The anisotropy is even more pronounced in the material's Young's modulus that is ∼1050 GPa in plane and only ∼35 GPa out of plane.

TPG is routinely used as a heat sink in high power electronics, e.g. as heat sinks for LEDs in automotive applications [115]. Due to its highly anisotropic mechanical properties, TPG is not suitable as beam intercepting device but it is used as a structural part and heat sink in the baseboard of the ATLAS inner tracking detector (ITk) upgrade for HL-LHC [348].

B.1.6 Expanded Graphite

As the name suggests, expanded graphite is produced by rapid expansion of chemically intercalated natural graphite flakes. After intercalation, the natural graphite flakes are exposed to rapid heating to 900 and 1200 °C that leads to the evaporation of the intercalation agent. The exfoliated graphite particles are then rolled or molded into sheets without assistance of a binder. Molding or rolling leads to mechanical interconnection between the individual particles that ultimately determines the final thickness and density of the sheet that usually vary between 0.1 and 3 mm and 0.7 and 1.4 $\mathrm{g\,cm^{-3}}$. The density heavily influences the thermomechanical properties of expanded graphite.

---

[3] It should be noted that glassy carbon is a trademark, but for historical reasons glassy carbon will be used synonymously for glass-like carbon.

All thermomechanical properties of expanded graphite exhibit large anisotropy because the order along the c-axis of the individual graphite particles is well preserved even after intercalation and expansion. By rolling or molding most of the graphite particles are oriented preferentially with the c-axis parallel to the thickness of the sheets. Hence, expanded graphite has a high in-plane thermal conductivity of ∼150 and 500 $\mathrm{W\,m^{-1}\,K^{-1}}$ and a low through-plane thermal conductivity of ∼5 and 20 $\mathrm{W\,m^{-1}\,K^{-1}}$. Expanded graphite retains all the beneficial properties of pure graphite like chemical inertness, high service temperature in vacuum and high thermal and electrical conductivity. Additionally, sheets can be easily shaped and have high compressibility. This makes expanded graphite a widely used material for high temperature gaskets (suitable for use in high-dose environments of nuclear power plants [117]) and thermal management applications. It is also used as the energy diluter in the LHC beam dumps due to its low density of 1 $\mathrm{g\,cm^{-3}}$ and excellent thermal conductivity [244, 336]. Expanded graphite is also a candidate material for the matrix of the new antiproton production target at CERN [271, 357].

B.1.7 Tantalum

Tantalum is a bcc metal with high density (16.69 $\mathrm{g\,cm^{-3}}$), high-Z (73) and a melting point of 3017 °C that belongs to the group of refractory metals (together with niobium, molybdenum, tungsten and rhenium) [358]. Tantalum exhibits a large resistance to chemical corrosion. Despite its bcc crystal structure, tantalum is relatively easy to machine at room temperature. Tantalum is quite strong with a Young's modulus of annealed tantalum of ∼190 GPa but exhibits a large degree of ductility. At room temperature, with a yield strength of ∼170 MPa and ultimate tensile strength of ∼320 MPa, annealed tantalum shows elongation at break above 30 % [359]. Additionally, tantalum exhibits a high spall strength of ∼5 GPa at room temperature determined by spall gas-gun-driven experiments [360].

Major industrial application of tantalum includes its use in high-capacitance capacitors for portable electronics. Its high corrosion resistance in particular to acids makes tantalum a low-cost alternative to platinum in chemical process equipment. Due to its high density and melting point, tantalum is used in shaped charge liners in warheads and explosively formed projectiles [361]. In this context, the dynamic mechanical properties of tantalum are extensively studied over a large range of temperatures and strain rates. These measurements were used to extract parameters for strength models, like the Johnson-Cook model, that are directly applicable in explicit numerical simulations. An extensive review of the dynamic behavior, its implementation into explicit codes and radiation damage is presented in reference [229, p. 24–27].

Tantalum itself is not directly a matter of research within this thesis, but tantalum was used as a "core" material within a dedicated target station of the FlexMat experiment to "drive" surrounding graphitic material to higher stresses in a beam impact experiment. A detailed description of these special targets is presented in subsection 10.2.2. Tantalum was chosen as the "core" material mainly due to its high density, large atomic number, and high mechanical robustness. The combination of high density and large atomic number leads to an increase of the specific energy deposition density by 440 GeV protons up to a factor of ∼20 in comparison to pure graphite (with a density of 1.8 $\mathrm{g\,cm^{-3}}$). In addition, its low specific heat of ∼0.2 $\mathrm{J\,g^{-1}\,K^{-1}}$, that is about 3 times smaller than graphite's, large temperature gradients of several hundreds of K can be generated with relatively low beam intensities of $\sim 1 \times 10^{11}$ ppp. The resulting thermo-mechanical stress is coupling into the surrounding graphite where it can induce failure. Tantalum was extensively studied for the redesign of the p-bar target at CERN and has shown excellent robustness towards beam impact. Even under beam impact conditions where plastic deformation is occurring, tantalum exhibited a quasi-elastic response due to its large ductility before fracture, that was replicated in numerical simulations [229, 271, 357, 362]. This allows the study of graphite at larger stresses than normally achievable in beam impacts on pure graphite while having a (numerically) well known and therefore predictable behaviour of the "core".

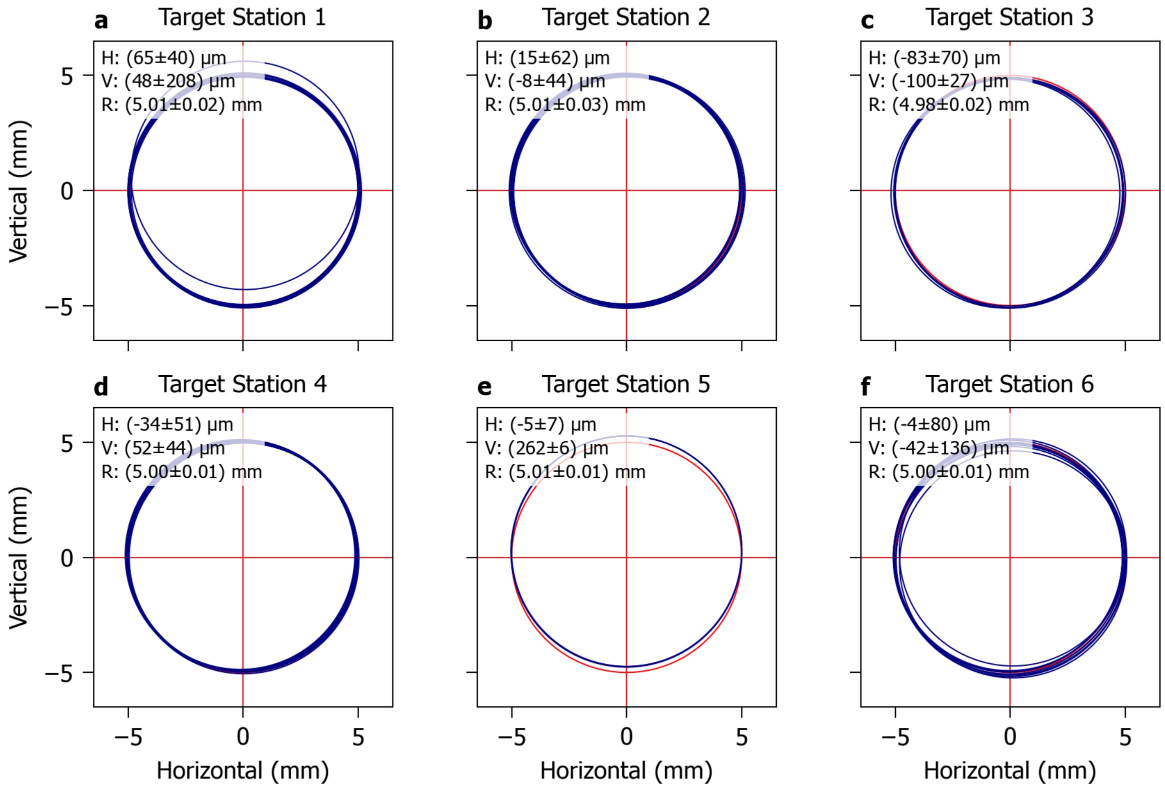

Figure B.2.: Horizontal and vertical displacement of the targets with respect to the virtual beam axis for target stations 1 through 6 (a-f). Red lines indicate the center of the beam axis. Circles indicate the position and radius of individual samples in the respective target stations. H and V indicate the average horizontal and vertical displacement of the targets within a target station while R indicates the average radius measured by metrology.

B.2 Geometry Measurement of the FlexMat Experiment

The experiment was designed with a single vertical displacement stage for the target holder. The displacement stage has a single fixed irradiation position with either one of the six target stations in the irradiation position or the target holder completely out of beam. Hence, determining the relative position of the targets within the target stations in the irradiation position and the absolute position of the irradiation position with respect to the experimental chamber was a crucial input to define a 'virtual beam axis' to align the experiment as precise as possible.

Each target of the experiment was measured with a scanning probe coordinate measurement device. Two line scans along the radius at the extremities of the targets were performed to measure the horizontal and vertical displacement (in the transverse plane normal to the beam axis) and the actual radius of each target. Results of the geometry measurement are shown in Figure B.2. The radius of all targets is well defined within (5.0 ± 0.5) mm in all target stations. Absolute vertical displacements are on average smaller than ±100 µm and are scattering well below ±150 µm. Only target station 5 had an exceptionally large vertical displacement of (262 ± 6) µm. Absolute horizontal displacements are also within ±100 µm.

With the smallest beam size requested for the experiment of $\sigma_{\mathrm{H,V}}$ =0.25 mm and the alignment uncertainty of about ≥100 µm, it can be summarized that all targets should be impacted within ±1 σ which corresponds to about 5 % of the radius of the targets. This level of precision is plenty enough to reduce contributions from axial bending modes induced by eccentric beam impacts. Also, the horizontal beam jitter for $\sigma_{\mathrm{H,V}}$ =0.5 mm and 1.5 mm is considerably larger than the precision of alignment (c.f. Figure 11.2).

B.3 Dynamic Response of Anisotropic Graphite Irradiated with High-Power Proton Beams

In addition to the dynamic response of isotropic polycrystalline graphite samples presented in section 11.2, the following section will qualitatively introduce the beam-induced dynamic response of anisotropic carbon-fiber reinforced graphite (CFCs) grades. As composite materials made up of a carbon-fiber phase and a graphite matrix, CFCs exhibit strong anisotropy. CFCs have large thermal conductivity, high Young's modulus and low coefficient of thermal expansion along the well-graphitized carbon fibers (the in-plane direction). Material properties in the matrix are in general considerably worse due to the low degree of graphitization and porosity of the matrix. The through-plane direction (normal to the fiber reinforcement planes) is hence dominated by the material properties of the matrix. Since the orientation and processing of the carbon fibers offers a lot of room for customization, three extremal cases will be presented: ArianeGroup Sepcarb, a 3D-reinforced CFC, SGL Carbon SIGRABOND Performance, a 2D unidirectionally reinforced CFC and SGL Carbon SIGRABOND Premium, a 2D-reinforced CFC with woven rovings.

The different types of reinforcement are schematically shown in Figure B.3. 3D reinforcement will generally produce less anisotropic material parameters at the expense of mechanical strength and thermal conductivity along the main reinforcement direction. 2D Unidirectional reinforcement refers to fibers that are oriented in a single direction per reinforcement layer, in the case of SIGRABOND Performance consecutive layers are rotated by 90° with respect to each other. Unidirectional reinforcement leads to better incorporation of the fibers into the matrix and larger strength. SIGRABOND Premium is reinforced by layers of woven rovings. In SIGRABOND Premium a single roving consists of (on average) 3000 individual carbon fibers. Individual reinforcement planes are rotated by 45° with respect to each other. In the following section, ⊥ will indicate samples where the main reinforcement direction was oriented normal to the beam axis (and parallel to the base surfaces of the sample cylinders). Vice versa, || denotes samples in which the main reinforcement direction was oriented parallel to the beam axis (and normal to the base surfaces of the sample cylinders).

An overview of the dynamic response of the different CFC samples after beam impact with 9×10^{12} ppp 440 GeV/c protons (1.8 µs pulse length) is shown in Figure B.4. Qualitatively, the CFCs exhibit a less 'clean' dynamic response in comparison to the polycrystalline graphite samples (c.f. Figure 11.4). This is also indicated by the overall damping envelope, which yields damping constants with considerable uncertainties. Albeit damping is much more efficient in the CFCs. Ignoring the uncertainties, damping is more efficient when the reinforcement planes are normal to the beam axis (⊥ orientation) in ArianeGroup Sepcarb and SGL Carbon Premium. The increased damping is explained by the large number of interfaces introduced by the reinforcement planes and the large porosity of the

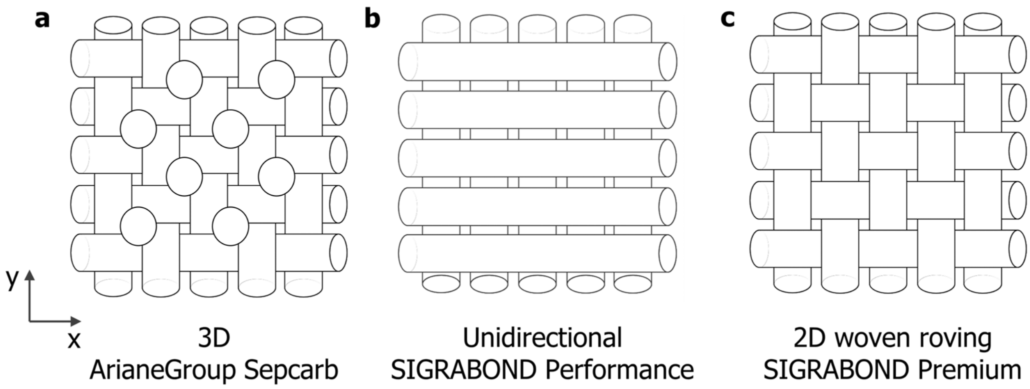

Figure B.3.: Schematic overview of different carbon fiber reinforcements. The YX plane indicates the reinforcement direction, which is generally called the in-plane direction according to suppliers. The YX surface normal indicates the non-reinforced direction that alternates between matrix and reinforcement planes, generally called the through-plane direction. 3D-reinforcement of a 2D-reinforced CFC by single fiber needling through the reinforcement plane (a). Unidirectional reinforcement where fibers within a single reinforcement plane are oriented strictly in one direction (b). 2D-reinforcement with a woven roving. A roving consists of several thousand of individual carbon fibers that are woven to form a single reinforcement plane (c).

matrix. The graphite fibers have densities that are comparable to ideal graphite, the low density of the CFCs, which is of the order of $1.5\,\mathrm{g\,cm^{-3}}$, is hence due to the porosity in the matrix.

Maximum (absolute) radial surface velocities are systematically below $100\,\mathrm{mm\,s^{-1}}$. This indicates that the coefficient of thermal expansion (CTE) has to be smaller than or comparable to the coefficient of thermal expansion of SGL Carbon R6300 with $3.1 \times 10^{-6}\,\mathrm{K^{-1}}$. Between the three CFCs, ArianeGroup Sepcarb has the lowest CTE as indicated by the smallest radial surface velocity in either sample orientation.

The strong anisotropy due to the fiber reinforcement planes is also seen in the large difference of the Fourier spectra of the two different sample orientation. Figure B.5 shows the normalized Fourier spectra of the CFCs. The dynamic response of ArianeGroup Sepcarb and SGL Carbon Performance have entirely different Fourier spectra when comparing the different sample orientations. The Fourier spectrum of ArianeGroup Sepcarb in the $\perp$ orientation consists of more frequency peaks of comparable amplitude in comparison to the ||| orientation which is dominated by two peaks below 200 kHz. SGL Carbon Performance exhibits the opposite trend, the ||| orientation has more peaks in the Fourier spectrum. The Fourier spectra of the different orientations in SGL Carbon Premium on the other hand are strikingly similar.

This is also confirmed by the continuous wavelet transform (CWT) of the dynamic response of SGL Carbon Premium. The CWTs shown in Figure B.6 of the two sample orientations are comparable. Photo documentation confirmed that both samples indeed had different orientations. According to the supplier, the CTE should vary between 0 (parallel to the fiber reinforcement plane) and $8 \times 10^{-6}\,\mathrm{K^{-1}}$ (perpendicular to the reinforcement plane) which is clearly not in line with the radial surface velocity measured between the two orientations.

Unfortunately, to simulate the dynamic response of the CFCs the knowledge of at least five different elastic constants is necessary. With the conclusion of this work, it was not possible to obtain a full dataset of mechanical properties to simulate the dynamic response. Due to the large phase space of elastic constants a parameter scan by FE simulation did not yield any meaningful results.

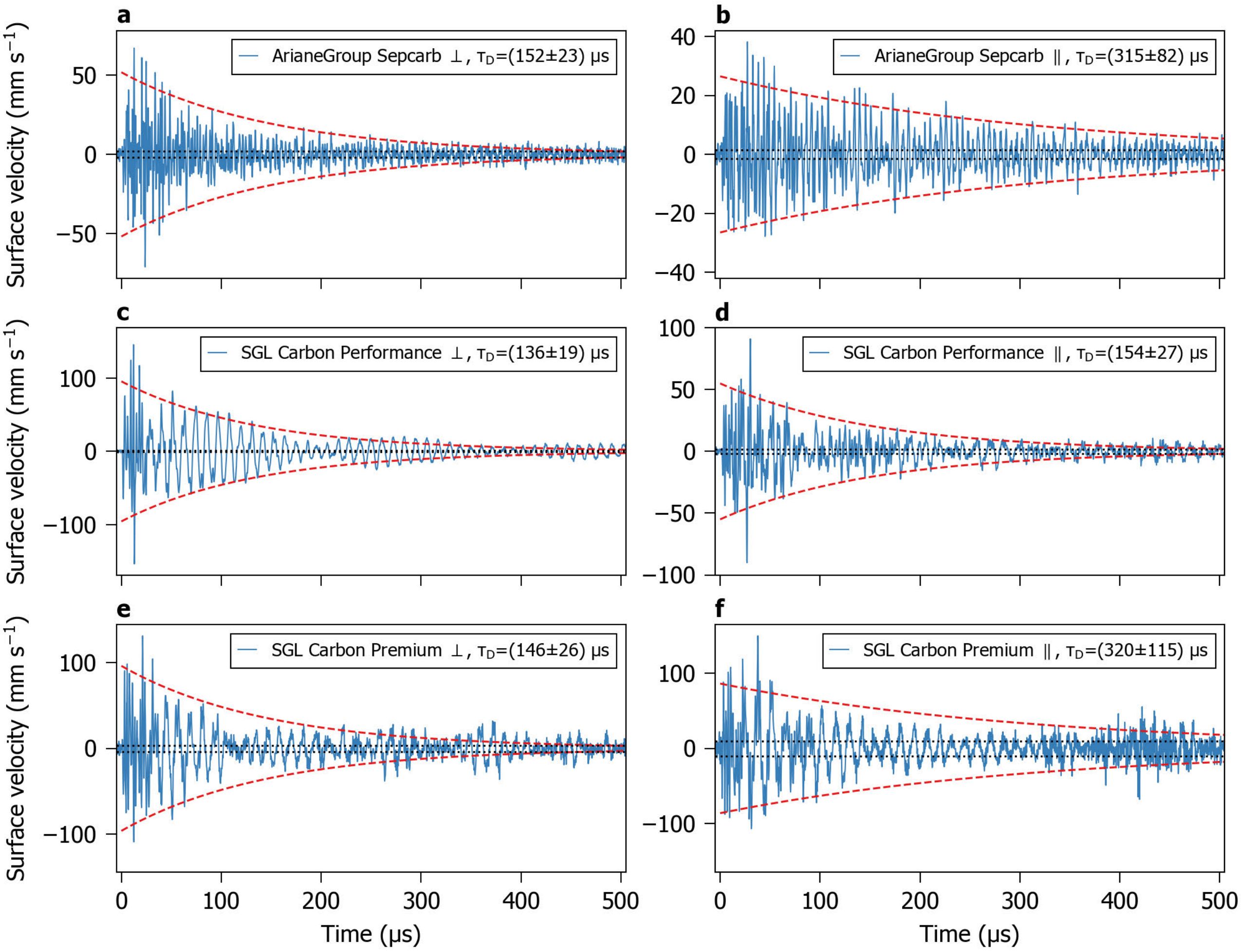

Figure B.4.: Comparison of the dynamic response of carbon fiber reinforced graphite samples impacted by 9×10^{12} ppp 440 GeV/c protons (1.8 μs pulse length). Fiber reinforcement planes are oriented normal $\perp$ (left column) and parallel $\|$ (right column) to the beam direction. Dynamic response of 3D-reinforced ArianeGroup Sepcarb (a, b), SGL Carbon Performance with unidirectional reinforcement (c, d) and 2D-reinforced SGL Carbon Premium (e, f). Dashed red line indicates the overall damping envelope with the damping constant given in the legend. Horizontal dashed lines indicate the $\pm 1\sigma$ noise level of the measurement.

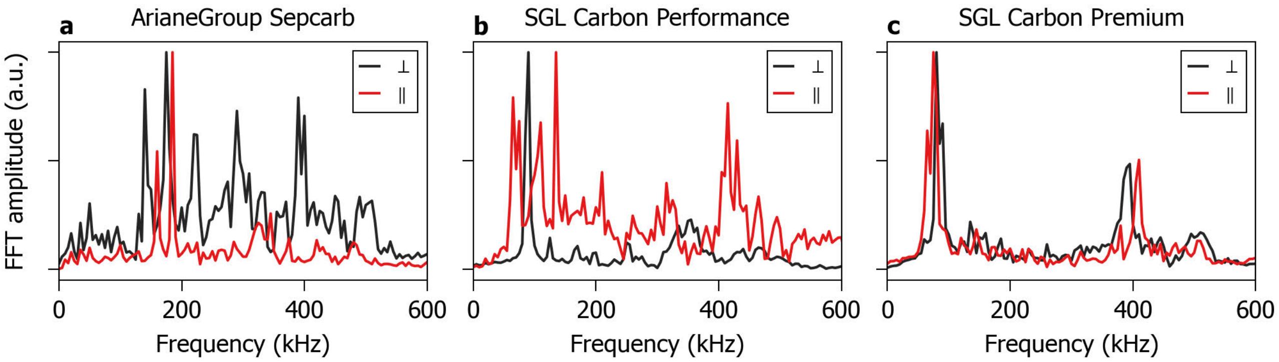

Figure B.5.: Self-normalized fast Fourier transform amplitude of the dynamic response for different CFC samples in two orientations after beam impact with 9×10^{12} ppp 440 GeV/c protons (1.8 µs pulse length). Fiber reinforcement planes are oriented normal ⊥ and parallel || (right column) to the beam direction. Fourier transform of the radial surface velocity measured by a laser Doppler vibrometer in the center of 3D-reinforced ArianeGroup Sepcarb (a), SGL Carbon Performance with unidirectional reinforcement (b) and 2D-reinforced SGL Carbon Premium (d). The input signals for the fast Fourier transformation are shown in Figure B.4.

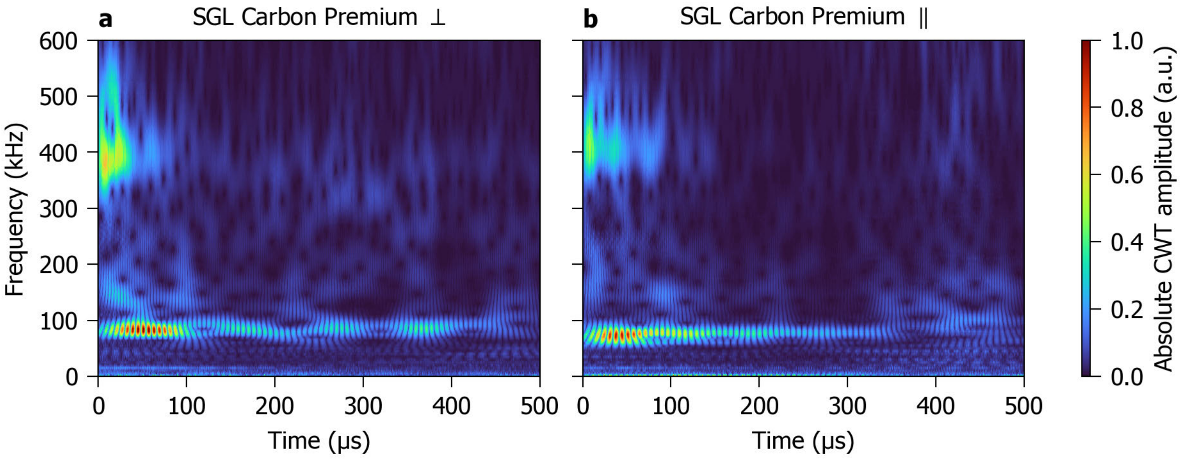

Figure B.6.: Continuous wavelet transform (CWT) of the radial surface velocity of SGL Carbon Premium CFC in two different sample orientations impacted with 9×10^{12} ppp 440 GeV/c protons (1.8 µs pulse length). Heatmap of the absolute CWT of the radial surface velocity measured on the sample with reinforcement planes normal (a) and parallel to the beam axis (b). The input signals for the continuous wavelet transformation are shown in Figure B.4.

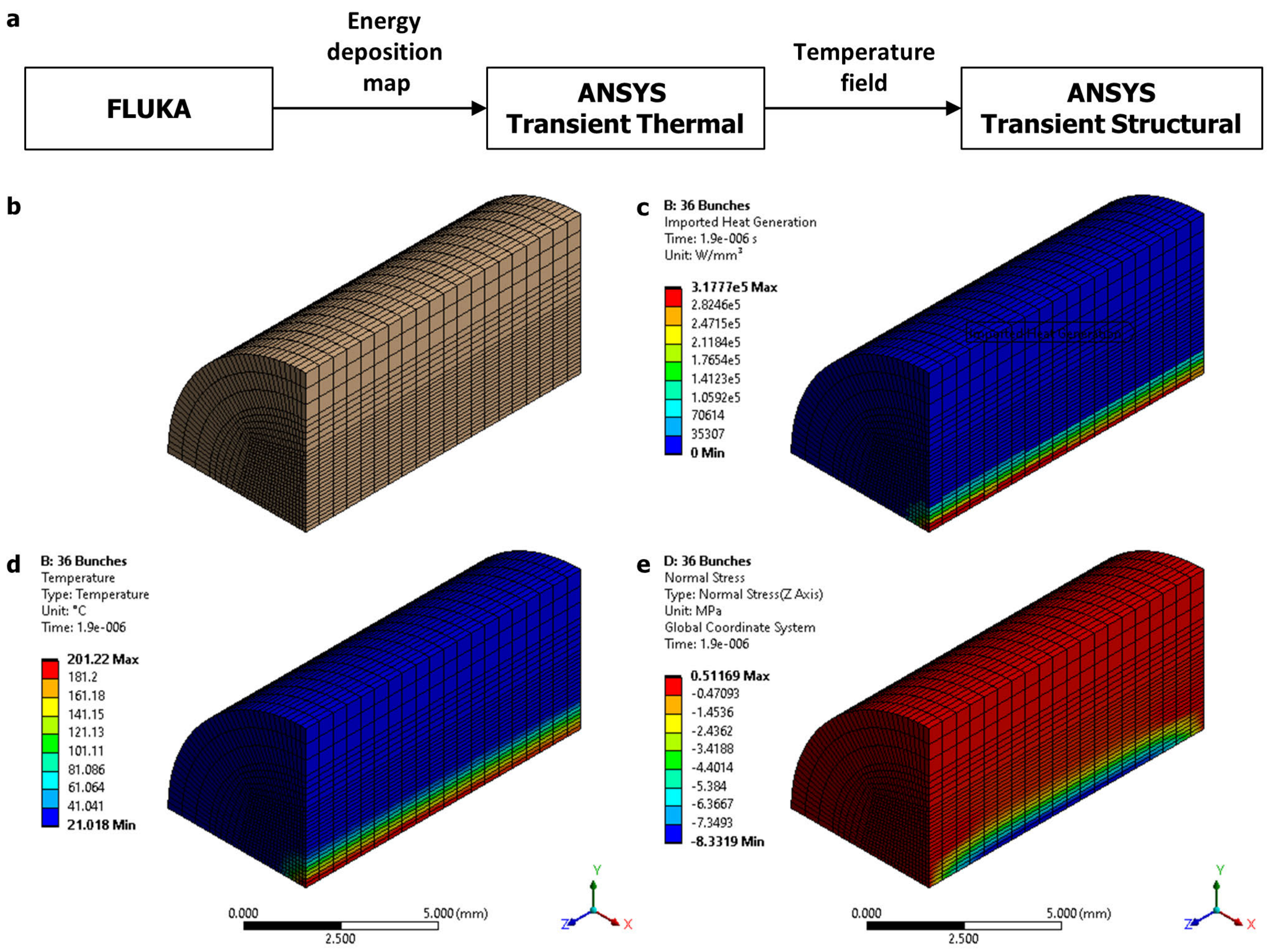
a
FLUKA
Energy deposition map
ANSYS Transient Thermal
Temperature field
ANSYS Transient Structural
b
c
B: 36 Bunches
Imported Heat Generation
Time: 1.9e-006 s
Unit: W/mm³
3.1777e5 Max
2.8246e5
2.4715e5
2.1184e5
1.7654e5
1.4123e5
1.0592e5
70614
35307
0 Min
d
B: 36 Bunches
Temperature
Type: Temperature
Unit: °C
Time: 1.9e-006
201.22 Max
181.2
161.18
141.15
121.13
101.11
81.086
61.064
41.041
21.018 Min
e
D: 36 Bunches
Normal Stress
Type: Normal Stress(Z Axis)
Unit: MPa
Global Coordinate System
Time: 1.9e-006
0.51169 Max
-0.47093
-1.4536
-2.4362
-3.4188
-4.4014
-5.384
-6.3667
-7.3493
-8.3319 Min
0.000
2.500
5.000 (mm)
Y
Z
X

Figure B.7.: Finite element analysis workflow. Schematic overview of the multi-stage approach to simulate the dynamic response of short pulse particle beam irradiation (a). Typical mesh used in a coupled thermo-mechanical FEA simulation (b). Extrapolation of the FLUKA energy deposition map to the mesh elements as an internal heat generation in ANSYS transient thermal (c) and the resulting temperature field (d). Axial stress from a transient structural analysis in ANSYS using the temperature field as a thermal load at every timestep (e). Simulation results from ANSYS 2019 R2.

B.4 Finite Element Analysis Workflow

To model the dynamic response of the irradiated samples, multi-stage finite element simulations were performed in the simulation software ANSYS Mechanical Release 19.2 [257]. For the given case of a beam-induced thermo-mechanical load, three sub steps are necessary to evaluate the dynamic response:

1. an energy deposition map that describes the energy per volume element deposited by the particle beam in the sample;
2. a temperature field that contains the temperature increase of the sample due to the energy deposition by the particle beam;
3. the mechanical loads due to coupling of the temperature field to thermal strain.

This approach is schematically shown in Figure B.7a. FLUKA [254] is a statistical code that employs the Monte Carlo method to describe the interaction of a particle beam with a sample. Particle beam parameters are introduced by a transverse intensity distribution, approximated by a bivariate normal distribution with $\sigma_{1,2}$ describing the standard deviation of the transverse beam spot size in the horizontal and vertical plane, the particle species and their momentum. The sample is introduced with its geometry, macroscopic density and atomic composition. The resulting energy deposition map describes the energy deposited per unit volume per particle (of the beam) in the sample.

The energy deposition map is introduced as an internal heat generation in $\mathrm{W\,m^{-3}}$ within ANSYS. The energy deposition map is scaled with the beam intensity and pulse length so that the product of pulse length and internal heat generation is identical to the energy deposited per unit volume (c.f. Equation 11.1). To reduce computational time, the sample is approximated by a quarter cylinder solid body with two symmetry planes that is able to reproduce bivariate intensity distributions (and therefore energy deposition) under the assumption of centered beam impact. A typical mesh is shown in Figure B.7b where the element size along the cylinder axis has a constant element size of 0.5 mm while the radial direction is meshed in the center with elements as small as 0.125 mm. Both mesh inflation and quadratic element order are necessary to replicate the large gradients of the internal heat generation produced by beam pulses with transverse beam sizes as small as $\sigma \approx 0.25$ mm. The energy deposition map is then projected onto the mesh elements in ANSYS using simple distanced based averages as shown in Figure B.7c. The exact same mesh was also used for modal analysis.

The time evolution of the temperature field is then simulated by applying the internal heat generation for the pulse length τ_{beam}. Convergence of the results shown in this work was achieved with a time step of 0.1 µs. The temperature field at the end of a beam pulse is shown in Figure B.7d. Due to the short time period of interest of a few hundreds of microseconds, the temperature field can be modelled adiabatically where, for the given case, the total (thermal) energy of the system remains constant after the initial energy deposition by the particle beam. This is justified by the characteristic thermal diffusion time of the system that is of the order of a few hundreds of milliseconds (c.f. Equation 9.2).

The mechanical analysis is conducted by importing the temperature field as a thermal load for every timestep into a transient structural simulation within ANSYS. Due to the used quarter geometry and symmetry no additional boundary conditions are necessary within ANSYS. The sample supports and their geometry in the experiment was chosen so that the resulting dynamic response is virtually identical to a freely suspended sample (c.f. Figure 10.5). The resulting axial stress distribution at the end of a beam pulse is shown in Figure B.7e. To verify the convergence and physical significance of results, they were verified in comparison to the analytical equations for the temperature field (c.f. Figure 11.3) and thermal stresses (c.f. Table 11.1).

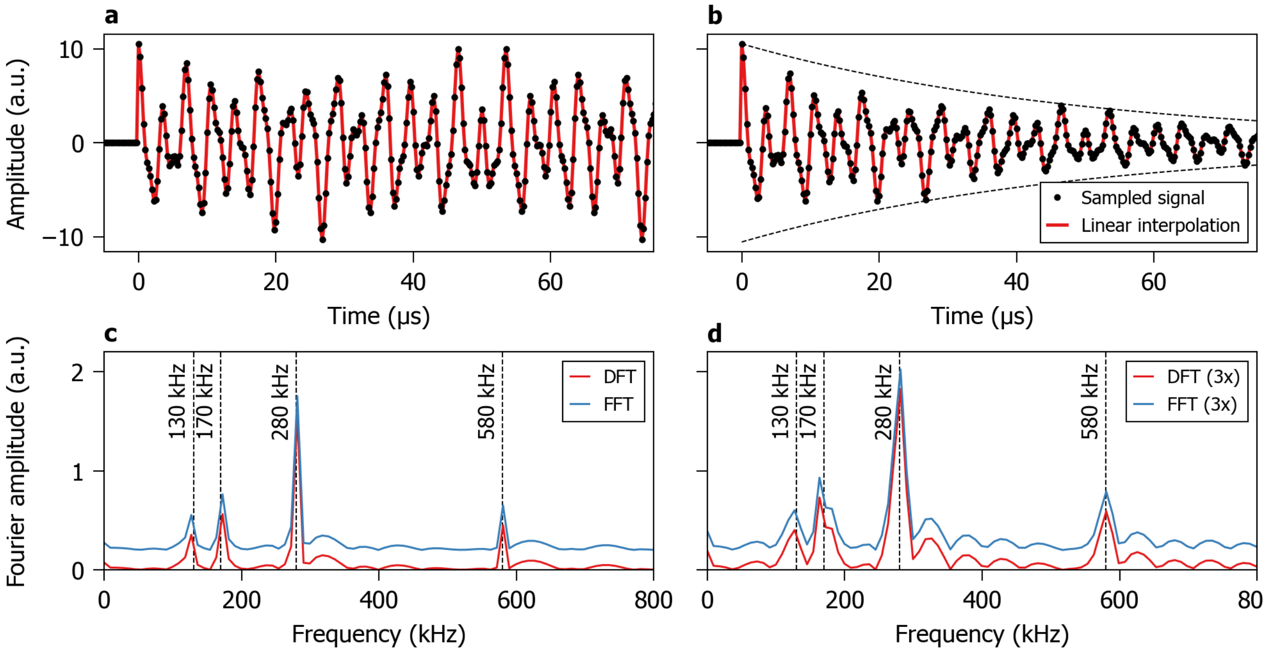

Figure B.8.: Sampled signal of Equation B.3 with 4 MHz sampling rate with dimensionless amplitudes $A_i = \{1, 2.5, 5, 2\}$, frequencies $f_i = \{130, 170, 280, 580\}$ (in kHz) as a function of time without (a) and with damping τ_D =50 µs (b). Comparison of discrete Fourier transform, calculated by numerically solving Equation B.6 (DFT) and using the FFT implementation in the NumPy package of python (FFT) for the undamped signal (c) and damped signal (d).

B.5 Numerical Analysis of Beam-Induced Dynamic Response

As introduced in the previous sections, beam-induced thermal shock leads to mechanical vibrations of the beam-impacted sample that is composed of several different vibration modes each with distinct vibration frequencies. Hence, the dynamic response of a target can be described by a linear combination of cosine waves with frequency f_i and amplitude A_i:

$$f(t) = \sum_{i=0}^{i=N} A_i \cos(2\pi f_i t)\,\mathrm{e}^{-t/\tau_{\mathrm{D},i}}, \tag{B.1}$$

where $\tau_{\mathrm{D},i}$ is the damping constant of each frequency f_i. Assuming that $\tau_{\mathrm{D},i}$ is independent of frequency, the equation simplifies to:

$$f(t) = \mathrm{e}^{-t/\tau_\mathrm{D}} \sum_{i=0}^{i=N} A_i \cos(2\pi f_i t). \tag{B.2}$$

In the context of the target, such an equation would qualitatively describe the variation of stress/pressure or strain as a function of time somewhere in the sample after the end of the beam pulse. Since the oscillations are induced by the beam impact (and are zero beforehand), Equation B.2 has to be slightly modified:

$$f(t) = \begin{cases} \sum_{i=0}^{i=N} A_i \cos(2\pi f_i t)\,\mathrm{e}^{-t/\tau_\mathrm{D}} & t \geq 0 \\ 0 & t < 0 \end{cases}. \tag{B.3}$$

In the experiment, the radial surface velocity of the cylindrical targets is measured by the laser Doppler vibrometer at $L = L/2$ (in the axial center) and $r = R$ (on the surface). Chapter 11 shows that the measured signal can be well approximated by the above equations. Hence, the following describes the numerical methods used to identify the different frequency components in the measured signal.

B.5.1 Fourier Analysis

In general, Fourier analysis refers to the approximation or representation of a given function by trigonometric functions. A time series of data points can be decomposed in into sinusoids of different frequencies with their amplitudes representing the frequency spectrum.

The (continuous) Fourier transform of a continuous function $x(t)$ is defined as:

$$\hat{x}(\xi) = \int_{-\infty}^{\infty} x(t)\mathrm{e}^{-i2\pi\xi t}\mathrm{d}t, \quad \forall t \in \mathbb{R}, \tag{B.4}$$

which is the amplitude $\hat{x}$ at pseudo-frequency ξ. Conveniently, if t refers to time (in seconds) the pseudo-frequency ξ is identical to frequency f (in Hertz). After evaluation of this equation for all values of ξ, the original function $x(t)$ can be represented as the integral of complex exponentials for all frequencies ξ:

$$x(t) = \int_{-\infty}^{\infty} \hat{f}(\xi)\mathrm{e}^{i2\pi\xi x}\mathrm{d}\xi, \quad \forall \xi \in \mathbb{R}, \tag{B.5}$$

which is the inverse Fourier transform. The complex number $\hat{x}$ contains both the amplitude and phase information for frequency ξ.

But experimental measurements of dynamic effects do not directly determine continuous functions. Instead, a series of data points evenly spaced in time is measured. In other words, a measurement device measures N data points $x(n)$ with a sampling rate of f_s (the time difference between two measurement points is $1/f_s$), which will simply be called 'signal'. The transform of such a discrete signal at k is described by the discrete Fourier transform:

$$\hat{x}(k) = \frac{1}{N}\sum_{n=0}^{N-1} x(n)\mathrm{e}^{-i\frac{2\pi k}{N}n}, \quad k \in \mathbb{N}. \tag{B.6}$$

This equation shows that $\hat{x}(k)$ is periodic with only N different values for k. If the signal is measured as a function of time, k is connected to the real frequency f by:

$$f(k) = f_s\frac{k}{N}. \tag{B.7}$$

This also defines the frequency resolution Δf of the frequency spectrum of the discrete Fourier transform which is simply f_s/N. The inverse of the discrete Fourier transform is defined by:

$$x(n) = \sum_{k=0}^{N-1} \hat{f}(k)e^{i\frac{2\pi k}{N}n}. \tag{B.8}$$

Let's assume Equation B.3 with frequencies $f_i = \{130, 170, 280, 580\}$ (in kHz) and corresponding dimensionless amplitudes $A_i = \{1, 2.5, 5, 2\}$, with $\tau = 50\mu$s and without damping ($\tau = \infty$). The continuous function is now sampled for $N = 441$ points with a sampling frequency $f_s = 4$MHz starting 5 µs prior to the excitation (beam impact). The resulting signals are shown in Figure B.8a and b which clearly indicate that the amplitude is zero prior to the excitation (beam impact).

Figure B.8c and d show the normalized frequency spectrum when applying Equation B.6 to Equation B.3. The frequency spectrum denoted as FFT (fast Fourier transformation) is calculated by the discrete Fourier transformation of the NumPy package [363] of python [364] which is ultimately going to be used for all frequency spectra in this work due to simple implementation that is computationally fast [365]. The Fourier transforms show clear peaks at the frequencies f_i. Even with a damped signal, identification of different frequencies in the Fourier transform is unambiguous. Albeit the damping leads to completely different Fourier amplitudes which might not be representative of the actual magnitude of a frequency component when damping also becomes a function of frequency.

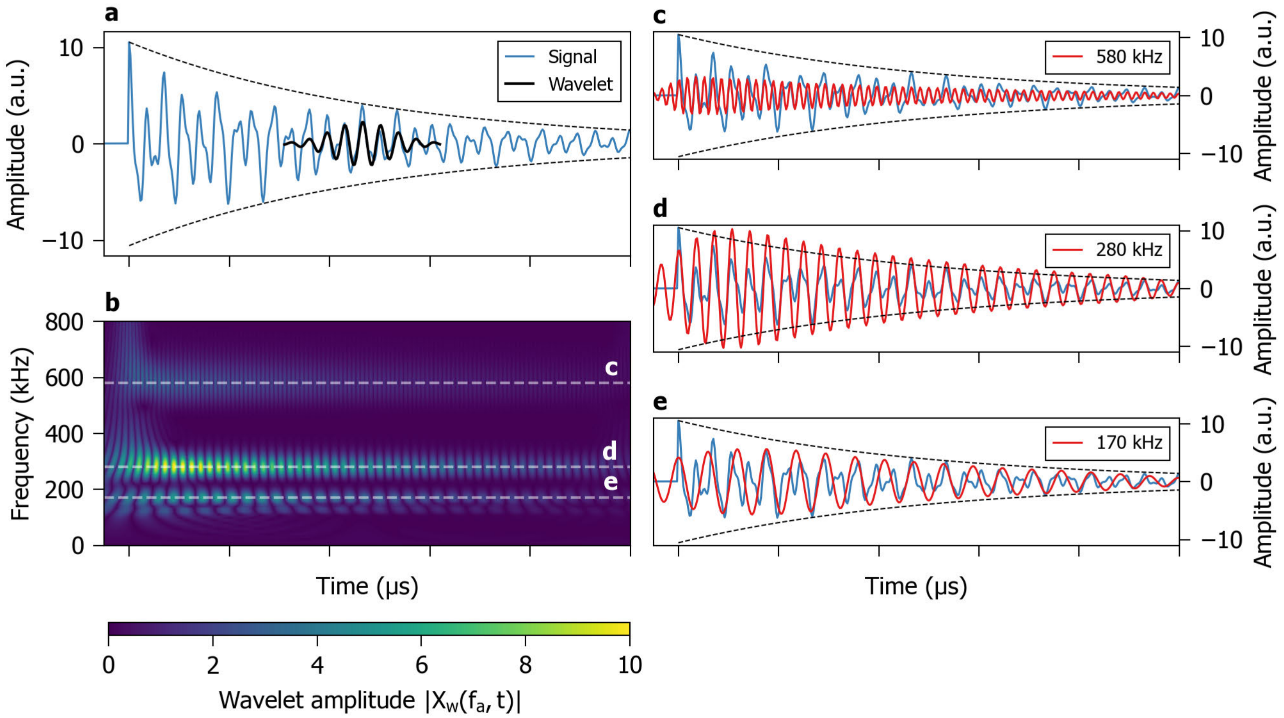

Figure B.9.: Continuous Wavelet Transformation. Damped signal calculated by Equation B.3 with with dimensionless amplitudes $A_i = \{1, 2.5, 5, 2\}$, frequencies $f_i = \{130, 170, 280, 580\}$ (in kHz) and damping $\tau = 50\,\mu\text{s}$. A wavelet is schematically overlayed (a). Heatmap of the modulus of the continuous wavelet transform calculated with the signal sampled at 4 MHz and a complex Morlet wavelet with center frequency 2.0 Hz and a bandwidth of 1.5 using Equation B.10 (b). Comparison between the CWT as a function of time in comparison to the original signal for 580 (c), 280 (d) and 170 kHz (e). The damping envelope indicated by the dashed line is identical between a, c, d and e.

B.5.2 Continuous Wavelet Transformation

The inherent drawback of Fourier transformation is that there is no information on how amplitudes of different frequencies are evolving over time (e.g., due to damping). To overcome this, continuous wavelet transformation can be used to calculate the time evolution of the frequency spectrum of a (discrete) signal [366]. Time resolution is achieved by scanning a wavelet that is displaced along the time axis by Δt and multiplying it with the original function. The integral of this product will be large if the frequencies contained in the Fourier transform of the wavelet are close to the frequency content of the signal. To scan through different frequencies the wavelet is multiplied by a set of different scale factors a that shift the frequency content of the wavelet.

The continuous wavelet transform (CWT) X_w of a continuous function $x(t)$ for scale a at time Δt is defined as:

$$X_w(a, \Delta t) = \frac{1}{\sqrt{|a|}} \int_{-\infty}^{\infty} x(t) \overline{\psi} \left(\frac{t - \Delta t}{a} \right) \mathrm{d}t, \;\; a \in \mathbb{N}, \tag{B.9}$$

where $\overline{\psi}$ is the complex wavelet function. For a discretely sampled signal the CWT changes to:

$$X_w(a, b) = \frac{1}{\sqrt{|a|}} \sum_{n=0}^{N-1} x(n) \overline{\psi} \left(\frac{n - b}{a} \right), \;\; b \in \mathbb{N}, 0 \leq b \leq N - 1, \tag{B.10}$$

which is the CWT for scale a at sample point b. Out of the different available wavelets this work will rely solely on the complex Morlet wavelet:

$$\overline{\psi}(t) = \frac{1}{\sqrt{\pi \tau}} \mathrm{e}^{2\pi i \omega_\psi t} \, \mathrm{e}^{\frac{-t^2}{\tau}}, \;\; \tau, \omega_\psi \in \mathbb{R}_{\geq 0}, \tag{B.11}$$

which is a complex exponential that is symmetrically damped in time by a Gaussian distribution. ω_ψ is the center frequency (in Hz) of the wavelet and τ is the bandwidth parameter. Both bandwidth and center frequency determine the non-linear tradeoff between time and frequency resolution. The bandwidth parameter determines how fast the wavelet decays. Increasing τ will lead to a better frequency resolution at the expense of the time resolution.

The center frequency on the other hand determines the 'center-of-mass' frequency in the Fourier transform of the wavelet. The complex Morlet wavelet also allows the direct calculation of the frequency f of a given scale a:

$$f(a) = \frac{\omega_\psi f_s}{a}. \tag{B.12}$$

Figure B.9a shows the damped signal presented in Figure B.8b that is schematically overlayed with the real part of a complex Morlet wavelet. The resulting CWT heatmap of the sampled signal ($N = 441$, $f_s = 4\,\text{MHz}$) is presented in Figure B.9b and shows the modulus of the wavelet amplitude. The three different frequency components of the signal are clearly visible, and the damping is replicated reasonably well. The three main frequency components are shown in more detail in Figure B.9c-e. But, it is also clear that the CWT has a worse frequency resolution in comparison to the DFT/FFT shown in Figure B.8d. The FFT has sharp peaks that are defined within a few tens of kHz whereas the CWT has broad peaks in the frequency spectrum that are up to hundreds of kHz wide.

In summary, a center frequency of 2.0 Hz and a bandwidth of 1.5 was chosen for all CWTs (if not explicitly mentioned otherwise) in this work as a reasonable tradeoff between time and frequency resolution. CWT was implemented in the data analysis workflow using the python PyWT package [367].

Abbreviations

AD	Antiproton Decelerator
APPA	Atomic, Plasma Physics and Applications
ATLAS	A Toroidal LHC Apparatus
CBM	Compressed Baryonic Matter
CERN	European Organization for Nuclear Research
CFC	Carbon-fiber reinforced graphite
CL	Cathodoluminescence
CMS	Compact Muon Solenoid
CNGS	CERN Neutrinos to Gran Sasso
CVD	Chemical vapor deposition
CWT	Continuous wavelet transform
DFT	Discrete Fourier transform / Density functional theory
ESS	European Spallation Source
FAIR	Facility for Antiproton and Ion Research
FE	Finite Element
FFT	Fast Fourier transform
FG	Flexible graphite
FNAL	Fermi National Accelerator Laboratory
FT-IR	Fourier-transform infrared (absorption spectroscopy)
GSI	GSI Helmholtz Centre for Heavy Ion Research
HADES	High Acceptance Di-Electron Spectrometer
HiRadMat	High-Radiation to Materials Facility
HL-LHC	High-Luminosity Large Hadron Collider
HPHT	High-pressure/high-temperature
IL	Ionoluminescence
LBNF	Long-Baseline Neutrino Facility
LHC	Large Hadron Collider
LDV	Laser Doppler Vibrometer
NuMI	Neutrinos at the Main Injector
ORNL	Oak Ridge National Laboratory
Pbar	Antiproton
PG	Polycrystalline (isostatic) graphite
PL	Photoluminescence
ppp	Protons per pulse
SIS	Heavy ion synchrotron
SHI	Swift heavy ion
SNS	Spallation Neutron Source
SPS	Super Proton Synchrotron
Super-FRS	Superconducting Fragment Separator
UNILAC	Universal Linear Accelerator

List of Figures

1.1 Layout of the existing GSI (blue) and FAIR (red) accelerator facilities. High-power rare-isotope (RIB) and antiproton (p-bar) targets that will be exposed to high-power beam conditions are indicated. Swift heavy ion irradiation experiments presented in this work were performed at the M-branch. APPA cave will host new materials research beamline for relativistic heavy ion beams from the future SIS100 accelerator. 4

2.1 Stopping power of ^{197}Au and protons as a function of specific energy in three different target materials. Solid lines represent the stopping power due to electronic energy loss (ionizing energy loss). Dashed lines represent the stopping power due to nuclear energy loss (non-ionizing energy loss). Calculated using SRIM-2013 [32]. 7

2.2 Evolution of ion-induced amorphization in irradiated materials. Different models to describe the increase of ion-induced amorphization as a function of fluence, adapted from [50] (a). Different number n of ion hits (red area) on an arbitrary material surface (grey area) that qualitatively describes the direct (or single) impact model (b). 11

3.1 Unit cells of the diamond and graphite lattice. Unit cell of the diamond lattice viewed off-axis and along three crystallographic directions showing four-fold (<100>), two-fold (<110> and three-fold symmetry (<111>) (a). Unit cell of the graphite lattice viewed off-axis and along the two crystallographic directions showing the large inter-planar distance (<1$\bar{1}$00>) and the six-fold symmetry along the c axis (<0001>) (b). Created using the Blender software [54]. 13

3.2 Pressure, temperature phase diagram of carbon. Adapted from [62, 93]. 16

3.3 Schematic representation of the high-pressure/high-temperature (HPHT) reaction cell and its contents. The reaction cell is surrounded by a graphite heater (not shown here) and placed in a press (a). Schematic representation of a microwave plasma chemical vapor deposition (MPCVD) reactor. Depending on the exact process the substrate can either be a seed diamond or an iridium (100) substrate (b). 17

4.1 Overview of ionoluminescence (IL) spectra under irradiation with MeV protons. IL signal at different integrated number of protons of natural type Ia diamond of unknown nitrogen impurity level and CVD diamond with 5 ppm nitrogen impurities adapted from [20] (a). IL signal of a 'detector grade' CVD diamond with ≤50 ppb at different fluences adapted from [22] (b). 23

5.1 Ground and excited state of a defect within the band gap of diamond. Each state contains several vibrational energy levels (dark blue horizontal lines) separated by $\hbar\omega$. The zero phonon line (ZPL) is the transition from and into the lowest vibrational state of the ground and excited state respectively (a). Schematic representation of the spectral shape of a defect within the band gap both in absorption and luminescence. The phonon sideband (PSB) is observed at energies larger than the ZPL in absorption while the reverse is true for luminescence (b). 26

5.2 Schematic representation of (elastic) Rayleigh scattering and (inelastic) Raman scattering. Depending on the energy difference between scattered and absorbed light, Raman scattering is split into Stokes and anti-Stokes Raman scattering (a). Raman spectrum on a low nitrogen monocrystalline CVD diamond under laser excitation with 473 nm with the Stokes Raman line at 1332 $\mathrm{cm^{-1}}$. The second order Raman spectrum is zoomed in and displaced vertically for clarity. The dashed line indicates the noise level of the spectrometer (b). 28

6.1 Energy loss of 4.8 MeV/n ions as a function of penetration depth for ^{48}Ca (a), ^{132}Xe (b), ^{197}Au (c) and ^{238}U (d) in diamond with a density of 3.51 $\mathrm{g\,cm^{-3}}$. The total energy loss at the sample surface is indicated by the value in keV/nm. Calculated with SRIM-2013 [32]. 32

6.2 Schematic overview of in-situ and on-line measurement set-ups at the spectroscopy chamber of the M3 beamline; in-situ FT-IR absorption spectroscopy (a), in-situ UV/vis absorption spectroscopy (b) and on-line ionoluminescence spectroscopy (c). "CL" denotes condenser lenses. During FT-IR absorption spectroscopy, infrared light is coupled in and out of the vacuum chamber using infrared transparent vacuum windows. For UV/vis and ionoluminescence the light is coupled in and out of the vacuum chamber using UV-grade optical fibers and two fiber-feedthroughs. 33
6.3 UV/vis absorption spectroscopy. An input spectrum is generated using a combined deuterium/halogen light source. After the sample is introduced into the beam path a transmitted spectrum is measured. The transmission is determined by the ratio of the transmitted and input spectrum. . . . 34
6.4 Cross sectional view of an irradiated diamond and photoluminescence mapping. After irradiation a "mapping", usually consisting of three line mappings that start 10 µm away from the diamond surface and extended at least 50 µm deep into the diamond. Lateral distance between the line mappings is 30 µm and longitudinal distance between single measurement points is 1 or 2 µm. The ion range for 4.8 MeV/n ^{197}Au ions is 30.0 µm according to SRIM-2013 [32]. 36

7.1 Ionoluminescence of diamond-based copper matrix composite (Cu-Dia) with an average diamond particle size of 45 µm during irradiation with 4.8 MeV/n ^{209}Bi. Courtesy of Marilena Tomut (a). Four different type Ib HPHT diamonds after 4.8 MeV/n ^{197}Au irradiation to different fluences. The beam spot was larger than the sample size. The apparent edges are the parallel surfaces on the back of the diamonds that are still visible below 5×10^{12} cm^{-2}. (b). Micrograph of HPHT-synthesized diamond powder with 45 µm average particle size. Similar diamonds are used in the manufacturing of Cu-Dia and Ti-Dia samples (c). 39
7.2 Optical micrographs of two series of diamond-based copper matrix (Cu-Dia) composites irradiated with 4.8 MeV/n ^{238}U (top row) and ^{209}Bi ions (bottom row). Top row: Cu-Dia with an average diamond particle size of 100 µm. Bottom row: Cu-Dia with 45 µm diamond particles. The scale bar applies to all images. 40
7.3 Ionoluminescence series of two HPHT diamonds during irradiation with 4.8 MeV/n ^{197}Au (top row) and ^{48}Ca ions (bottom row) recorded with a CCD camera. The start image corresponds to the first image recorded upon beam on target. Integration time and gain setting of the camera are different between the two rows. Each column corresponds to a similar dose on the sample. 40
7.4 Self-normalized spectral ionoluminescence yield heatmaps of four different samples irradiated with 4.8 MeV/n ^{197}Au up to 1×10^{12} cm^{-2}: diamond-based copper matrix composite (Cu-Dia) with 100 µm (a), Cu-Dia with 45 µm (b), diamond-based titanium matrix composite (Ti-Dia) with 45 µm (c) average diamond particle size and a HPHT synthesized type Ib diamond monocrystal (d). Spectra are normalized to the ion flux during irradiation and self-normalized to the largest ionoluminescence intensity. 41
7.5 Integrated ionoluminescence in the range between 350 and 950 nm of different diamonds and diamond-based metal matrix (Cu-Dia and Ti-Dia) composite samples irradiated with 4.8 MeV/n ^{197}Au. Integrated luminescence yield normalized by the ion flux measured during irradiation (a, b) and self-normalized (c, d). The left row has linear-log scales and the right row with linear scales. . . 42
7.6 Integrated (top row) and maximum (bottom row) ionoluminescence intensity of diamonds and diamond-based metal matrix (Cu-Dia and Ti-Dia) composite samples irradiated with 4.8 MeV/n ^{197}Au in the two wavelength ranges between 450 and 675 nm (a, c) and between 850 and 950 nm (b, d). 43
7.7 Ionoluminiscence (IL) spectra of type Ib diamond during irradiation with 4.8 MeV/n ^{48}Ca. Ionoluminescence intensities have been normalized to the first spectrum recorded during irradiation up to 1.9×10^{11} cm^{-2}. IL heatmap with characteristic emission lines (a). Evolution of IL spectra at different ion fluences (b). IL spectra at the highest ion fluences below 500 nm (c) and above 650 nm (d). Dashed vertical lines indicate the edges of the individual spectra recorded by the moving grating spectrometer leading to intensity discontinuities. The relative error of the fluence is estimated to be at least 20 %. 44

7.8 Photoluminescence spectra of pristine and irradiated type Ib diamond samples exposed to different fluences of 4.8 MeV/n ^{197}Au in units of cm^{-2} and excited with 473 nm (blue spectra) and 633 nm (red spectra). Spectra were measured at different positions, corresponding to different electronic and nuclear energy loss dE/dx along the ion penetration depth: 0 µm (a), 10 µm (b), 25 µm (c) and 30 µm (d). Intensities are normalized to the average intensity of the diamond Raman line between 40 and 50 µm. Spectra are displaced vertically. 47

7.9 Depth-resolved photoluminescence (PL) heatmaps of type Ib diamonds exposed to different fluences of 4.8 MeV/n ^{197}Au in units of cm^{-2}. Excitation under 473 nm (a) and 633 nm (b). The ion range is indicated by the dashed vertical line. Intensities are normalized to the average intensity of the diamond Raman line between 40 and 50 µm. 48

7.10 Intensity of the diamond Raman line as a function of depth in type Ib diamonds exposed to different fluences of 4.8 MeV/n ^{197}Au under excitation with 473 nm (a) and 633 nm (b). The ion range is indicated by the dotted vertical line. Intensities are normalized to the average intensity of the diamond Raman line between 40 and 50 µm. Shaded areas indicate the standard deviation of three measurements. 49

7.11 Raman spectra around the diamond Raman line close to the end of the ion range for the three highest irradiation fluences with 4.8 MeV/n ^{197}Au ions under excitation with 473 nm (a) and 633 nm (b). Values in keV/nm correspond to the nuclear energy loss at the measured ion penetration depths. Dashed vertical lines indicate the position of the Raman line in defect-free diamond at 1332 cm^{-1}. 50

7.12 Intensity of the 3H center phonon sideband (a) and the NV$^-$center ZPL (b) as a function of depth in diamond samples irradiated with different fluences of 4.8 MeV/n ^{197}Au in units of cm^{-2} for excitation with 473 nm. Intensities are normalized to the average intensity of the diamond Raman line between 40 and 50 µm. Shaded areas indicate the standard deviation of three measurements. . . 50

7.13 Photoluminescence spectra of type Ib diamonds samples exposed to different fluences of 4.8 MeV/n ^{197}Au in units of cm^{-2}. Photoluminescence spectra under 473 nm excitation around the 3H (a) and the NV^0& NV$^-$centers (b) measured close to the surface (depth ∼0 µm). The diamond Raman line is indicated by the *. Intensities are normalized to the average intensity of the diamond Raman line between 40 and 50 µm. 51

7.14 In-situ transmission (a, c) and absorbance (b, d) of a type Ib diamond at different fluences of 4.8 MeV/n ^{197}Au ions. The upper row was measured and irradiated at room temperature, while the lower row was measured and irradiated at 50 K. 52

7.15 Absorption of type Ib diamond at different wavelengths as a function fluence for irradiation with 4.8 MeV/n ^{197}Au ions at room temperature (a) and at 50 K (b). Dashed horizontal lines represent the absorption at the given wavelength of the pristine sample. Solid lines are fits of the direct impact model, Equation 2.12, to the measurement data with the damage cross section σ given in the legend. 53

7.16 Characteristic absorption range of the GR1 center with its ZPL (a) and phonon sideband (PSB) (b) in type Ib diamond irradiated and measured at room temperature for different fluences of 4.8 MeV/n ^{197}Au ions. All spectra are background corrected. Absorbance of the GR1 center ZPL (c) and the GR1 center PSB at 2 eV (d) as a function of fluence. Solid lines are fits of the single impact model to the measurement data with the damage cross section σ given in the legend. Shaded areas represent the standard deviation of the fit. 54

7.17 Characteristic absorption range of the 3H center (a) and the 1.859 eV & 1.890 eV centers (b) in type Ib diamond irradiated and measured at room temperature for different fluences of 4.8 MeV/n ^{197}Au ions. All spectra are background corrected. Absorbance of the 3H ZPL (c) and the 1.859 eV & 1.890 eV centers (d) as a function of fluence. Solid lines are fits of the single impact model to the measurement data with the damage cross section σ given in the legend. Shaded area represent the standard deviation of the fit. Dashed lines are guides to the eye. 55

7.18 Characteristic absorption range of the GR1 center with its ZPL (a) and phonon sideband (PSB) (b) in type Ib diamond irradiated and measured at 50 K for different fluences of 4.8 MeV/n ^{197}Au ions. All spectra are background corrected. Absorbance of the GR1 center ZPL (c) and the GR1 center side band at 2 eV (d) as a function of fluence. Solid lines are fits of the single impact model to the measurement data with the damage cross section σ given in the legend. Shaded areas represent the standard-deviation of the fit. 56

7.19 Characteristic absorption range of the 3H center (a) and the 1.859 eV & 1.890 eV centers (b) in type Ib diamond irradiated and measured at 50 K for different fluences of 4.8 MeV/n ^{197}Au ions. All spectra are background corrected. Absorbance of the 3H ZPL (c) and the 1.859 eV & 1.890 eV centers (d) as a function of fluence. Solid lines are fits of the single impact model to the measurement data with the damage cross section σ given in the legend. Shaded area represent the standard-deviation of the fit. Dashed lines are guides to the eye. 57

7.20 In-situ transmission (a, c) and absorbance (b, d) measurements of a type IIa diamond at different fluences of 4.8 MeV/n ^{197}Au ions. The upper row was measured and irradiated at room temperature, while the lower row was measured and irradiated at 50 K. 58

7.21 Absorption of a type IIa diamond at different wavelenths as a function fluence for irradiation with 4.8 MeV/n ^{197}Au ions at room temperature (a) and at 50 K (b). Dashed horizontal lines represent the absorbance of the pristine sample at the given wavelength. Solid lines are fits of the single impact model, Equation 2.12, to the measurement data with the damage cross section σ given in the legend. 59

7.22 Characteristic absorption range of the GR1 center with its ZPL (a) and side band (b) in type IIa diamond irradiated and measured at room temperature for different fluences of 4.8 MeV/n ^{197}Au ions. All spectra are background corrected. Absorbance of the GR1 center ZPL (c) and the GR1 center side band at 2 eV (d) as a function of fluence. Solid lines are fits of the direct impact model to the measurement data with the damage cross section σ given in the legend. Shaded areas represent the standard-deviation of the fit. 60

7.23 Normalized absorbance as a function of fluence of 4.8 MeV/n ^{197}Au ions for irradiation and measurement at room temperature and 50 K in type Ib and type IIa diamond with ∼200 ppm and ≤5 ppb N_s respectively. Evolution of the GR1 center ZPL (a), GR1 center ZPL phonon replica at $\hbar\omega = 41$ meV (b), GR1 center phonon sideband (c), 3H ZPL (d), 1.859 eV center (e) and 1.889 eV center (f). Errors are omitted for clarity. Solid lines are fits of the single impact model with the damage cross section σ in units of nm^2 given in the legend. 61

7.24 Infrared transmission spectra of type Ib diamond irradiated to different fluences of 4.8 MeV/n ^{197}Au ions in units of cm^{-2} (a). Zoomed regions of the nitrogen absorption range (b) and the C-H / O-H / N-H bond stretching region (c). Arrows indicate increasing fluences. 63

7.25 Infrared transmission spectra of a type Ib diamond before (pristine) and after irradiation with 4.8 MeV/n ^{197}Au in the nitrogen absorption region (a) and the C-H / O-H / N-H stretching region (b). The corresponding absorption spectra after background subtraction are shown in (c) and (d), respectively. 64

7.26 Absorbance at different infrared wavenumbers as a function of fluence of 4.8 MeV/n ^{197}Au ions in type Ib diamond. A_0 is the pristine absorbance. Absorbance of the C center (N_s) at 1130 and 1344 cm^{-1} (a) and of the A (N=N), 1282 cm^{-1} & B center (4N-V), 1175 cm^{-1} and O-H, N-H bond stretching modes at 3230 cm^{-1} (b). Solid lines are fits of the direct impact model to the measurement data with the damage cross section σ given in the legend. Dashed lines represent guides to the eye. 65

8.1 Figures of merit for high-power accelerator facilities. Stored beam energy as a function of (specific) beam momentum of various (anti-)proton colliders (a). Average beam current (ratio of beam intensity and pulse length multiplied by mass number) as a function of specific beam momentum for various high-power production targets (b). Adapted from [221, 222]. 70

9.1 Energy deposition rate as a function of time for (i) steady state, (ii) slow transient and (iii) fast transient energy deposition events that are experienced by beam intercepting devices. The magnitude of energy deposition rates is based on the estimated beam losses on the LHC collimation system [244]. 75

9.2 Schematic stress-strain (or pressure-volume change) curve that shows the three different dynamic regimes that can be provoked by transient energy deposition events. $\sigma_{\text{y, static}}$ is the tensile strength (at a strain of $E \cdot \sigma_{y1}$) of the material under quasi-static loading conditions with a strain rate of $\dot{\varepsilon} = 10^{-3}\,\text{s}^{-1}$. $\sigma_{\text{y, dyn.}}$ denotes the tensile strength at high strain rates of $\dot{\varepsilon} = 10^{3}\,\text{s}^{-1}$. σ_c and ε_c are the critical stress and strain above which shock wave propagation occurs. Adapted from [235]. . . . 77

9.3 Energy deposition distribution in a cylindrical target. Schematic representation of the target in quarter-cut geometry with the energy deposition density overlayed qualitatively (a). Radial energy deposition density of a 7.2 µs long 440 GeV/c proton beam pulse with a 1σ beam spot size of 0.3 mm in a 1.84 g cm^{-3} graphite target (b). Energy deposition can be simply calculated by dividing the deposited energy density with the volumetric mass density of the target. Power deposition density is calculated by dividing the energy deposition density by the pulse length. 79

9.4 Analytical solution of thermal field evolution with time. Radial distribution of the beam-induced temperature for different times after the beam pulse length τ (a). Time evolution of the temperature at different radial positions (b). 80

9.5 Analytical solution of quasi-static and dynamic stresses induced by the thermal field shown in Figure 9.4. Radial distribution of the quasi-static radial σ_r, circumferential σ_θ, and axial σ_z, stress at the end of the beam pulse (a). Evolution of the quasi-static and dynamic axial stress in the center of the target (b). Horizontal dashed lines indicate two simple solutions to the thermal stress magnitude that are independent of both target geometry and spatial distribution of the thermal field. 81

10.1 Scheme of the CERN accelerator complex with the HiRadMat facility at the TT60/TT66 extraction line of the SPS. HiRadMat delivers proton beams with a momentum of 440 GeV/c from the SPS. Reprinted with permission from [255]. 86

10.2 HRMT38 FlexMat experiment. Exterior view of the experimental chamber prior to installation in the HiRadMat target area with the bending mirror for the on-line laser Doppler vibrometer (LDV) diagnostic (a). Target holder and target stations without the vacuum chamber (b). Experimental chamber inside the HiRadMat target area with the beam television (BTV) for on-line beam size and displacement monitoring and the radiation-hard camera (Cam.) (c). 87

10.3 Different sample geometries used for the FlexMat experiment in front view. Single material cylindrical samples (a). Tantalum-core graphite-shell samples (b). FAIR pbar mock-up target with inconel core, graphite shell and aluminum sleeve (c). 88

10.4 Details of the target holder. Front view (in beam direction) of the target holder (a). Detail view of the target holder (b). Overview of the target holder with overall dimensions indicated (c). 10 mm long sample of target station 6 (d). Front view of a 20 mm long sample (e). Red arrows indicate the direction of the beam and numbers the respective target stations. Samples (and their materials) are summarized in Table 10.2. 89

10.5 Influence of the sample support on the dynamic response of a cylindrical polycrstalline graphite sample (diameter 10 mm, length 10 mm) irradiated with a high-intensity 440 GeV/c proton beam (7.2 µs pulse length). Simulated radial surface velocity (with energy deposition density calculated by FLUKA) at 5 mm length of the sample as a function of time after the beam pulse (a). FFT of the simulated dynamic response (b). 90

10.6 Laser Doppler vibrometer beam paths. CAD model of the beam paths in the HiRadMat facility with yellow and pink lines indicating the beam paths of the LDVs. Courtesy of Vincent Clerc, CERN (a). Location of the two LDV measurement heads in the 'bunker' (b). Final set of mirrors installed on the linear displacement stage in front of the experimental chamber (c). Green dashed arrows indicate the LDV beam paths. The red arrow indicates the beam direction. 92

10.7 Schematic layout of the basic components of a laser Doppler vibrometer using a laser with frequency f_0. The test beam is shifted by a known frequency f_b using an acousto-optic modulator (a Bragg cell). The reflected test beam is Doppler shifted by f_d which is proportional to the target's velocity. The interference between the test beam and the reference beam generates a frequency-modulated signal with carrier frequency f_b and modulation frequency f_d. 93

11.1 Overview of 440 GeV/c proton beam pulses sent to the HRMT38 FlexMat experiment. Extracted beam intensity in protons per pulse (ppp) from the SPS accelerator and integrated numbers of protons on target as a function of time. Vertical dashed lines indicate the end of the irradiation for the different target stations #1 to #6. 95

11.2 Beam position jitter and spot size analysis recorded on the HiRadMat BTV for the different optics used in the HRMT38 FlexMat experiment. Z score of the horizontal and vertical beam displacement for a requested beam sigma of 0.25 mm (a), 0.5 mm (c) and 1.5 mm (e). Histogram of horizontal and vertical beam sigmas for the different requested beam sigmas (b, d and f). 96

11.3 Peak deposited energy density of per 440 GeV/c protons and peak temperature rise at the end of a beam pulse with maximum beam intensity in target stations 1 (a), 2 (b), 3 (c) and 6 (d) along the length of the target stations. FLUKA simulations were conducted taking the average beam spot size for each target station into account (c.f. Figure 11.2). The temperature rise is calculated analytically ('FLUKA temperature') and numerically ('ANSYS transient thermal' with an initial temperature of 293 K. 97

11.4 Dynamic response of different isotropic polycrystalline graphite samples after irradiation with 4.3×10^{12} ppp 440 GeV/c proton beams (0.9 µs pulse length) with a transverse beam size of $\sigma_{x,y}$~0.3 mm. Radial surface velocity (blue line) measured by a laser Doppler vibrometer in the center of SGL R6300 (a), SGL R6550 (b), SGL R6650 (c) and POCO ZEE (d). Particle sizes according to the supplier are given in parentheses. Dashed red lines represent the damping envelope obtained by a fit of an exponential decay function to the local absolute maxima with the obtained damping time constant τ_D stated in the legend. 99

11.5 Detailed overview of the dynamic response of different isotropic polycrystalline graphite samples after irradiation with 4.3×10^{12} ppp 440 GeV/c proton beams (0.9 µs pulse length) with a transverse beam size of $\sigma_{x,y}$~0.3 mm. Radial surface velocity measured by a laser Doppler vibrometer in the center of SGL R6300 (a), SGL R6550 (b), SGL R6650 (c) and POCO ZEE (d). Particle sizes according to the supplier are given in parentheses. 100

11.6 Self-normalized fast Fourier transform amplitude of the dynamic response for different isotropic polycrystalline graphite samples after irradiation with individual 440 GeV/c proton beam pulses of increasing intensities (transverse beam size $\sigma_{x,y}$~0.3 mm). Fourier transform of the radial surface velocity measured by a laser Doppler vibrometer in the center of SGL R6300 (a), SGL R6550 (b), SGL R6650 (c) and POCO ZEE (d). Particle sizes according to the supplier are given in parentheses. Fourier transform spectra are shifted vertically for clarity. Dashed lines indicate different experimental axial f_a and i-th order radial vibration frequencies $f_{r,i}$. 101

11.7 Self-normalized absolute continuous wavelet transform. Heatmap of the CWT of the radial surface velocity for 500 µs after irradiation with ~8.6×10^{12} ppp 440 GeV/c proton beams (1.8 µs pulse length). Heatmap of the CWT of SGL R6300 (a), SGL R6550 (b), SGL R6650 (c) and POCO ZEE (d). Particle sizes according to the supplier are given in parentheses. Self-normalized Fourier transform spectra of the radial surface velocity are overlayed on top of the data for comparison (c.f. Figure 11.6).103

11.8 Damping time constant τ_D as a function of frequency. τ_D has been obtained from an exponential decay fit of the local maxima of the absolute CWT at frequency f for SGL R6300 (a), SGL R6550 (b), SGL R6650 (c) and POCO ZEE (d). Damping time constant at zero frequency indicates the damping of the overall signal. Particle sizes according to the supplier are given in parentheses. * indicate the frequency with the largest amplitude in the Fourier spectrum of the dynamic response shown in Figure 11.6. 104

11.9 Beam-induced dynamic response from experiment (red) and FE simulation (blue) for a SGL Carbon R6650 sample irradiated with a 4.53×10^{12} ppp 440 GeV/c proton beam (0.9 µs pulse length). Radial surface velocity as a function of time (a). Fourier transform of the radial surface velocity for 200 µs after the beam pulse (b). Dashed vertical lines indicate axial, f_a and radial vibration modes with frequencies $f_{r,i}$ that are presented in Table 11.2. 106

11.10 Continuous wavelet transform (CWT) of the radial surface velocity of the SGL Carbon R6650 sample irradiated with a 4.53×10^{12} ppp 440 GeV/c proton beam (0.9 µs pulse length). Heatmap of the absolute CWT of the radial surface velocity measured experimentally (a) and of a FE simulation (b). The input signals for the continuous wavelet transformation are shown in Figure 11.9. 107

11.11 Modal analysis of the sample geometry with mechanical properties of SGL R6650. Extremal cases of the total deformation of different fundamental vibration modes. Blue indicates negative displacement of the mesh point from its original position, while red indicates positive displacement. (Anti-phase) Axial vibration mode with f_a (a), in-phase axial vibration mode (b), 143 kHz vibration mode (c), first radial vibration mode $f_{\mathrm{r},1}$ (d), in-phase axial vibration harmonic mode $f_{\mathrm{a, har.}}$ (e), second radial vibration mode $f_{\mathrm{r},2}$ (f). Length and diameter of the cylinders are 10 mm. 107

11.12 Beam-induced dynamic response from experiment (red) and FE simulation (blue) for a POCO ZEE sample irradiated with a 4.53×10^{12} ppp 440 GeV/c proton beam (0.9 µs pulse length). Radial surface velocity as a function of time (a). Fourier transform of the radial surface velocity for 200 µs after the beam pulse (b). Dashed vertical lines indicate axial, f_a and radial vibration modes with frequencies $f_{r,i}$ that are presented in Table 11.2. 108

11.13 Continuous wavelet transform (CWT) of the radial surface velocity of the POCO ZEE sample irradiated with a 4.53×10^{12} ppp 440 GeV/c proton beam (0.9 µs pulse length). Heatmap of the absolute CWT of the radial surface velocity measured experimentally (a) and of a FE simulation (b). The input signals for the continuous wavelet transformation are shown in Figure 11.12. 109

11.14 Radial surface velocity of sample #1 R6650 after irradiation with a 1×10^{11} ppp 440 GeV/c proton beam (25 ns pulse length). Dynamic response within the first 400 µs (a). Response within the first 25 µs (b). Response between 150 and 180 µs (c). The dashed red lines represent a guide to the eye for the damping envelope. 110

11.15 Frequency analysis of the dynamic response of sample #1 Ta/R6650 after irradiation with 1×10^{11} ppp within the first 200 µs. Power spectral density as a function of frequency with dashed lines indicating different fundamental vibration frequencies (a). Continuous wavelet transform of the absolute radial surface velocity. Color coding represents the values of the normalized absolute radial surface velocity (b). 111

11.16 Comparison between experimental and simulation results for sample #1 Ta/SGL R6650. Experimental (blue) and simulated (black) radial surface velocity as a function of time for 20 µs after the beam pulse of 1×10^{11} ppp (25 ns pulse length) (a). Normalized power spectral densities for the first 100 µs of the simulation and the experiment at two different beam intensities (b). 113

11.17 Qualitative opposite extreme deformation (left and right) of different vibration modes obtained by modal analysis of sample #1 SGL R6650 that coincide with dominant frequency contributions measured during the experiment. The vibration modes have frequencies of 153.4 (a), 186.4 (b), 319.5 (c), 477.3 (d), 804.0 (e), 899.7 (f) and 978.4 kHz (g). Color coding qualitatively represents the normalized magnitude of deformation. Scale bars correspond to 10 mm. 114

11.18 Continuous wavelet transform of the measured and simulated radial surface velocity of sample #1 SGL R6650. The normalized power spectral density plot is overlaid in white. Solid lines indicate vibration modes of the sample geometry obtained by modal analysis. Experimental result at 1×10^{11} ppp and 25 ns pulse length (a), 6×10^{11} ppp, 300 ns (b), and simulation result at 1×10^{11} ppp, 25 ns (c). 115

11.19 Radial surface velocity (solid blue line) and calculated damping envelope (red dashed line) for 200 µs after irradiation of three different polycrystalline graphite samples: #1 Ta/SGL R6650 (a), #6 Ta/SGL R6650 (b), and #3 Ta/POCO ZEE (c) at beam intensities of 1×10^{11} ppp, 25 ns pulse length (top) and 6×10^{11} ppp, 300 ns (bottom) beam intensity. The energy density indicates the peak deposited energy density in the tantalum core averaged over the length of the sample calculated with FLUKA. 116

11.20 Damping time constant τ of the overall dynamic response for samples #1 Ta/SGL R6650, #6 Ta/SGL R6650 and #3 Ta/POCO ZEE as a function of pulse intensity (a). Damping time constant as a function of beam intensity for different frequencies (blue circles) of sample #1 Ta/SGL R6650 obtained from continuous wavelet transform in comparison to the overall damping time constant (black line) of the radial surface velocity (b–g). Frequencies have a systematic error of ±10 kHz. . . 116

11.21 Frequency analysis of the radial surface velocity shown in Figure 11.19. The normalized spectral power density within the first 100 µs after irradiation is shown for beam pulses with intensities of 1 and 6×10^{11} ppp of samples #1 Ta/SGL R6650 (a), #6 Ta/SGL R6650 (b) and #3 Ta/POCO ZEE (c). 117

11.22 Continuous wavelet transform of the radial surface velocity presented in Figure 11.19 for three different polycrystalline graphite samples #1 Ta/SGL R6650 (a), #6 Ta/SGL R6650 (b) and #3 Ta/POCO ZEE (c) at 1×10^{11} ppp (top) and 6×10^{11} ppp (bottom) pulse intensity. 118

11.23 Radial surface velocity (solid blue line) and calculated damping envelope (red dashed line) as a function of time for 100 and 200 µs after the beam pulse for two different carbon-fiber reinforced graphite composites and graphitic foam: #4 Ta/SGL Premium PyC (a), #7 Ta/ArianeGroup Sepcarb (b) and #3 Ta/POCO FOAM (c) at 1×10^{11} ppp, 25 ns pulse length (top) and 6×10^{11} ppp, 300 ns (bottom) pulse intensity. The energy density indicates the peak energy deposition in the tantalum core averaged over the length of the sample calculated with FLUKA. The perturbations in (c) are nonperiodic. 119

11.24 FFY analysis of the radial surface velocity shown in Figure 11.23. The normalized spectral power density within the first 100 µs after irradiation is shown for beam pulses with intensities of 1 and 6×10^{11} ppp of samples #4 Ta/SGL Premium PyC (a), #7 Ta/ArianeGroup Sepcarb (b) and #3 Ta/POCO FOAM (c). 120

11.25 Continuous wavelet transform of the radial surface velocity presented in Figure 11.23 for three different polycrystalline graphite samples #4 Ta/SGL Premium PyC (a), #7 Ta/ArianeGroup Sepcarb (b) and #3 Ta/POCO FOAM (c) at 1×10^{11} ppp (top) and 6×10^{11} ppp (bottom) pulse intensity. . . 120

11.26 Measured dynamic response for maximum applied pulse intensity on samples #1 Ta/SGL R6650 (a), #6 Ta/SGL R6650 (b) and #3 Ta/POCO ZEE (c). Left: radial surface velocity (solid blue line) and calculated damping envelope (red dashed line). Right: continuous wavelet transform as a function of time for 100 µs after the beam pulse. 122

11.27 Measured dynamic response for maximum applied pulse intensity on samples #4 Ta/SGL Premium PyC (a), #7 Ta/ArianeGroup Sepcarb (b) and #3 Ta/POCO FOAM (c). Left: radial surface velocity (solid blue line) and calculated damping envelope (red dashed line). Right: continuous wavelet transform as a function of time for 100 µs after the beam pulse. 123

11.28 Absolute maximum surface velocity (symbols) as a function of deposited energy in the tantalum core for samples #1, #3, and #6 (a) and samples #4, #7, and #10 (b). The inset is a blow-up of the dashed box. Lines represent a guide to the eye for the proposed range of deposited energy where the sample shows an overall elastic response. Error bars are smaller than the symbols. 124

A.1 Perfect diamond lattice (a). Diamond lattice with a vacancy, indicated by the dashed circle (b). . . . 134

A.2 Perfect diamond lattice (a). Neutral <001>-split interstitial (b). 3H center, di-<001> split interstitial in the Humble configuration (c). Threefold coordinated interstitials are indicated in gray and fully coordinated interstitials in black. Reprinted figure with permission from Goss, J.P. *et al.* , Physical Review B, 63, 195208 2001. Copyright 2021 by the American Physical Society. 134

A.3 Characteristic infrared absorption of a pristine type Ib diamond. The one phonon range relates to defect-induced absorption bands and especially nitrogen. Intrinsic absorption of the diamond lattice corresponds to the two phonon region. The three phonon region is created by hydrogen-bond vibrations. Zoomed regions of the spectrum are presented in red. The insets show the features of the different nitrogen centers and the aggregation pathway by annealing. Important absorption features are indicated by the dashed lines. The standard spectra of the nitrogen centers are adapted from the "DiaMap" software [200]. 136

A.4 Structure of infrared active nitrogen defects in diamond. The C center, N_s (a). The A center, N_2 (b). The B center, N_4V (c). Nitrogen atoms are indicated in blue. 137

A.5 Perfect diamond lattice (a). NV center, NV (b). H3 center, N_2V (c). N3 center, N_3V (d). Nitrogen atoms are indicated in blue. 138

A.6 Photoluminescence spectra of different diamond-based metal matrix composites under 473 nm excitation irradiated with different 4.8 MeV/n ions. Spectral intensities are normalized to the intensity of the diamond Raman line at 504.8 nm. Diamond-based titanium matrix (Ti-Dia) composite under irradiation with ^{132}Xe (a), diamond-based copper matrix (Cu-Dia) composite with 45 µm average diamond size and irradiation with 4.8 MeV/n ^{197}Au (b) and Cu-Dia with 100 µm average diamond size and irradiation with ^{238}U. Color coding represents the normalized probability to measure a given photoluminescence intensity as a function of wavelength for at least 100 individual measurement locations. Higher opacity indicates higher probabilities. 141

A.7 Photoluminescence spectra of Sumitomo PDXC HPHT diamonds on pristine and irradiated samples with different fluences of 4.8 MeV/n ^{197}Au in units of cm^{-2} excited with 473 nm (blue spectra) and 633 nm (red spectra). Spectra are normalized to the intensity of the diamond Raman line indicated by the star sign and are displaced vertically for easier visibility. 143

B.1 Schematic representation of the graphite basal plane orientation in PAN-derived carbon fibers. Reprinted with permission from [339] 147

B.2 Horizontal and vertical displacement of the targets with respect to the virtual beam axis for target stations 1 through 6 (a-f). Red lines indicate the center of the beam axis. Circles indicate the position and radius of individual samples in the respective target stations. H and V indicate the average horizontal and vertical displacement of the targets within a target station while R indicates the average radius measured by metrology. 150

B.3 Schematic overview of different carbon fiber reinforcements. The YX plane indicates the reinforcement direction, which is generally called the in-plane direction according to suppliers. The YX surface normal indicates the non-reinforced direction that alternates between matrix and reinforcement planes, generally called the through-plane direction. 3D-reinforcement of a 2D-reinforced CFC by single fiber needling through the reinforcement plane (a). Unidirectional reinforcement where fibers within a single reinforcement plane are oriented strictly in one direction (b). 2D-reinforcement with a woven roving. A roving consists of several thousand of individual carbon fibers that are woven to form a single reinforcement plane (c). 152

B.4 Comparison of the dynamic response of carbon fiber reinforced graphite samples impacted by 9×10^{12} ppp 440 GeV/c protons (1.8 µs pulse length). Fiber reinforcement planes are oriented normal ⊥ (left column) and parallel || (right column) to the beam direction. Dynamic response of 3D-reinforced ArianeGroup Sepcarb (a, b), SGL Carbon Performance with unidirectional reinforcement (c, d) and 2D-reinforced SGL Carbon Premium (e, f). Dashed red line indicates the overall damping envelope with the damping constant given in the legend. Horizontal dashed lines indicate the $\pm 1\sigma$ noise level of the measurement. 153

B.5 Self-normalized fast Fourier transform amplitude of the dynamic response for different CFC samples in two orientations after beam impact with 9×10^{12} ppp 440 GeV/c protons (1.8 µs pulse length). Fiber reinforcement planes are oriented normal ⊥ and parallel || (right column) to the beam direction. Fourier transform of the radial surface velocity measured by a laser Doppler vibrometer in the center of 3D-reinforced ArianeGroup Sepcarb (a), SGL Carbon Performance with unidirectional reinforcement (b) and 2D-reinforced SGL Carbon Premium (d). The input signals for the fast Fourier transformation are shown in Figure B.4. 154

B.6 Continuous wavelet transform (CWT) of the radial surface velocity of SGL Carbon Premium CFC in two different sample orientations impacted with 9×10^{12} ppp 440 GeV/c protons (1.8 µs pulse length). Heatmap of the absolute CWT of the radial surface velocity measured on the sample with reinforcement planes normal (a) and parallel to the beam axis (b). The input signals for the continuous wavelet transformation are shown in Figure B.4. 154

B.7 Finite element analysis workflow. Schematic overview of the multi-stage approach to simulate the dynamic response of short pulse particle beam irradiation (a). Typical mesh used in a coupled thermo-mechanical FEA simulation (b). Extrapolation of the FLUKA energy deposition map to the mesh elements as an internal heat generation in ANSYS transient thermal (c) and the resulting temperature field (d). Axial stress from a transient structural analysis in ANSYS using the temperature field as a thermal load at every timestep (e). Simulation results from ANSYS 2019 R2. 155

B.8 Sampled signal of Equation B.3 with 4 MHz sampling rate with dimensionless amplitudes $A_i = \{1, 2.5, 5, 2\}$, frequencies $f_i = \{130, 170, 280, 580\}$ (in kHz) as a function of time without (a) and with damping τ_D =50 µs (b). Comparison of discrete Fourier transform, calculated by numerically solving Equation B.6 (DFT) and using the FFT implementation in the NumPy package of python (FFT) for the undamped signal (c) and damped signal (d). 157

B.9 Continuous Wavelet Transformation. Damped signal calculated by Equation B.3 with with dimensionless amplitudes $A_i = \{1, 2.5, 5, 2\}$, frequencies $f_i = \{130, 170, 280, 580\}$ (in kHz) and damping $\tau = 50\mu s$. A wavelet is schematically overlayed (a). Heatmap of the modulus of the continuous wavelet transform calculated with the signal sampled at 4 MHz and a complex Morlet wavelet with center frequency 2.0 Hz and a bandwidth of 1.5 using Equation B.10 (b). Comparison between the CWT as a function of time in comparison to the original signal for 580 (c), 280 (d) and 170 kHz (e). The damping envelope indicated by the dashed line is identical between a, c, d and e. 159

List of Tables

3.1 Classification system of diamond, adapted from [76]. 15

4.1 Overview of color centers active in ionoluminescence that were reported in literature. Ionoluminescence spectra from references [20, 22] are shown in Figure 4.1. 24

6.1 Overview of irradiation experiments and samples used. The specific energy of all ions was 4.8 MeV/n. More details about the beam parameters are provided in table 6.2. 31

6.2 Beam parameters of the ions used in this work. The specific energy of all ions was 4.8 MeV/n. 33

7.1 Spectral components during ionoluminescence spectroscopy with 4.8 MeV/n ^{48}Ca shown in Figure 7.7 and attribution to crystallographic defects of diamond. All color centers are active in cathodoluminescence [140]. Measured wavelengths have a systematic error of ±2 nm, the systematic error of the energy is thus between 3 and 20 meV depending on the wavelength. Given fluences have a systematic error of ±20 % and correspond to ion fluence where a peak at the measured wavelength can be clearly identified. 45

7.2 Single impact damage cross sections σ obtained from fits of the direct impact model, Equation 2.12 to the increase of absorption for different color centers in HPHT-synthesized type Ib ($\sim$200 ppm N_s) and CVD-synthesized type IIa ($\leq$5 ppb N_s) diamonds irradiated with 4.8 MeV/n ^{197}Au ions. Spectral positions for the different color centers is taken from [140]. ** indicates fits that yielded non-physical cross sections. – indicates no change of the absorption intensity. 62

8.1 Overview of different pulsed beam facilities and their (maximum) design parameters. Except CNGS all facilities are currently in operation or are expected to come on-line until 2030. The average beam power can be calculated by the ratio of pulse energy and cycle rate (in seconds). 71

8.2 Overview of materials for beam intercepting devices and their material properties. R denotes the figure of merit of materials for robustness towards thermal shock calculated with Equation 8.1. R_{BID} denotes the figure of merit for robustness of materials towards pulsed beam operation calculated with Equation 8.3. Both figures of merit are calculated using the numerical values of the different material properties for the given units and are assumed dimensionless. Glidcop is an dispersion-strengthened copper alloy with $\sim$0.15 % alumina. Adapted from [235]. 73

9.1 Target geometry, beam and material properties used for the analytical model. Beam properties are an approximation of the beam properties at the HiRadMat facility for 440 GeV/c proton beams [252] that is relevant for the discussion of the results presented in chapter 11. Material properties reflect an isotropic graphite like SGL Carbon R6650 and are mean values over a temperature range between 300 and 1500 K. 78

10.1 Proton beam parameters of the HiRadMat Facility at SPS, CERN. Values taken from [252]. 86

10.2 Sample distribution in the experiment target stations. Pulse intensities indicate the overall maximum pulse intensity extracted on the target station. Maximum pulse intensity per sample may be lower. Average beam sizes are calculated for all shots using the same beam optics (Target Stations 1 to 3 and Target Stations 4 & 5, respectively). Densities are taken from material datasheets provided by the manufacturer. Anisotropic samples with their main reinforcement direction parallel to the irradiated surface are indicated by ||, while anisotropic samples with main reinforcement direction perpendicular to the irradiated surface are indicated by ⊥ (c.f. Figure 10.4). 91

11.1 Calculated maximum axial stresses σ_t in various isotropic graphite samples induced by the highest pulse intensities. Density ρ, Young's modulus E and compressive strength σ_c were taken from the supplier datasheets. Poisson's ratio ν are estimated. Flexural strength σ_f has been determined by three-point bending and is taken from [260]. E_d corresponds to the deposited peak energy density shown in Figure 11.3 averaged over the sample length for a beam intensity of 3.5×10^{13} ppp. T_max is the resulting peak temperature calculated with Equation 11.1. The last two columns are first-order approximations of the beam-induced thermal stresses σ_t calculated with Equation 9.27 and 9.28, respectively. 98

11.2 Axial f_a and i-th order radial $f_{\mathrm{r},i}$ vibration frequencies in polycrystalline graphite samples ($R = 5\,\mathrm{mm}$, $L = 10\,\mathrm{mm}$). Frequencies in the rows indicated by "Supplier" were calculated using Equations 9.31 and 9.29 with the Young's modulus E provided by the supplier. Frequencies in the rows indicated by "Exp." were experimentally observed in the FFT and CWT of the dynamic response of the samples and E and Poisson's ratio ν were extracted in a parametric fit of Equations 9.31 and 9.29 to these equations. Frequencies in the rows indicated by "FEM" are observed in the FFT of the dynamic response simulated with ANSYS Mechanical using the given E and ν. In rows indicated by "Modal", frequencies correspond to modes with axisymmetric total deformation simulated by modal analysis. Experimental frequencies have a systematic error of ±2 kHz and FEM frequencies ±5 kHz. 102

11.3 Damping time constant $\tau_{\mathrm{D},i}$ at different frequencies f_i in isotropic graphite determined by continuous wavelet transformation. Values are averaged over all beam intensities as variance-weighted means and errors are the standard error. f_a and $f_{r,i}$ correspond to axial and radial vibration modes, respectively. $f_{a,har}$ indicates an overtone of the axial vibration mode. * indicates the damping of the frequency with the highest amplitude in the Fourier spectra of a sample. Frequencies of these modes are given in Table 11.2. The value at zero frequency corresponds to the damping time constant of the measured LDV signal. 105

11.4 Material properties of tantalum and polycrystalline graphite SGL R6650 used in the coupled transient thermal/transient structural ANSYS simulation. 112

11.5 Comparison of frequency components identified in the FFT of the experimental results, the FFT of the simulations for a beam intensity of 1×10^{11} ppp and modal analysis of the sample geometry. Frequencies obtained from FFT have a systematic error of ±10 kHz. 113

Bibliography

1. Geissel, H. *et al. Technical Design Report on the Super-FRS* http://repository.gsi.de/record/54552 (NUSTAR, Darmstadt, 2008).
2. Polzin, T. *et al.* Modeling of a Dynamic Thermal Load Generated by a 7TeV Proton Beam Impacting the Beam Dump of the Large Hadron Collider at CERN. *EPJ Web of Conferences* **183,** 01065. doi:10.1051/epjconf/201818301065 (2018).
3. Kramer, T. *et al.* Considerations for the Beam Dump System of a 100 TeV Centre-of-mass FCC hh Collider. *Proceedings of the 6th Int. Particle Accelerator Conf.* **IPAC2015,** 4 pages, 0.460 MB. doi:10.18429/JACOW-IPAC2015-TUPTY050 (2015).
4. Sigmund, P. *Particle Penetration and Radiation Effects* doi:10.1007/3-540-31718-x (Springer Berlin Heidelberg, 2006).
5. Kiselev, D., Bergmann, R., Schumann, D., Talanov, V. & Wohlmuther, M. Proton induced activity in graphite - comparison between measurement and simulation. *Journal of Physics: Conference Series* **1046,** 012003. doi:10.1088/1742-6596/1046/1/012003 (2018).
6. Prosvetov, A. *et al.* Degradation of thermal transport properties in fine-grained isotropic graphite exposed to swift heavy ion beams. *Acta Materialia* **184,** 187–198. doi:10.1016/j.actamat.2019.11.037 (2020).
7. Ammigan, K. *et al. Novel Materials and Concepts for Next-Generation High Power Target Applications* 2022. eprint: arXiv:2203.08357.
8. Peroni, L., Scapin, M., Carra, F. & Mariani, N. Investigation of Dynamic Fracture Behavior of Graphite. *Key Engineering Materials* **569-570,** 103–110. doi:10.4028/www.scientific.net/KEM.569-570.103 (2013).
9. Simos, N. *et al.* 120 GeV neutrino physics graphite target damage assessment using electron microscopy and high-energy x-ray diffraction. *Physical Review Accelerators and Beams* **22.** doi:10.1103/physrevaccelbeams.22.041001 (2019).
10. Bäni, L. *et al.* Diamond detectors for high energy physics experiments. *Journal of Instrumentation* **13,** C01029–C01029. doi:10.1088/1748-0221/13/01/c01029 (2018).
11. Nociforo, C., Schirru, F., Kiš, M. & Schlemme, S. Detector developments for the Super-FRS. *EPJ Web of Conferences* **117** (eds Greco, V., Cognata, M. L., Pirrone, S., Rizzo, F. & Spitaleri, C.) 10007. doi:10.1051/epjconf/201611710007 (2016).
12. Schirru, F. *et al.* Development of large area polycrystalline diamond detectors for fast timing application of high-energy heavy-ion beams. *Journal of Instrumentation* **7,** P05005–P05005. doi:10.1088/1748-0221/7/05/p05005 (2012).
13. Bossini, E. & Minafra, N. Diamond Detectors for Timing Measurements in High Energy Physics. *Frontiers in Physics* **8.** doi:10.3389/fphy.2020.00248 (2020).
14. Bacher, S. *et al.* Performance of the diamond-based beam-loss monitor system of Belle II. *Nuclear Instruments and Methods in Physics Research Section A: Accelerators, Spectrometers, Detectors and Associated Equipment* **997,** 165157. doi:10.1016/j.nima.2021.165157 (2021).
15. Nordlund, K. *et al.* Primary radiation damage: A review of current understanding and models. *Journal of Nuclear Materials* **512,** 450–479. doi:10.1016/j.jnucmat.2018.10.027 (2018).
16. Sullivan, P. A. & Baragiola, R. A. Ion beam induced luminescence in natural diamond. *Journal of Applied Physics* **76,** 4847–4852. doi:10.1063/1.357258 (1994).
17. Vittone, E. *et al.* Micro-IBICC and micro-IL analyses of CVD diamond microdosimeters. *Nuclear Instruments and Methods in Physics Research Section B: Beam Interactions with Materials and Atoms* **181,** 349–353. doi:10.1016/S0168-583X(01)00527-4 (2001).
18. Manfredotti, C. *et al.* Ionoluminescence in CVD diamond and in cubic boron nitride. *Diamond and Related Materials* **10,** 568–573. doi:10.1016/S0925-9635(00)00604-X (2001).
19. Calvo del Castillo, H., Ruvalcaba-Sil, J. L., Barboza-Flores, M., Belmont, E. & Calderón, T. Ionoluminescence of diamond, synthetic diamond and simulants. *Nuclear Instruments and Methods in Physics Research Section A: Accelerators, Spectrometers, Detectors and Associated Equipment* **580,** 400–403. doi:10.1016/j.nima.2007.05.064 (2007).
20. Calvo del Castillo, H. *et al.* Ionoluminescence characterization of microwave and hot-filament CVD diamonds. *physica status solidi (a)* **205,** 2221–2225. doi:10.1002/pssa.200879727 (2008).

21. Lo Giudice, A. *et al.* Micro-IL and micro-PIXE studies of rich diamond meteorites at Legnaro nuclear microprobe. *Nuclear Instruments and Methods in Physics Research Section B: Beam Interactions with Materials and Atoms* **210,** 429–433. doi:10.1016/S0168-583X(03)01099-1 (2003).

22. Manfredotti, C. *et al.* Luminescence centers in proton irradiated single crystal CVD diamond. *Diamond and Related Materials* **19,** 854–860. doi:10.1016/j.diamond.2010.02.004 (2010).

23. Krauser, J., Zollondz, J.-H., Weidinger, A. & Trautmann, C. Conductivity of nanometer-sized ion tracks in diamond-like carbon films. *Journal of Applied Physics* **94,** 1959–1964. doi:10.1063/1.1587263 (2003).

24. Carra, F. *et al.* Mechanical robustness of HL-LHC collimator designs. *Journal of Physics: Conference Series* **1350,** 012083. doi:10.1088/1742-6596/1350/1/012083 (2019).

25. Lederer, S. *Strahlenschäden in Szintillator-Materialien für die Hochstrom-Diagnose von Schwerionenstrahlen* PhD Thesis (Technische Universität Darmstadt, Darmstadt). http://tuprints.ulb.tu-darmstadt.de/5282/.

26. Hubert, C. *et al.* Swift heavy ion-induced radiation damage in isotropic graphite studied by micro-indentation and in-situ electrical resistivity. *Nuclear Instruments and Methods in Physics Research Section B: Beam Interactions with Materials and Atoms* **365,** 509–514. doi:10.1016/j.nimb.2015.08.056 (2015).

27. Pellemoine, F. *et al.* Study on structural recovery of graphite irradiated with swift heavy ions at high temperature. *Nuclear Instruments and Methods in Physics Research Section B: Beam Interactions with Materials and Atoms* **365,** 522–524. doi:10.1016/j.nimb.2015.09.007 (2015).

28. Fernandes, S. *et al.* In-situ electric resistance measurements and annealing effects of graphite exposed to swift heavy ions. *Nuclear Instruments and Methods in Physics Research Section B: Beam Interactions with Materials and Atoms* **314,** 125–129. doi:10.1016/j.nimb.2013.04.060 (2013).

29. Pasquali, M. *et al.* Dynamic Response of Advanced Materials Impacted by Particle Beams: The MultiMat Experiment. *Journal of Dynamic Behavior of Materials* **5,** 266–295. doi:10.1007/s40870-019-00210-1 (2019).

30. Nuiry, F.-.-X. *et al.* 3D Carbon/Carbon composites for beam intercepting devices at CERN. *Material Design & Processing Communications* **1,** e33. doi:10.1002/mdp2.33 (2019).

31. Scapin, M., Peroni, L., Dallocchio, A. & Bertarelli, A. Shock Loads Induced on Metal Structures by LHC Proton Beams: Modelling of Thermo-Mechanical Effects. *Applied Mechanics and Materials* **82,** 338–343. doi:10.4028/www.scientific.net/AMM.82.338 (2011).

32. Ziegler, J. F., Ziegler, M. & Biersack, J. SRIM – The stopping and range of ions in matter (2010). *Nuclear Instruments and Methods in Physics Research Section B: Beam Interactions with Materials and Atoms* **268,** 1818–1823. doi:10.1016/j.nimb.2010.02.091 (2010).

33. Podgoršak, E. B. in *Radiation Physics for Medical Physicists* 209–228 (Springer International Publishing, Cham, 2016). doi:10.1007/978-3-319-25382-4_5.

34. Bethe, H. Zur Theorie des Durchgangs schneller Korpuskularstrahlen durch Materie. *Annalen der Physik und Chemie* **397,** 325–400. doi:10.1002/andp.19303970303 (1930).

35. Bloch, F. Bremsvermgen von Atomen mit mehreren Elektronen. *The European Physical Journal A* **81,** 363–376. doi:10.1007/BF01344553 (1933).

36. Bloch, F. Zur Bremsung rasch bewegter Teilchen beim Durchgang durch Materie. *Annalen der Physik und Chemie* **408,** 285–320. doi:10.1002/andp.19334080303 (1933).

37. Bohr, N. Scattering and Stopping of Fission Fragments. *Physical Review* **58,** 654–655. doi:10.1103/PhysRev.58.654 (1940).

38. Bohr, N. Velocity-Range Relation for Fission Fragments. *Physical Review* **59,** 270–275. doi:10.1103/PhysRev.59.270 (1941).

39. Ziegler, J. F. Stopping of energetic light ions in elemental matter. *Journal of Applied Physics* **85,** 1249–1272. doi:10.1063/1.369844 (1999).

40. Lindhard, J., Scharff, M. & Schiøtt, H. E. Range concepts and heavy ion ranges: (Notes on atomic collisions, II). *Det Kgl. Danske videnskabernes selskab, Copenhagen. Matematiskfysiske meddelelser* **33** (1963).

41. Waligórski, M., Hamm, R. N. & Katz, R. The radial distribution of dose around the path of a heavy ion in liquid water. *International Journal of Radiation Applications and Instrumentation. Part D. Nuclear Tracks and Radiation Measurements* **11,** 309–319. doi:10.1016/1359-0189(86)90057-9 (1986).

42. Gervais, B. & Bouffard, S. Simulation of the primary stage of the interaction of swift heavy ions with condensed matter. *Nuclear Instruments and Methods in Physics Research Section B: Beam Interactions with Materials and Atoms* **88,** 355–364. doi:10.1016/0168-583X(94)95384-8 (1994).

43. Fleischer, R. L., Price, P. B. & Walker, R. M. Ion Explosion Spike Mechanism for Formation of Charged–Particle Tracks in Solids. *Journal of Applied Physics* **36,** 3645–3652. doi:10.1063/1.1703059 (1965).

44. Dessauer, F. ber einige Wirkungen von Strahlen. I. *The European Physical Journal A* **12,** 38–47. doi:10.1007/BF01328080 (1923).

45. Toulemonde, Dufour & Paumier. Transient thermal process after a high-energy heavy-ion irradiation of amorphous metals and semiconductors. *Physical review. B, Condensed matter* **46,** 14362–14369. doi:10.1103/PhysRevB.46.14362 (1992).

46. Toulemonde, M., Assmann, W., Dufour, C., Meftah, A. & Trautmann, C. Nanometric transformation of the matter by short and intense electronic excitation: Experimental data versus inelastic thermal spike model. *Nuclear Instruments and Methods in Physics Research Section B: Beam Interactions with Materials and Atoms* **277,** 28–39. doi:10.1016/j.nimb.2011.12.045 (2012).

47. Toulemonde, M., Dufour, C., Meftah, A. & Paumier, E. Transient thermal processes in heavy ion irradiation of crystalline inorganic insulators. *Nuclear Instruments and Methods in Physics Research Section B: Beam Interactions with Materials and Atoms* **166-167,** 903–912. doi:10.1016/S0168-583X(99)00799-5 (2000).

48. Szenes, G. Comparison of two thermal spike models for ion–solid interaction. *Nuclear Instruments and Methods in Physics Research Section B: Beam Interactions with Materials and Atoms* **269,** 174–179. doi:10.1016/j.nimb.2010.11.009 (2011).

49. Trautmann, C., Toulemonde, M., Schwartz, K., Costantini, J. & Müller, A. Damage structure in the ionic crystal LiF irradiated with swift heavy ions. *Nuclear Instruments and Methods in Physics Research Section B: Beam Interactions with Materials and Atoms* **164-165,** 365–376. doi:10.1016/S0168-583X(99)01066-6 (2000).

50. Weber, W. Models and mechanisms of irradiation-induced amorphization in ceramics. *Nuclear Instruments and Methods in Physics Research Section B: Beam Interactions with Materials and Atoms* **166-167,** 98–106. doi:10.1016/S0168-583X(99)00643-6 (2000).

51. Mokhov, N. V. Beam–Materials Interactions. *Reviews of Accelerator Science and Technology* **06,** 275–290. doi:10.1142/S1793626813300132 (2013).

52. Mokhov, N. V. & Cerutti, F. Beam–Material Interactions: 83 Pages / CERN Yellow Reports, Vol 2 (2016): Proceedings of the 2014 Joint International Accelerator School: Beam Loss and Accelerator Protection / CERN Yellow Reports, Vol 2 (2016): Proceedings of the 2014 Joint International Accelerator School: Beam Loss and Accelerator Protection. doi:10.5170/CERN-2016-002.83 (2016).

53. Beringer, J. *et al.* Review of Particle Physics. *Physical Review D* **86.** doi:10.1103/PhysRevD.86.010001 (2012).

54. Community, B. O. *Blender - a 3D modelling and rendering package* Blender Foundation (Stichting Blender Foundation, Amsterdam, 2018). http://www.blender.org.

55. Hirsch, A. The era of carbon allotropes. *Nature materials* **9,** 868–871. doi:10.1038/nmat2885 (2010).

56. Geim, A. K. & Novoselov, K. S. The rise of graphene. *Nature materials* **6,** 183–191. doi:10.1038/nmat1849 (2007).

57. Iijima, S. & Ichihashi, T. Single-shell carbon nanotubes of 1-nm diameter. *Nature* **363,** 603–605. doi:10.1038/363603a0 (1993).

58. Kroto, H. W., Heath, J. R., O'Brien, S. C., Curl, R. F. & Smalley, R. E. C60: Buckminsterfullerene. *Nature* **318,** 162–163. doi:10.1038/318162a0 (1985).

59. Pauling, L. THE NATURE OF THE CHEMICAL BOND. APPLICATION OF RESULTS OBTAINED FROM THE QUANTUM MECHANICS AND FROM A THEORY OF PARAMAGNETIC SUSCEPTIBILITY TO THE STRUCTURE OF MOLECULES. *Journal of the American Chemical Society* **53,** 1367–1400. doi:10.1021/ja01355a027 (1931).

60. Brittin, W. E. Valence angle of the tetrahedral carbon atom. *Journal of Chemical Education* **22,** 145. doi:10.1021/ed022p145 (1945).

61. Bernal, J. D. The structure of graphite. *Proceedings of the Royal Society of London. A. Mathematical and Physical Sciences* **106,** 749–773. doi:10.1098/rspa.1924.0101 (1924).

62. Bundy, F. P. *et al.* The pressure-temperature phase and transformation diagram for carbon; updated through 1994. *Carbon* **34,** 141–153. doi:10.1016/0008-6223(96)00170-4 (1996).

63. Holloway, Hass, Tamor, Anthony & Banholzer. Isotopic dependence of the lattice constant of diamond. *Physical review. B, Condensed matter* **44,** 7123–7126. doi:10.1103/PhysRevB.44.7123 (1991).

64. Howe, J. Y. *The Oxidation of Diamond* Dissertation (Alfred University, Alfred, NY, 2001). http://hdl.handle.net/10829/7389.

65. Davies, G. & Evans, T. Graphitization of diamond at zero pressure and at a high pressure. *Proceedings of the Royal Society of London. A. Mathematical and Physical Sciences* **328,** 413–427. doi:10.1098/rspa.1972.0086 (1972).

66. Clark, C. D., Dean, P. J. & Harris, P. V. Intrinsic edge absorption in diamond. *Proceedings of the Royal Society of London. Series A. Mathematical and Physical Sciences* **277,** 312–329. doi:10.1098/rspa.1964.0025 (1964).
67. Yamamoto, Y. *et al.* The measurement of thermal properties of diamond. *Diamond and Related Materials* **6,** 1057–1061. doi:10.1016/S0925-9635(96)00772-8 (1997).
68. Wei, Kuo, Thomas, Anthony & Banholzer. Thermal conductivity of isotopically modified single crystal diamond. *Physical review letters* **70,** 3764–3767. doi:10.1103/PhysRevLett.70.3764 (1993).
69. Olson *et al.* Thermal conductivity of diamond between 170 and 1200 K and the isotope effect. *Physical review. B, Condensed matter* **47,** 14850–14856. doi:10.1103/PhysRevB.47.14850 (1993).
70. McSkimin, H. J., Andreatch, P. & Glynn, P. The Elastic Stiffness Moduli of Diamond. *Journal of Applied Physics* **43,** 985–987. doi:10.1063/1.1661318 (1972).
71. Brazhkin, V. V., Lyapin, A. G. & Hemley, R. J. Harder than diamond: Dreams and reality. *Philosophical Magazine A* **82,** 231–253. doi:10.1080/01418610208239596 (2002).
72. Harano, K., Satoh, T. & Sumiya, H. Cutting performance of nano-polycrystalline diamond. *Diamond and Related Materials* **24,** 78–82. doi:10.1016/j.diamond.2011.11.005 (2012).
73. Catledge, S. A. & Vohra, Y. K. Effect of nitrogen addition on the microstructure and mechanical properties of diamond films grown using high-methane concentrations. *Journal of Applied Physics* **86,** 698–700. doi:10.1063/1.370787 (1999).
74. Ekimov, E. A. *et al.* Superconductivity in diamond. *Nature* **428,** 542–545. doi:10.1038/nature02449 (2004).
75. Hainschwang, T., Fritsch, E., Massi, L., Rondeau, B. & Notari, F. The C center isolated nitrogen-related infrared absorption at 2688 cm–1: perfect harmony in diamond. *Journal of Applied Spectroscopy* **79,** 737–743. doi:10.1007/s10812-012-9664-5 (2012).
76. Breeding, C. M. & Shigley, J. E. The "Type" Classification System of Diamonds and Its Importance in Gemology. *Gems & Gemology* **45,** 96–111. doi:10.5741/GEMS.45.2.96 (2009).
77. Davies, G. The A nitrogen aggregate in diamond-its symmetry and possible structure. *Journal of Physics C: Solid State Physics* **9,** L537–L542. doi:10.1088/0022-3719/9/19/005 (1976).
78. Jones, R., Briddon, P. R. & Öberg, S. First-principles theory of nitrogen aggregates in diamond. *Philosophical Magazine Letters* **66,** 67–74. doi:10.1080/09500839208214688 (1992).
79. Chrenko, R. M., Strong, H. M. & Tuft, R. E. Dispersed paramagnetic nitrogen content of large laboratory diamonds. *Philosophical Magazine* **23,** 313–318. doi:10.1080/14786437108216387 (1971).
80. Collins, A. T. & Williams, A. W. S. The nature of the acceptor centre in semiconducting diamond. *Journal of Physics C: Solid State Physics* **4,** 1789–1800. doi:10.1088/0022-3719/4/13/030 (1971).
81. Chrenko, R. M. Boron, the Dominant Acceptor in Semiconducting Diamond. *Physical Review B* **7,** 4560–4567. doi:10.1103/PhysRevB.7.4560 (1973).
82. Turri, G. *et al.* Index of refraction from the near-ultraviolet to the near-infrared from a single crystal microwave-assisted CVD diamond. *Optical Materials Express* **7,** 855. doi:10.1364/OME.7.000855 (2017).
83. Kasugai, A., Sakamoto, K., Takahashi, K., Kajiwara, K. & Kobayashi, N. Steady-state operation of 170 GHz–1 MW gyrotron for ITER. *Nuclear Fusion* **48,** 054009. doi:10.1088/0029-5515/48/5/054009 (2008).
84. Maquet, P. *et al.* Development of ITER diagnostic window assemblies. *Fusion Engineering and Design* **88,** 2641–2645. doi:10.1016/j.fusengdes.2013.03.044 (2013).
85. Danilenko, V. V. On the history of the discovery of nanodiamond synthesis. *Physics of the Solid State* **46,** 595–599. doi:10.1134/1.1711431 (2004).
86. Lin, C. R., Wei, D. H., Dao, M. K. B., Chung, R. J. & Chang, M. H. Nanocrystalline Diamond Particles Prepared by High-Energy Ball Milling Method. *Applied Mechanics and Materials* **284-287,** 168–172. doi:10.4028/www.scientific.net/AMM.284-287.168 (2013).
87. Panich, A. M., Shames, A. I., Zousman, B. & Levinson, O. Magnetic resonance study of nanodiamonds prepared by laser-assisted technique. *Diamond and Related Materials* **23,** 150–153. doi:10.1016/j.diamond.2011.12.047 (2012).
88. Chang, Y.-R. *et al.* Mass production and dynamic imaging of fluorescent nanodiamonds. *Nature nanotechnology* **3,** 284–288. doi:10.1038/nnano.2008.99 (2008).
89. Mohan, N., Chen, C.-S., Hsieh, H.-H., Wu, Y.-C. & Chang, H.-C. In vivo imaging and toxicity assessments of fluorescent nanodiamonds in Caenorhabditis elegans. *Nano Letters* **10,** 3692–3699. doi:10.1021/nl1021909 (2010).
90. Kuznetsov, V. *et al.* Study of ultradispersed diamond powders obtained using explosion energy. *Carbon* **29,** 665–668. doi:10.1016/0008-6223(91)90135-6 (1991).

91. Chow, E. K. *et al.* Nanodiamond therapeutic delivery agents mediate enhanced chemoresistant tumor treatment. *Science translational medicine* **3,** 73ra21. doi:10.1126/scitranslmed.3001713 (2011).

92. Mochalin, V. N., Shenderova, O., Ho, D. & Gogotsi, Y. The properties and applications of nanodiamonds. *Nature nanotechnology* **7,** 11–23. doi:10.1038/NNANO.2011.209 (2011).

93. Zazula, J. M. *On Graphite Transformations at High Temperature and Pressure Induced By Absorption of the LHC Beam* tech. rep. LHC-Project-Note-78 (CERN, Geneva, 1997). https://cds.cern.ch/record/691793.

94. Finnerty, A. & Boyd, F. Evaluation of thermobarometers for garnet peridotites. *Geochimica et Cosmochimica Acta* **48,** 15–27. doi:10.1016/0016-7037(84)90346-6 (1984).

95. Bundy, F. P., HALL, H. T., Strong, H. M. & WENTORFJUN., R. H. Man-Made Diamonds. *Nature* **176,** 51–55. doi:10.1038/176051a0 (1955).

96. Bundy, F. P. Melting of Graphite at Very High Pressure. *The Journal of Chemical Physics* **38,** 618–630. doi:10.1063/1.1733715 (1963).

97. Sumiya, H., Toda, N. & Satoh, S. Growth rate of high-quality large diamond crystals. *Journal of Crystal Growth* **237-239,** 1281–1285. doi:10.1016/S0022-0248(01)02145-5 (2002).

98. Burns, R. C. *et al.* HPHT growth and x-ray characterization of high-quality type IIa diamond. *Journal of Physics: Condensed Matter* **21,** 364224. doi:10.1088/0953-8984/21/36/364224 (2009).

99. Schreck, M., Asmussen, J., Shikata, S., Arnault, J.-C. & Fujimori, N. Large-area high-quality single crystal diamond. *MRS Bulletin* **39,** 504–510. doi:10.1557/mrs.2014.96 (2014).

100. Kamo, M., Yurimoto, H. & Sato, Y. Epitaxial growth of diamond on diamond substrate by plasma assisted CVD. *Applied Surface Science* **33-34,** 553–560. doi:10.1016/0169-4332(88)90352-2 (1988).

101. Schreck, M., Gsell, S., Brescia, R. & Fischer, M. Ion bombardment induced buried lateral growth: the key mechanism for the synthesis of single crystal diamond wafers. *Scientific reports* **7,** 44462. doi:10.1038/srep44462 (2017).

102. Müller–Sebert, W., Wörner, E., Fuchs, F., Wild, C. & Koidl, P. Nitrogen induced increase of growth rate in chemical vapor deposition of diamond. *Applied physics letters* **68,** 759–760. doi:10.1063/1.116733 (1996).

103. Dunst, S., Sternschulte, H. & Schreck, M. Growth rate enhancement by nitrogen in diamond chemical vapor deposition—a catalytic effect. *Applied physics letters* **94,** 224101. doi:10.1063/1.3143631 (2009).

104. Yiming, Z., Larsson, F. & Larsson, K. Effect of CVD diamond growth by doping with nitrogen. *Theoretical Chemistry Accounts* **133.** doi:10.1007/s00214-013-1432-y (2014).

105. Yan, C.-S., Vohra, Y. K., Mao, H.-K. & Hemley, R. J. Very high growth rate chemical vapor deposition of single-crystal diamond. *Proceedings of the National Academy of Sciences of the United States of America* **99,** 12523–12525. doi:10.1073/pnas.152464799 (2002).

106. Balmer, R. S. *et al.* Chemical vapour deposition synthetic diamond: materials, technology and applications. *Journal of Physics: Condensed Matter* **21,** 364221. doi:10.1088/0953-8984/21/36/364221 (2009).

107. Howe, J. Y., Rawn, C. J., Jones, L. E. & Ow, H. Improved crystallographic data for graphite. *Powder Diffraction* **18,** 150–154. doi:10.1154/1.1536926 (2003).

108. Abrahamson, J. Graphite sublimation temperatures, carbon arcs and crystallite erosion. *Carbon* **12,** 111–141. doi:10.1016/0008-6223(74)90019-0 (1974).

109. Xiaowei, L., Jean-Charles, R. & Suyuan, Y. Effect of temperature on graphite oxidation behavior. *Nuclear Engineering and Design* **227,** 273–280. doi:10.1016/j.nucengdes.2003.11.004 (2004).

110. Fugallo, G. *et al.* Thermal conductivity of graphene and graphite: collective excitations and mean free paths. *Nano Letters* **14,** 6109–6114. doi:10.1021/nl502059f (2014).

111. Primak, W. & Fuchs, L. H. Electrical Conductivities of Natural Graphite Crystals. *Physical Review* **95,** 22–30. doi:10.1103/PhysRev.95.22 (1954).

112. Xiao, J. *et al.* Anisotropic friction behaviour of highly oriented pyrolytic graphite. *Carbon* **65,** 53–62. doi:10.1016/j.carbon.2013.07.101 (2013).

113. Grigorieva, I., Antonov, A. & Gudi, G. Graphite Optics—Current Opportunities, Properties and Limits. *Condensed Matter* **4,** 18. doi:10.3390/condmat4010018 (2019).

114. Schneider, M. *et al.* *Large Area HOPG Monochromators with Low Mosaic* in *Proceedings of the International Conference on Neutron Optics (NOP2017)* (Journal of the Physical Society of Japan, 11292018). doi:10.7566/JPSCP.22.011012.

115. Fan, W., Galestien, E., Tomek, C. & Manjunath, S. *Doubling the output of automotive LED headlight with efficient cooling using Thermal Pyrolytic Graphite* in *2016 15th IEEE Intersociety Conference on Thermal and Thermomechanical Phenomena in Electronic Systems (ITherm)* (IEEE, 2016), 180–184. doi:10.1109/ITHERM.2016.7517547.

116. Reitsma, F. & Yasar, T. *IAEA Nuclear Graphite Knowledge Base* 2015. https://nucleus.iaea.org/sites/graphiteknowledgebase/wiki/Pages/Home.aspx.

117. *Resistance to radioactivity of SIGRAFLEX® sealing materials* 2018. https://www.sglcarbon.com/pdf/SGL-Technical-Info-SIGRAFLEX-Resistance-Radioactivity-EN.pdf.

118. Gallego, N. C. & Klett, J. W. Carbon foams for thermal management. *Carbon* **41,** 1461–1466. doi:10.1016/S0008-6223(03)00091-5 (2003).

119. Glass, D. *Ceramic Matrix Composite (CMC) Thermal Protection Systems (TPS) and Hot Structures for Hypersonic Vehicles* in *15th AIAA International Space Planes and Hypersonic Systems and Technologies Conference* (American Institute of Aeronautics and Astronautics, 2008). doi:10.2514/6.2008-2682.

120. Blackman, L. C. F. & Ubbelohde, A. R. J. P. Stress recrystallization of graphite. *Proceedings of the Royal Society of London. A. Mathematical and Physical Sciences* **266,** 20–32. doi:10.1098/rspa.1962.0044 (1962).

121. Kania, D. R., Landstrass, M. I., Plano, M. A., Pan, L. S. & Han, S. Diamond radiation detectors. *Diamond and Related Materials* **2,** 1012–1019. doi:10.1016/0925-9635(93)90266-5 (1993).

122. Gracio, J. J., Fan, Q. H. & Madaleno, J. C. Diamond growth by chemical vapour deposition. *Journal of Physics D: Applied Physics* **43,** 374017. doi:10.1088/0022-3727/43/37/374017 (2010).

123. Erich, G. *Diamond Detectors for beam instrumentation* in *Proceedings of Technology and Instrumentation in Particle Physics 2014 — PoS(TIPP2014)* (eds Koffeman, E. *et al.*) (Sissa Medialab, Trieste, Italy, 2014), 088. doi:10.22323/1.213.0088.

124. Kumar, S., Reshi, B. A. & Varma, R. Comparison of Silicon, Germanium, Gallium Nitride, and Diamond for using as a detector material in experimental high energy physics. *Results in Physics* **11,** 461–474. doi:10.1016/j.rinp.2018.08.045 (2018).

125. De Boer, W. *et al.* Radiation hardness of diamond and silicon sensors compared. *physica status solidi (a)* **204,** 3004–3010. doi:10.1002/pssa.200776327 (2007).

126. Jahn, D. *et al.* Chemical-vapor deposited ultra-fast diamond detectors for temporal measurements of ion bunches. *Review of Scientific Instruments* **89,** 093304. doi:10.1063/1.5048667 (2018).

127. Liu, L., Ouyang, X., Zhang, J., Zhang, X. & Zhong, Y. Polycrystalline CVD diamond detector: Fast response and high sensitivity with large area. *AIP Advances* **4,** 017114. doi:10.1063/1.4862671 (2014).

128. Schwertel, S. *et al. Diamond Detectors for the R3B Experiment* 2008. http://repository.gsi.de/record/53524.

129. Venturi, N. Diamond Pixel Detectors and 3D Diamond Devices. *Journal of Instrumentation* **11,** C12062–C12062. doi:10.1088/1748-0221/11/12/C12062 (2016).

130. Domke, M. *et al. Commissioning of the beam conditions monitor of the LHCb experiment at CERN* in *2008 IEEE Nuclear Science Symposium Conference Record* (IEEE, 2008), 3306–3307. doi:10.1109/NSSMIC.2008.4775052.

131. Cindro, V. *et al.* The ATLAS Beam Conditions Monitor. *Journal of Instrumentation* **3,** P02004–P02004. doi:10.1088/1748-0221/3/02/P02004 (2008).

132. Bachmair, F. Diamond sensors for future high energy experiments. *Nuclear Instruments and Methods in Physics Research Section A: Accelerators, Spectrometers, Detectors and Associated Equipment* **831,** 370–377. doi:10.1016/j.nima.2016.03.039 (2016).

133. Liu, J. *et al.* Design, fabrication and testing of CVD diamond detectors with high performance. *AIP Advances* **9,** 045205. doi:10.1063/1.5094516 (2019).

134. Carra, F. *et al.* Mechanical Engineering and Design of Novel Collimators for HL-LHC. *Proceedings of the 5th Int. Particle Accelerator Conf.* **IPAC2014,** 4 pages, 0.686 MB. doi:10.18429/JACOW-IPAC2014-MOPRO116 (2014).

135. Robinson, M. T. & Oen, O. S. THE CHANNELING OF ENERGETIC ATOMS IN CRYSTAL LATTICES. *Applied physics letters* **2,** 30–32. doi:10.1063/1.1753757 (1963).

136. Biryukov, V. M. *Crystal Channelling in Accelerators* in *Proc. of European Particle Accelerator Conference (EPAC'06), Edinburgh, Scotland, 26–30 June, 2006* (JACoW, Geneva, Switzerland), 945–949. https://accelconf.web.cern.ch/e06/PAPERS/TUZBPA02.PDF.

137. Rossi, R. *et al. Status of Crystal Collimation Studies at the LHC* in *Proc. of International Particle Accelerator Conference (IPAC'17), Copenhagen, Denmark, 14–19 May, 2017* Copenhagen, Denmark (JACoW, Geneva, Switzerland, 2017), 84–87. doi:10.18429/JACoW-IPAC2017-MOPAB007.

138. Rossi, R. *Experimental Assessment of Crystal Collimation at the Large Hadron Collider* Dissertation (2017). https://cds.cern.ch/record/2644175.

139. Manfredotti, C. *et al.* Ion beam induced luminescence and charge collection in CVD diamond. *Diamond and Related Materials* **7,** 742–747. doi:10.1016/S0925-9635(97)00197-0 (1998).

140. Zaitsev, A. M. *Optical Properties of Diamond* doi:10.1007/978-3-662-04548-0 (Springer Berlin Heidelberg, Berlin, Heidelberg, 2001).

141. Koike, J., Parkin, D. M. & Mitchell, T. E. Displacement threshold energy for type IIa diamond. *Applied physics letters* **60,** 1450–1452. doi:10.1063/1.107267 (1992).

142. Zinkle, S. J. & Kinoshita, C. Defect production in ceramics. *Journal of Nuclear Materials* **251,** 200–217. doi:10.1016/S0022-3115(97)00224-9 (1997).

143. Steeds, J. W. Orientation dependence of near-threshold damage production by electron irradiation of 4H SiC and diamond and outward migration of defects. *Nuclear Instruments and Methods in Physics Research Section B: Beam Interactions with Materials and Atoms* **269,** 1702–1706. doi:10.1016/j.nimb.2010.12.029 (2011).

144. Bauer, C. *et al. Development of diamond tracking detectors for high luminosity experiments at the LHC* tech. rep. CERN-LHCC-95-43. LDRB-Status-Report-RD42 (CERN, Geneva, 1995). http://cds.cern.ch/record/303661.

145. Kagan, H. & Trischuk, W. *Development of Diamond Tracking Detectors for High Luminosity Experiments at the LHC, HL-LHC and Beyond* tech. rep. CERN-LHCC-2018-015. LHCC-SR-005 (CERN, Geneva, 2018). https://cds.cern.ch/record/2320382.

146. Bhattacharya, A., Grotjohn, T. A. & Stolz, A. Degradation of single crystal diamond detectors in swift heavy ion beams. *Diamond and Related Materials* **70,** 124–131. doi:10.1016/j.diamond.2016.10.009 (2016).

147. Mita, Y., Nisida, Y. & Okada, M. Formation of the nitrogen aggregates in annealed diamond by neutron irradiation. *AIP Advances* **8,** 025106. doi:10.1063/1.5011262 (2018).

148. Primak, W., Fuchs, L. H. & Day, P. P. Radiation Damage in Diamond and Silicon Carbide. *Physical Review* **103,** 1184–1192. doi:10.1103/PhysRev.103.1184 (1956).

149. Nikolaenko, V. A. & Gordeev, V. G. Diamond amorphization in neutron irradiation. *Radiation Effects and Defects in Solids* **139,** 183–188. doi:10.1080/10420159608211545 (1996).

150. Battiato, A. *et al.* Softening the ultra-stiff: Controlled variation of Young's modulus in single-crystal diamond by ion implantation. *Acta Materialia* **116,** 95–103. doi:10.1016/j.actamat.2016.06.019 (2016).

151. Lagomarsino, S. *et al.* Refractive index variation in a free-standing diamond thin film induced by irradiation with fully transmitted high-energy protons. *Scientific reports* **7,** 385. doi:10.1038/s41598-017-00343-0 (2017).

152. Lagomarsino, S. *et al.* Complex refractive index variation in proton-damaged diamond. *Optics express* **20,** 19382–19394. doi:10.1364/OE.20.019382 (2012).

153. Vance, E. R., Harris, J. W. & Milledge, H. J. Possible origins of α-damage in diamonds from kimberlite and alluvial sources. *Mineralogical Magazine* **39,** 349–360. doi:10.1180/minmag.1973.039.303.12 (1973).

154. Orwa, J. O., Nugent, K. W., Jamieson, D. N. & Prawer, S. Raman investigation of damage caused by deep ion implantation in diamond. *Physical Review B* **62,** 5461–5472. doi:10.1103/PhysRevB.62.5461 (2000).

155. Braunstein, G., Talmi, A., Kalish, R., Bernstein, T. & Beserman, R. Radiation damage and annealing in Sb implanted diamond. *Radiation Effects* **48,** 139–143. doi:10.1080/00337578008209244 (1980).

156. Adel, M., Kalish, R. & Richter, V. Light-ion-beam-induced annealing of implantation damage in diamond. *Journal of Materials Research* **1,** 503–509. doi:10.1557/JMR.1986.0503 (1986).

157. Prawer & Kalish. Ion-beam-induced transformation of diamond. *Physical review. B, Condensed matter* **51,** 15711–15722. doi:10.1103/PhysRevB.51.15711 (1995).

158. Uzan–Saguy, C. *et al.* Damage threshold for ion–beam induced graphitization of diamond. *Applied physics letters* **67,** 1194–1196. doi:10.1063/1.115004 (1995).

159. Brunetto, R., Baratta, G. A. & Strazzulla, G. Amorphization of diamond by ion irradiation: a Raman study. *Journal of Physics: Conference Series* **6,** 120–125. doi:10.1088/1742-6596/6/1/011 (2005).

160. Khmelnitsky, R. A. *et al.* Mechanical stresses and amorphization of ion-implanted diamond. *Nuclear Instruments and Methods in Physics Research Section B: Beam Interactions with Materials and Atoms* **304,** 5–10. doi:10.1016/j.nimb.2013.03.030 (2013).

161. Khmelnitsky, R. A. *et al.* Damage accumulation in diamond during ion implantation. *Journal of Materials Research* **30,** 1583–1592. doi:10.1557/jmr.2015.21 (2015).

162. Agulló-Rueda, F. *et al.* Lattice damage in 9-MeV-carbon irradiated diamond and its recovery after annealing. *Carbon* **123,** 334–343. doi:10.1016/j.carbon.2017.07.076 (2017).

163. Agulló-Rueda, F. *et al.* Micro-Raman spectroscopy of near-surface damage in diamond irradiated with 9-MeV boron ions. *Diamond and Related Materials* **72,** 94–98. doi:10.1016/j.diamond.2017.01.010 (2017).

164. Aprà, P. *et al.* Structural characterization of 8 MeV 11B implanted diamond. *Diamond and Related Materials* **104,** 107770. doi:10.1016/j.diamond.2020.107770 (2020).

165. García, G. *et al.* Structural damage on single-crystal diamond by swift heavy ion irradiation. *Diamond and Related Materials* **58,** 226–229. doi:10.1016/j.diamond.2015.08.014 (2015).

166. García, G. *et al.* Micro and nano-patterning of single-crystal diamond by swift heavy ion irradiation. *Diamond and Related Materials* **69,** 1–7. doi:10.1016/j.diamond.2016.06.015 (2016).

167. Bunk, K. *et al.* Surface and subsurface damage in 14 MeV Au ion-irradiated diamond. *Journal of Applied Physics* **130,** 105303. doi:10.1063/5.0060445 (2021).

168. Kazuchits, N. M. *et al.* Raman scattering in diamond irradiated with high-energy xenon ions. *Nuclear Instruments and Methods in Physics Research Section B: Beam Interactions with Materials and Atoms* **472,** 19–23. doi:10.1016/j.nimb.2020.03.034 (2020).

169. Chen, H.-C. *et al.* Effect of gigaelectron volt Au-ion irradiation on the characteristics of ultrananocrystalline diamond films. *Journal of Applied Physics* **108,** 123712. doi:10.1063/1.3524541 (2010).

170. Zhang, F., Lang, M., Zhang, J. & Ewing, R. C. Swift heavy ion irradiation of diamond powder. *Nuclear Instruments and Methods in Physics Research Section B: Beam Interactions with Materials and Atoms* **286,** 262–265. doi:10.1016/j.nimb.2011.11.035 (2012).

171. Schwartz, J. *et al.* Local formation of nitrogen-vacancy centers in diamond by swift heavy ions. *Journal of Applied Physics* **116,** 214107. doi:10.1063/1.4903075 (2014).

172. Khmelnitski, R. A. *et al.* Effect of the electronic kinetics on graphitization of diamond irradiated with swift heavy ions and fs-laser pulses. *Nuclear Instruments and Methods in Physics Research Section B: Beam Interactions with Materials and Atoms* **460,** 47–51. doi:10.1016/j.nimb.2018.11.021 (2019).

173. Buchan, J. T. *et al.* Molecular dynamics simulation of radiation damage cascades in diamond. *Journal of Applied Physics* **117,** 245901. doi:10.1063/1.4922457 (2015).

174. Fairchild, B. A. *et al.* Mechanism for the Amorphisation of Diamond. *Advanced Materials* **24,** 2024–2029. doi:10.1002/adma.201104511 (2012).

175. Bosia, F. *et al.* Modification of the structure of diamond with MeV ion implantation. *Diamond and Related Materials* **20,** 774–778. doi:10.1016/j.diamond.2011.03.025 (2011).

176. Wang, W., Smith, C. P., Hall, M. S., Breeding, C. M. & Moses, T. M. Treated-Color Pink-to-Red Diamonds from Lucent Diamonds Inc. *Gems & Gemology* **41,** 6–19. doi:10.5741/gems.41.1.6 (2005).

177. Wang, M., Shi, G., Yuan, J. C. C., Han, W. & Bai, Q. Spectroscopic Characteristics of Treated-Color Natural Diamonds. *Journal of Spectroscopy* **2018,** 1–10. doi:10.1155/2018/8153941 (2018).

178. Lühmann, T. *et al.* Screening and engineering of colour centres in diamond. *Journal of Physics D: Applied Physics* **51,** 483002. doi:10.1088/1361-6463/aadfab (2018).

179. Kumar, R. *et al.* Engineering bright fluorescent nitrogen-vacancy (NV) nano-diamonds: Role of low-energy ion-irradiation parameters. *AIP Advances* **8,** 085023. doi:10.1063/1.5012068 (2018).

180. Kalish, R. *et al.* Nitrogen doping of diamond by ion implantation. *Diamond and Related Materials* **6,** 516–520. doi:10.1016/S0925-9635(96)00657-7 (1997).

181. Iakoubovskii, K. & Adriaenssens, G. J. Trapping of vacancies by defects in diamond. *Journal of Physics: Condensed Matter* **13,** 6015. doi:10.1088/0953-8984/13/26/316 (2001).

182. Deák, P., Aradi, B., Kaviani, M., Frauenheim, T. & Gali, A. Formation of NV centers in diamond: A theoretical study based on calculated transitions and migration of nitrogen and vacancy related defects. *Physical Review B* **89.** doi:10.1103/PhysRevB.89.075203 (2014).

183. Lake, R. E. *et al.* Direct formation of nitrogen-vacancy centers in nitrogen doped diamond along the trajectories of swift heavy ions. *Applied Physics Letters* **118,** 084002. doi:10.1063/5.0036643 (2021).

184. Lambert, J. H. *Photometria, sive de mensura et gradibus luminis, colorum et umbrae* (Sumptibus Vidae Eberhardi Klett, Augsburg, 1760).

185. Beer. Bestimmung der Absorption des rothen Lichts in farbigen Flüssigkeiten. *Annalen der Physik und Chemie* **162,** 78–88. doi:10.1002/andp.18521620505 (1852).

186. Braslavsky, S. E. Glossary of terms used in photochemistry, 3rd edition (IUPAC Recommendations 2006). *Pure and Applied Chemistry* **79,** 293–465. doi:10.1351/pac200779030293 (2007).

187. Vogelgesang, R. *et al.* Multiphonon Raman and infrared spectra of isotopically controlled diamond. *Phys. Rev. B* **58,** 5408–5416. doi:10.1103/PhysRevB.58.5408 (9 1998).

188. Ahmed, F. *et al.* In-situ tensile testing of crystalline diamond coatings using Raman spectroscopy. *Surface and Coatings Technology* **204,** 1022–1025. doi:10.1016/j.surfcoat.2009.04.030 (2009).

189. Kitzmantel, M. & Neubauer, E. *Innovative hybrid heat sink materials with high thermal conductivities and tailored CTE* in *SPIE Proceedings* (eds Glebov, A. L. & Leisher, P. O.) (SPIE, 2015). doi:10.1117/12.2077518.

190. Reinitz, I. M., Buerki, P. R., Shigley, J. E., McClure, S. F. & Moses, T. M. Identification of HPHT-Treated Yellow to Green Diamonds. *Gems & Gemology* **36,** 128–137. doi:10.5741/gems.36.2.128 (2000).

191. Zaitsev, A. M., Moe, K. S. & Wang, W. Optical centers and their depth distribution in electron irradiated CVD diamond. *Diamond and Related Materials* **71,** 38–52. doi:10.1016/j.diamond.2016.11.015 (2017).

192. Iakoubovskii, K. & Adriaenssens, G. J. Photoluminescence in CVD Diamond Films. *physica status solidi (a)* **172,** 123–129. doi:10.1002/(sici)1521-396x(199903)172:1<123::aid-pssa123>3.0.co;2-e (1999).

193. Xu, Y. *et al.* Strong anti-Stokes luminescence from H+-irradiated diamond. *Applied physics letters* **83,** 1968–1970. doi:10.1063/1.1608465 (2003).

194. Nistor, S. V., Stefan, M., Ralchenko, V., Khomich, A. & Schoemaker, D. Nitrogen and hydrogen in thick diamond films grown by microwave plasma enhanced chemical vapor deposition at variable H2 flow rates. *Journal of Applied Physics* **87,** 8741–8746. doi:10.1063/1.373604 (2000).

195. Hainschwang, T., Respinger, A., Notari, F., Hartmann, H. J. & Günthard, C. A comparison of diamonds irradiated by high fluence neutrons or electrons, before and after annealing. *Diamond and Related Materials* **18,** 1223–1234. doi:10.1016/j.diamond.2009.04.011 (2009).

196. Hounsome, L. S. *et al.* Role of extended defects in brown colouration of diamond. *physica status solidi c* **4,** 2950–2957. doi:10.1002/pssc.200675443 (2007).

197. Iakoubovskii, K. *et al.* Annealing of vacancies and interstitials in diamond. *Physica B: Condensed Matter* **340-342,** 67–75. doi:10.1016/j.physb.2003.09.005 (2003).

198. Chen, X.-D. *et al.* Temperature dependent energy level shifts of nitrogen-vacancy centers in diamond. *Applied Physics Letters* **99,** 161903. doi:10.1063/1.3652910 (2011).

199. Petit, T. & Puskar, L. FTIR spectroscopy of nanodiamonds: Methods and interpretation. *Diamond and Related Materials* **89,** 52–66. doi:10.1016/j.diamond.2018.08.005 (2018).

200. Howell, D. *et al.* μ-FTIR mapping: Distribution of impurities in different types of diamond growth. *Diamond and Related Materials* **29,** 29–36. doi:10.1016/j.diamond.2012.06.003 (2012).

201. Lawson, S. C., Fisher, D., Hunt, D. C. & Newton, M. E. On the existence of positively charged single-substitutional nitrogen in diamond. *Journal of Physics: Condensed Matter* **10,** 6171–6180. doi:10.1088/0953-8984/10/27/016 (1998).

202. Boyd, S. R., Kiflawi, I. & Woods, G. S. The relationship between infrared absorption and the A defect concentration in diamond. *Philosophical Magazine B* **69,** 1149–1153. doi:10.1080/01418639408240185 (1994).

203. Boyd, S. R., Kiflawi, I. & Woods, G. S. Infrared absorption by the B nitrogen aggregate in diamond. *Philosophical Magazine B* **72,** 351–361. doi:10.1080/13642819508239089 (1995).

204. Fang, C. *et al.* Preparation of "natural" diamonds by HPHT annealing of synthetic diamonds. *CrystEngComm* **20,** 505–511. doi:10.1039/c7ce02013a (2018).

205. Gentile, F. S. *et al.* Hydrogen, boron and nitrogen atoms in diamond: a quantum mechanical vibrational analysis. *Theoretical Chemistry Accounts* **137.** doi:10.1007/s00214-018-2375-0 (2018).

206. Goss, J. P. *et al.* Theory of hydrogen in diamond. *Physical Review B* **65.** doi:10.1103/physrevb.65.115207 (2002).

207. Salustro, S. *et al.* Hydrogen atoms in the diamond vacancy defect. A quantum mechanical vibrational analysis. *Carbon* **129,** 349–356. doi:10.1016/j.carbon.2017.12.011 (2018).

208. Mustafin, E., Strasik, I., Plotnikov, A. & Smolyakov, A. *Radiation damage problems in slow extration area and internal beam dump of SIS100* in *Proc. 18th International Conference on Applied Physics of Condensed Matter* (2012), 43. http://kf.elf.stuba.sk/~apcom/apcom12/proceedings/pdf/043mustafin.pdf.

209. Bozyk, L. & Spiller, P. *Ionization Loss and Dynamic Vacuum in Heavy Ion Synchrotrons* in *Proc. of International Particle Accelerator Conference (IPAC'17), Copenhagen, Denmark, 14–19 May, 2017* Copenhagen, Denmark (JACoW, Geneva, Switzerland, 2017), 2201–2204. doi:10.18429/JACoW-IPAC2017-TUPVA056.

210. Bozyk, L., Ahmed, S. & Spiller, P. *Series Production of the SIS100 Cryocatchers* in *Proc. IPAC'21* Campinas, SP, Brazil (JACoW Publishing, Geneva, Switzerland, 2021), 3529–3532. doi:10.18429/JACoW-IPAC2021-WEPAB355.

211. Kupka, K. *et al.* Graphitization of amorphous carbon by swift heavy ion impacts: Molecular dynamics simulation. *Diamond and Related Materials* **83,** 134–140. doi:10.1016/j.diamond.2018.01.015 (2018).

212. Forck, P. *et al. Beam-based Tests of Intercepting Transverse Profile Diagnostics for FAIR* in *Proc. 5th International Particle Accelerator Conference (IPAC'14), Dresden, Germany, June 15-20, 2014* Dresden, Germany (JACoW, Geneva, Switzerland, 2014), 3480–3482. doi:10.18429/JACoW-IPAC2014-THPME102.

213. Pyka, N. *et al. Challenges of the Technical Layout of the SIS 100 Extraction System* in *Proc. 5th International Particle Accelerator Conference (IPAC'14), Dresden, Germany, June 15-20, 2014* Dresden, Germany (JACoW, Geneva, Switzerland, 2014), 815–817. doi:10.18429/JACoW-IPAC2014-MOPRI087.

214. Knie, K. *et al.* Concept for the Antiproton Production Target at FAIR. *Conf. Proc.* **C1205201,** WEPPD030. 3 p. https://cds.cern.ch/record/1558377 (2012).

215. Senger, P. Astrophysics in the Laboratory – The CBM Experiment at FAIR. *Particles* **3,** 320–335. doi:10.3390/particles3020024 (2020).

216. Leibrock, H., Muehle, C., Rottländer, P. & Kalimov, A. Radiation Resistant Magnets for the Super-FRS of the FAIR Project. *IEEE Transactions on Applied Superconductivity* **30,** 1–4. doi:10.1109/TASC.2020.2974696 (2020).

217. Smolyakov, A., Mustafin, E., Pyka, N. & Spiller, P. J. *Radiation Damage Studies for the Slow Extraction from SIS100* in *11th European Particle Accelerator Conference, Genoa, Italy, 23 - 27 Jun 2008* (JACoW, 2008). https://accelconf.web.cern.ch/e08/papers/thpp102.pdf.

218. Boutachkov, P. *et al. Radiation hardness investigation of Zinc oxide fast scintillators with relativistic heavy ion beams* in *Proc. IBIC'19* Malmö, Sweden (JACoW Publishing, Geneva, Switzerland, 2019), 71–73. doi:10.18429/JACoW-IBIC2019-MOPP005.

219. Lederer, S. *et al.* Thermal annealing behavior of α-Al2O3 scintillation screens. *Nuclear Instruments and Methods in Physics Research Section B: Beam Interactions with Materials and Atoms* **365,** 548–552. doi:10.1016/j.nimb.2015.08.024 (2015).

220. Lieberwirth, A., Ensinger, W., Forck, P. & Lederer, S. Response from inorganic scintillation screens induced by high energetic ions. *Nuclear Instruments and Methods in Physics Research Section B: Beam Interactions with Materials and Atoms* **365,** 533–539. doi:10.1016/j.nimb.2015.07.111 (2015).

221. Wenninger, J. Machine Protection and Operation for LHC. en. *CERN Yellow Reports,* Vol 2 (2016): Proceedings of the 2014 Joint International Accelerator School: Beam Loss and Accelerator Protection. doi:10.5170/CERN-2016-002.377 (2016).

222. Wei, J. The Very High Intensity Future. en. *Proceedings of the 5th Int. Particle Accelerator Conf.* **IPAC2014,** Germany. doi:10.18429/JACOW-IPAC2014-MOYBA01 (2014).

223. CERN Yellow Reports: Monographs. *CERN Yellow Reports: Monographs, Vol. 10 (2020): High-Luminosity Large Hadron Collider (HL-LHC): Technical design report* en. doi:10.23731/CYRM-2020-0010 (CERN Yellow Reports: Monographs, 2020).

224. Barna, D., Facskó, B., Lechner, A. & Renner, E. Realization of the optimal beam dilution pattern of the FCC-hh ring using beating frequencies. *Nuclear Instruments and Methods in Physics Research Section A: Accelerators, Spectrometers, Detectors and Associated Equipment* **992,** 165048. doi:10.1016/j.nima.2021.165048 (2021).

225. Pianese, S. *et al. Design of the Future High Energy Beam Dump for the CERN SPS* in *Proc. 9th International Particle Accelerator Conference (IPAC'18), Vancouver, BC, Canada, April 29-May 4, 2018* Vancouver, BC, Canada (JACoW Publishing, Geneva, Switzerland, 2018), 2612–2615. doi:doi:10.18429/JACoW-IPAC2018-WEPMG004.

226. Gschwendtner, E. *et al.* Performance and Operational Experience of the CNGS Facility, 3 p. https://cds.cern.ch/record/1277917 (2010).

227. Lee, Y. Dynamic Response of Spallation Volume to Beam Raster on the European Spallation Source Target. en. *Proceedings of the 12th International Particle Accelerator Conference* **IPAC2021,** Brazil. doi:10.18429/JACOW-IPAC2021-WEPAB363 (2021).

228. Riemer, B. *The Spallation Neutron Source, Target Design and Operating Experience* 2013. https://indico.cern.ch/event/272646/.

229. Torregrosa-Martin, C. L. *Comprehensive Study for an Optimized Redesign of the CERN's Antiproton Decelerator Target* (2018). https://cds.cern.ch/record/2314375.

230. Dolinskii, A. *et al.* Antiproton complex at the FAIR project. *Nuclear Instruments and Methods in Physics Research Section A: Accelerators, Spectrometers, Detectors and Associated Equipment* **629,** 16–24. doi:10.1016/j.nima.2010.11.037 (2011).

231. Bauer, G. Physics and technology of spallation neutron sources. *Nuclear Instruments and Methods in Physics Research Section A: Accelerators, Spectrometers, Detectors and Associated Equipment* **463,** 505–543. doi:10.1016/s0168-9002(01)00167-x (2001).

232. Lee, Y. *Material Selection and Lifetime Criteria for the ESS Target Station* in *Proceedings of the 13th International Topic Meeting on Nuclear Applications of Accelerators.* **AccApp '17** (2017), 334–343. http://accapp20.org/wp-content/2017/data/pdfs/145-22822.pdf.

233. Ashby, M. F. *Materials Selection in Mechanical Design* doi:10.1016/c2009-0-25539-5 (Elsevier, 2011).

234. Niedermayer, U. & Boine-Frankenheim, O. *Beam Coupling Impedance Simulation in the Frequency Domain for the SIS100 Synchrotron* in *Proc. 5th International Particle Accelerator Conference (IPAC'14), Dresden, Germany, June 15-20, 2014* Dresden, Germany (JACoW, Geneva, Switzerland, 2014), 1665–1667. doi:10.18429/JACoW-IPAC2014-TUPRI045.

235. Bertarelli, A. Beam-Induced Damage Mechanisms and their Calculation. *CERN Yellow Reports,* 159 Pages. doi:10.5170/CERN-2016-002.159 (2016).

236. Ammigan, K. *et al.* Examination of Beryllium under Intense High Energy Proton Beam at CERN's HiRadMat Facility. *Proceedings of the 6th Int. Particle Accelerator Conf.* **IPAC2015,** 4 pages, 0.783 MB. doi:10.18429/JACOW-IPAC2015-WEPTY015 (2015).

237. Tomastik, C., Werner, W. & Störi, H. Oxidation of beryllium—a scanning Auger investigation. *Nuclear Fusion* **45,** 1061–1065. doi:10.1088/0029-5515/45/9/005 (2005).

238. Zhang, G., Wen, M., Wang, S., Chen, J. & Wang, J. Insights into thermal reduction of the oxidized graphite from the electro-oxidation processing of nuclear graphite matrix. *RSC Advances* **8,** 567–579. doi:10.1039/c7ra11578d (2018).

239. Assmann, R. *Collimation for the LHC high intensity beams* in *Proceedings of HB2010* (Morschach, Switzerland, 2010), 21–33. https://accelconf.web.cern.ch/HB2010/papers/moib03.pdf.

240. Antipov, S. A. *et al.* Transverse beam stability with low-impedance collimators in the High-Luminosity Large Hadron Collider: Status and challenges. *Phys. Rev. Accel. Beams* **23,** 034403. doi:10.1103/PhysRevAccelBeams.23.034403 (3 2020).

241. Guardia-Valenzuela, J. *et al.* Development and properties of high thermal conductivity molybdenum carbide - graphite composites. *Carbon* **135,** 72–84. doi:10.1016/j.carbon.2018.04.010 (2018).

242. Quaranta, E. *et al.* Modeling of beam-induced damage of the LHC tertiary collimators. *Physical Review Accelerators and Beams* **20,** 091002. doi:10.1103/PhysRevAccelBeams.20.091002 (2017).

243. Bertarelli, A. *et al.* Behaviour of advanced materials impacted by high energy particle beams. *Journal of Physics: Conference Series* **451,** 012005. doi:10.1088/1742-6596/451/1/012005 (2013).

244. *LHC Design Report* tech. rep. (2004). doi:10.5170/CERN-2004-003-V-1.

245. Tahir, N. A. *et al.* Calculations of high-power production target and beamdump for the GSI future Super-FRS for a fast extraction scheme at the FAIR Facility. *Journal of Physics D: Applied Physics* **38,** 1828–1837. doi:10.1088/0022-3727/38/11/023 (2005).

246. Bertarelli, A., Dallocchio, A. & Kurtyka, T. Dynamic Response of Rapidly Heated Cylindrical Rods: Longitudinal and Flexural Behavior. *Journal of Applied Mechanics* **75,** 031010. doi:10.1115/1.2839901 (2008).

247. Bertarelli, A. *et al. Permanent Deformation of the LHC Collimator Jaws Induced by Shock Beam Impact: an Analytical and Numerical Interpretation* in *Proceedings of the 10th European Particle Accelerator Conference, Edinburgh, Scotland* (2006), 1801–1803.

248. Torregrosa Martin, C., Perillo-Marcone, A., Calviani, M. & Muñoz-Cobo, J.-L. CERN antiproton target: Hydrocode analysis of its core material dynamic response under proton beam impact. *Physical Review Accelerators and Beams* **19,** 073402. doi:10.1103/PhysRevAccelBeams.19.073402 (2016).

249. Tahir, N. A., Burkart, F., Schmidt, R., Shutov, A. & Piriz, A. R. Review of hydrodynamic tunneling issues in high power particle accelerators. *Nuclear Instruments and Methods in Physics Research Section B: Beam Interactions with Materials and Atoms* **427,** 70–86. doi:10.1016/j.nimb.2018.04.009 (2018).

250. Bolz, P. *et al.* Dynamic Radiation Effects Induced by Short-Pulsed GeV U-Ion Beams in Graphite and h-BN Targets. *Shock and Vibration* **2021** (ed Lallart, M.) 1–11. doi:10.1155/2021/8825142 (2021).

251. Simos, N. *et al.* Proton irradiation effects in Molybdenum-Carbide-Graphite composites. *Journal of Nuclear Materials* **553,** 153049. doi:10.1016/j.jnucmat.2021.153049 (2021).

252. Harden, F., Bouvard, A., Charitonidis, N. & Kadi, Y. *HiRadMat: A Facility Beyond the Realms of Materials Testing* in *Proceedings of the 10th Int. Particle Accelerator Conf.* **IPAC2019** (2019), 4 pages, 1.520 MB. doi:10.18429/JACOW-IPAC2019-THPRB085.

253. Lin, S.-Y. Coupled vibration and natural frequency analysis of isotropic cylinders or disks of finite dimensions. *Journal of Sound and Vibration* **185,** 193–199. doi:10.1006/jsvi.1995.0374 (1995).

254. Ferrari, A., Sala, P. R., Fasso, A. & Ranft, J. *FLUKA: A Multi-Particle Transport Code* 2005. doi:10.2172/877507.

255. Mobs, E. *The CERN accelerator complex - 2019. Complexe des accélérateurs du CERN - 2019* 2019. https://cds.cern.ch/record/2684277.

256. Efthymiopoulos, I. *et al. HiRadMat: A New Irradiation Facility for Material Testing at CERN* in *Proceedings of the 2nd Int. Particle Accelerator Conf.* **IPAC2011** (2011), 1665–1667. https://cds.cern.ch/record/1403043.

257. *ANSYS Mechanical User's Guide – Release 19.2*

258. Carra, F., Charrondiere, C., Guinchard, M. & de Frutos, O. S. Design and Construction of an Instrumentation System to Capture the Response of Advanced Materials Impacted by Intense Proton Pulses. *Shock and Vibration* **2021** (ed Antonaci, P.) 1–20. doi:10.1155/2021/8855582 (2021).

259. Simon, P. *et al.* Dynamic Response of Graphitic Targets with Tantalum Cores Impacted by Pulsed 440-GeV Proton Beams. *Shock and Vibration* **2021,** 1–19. doi:10.1155/2021/8884447 (2021).

260. Fabian, J. *Characterization of carbon materials for high power-density beam impact applications* Master's thesis (2018).

261. Milošević, N. D., Vuković, G. S., Pavičić, D. Z. & Maglić, K. D. *International Journal of Thermophysics* **20,** 1129–1136. doi:10.1023/a:1022659005050 (1999).

262. Samoilov, V. M. & Shilo, D. V. Effect of Grain Size on the Thermal Expansion of Isotropic Synthetic Graphites. *Inorganic Materials* **41,** 1283–1288. doi:10.1007/s10789-005-0302-y (2005).

263. Politano, A. & Chiarello, G. Probing the Young's modulus and Poisson's ratio in graphene/metal interfaces and graphite: a comparative study. *Nano Research* **8,** 1847–1856. doi:10.1007/s12274-014-0691-9 (2015).

264. Morrison, C., Jivkov, A., Vertyagina, Y. & Marrow, T. Multi-scale modelling of nuclear graphite tensile strength using the site-bond lattice model. *Carbon* **100,** 273–282. doi:10.1016/j.carbon.2015.12.100 (2016).

265. Burger, C. P. & Riley, W. F. Effects of impedance mismatch on the strength of waves in layered solids. *Experimental Mechanics* **14,** 129–137. doi:10.1007/bf02322835 (1974).

266. Drechsel, P. *ANSYS® Mechanical*^{TM} *and Autodyn® Simulations of Thermo-mechanical Response of Graphite/Tantalum Targets Exposed to Short High Intensity Proton Beam Pulses* Master's thesis (2018).

267. Martin, C. T. *et al.* Experiment exposing refractory metals to impacts of 440 GeV/c proton beams for the future design of the CERN antiproton production target: Experiment design and online results. *Phys. Rev. Accel. Beams* **22,** 013401. doi:10.1103/PhysRevAccelBeams.22.013401 (1 2019).

268. Torregrosa Martin, C. *et al.* Scaled prototype of a tantalum target embedded in expanded graphite for antiproton production: Design, manufacturing, and testing under proton beam impacts. *Phys. Rev. Accel. Beams* **21,** 073001. doi:10.1103/PhysRevAccelBeams.21.073001 (7 2018).

269. Mohammadimehr, A., Solmus, İ., Ozyer, B. & Rees, D. A. S. Determination of Physical Properties and Thermal Conductivity of Graphite Foam with Image Analysis. *International Journal of Thermophysics* **41,** 45. doi:10.1007/s10765-020-02623-w (2020).

270. Calvo, D., Coli, S., Giraudo, G., Wheadon, R. & Zotti, L. Thermal performance of carbon foams used as heat sink for the pixel MVD PANDA. *Journal of Instrumentation* **6,** C12015–C12015. doi:10.1088/1748-0221/6/12/C12015 (2011).

271. Torregrosa Martin, C. *et al.* Scaled prototype of a tantalum target embedded in expanded graphite for antiproton production: Design, manufacturing, and testing under proton beam impacts. *Physical Review Accelerators and Beams* **21,** 073001. doi:10.1103/PhysRevAccelBeams.21.073001 (2018).

272. Zaitsev, A. M., Wang, W., Moe, K. S. & Johnson, P. Spectroscopic studies of yellow nitrogen-doped CVD diamonds. *Diamond and Related Materials* **68,** 51–61. doi:10.1016/j.diamond.2016.06.002 (2016).

273. Williams, G. *et al. Thermal Conductivity of Electrically Conductive Highly Boron Doped Diamond and its Applications at High Frequencies* in *2018 17th IEEE Intersociety Conference on Thermal and Thermomechanical Phenomena in Electronic Systems (ITherm)* (IEEE, 2018), 235–239. doi:10.1109/ITHERM.2018.8419493.

274. Walker, J. Optical absorption and luminescence in diamond. *Reports on Progress in Physics* **42,** 1605–1659. doi:10.1088/0034-4885/42/10/001 (1979).

275. Clark, C. D., Ditchburn, R. W., Dyer, H. B. & Mott, N. F. The absorption spectra of natural and irradiated diamonds. *Proceedings of the Royal Society of London. Series A. Mathematical and Physical Sciences* **234,** 363–381. doi:10.1098/rspa.1956.0040 (1956).

276. Lannoo, M. & Stoneham, A. M. The optical absorption of the neutral vacancy in diamond. *Journal of Physics and Chemistry of Solids* **29,** 1987–2000. doi:10.1016/0022-3697(68)90049-8 (1968).

277. Clark, C. D., Walker, J. & Ditchburn, R. W. The neutral vacancy in diamond. *Proceedings of the Royal Society of London. A. Mathematical and Physical Sciences* **334,** 241–257. doi:10.1098/rspa.1973.0090 (1973).

278. Davies, Lawson, Collins, Mainwood & Sharp. Vacancy-related centers in diamond. *Physical review. B, Condensed matter* **46,** 13157–13170. doi:10.1103/PhysRevB.46.13157 (1992).

279. Collins, A. T. & Kiflawi, I. The annealing of radiation damage in type Ia diamond. *Journal of physics. Condensed matter : an Institute of Physics journal* **21,** 364209. doi:10.1088/0953-8984/21/36/364209 (2009).

280. Kiflawi, I., Collins, A. T., Iakoubovskii, K. & Fisher, D. Electron irradiation and the formation of vacancy–interstitial pairs in diamond. *Journal of Physics: Condensed Matter* **19,** 046216. doi:10.1088/0953-8984/19/4/046216 (2007).

281. Newton, M. E., Campbell, B. A., Twitchen, D. J., Baker, J. M. & Anthony, T. R. Recombination-enhanced diffusion of self-interstitial atoms and vacancy–interstitial recombination in diamond. *Diamond and Related Materials* **11,** 618–622. doi:10.1016/S0925-9635(01)00623-9 (2002).

282. Twitchen, D. J., Hunt, D. C., Smart, V., Newton, M. E. & Baker, J. M. Correlation between ND1 optical absorption and the concentration of negative vacancies determined by electron paramagnetic resonance (EPR). *Diamond and Related Materials* **8,** 1572–1575. doi:10.1016/S0925-9635(99)00038-2 (1999).

283. Hyde-Volpe, D., Slepetz, B. & Kertesz, M. The [V-C=C-V] Divacancy and the Interstitial Defect in Diamond: Vibrational Properties. *The Journal of Physical Chemistry C* **114,** 9563–9567. doi:10.1021/jp9105508 (2010).

284. Slepetz, B. & Kertesz, M. Divacancies in diamond: a stepwise formation mechanism. *Physical chemistry chemical physics : PCCP* **16,** 1515–1521. doi:10.1039/C3CP53384K (2014).

285. Lowther. Excited states of the vacancy in diamond. *Physical review. B, Condensed matter* **48,** 11592–11601. doi:10.1103/PhysRevB.48.11592 (1993).

286. Davies, G. Charge states of the vacancy in diamond. *Nature* **269,** 498–500. doi:10.1038/269498a0 (1977).

287. Hunt, D. C. *et al.* Identification of the neutral carbon <100>-split interstitial in diamond. *Physical Review B* **61,** 3863–3876. doi:10.1103/PhysRevB.61.3863 (2000).

288. Faulkner, E. A. & Lomer, J. N. Electron spin resonance in electron-irradiated diamond. *Philosophical Magazine* **7,** 1995–2002. doi:10.1080/14786436208214468 (1962).

289. Li, L. H. & Lowther, J. E. Plane-wave pseudopotential calculations of intrinsic defects in diamond. *Journal of Physics and Chemistry of Solids* **58,** 1607–1610. doi:10.1016/S0022-3697(97)00029-2 (1997).

290. Walker, J. An optical study of the TR12 and 3H defects in irradiated diamond. *Journal of Physics C: Solid State Physics* **10,** 3031–3037. doi:10.1088/0022-3719/10/16/013 (1977).

291. Davies, G., Smith, H. & Kanda, H. Self-interstitial in diamond. *Physical Review B* **62,** 1528–1531. doi:10.1103/PhysRevB.62.1528 (2000).

292. Allers, L., Collins, A. T. & Hiscock, J. The annealing of interstitial-related optical centres in type II natural and CVD diamond. *Diamond and Related Materials* **7,** 228–232. doi:10.1016/S0925-9635(97)00161-1 (1998).

293. Davies, G. Optical Properties of Electron-Irradiated Type Ia Diamond. *Proceedings of the Royal Society of London. Series A. Mathematical and Physical Sciences* **336,** 507–523. http://www.jstor.org/stable/78563 (1974).

294. Iakoubovskii, K. & Adriaenssens, G. J. Optical Study of Some Interstitial-Related Centres in CVD Diamond. *physica status solidi (a)* **181,** 59–64. doi:10.1002/1521-396X(200009)181:1{\textless}59::AID-PSSA59{\textgreater}3.0.CO;2-D (2000).

295. Goss, J. P. *et al.* Self-interstitial aggregation in diamond. *Physical Review B* **63.** doi:10.1103/PhysRevB.63.195208 (2001).

296. Thrower, P. A. *Chemistry and physics of carbon: A series of advances : vol. 21* (Marcel Dekker, Basel, 1989).

297. Soltamova, A. A. *et al.* Electron paramagnetic resonance detection of the giant concentration of nitrogen vacancy defects in sintered detonation nanodiamonds. *JETP Letters* **92,** 102–106. doi:10.1134/S0021364010140067 (2010).

298. Kiflawi, Mainwood, Kanda & Fisher. Nitrogen interstitials in diamond. *Physical review. B, Condensed matter* **54,** 16719–16726. doi:10.1103/physrevb.54.16719 (1996).

299. Goss, J. P., Briddon, P. R., Papagiannidis, S. & Jones, R. Interstitial nitrogen and its complexes in diamond. *Physical Review B* **70.** doi:10.1103/PhysRevB.70.235208 (2004).

300. Taylor, W. R., Canil, D. & Judith Milledge, H. Kinetics of Ib to IaA nitrogen aggregation in diamond. *Geochimica et Cosmochimica Acta* **60,** 4725–4733. doi:10.1016/S0016-7037(96)00302-X (1996).

301. Evans, T. & Zengdu, Q. The kinetics of the aggregation of nitrogen atoms in diamond. *Proceedings of the Royal Society of London. Series A. Mathematical and Physical Sciences* **381,** 159–178. doi:10.1098/rspa.1982.0063 (1982).

302. Shigley, J. E., Breeding, C. M. & Shen, A. H.-T. An Updated Chart on The Characteristics of HPHT-Grown Synthetic Diamonds. *Gems & Gemology* **40,** 303–313. doi:10.5741/GEMS.40.4.303 (2004).

303. Kiflawi, I., Mayer, A. E., Spear, P. M., Wyk, J. A. V. & Woods, G. S. Infrared absorption by the single nitrogen and A defect centres in diamond. *Philosophical Magazine B* **69,** 1141–1147. doi:10.1080/01418639408240184 (1994).

304. Collins, A. T. Things we still don't know about optical centres in diamond. *Diamond and Related Materials* **8,** 1455–1462. doi:10.1016/S0925-9635(99)00013-8 (1999).

305. Collins, A. T. Vacancy enhanced aggregation of nitrogen in diamond. *Journal of Physics C: Solid State Physics* **13,** 2641–2650. doi:10.1088/0022-3719/13/14/006 (1980).

306. Beveratos, A. *et al.* Room temperature stable single-photon source. *The European Physical Journal D - Atomic, Molecular and Optical Physics* **18,** 191–196. doi:10.1140/epjd/e20020023 (2002).

307. Gruber, A. Scanning Confocal Optical Microscopy and Magnetic Resonance on Single Defect Centers. *Science* **276,** 2012–2014. doi:10.1126/science.276.5321.2012 (1997).

308. Knowles, H. S., Kara, D. M. & Atatüre, M. Observing bulk diamond spin coherence in high-purity nanodiamonds. *Nature materials* **13,** 21–25. doi:10.1038/nmat3805 (2014).

309. Doherty, M. W. *et al.* The nitrogen-vacancy colour centre in diamond. *Physics Reports* **528,** 1–45. doi:10.1016/j.physrep.2013.02.001 (2013).

310. Davies, G. Dynamic Jahn-Teller distortions at trigonal optical centres in diamond. *Journal of Physics C: Solid State Physics* **12,** 2551–2566. doi:10.1088/0022-3719/12/13/019 (1979).

311. Du Preez, L. *Electron Paramagnetic Resonance and Optical Investigations of Defect Centres in Diamond* Dissertation (University of the Witwatersrand, Johannesburg, 1965). http://wiredspace.wits.ac.za/bitstream/handle/10539/20866/du%20Preez,%20L.%201965.pdf?sequence=1&isAllowed=y.

312. Loubser, J. & Van Wyk, J. Optical spin-polarisation in a triplet state in irradiated and annealed type 1b diamonds. *Diamond Research,* 11–14 (1977).

313. Mita. Change of absorption spectra in type-Ib diamond with heavy neutron irradiation. *Physical review. B, Condensed matter* **53,** 11360–11364. doi:10.1103/PhysRevB.53.11360 (1996).

314. Manson, N. B. & Harrison, J. P. Photo-ionization of the nitrogen-vacancy center in diamond. *Diamond and Related Materials* **14,** 1705–1710. doi:10.1016/j.diamond.2005.06.027 (2005).

315. Mainwood. Nitrogen and nitrogen-vacancy complexes and their formation in diamond. *Physical review. B, Condensed matter* **49,** 7934–7940. doi:10.1103/PhysRevB.49.7934 (1994).

316. Jones, R., Goss, J. P., Pinto, H. & Palmer, D. W. Diffusion of nitrogen in diamond and the formation of A-centres. *Diamond and Related Materials* **53,** 35–39. doi:10.1016/j.diamond.2015.01.002 (2015).

317. Meijer, J. *et al.* Generation of single color centers by focused nitrogen implantation. *Applied physics letters* **87,** 261909. doi:10.1063/1.2103389 (2005).

318. Sumikura, H., Hirama, K., Nishiguchi, K., Shinya, A. & Notomi, M. Highly nitrogen-vacancy doped diamond nanostructures fabricated by ion implantation and optimum annealing. *APL Materials* **8,** 031113. doi:10.1063/5.0001922 (2020).

319. Green, B. *Optical and magnetic resonance studies of point defects in single crystal diamond* Dissertation (University of Warwick, Coventry, 2013). http://wrap.warwick.ac.uk/58600/.

320. Mita, Y., Nisida, Y., Suito, K., Onodera, A. & Yazu, S. Photochromism of H2 and H3 centres in synthetic type Ib diamonds. *Journal of Physics: Condensed Matter* **2,** 8567–8574. doi:10.1088/0953-8984/2/43/002 (1990).

321. Mita, Y. *et al.* Recovery process of photochromism of H2 and H3 centres in diamond. *Diamond and Related Materials* **2,** 768–772. doi:10.1016/0925-9635(93)90220-V (1993).

322. Nadolinny, V. A. *et al.* Mechanisms of nitrogen aggregation in nickel- and cobalt-containing synthetic diamonds. *Diamond and Related Materials* **9,** 883–886. doi:10.1016/S0925-9635(99)00356-8 (2000).

323. Lowther, J. E. Nickel defect centers in diamond. *Physical Review B* **51,** 91–96. doi:10.1103/physrevb.51.91 (1995).

324. Chanier, T., Pryor, C. E. & Flatté, M. E. Substitutional nickel impurities in diamond: Decoherence-free subspaces for quantum information processing. *EPL (Europhysics Letters)* **99,** 67006. doi:10.1209/0295-5075/99/67006 (2012).

325. Thiering, G. & Gali, A. Magneto-optical spectra of the split nickel-vacancy defect in diamond. *Physical Review Research* **3.** doi:10.1103/physrevresearch.3.043052 (2021).

326. Collins, A. T. & Spear, P. M. The 1.40 eV and 2.56 eV centres in synthetic diamond. *Journal of Physics C: Solid State Physics* **16,** 963–973. doi:10.1088/0022-3719/16/5/023 (1983).

327. Nazaré, M. H., Neves, A. J. & Davies, G. Optical studies of the 1.40-eV Ni center in diamond. *Physical Review B* **43,** 14196–14205. doi:10.1103/physrevb.43.14196 (1991).

328. Karaveli, S. *et al.* Modulation of nitrogen vacancy charge state and fluorescence in nanodiamonds using electrochemical potential. *Proceedings of the National Academy of Sciences* **113,** 3938–3943. doi:10.1073/pnas.1504451113 (2016).

329. Larena, A. & Pinto, G. Measuring Properties of Industrial Polymer Films Using Interference Fringes in the Infrared Region. *Spectroscopy Letters* **25,** 447–461. doi:10.1080/00387019208021520 (1992).

330. Orwa, J. O. *et al.* Engineering of nitrogen-vacancy color centers in high purity diamond by ion implantation and annealing. *Journal of Applied Physics* **109,** 083530. doi:10.1063/1.3573768 (2011).

331. Everall, N. J. Confocal Raman Microscopy: Why the Depth Resolution and Spatial Accuracy Can Be Much Worse Than You Think. *Applied Spectroscopy* **54,** 1515–1520. doi:10.1366/0003702001948439 (2000).

332. Klinger, T. *et al.* Overview of first Wendelstein 7-X high-performance operation. *Nuclear Fusion* **59,** 112004. doi:10.1088/1741-4326/ab03a7 (2019).

333. Weick, H. *Material Testing Demands by Heavy-Ion Pulsed Beams* in (Presented at the International HiRadMat Workshop, CERN, CH, 2019). https://indico.cern.ch/event/767689/sessions/311786/attachments/1878457/3094042/HiRadMat_Weick.pdf.

334. Spiller, P. *et al.* The FAIR Heavy Ion Synchrotron SIS100. *Journal of Instrumentation* **15,** T12013–T12013. doi:10.1088/1748-0221/15/12/t12013 (2020).

335. Maciariello, F. *et al. High Intensity Beam Test of Low Z Materials for the Upgrade of SPS-to-LHC Transfer Line Collimators and LHC Injection Absorbers* in *Proc. of International Particle Accelerator Conference (IPAC'16), Busan, Korea, May 8-13, 2016* (JACoW, Geneva, Switzerland, 2016), 1218–1221. doi:10.18429/JACoW-IPAC2016-TUPMB052.

336. Solfiti, E. *et al.* Flexible graphite as beam dumping material in the TDE blocks of the Large Hadron Collider. *Procedia Structural Integrity* **28,** 2228–2234. doi:10.1016/j.prostr.2020.11.051 (2020).

337. Yonehara, K. *Megawatt upgrade of NuMI target system* in *Proceedings of The 22nd International Workshop on Neutrinos from Accelerators — PoS(NuFact2021)* (Sissa Medialab, 2022). doi:10.22323/1.402.0107.

338. Tariq, S. *et al.* Design of the LBNF Beamline Target Station. en. *Proceedings of the North American Particle Accelerator Conf.* **NAPAC2016,** USA. doi:10.18429/JACOW-NAPAC2016-MOPOB35 (2017).

339. Johnson, D. J. Structure-property relationships in carbon fibres. *Journal of Physics D: Applied Physics* **20,** 286–291. doi:10.1088/0022-3727/20/3/007 (1987).

340. Huang, X. Fabrication and Properties of Carbon Fibers. *Materials* **2,** 2369–2403. doi:10.3390/ma2042369 (2009).

341. Huang, Y. & Young, R. J. Effect of fibre microstructure upon the modulus of PAN- and pitch-based carbon fibres. *Carbon* **33,** 97–107. doi:10.1016/0008-6223(94)00109-D (1995).

342. Wang, J.-l., Gu, M., Ma, W.-g., Zhang, X. & Song, Y. Temperature dependence of the thermal conductivity of individual pitch-derived carbon fibers. *New Carbon Materials* **23,** 259–263. doi:10.1016/S1872-5805(08)60029-3 (2008).

343. Windhorst, T. & Blount, G. Carbon-carbon composites: a summary of recent developments and applications. *Materials & Design* **18,** 11–15. doi:10.1016/S0261-3069(97)00024-1 (1997).

344. Chen, X., Chen, L., Zhang, C., Song, L. & Zhang, D. Three-dimensional needle-punching for composites – A review. *Composites Part A: Applied Science and Manufacturing* **85,** 12–30. doi:10.1016/j.compositesa.2016.03.004 (2016).

345. Lacombe, A., Pichon, T. & Lacoste, M. *High Temperature Composite Nozzle Extensions: A Mature and Efficient Technology to Improve Upper Stage Liquid Rocket Engine Performance* in *43rd AIAA/ASME/SAE/ASEE Joint Propulsion Conference & Exhibit* (American Institute of Aeronautics and Astronautics, Reston, Virigina, 2007). doi:10.2514/6.2007-5470.

346. Devi, G. R. & Rao, K. R. Carbon Carbon Composites: An Overview. *Defence Science Journal* **43,** 369–383. doi:10.14429/dsj.43.4291 (1993).

347. Klett, J. in *Cellular Ceramics* (eds Scheffler, M. & Colombo, P.) 137–157 (Wiley-VCH Verlag GmbH & Co. KGaA, Weinheim, FRG, 2005). doi:10.1002/3527606696.ch2f.

348. Barbier, G. *et al.* Mechanical studies towards a silicon micro-strip super module for the ATLAS inner detector upgrade at the high luminosity LHC. *Journal of Instrumentation* **9,** P04018–P04018. doi:10.1088/1748-0221/9/04/P04018 (2014).

349. PANDA Collaboration *et al. Technical Design Report for the: PANDA Micro Vertex Detector* 2012. arXiv: `1207.6581 [physics.ins-det]`.

350. Lechner, A. *et al. Dilution requirements for the FCC-hh dump* in (Presented as the 4th Annual Meeting of the Future Circular Collider Study, Amsterdam, NL, 2018). https://indico.cern.ch/event/656491/contributions/2947272/attachments/1631698/2601617/2018_12_04_fccdump.pdf.

351. Harris, P. J. F. New Perspectives on the Structure of Graphitic Carbons. *Critical Reviews in Solid State and Materials Sciences* **30,** 235–253. doi:10.1080/10408430500406265 (2005).

352. Jurkiewicz, K., Duber, S., Fischer, H. E. & Burian, A. Modelling of glass-like carbon structure and its experimental verification by neutron and X-ray diffraction. *Journal of Applied Crystallography* **50,** 36–48. doi:10.1107/S1600576716017660 (2017).

353. Jurkiewicz, K. *et al.* Evolution of glassy carbon under heat treatment: correlation structure–mechanical properties. *Journal of Materials Science* **53,** 3509–3523. doi:10.1007/s10853-017-1753-7 (2018).

354. Sharma, S., Shyam Kumar, C. N., Korvink, J. G. & Kübel, C. Evolution of Glassy Carbon Microstructure: In Situ Transmission Electron Microscopy of the Pyrolysis Process. *Scientific reports* **8,** 16282. doi:10.1038/s41598-018-34644-9 (2018).

355. Shiell, T. B. *et al.* The composition, structure and properties of four different glassy carbons. *Journal of Non-Crystalline Solids* **522,** 119561. doi:10.1016/j.jnoncrysol.2019.119561 (2019).

356. Vomero, M. *et al.* Highly Stable Glassy Carbon Interfaces for Long-Term Neural Stimulation and Low-Noise Recording of Brain Activity. *Scientific reports* **7,** 40332. doi:10.1038/srep40332 (2017).

357. Torregrosa Martin, C. *et al.* First prototypes of the new design of the CERN's antiproton production target. *Material Design & Processing Communications* **1,** e38. doi:10.1002/mdp2.38 (2019).

358. Cardonne, S. M., Kumar, P., Michaluk, C. A. & Schwartz, H. D. Tantalum and its alloys. *International Journal of Refractory Metals and Hard Materials* **13,** 187–194. doi:10.1016/0263-4368(95)94023-R (1995).

359. Schmidt, F. F. & Ogden, H. R. *The Engineering Properties of Tantalum and Tantalum Alloys* 1963. https://apps.dtic.mil/dtic/tr/fulltext/u2/426344.pdf.

360. Llorca, F., Roy, G. & Antoine, P. Ductile damage of tantalum under spalling effects. Experimental and metallurgical analysis. *Le Journal de Physique IV* **10,** Pr9-775-Pr9–780. doi:10.1051/jp4:20009128 (2000).

361. Walters, W., Gooch, W. & Burkins, M. The penetration resistance of a titanium alloy against jets from tantalum shaped charge liners. *International Journal of Impact Engineering* **26,** 823–830. doi:10.1016/S0734-743X(01)00135-X (2001).

362. Torregrosa Martin, C. *et al.* Experiment exposing refractory metals to impacts of 440 GeV / c proton beams for the future design of the CERN antiproton production target: Experiment design and online results. *Physical Review Accelerators and Beams* **22,** 013401. doi:10.1103/PhysRevAccelBeams.22.013401 (2019).

363. van der Walt, S., Colbert, S. C. & Varoquaux, G. The NumPy Array: A Structure for Efficient Numerical Computation. *Computing in Science & Engineering* **13,** 22–30. doi:10.1109/MCSE.2011.37 (2011).

364. Van Rossum, G. & Drake, F. L. *Python 3 Reference Manual* (CreateSpace, Scotts Valley, CA, 2009).

365. Cooley, J. W. & Tukey, J. W. An algorithm for the machine calculation of complex Fourier series. *Mathematics of Computation* **19,** 297. doi:10.1090/S0025-5718-1965-0178586-1 (1965).

366. Grossmann, A. & Morlet, J. Decomposition of Hardy Functions into Square Integrable Wavelets of Constant Shape. *SIAM Journal on Mathematical Analysis* **15,** 723–736. doi:10.1137/0515056 (1984).

367. Lee, G., Gommers, R., Waselewski, F., Wohlfahrt, K. & O'Leary, A. PyWavelets: A Python package for wavelet analysis. *Journal of Open Source Software* **4,** 1237. doi:10.21105/joss.01237 (2019).

Acknowledgements

This thesis would not have been possible without the support of a great number of people. In particular, I sincerely thank:

- **Prof. Dr. Christina Trautmann** for her support, guidance and persistent encouragement to wrap up my thesis. I thank her especially for all the time and evenings spent, even during holidays, on reading and correcting my manuscripts and this work.
- **Prof. Dr. Maria Eugenia Toimil-Molares** for accepting to referee this thesis under anything but normal circumstances.
- **Prof. Dr. Gerhard Wilde** for acting as a referee.
- **Prof. Dr. Wolfgang Ensinger and Prof. Dr. Karsten Durst** for being members of the examination committee.
- **Dr. Marilena Tomut** for all the opportunities that I was able to explore due to her continuous support since starting my academic journey, for sharing her ideas and previous work that lead to this thesis and for allowing me the liberty to pursue them as I see fit.
- **Dr. Daniel Severin and Dr. Markus Bender** for introducing me to the M-branch, their valuable help during beam time, support and advice.
- **Dr. Kay-Obbe Voss** for his sheer unlimited amount of experimental wisdom and patience that were essential for all irradiation experiments and his support during beam time.
- **Dr. Peter Katrik** for providing FLUKA simulations, sharing his knowledge about simulation and the tons of fun we had in the office.
- **Arne Siegmund and Elko Schubert** for their technical help in realizing all irradiation experiments.
- **Dr. Bettina Lommel** for never flinching away whenever I requested another hundred or so graphite samples for either me or my students.
- **Dr. Ioannis Tzifas** for setting up the on-line Raman spectrometer at M-branch and nights spent in the control room.
- **Dr. Michael Wagner, Dr. Alexey Prosvetov, Dr. Philipp Bolz and Jacob Lee** for being there with me on this very intense ride from the very start (or even earlier), all the discussions, all the help that you've provided to navigate issues and many thanks for all the fun times.
- **Philipp Drechsel** for the infinite number of ANSYS simulations to actually make sense of the experimental data and double checking all of my analytical calculations.
- **Eva Spomer, Marvin Hoffer, Jan-Hendrik Rockstedt and Fabian Jäger** who contributed to this work by measuring and cataloging countless of samples in the lab even before the first irradiation, by their support during beam time and by their great enthusiasm.
- **Dr. Katharina Kupka, Dr. Christian Hubert, Dr. Anton Romanenko** for sharing countless hours with me in a small blue container during beam time and for their insights during all of our discussions.
- **Materials Research group at GSI** for all the fun times, great coffee and cake breaks, helpful discussions and support during beam time.

- **RHP Technologies GmbH** for providing the diamond-based copper and titanium composite samples used in this work.
- **Dr. Yacine Kadi, Dr. Fiona Harden and Aymeric Bouvard** for their valuable support during my time as an external user at HiRadMat.
- **Dr. Nikolaos Charitonidis** for always having my back.
- **My loved ones** for their unlimited patience and support. Without you, I wouldn't have managed.

EuCARD-2 is co-funded by the partners and the European Commission under Capacities 7th Framework Programme, Grant Agreement 312453

This project has received funding from the European Union's Horizon 2020 Research and Innovation programme under Grant Agreement No 730871.

Wissenschaftlicher Werdegang

Pascal Simon

2009	Abitur an der Prälat-Diehl-Schule, Groß-Gerau
10/2010 – 12/2016	Studium Materialwissenschaft an der Technischen Universität Darmstadt
01/2017 – 08/2023	Promotion an der Technischen Universität Darmstadt, Fachbereich Materialwissenschaft, durchgeführt im Bereich Materialforschung am GSI Helmholtzzentrum für Schwerionenforschung